Aus dem Max-Planck-Institut für Kolloid- und Grenzflächenforschung

A neglected World:

Transition Metal Nitride and Metal Carbide Based Nanostructures

Novel Synthesis and Future Perspectives

Habilitationsschrift

Zur Erlangung des akademischen Grades

Doktor rerum naturalium habilitatus

(Dr. rer. nat. habil.)

in der Wissenschaftsdisziplin Physikalische Chemie

eingereicht an der

Mathematisch-Naturwissenschaftlichen Fakultät

der Universität Potsdam

von

Dr. Cristina Giordano

geboren am 07.05.1974 in Palermo

Potsdam, im März 2014

Alla mia famiglia,

per l´infinito amore…

TABLE OF CONTENTS

M´illumino

d´Immenso

Mattina, Giuseppe Ungaretti

1917

1. Introduction/Motivation

The most fascinating aspect of nature is surely its multiplicity and, through evolution, its capacity to adapt to current necessities. Similarly, humankind has adapted and, with a bit of ingenuity, has revolutionized its everyday life in the name of progress. In this (re)evolution, materials have surely fulfilled a key role, so much that key steps of human development have been denoted with material names (age of stone, bronze, iron, etc.). However, while earliest craftsmen based their processes on the "*trial and error*" approach, nowadays new materials are prepared with awareness and, thanks to technology, enhanced control over the whole process. This way, the attention can be more and more focused toward complex materials (ternary and quaternary systems, smart materials, composites, etc.), in some cases taking again inspiration from nature (biomimetic approach).

One important contribution in the search for new materials is surely the discovery of the nano-world. In this realm, properties are sensible to size and morphology, so that each nano-system can be considered as a potential new material.

Potentiality of nano-sized materials has been largely proved, and a massive part of both fundamental and applied research is today devoted to the study and field of applications of these materials. It will be sufficient to go to Web of Knowledge[SM] and type "nano*" to find more than 1 Million[1] entries concerning related publications, about 130.000 only in 2012. However, a closer look will show that a significant percentage of this research is related to oxides and metals (over 40.000 entries), while the number drastically drops when searching for other systems, such as metallic ceramics (namely transition metal nitrides and metal carbides), which display less than 100 entries (2012). These numbers have to be considered just as a rough estimation of course, but can still give an idea about the worldwide predilection for some classes of materials over others. Specifically for metallic ceramics, the lack of publications does not reflect their potential but rather the difficulties related to their synthesis as dense (compact) and defect-free structures, fundamental prerequisites for advanced mechanical applications. However, potentialities of these materials go far beyond engineering purposes. As suggested by their name, metallic ceramics possess an intriguing combination of properties that place them between high performance ceramics and pure metals. The number of

---

[1] This number does not contain medical, biomedical, geological and environmental entries.

envisaged applications can then be very broad and can even be broadened going to the nanoscale (e.g. higher surface area, tailored properties via size-control, easier shaping and processing, quantum effects, etc.). In simpler words, there is more than just tougher cutting tools to be discovered. One steady step, however, must be overcome: the necessity to simplify their production to make these systems readily available, in reasonable amounts, both for better investigation and easier testing/processing.

The present *habilitation* work aims to close the gap between preparation and processing, indicating novel synthetic pathways for an easier, unexpansive, and sustainable synthesis of transition metal nitride and carbide based nanostructures and easier processing thereafter. In particular, aiming at expanding the coverage of ceramic materials in applied science, several key-points are encompassed in the present work, for instance the influence of the starting materials was carefully studied, also using complex precursors (e.g. biopolymers), to gain control over composition, size and morphology. In this way, hierarchical structures (such as fibres, mesoporous materials, replica of bio-objects etc.) could also be obtained. The presented routes are, concept-wise, similar, and they all start by building up a secondary metal ion-N/C precursor network. This starting ionic glass can be further processed, e.g. it can be printed or coated, form fibres or films, and can be transferred by calcination into a variety of binary, ternary and quaternary transition metal nitride and carbide based nanostructures of high degree of crystallinity and definition. All this flexibility of shape is still gained without losing simplicity, sustainability and reliability of the process. Implicitly, a control over size/shape will reflect different reactivity, bringing tailored system for selected applications. Just to give an example: a material with high porosity will be highly desirable for catalytic applications and, if porosity is accompanied by "continuity", this material will be a perfect candidate in electrochemistry applications. However, in both cases, the resulting material will have poor mechanical properties in terms of ductility and hardness, for which a dense and pore-free structure must be favoured[2]. Furthermore, since MN/MC properties are strongly dependent on the metal/non-metal ratio (M/nM), in this thesis special attention was devoted to characterization. Finally, some applications will be shown, using model reactions as proof of principles.

---

[2] The pores represent stress points, where the fractures can begin.

Summarizing, the main achievement of this *habilitation* work was to establish sustainable and easy-to-handle routes towards a wide variety of nano-sized metal nitride and carbide based systems, employing readily available materials and reducing cost/temperature. These routes can be considered "beyond the lab process" allowing large scale synthesis, far beyond the usual chemistry lab amounts. Control over composition, size and morphology could also be obtained with simple adjustment of the main route. Last but not least, the nature of the precursor materials also allows easy processing, including printing, coating, casting, film and thin layers preparation, etc.

In the present manuscript the next two chapters are dedicated to a brief overview about nano-sized material (chapter 2) and about metal nitride and carbide properties, fields of application and classical synthetic strategies (chapter 3). The following chapters discuss the main results obtained by our research work, starting with devising novel synthetic strategies (chapter 4), subsequent processing (chapter 5 and 6) and examples of applications of the prepared systems (chapter 7). Titles of sessions, which describe published results from our group, are marked with the corresponding reference number. In chapter 8 final remarks are given, including outlook on future research directions.

The research performed up to now represents just a beginning, disclosing the tip of an iceberg. Once the synthesis of these materials can be made straightforward, thanks to our research, any further modification, combination, manipulation, is in principle possible and new systems can be designed in a well-controlled manner.

2. Nanosized Materials: into the world of discontinuity

2.1 The Importance of Materials

After a rich period, culminating in the Iron Age (~500 BC), the discovery of new materials somehow slowed down, and up to the XIX century, mainly known materials were used, with the only exception of *hydraulic concrete* invented by the Romans, whose shining accomplishment is the Coliseum (~70 AC) in Rome [1]. This hibernation time (synthesis-wise) lasted until the discovery by Friedrich Wöhler of the synthetic pathway to produce urea in 1828[3] [4]. According to a popular myth Wöhler's discovery dramatically crashed into the *theory of vitalism*[4] [5] and gave birth to modern organic chemistry. In XIX, the new challenge was to replace natural compounds (sometimes difficult to obtain or available in limited quantity) with synthetic materials[5] [1]. On the other side, inorganic chemistry mainly concentrated toward the production of alloys, and between the end of the XIX and the beginning of the XX centuries, the age of steel ended and the age of plastic began. A few decades later, the age of "nano" silently made its entrance. Milestone of the age of "nano" are surely the work of Wolfgang Ostwald [6] outlined in his book *"Die Welt der vernachlässigten Dimensionen"* (The world of the lost dimensions) in 1915, then with Richard Zsigmondy, one of the pioneers of Colloid Chemistry, Nobel Prize winner in chemistry in 1925 for his accurate work on colloidal Gold [7]. In 1959, nano-science was still an exotic land and I like thinking that it has been evolving between the prophetic speech of Richard Feynman *"There is plenty of room at the bottom"* [8] and the Drexler vision of molecular manufacturing, allowing us to build one day nano-robots able to perform at the nanoscale individually.

Experiments made at IBM can be considered an amusing landmark of this evolution. The first was in 1989 conducted by Eigler and Schweizer, who wrote the smallest logo ever (IBM) with 35 Xenon atoms on a nickel crystal, at low temperature (3K, to reduce atom motion) using a scanning tunnelling microscope (STM).

---

[3] Funny enough beside his intensive work on urea (a key compound in this *Habilitation* work), Wöhler also discovered (together with Deville) Si_3N_4 [2], along the synthesis of some carbides of alkaline earth metal (e.g. CaC_2) [3]

[4] *"A doctrine that the processes of life are not explicable by the laws of physics and chemistry alone and that life is in some part self-determining."* Merriam-Webster dictionary definition.

[5] For instance substituting the ivory of billiard balls with celluloid (with great relief of elephants), or finding new types of colorants to enlarge the range of available colours.
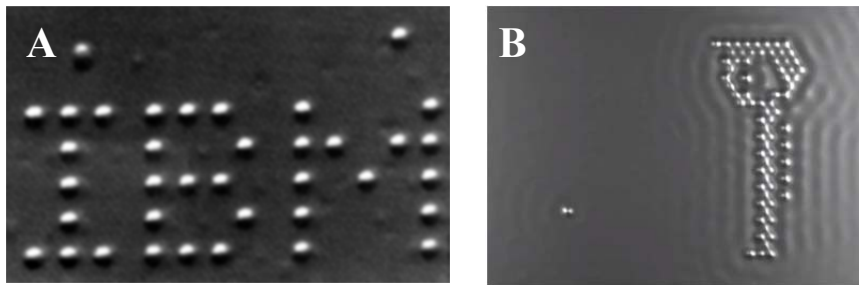
Figure 2.1. A) IBM logo written using xenon atoms on a nickel crystal,
source: http://www.nytimes.com/1990/04/05/us/2-researchers-spell-ibm-atom-by-atom.html.
B) A photogram of the IBM movie "*A Boy and his Atom: The World's Smallest Movie*" source:
http://www.youtube.com/watch?v=oSCX78-8-q0.

Today (2013) IBM surprises us again with the video "*A Boy and his Atom: The World's Smallest Movie*" (a photogram is displayed in figure 2.1.B).

This does not cover the gap with Drexler dreams, and his approach can be still considered visionary[6] but nano-research is still relatively young compared to other disciplines and nevertheless, compared to its age, it has already progressed enormously.

In the end, we should not forget that only 50 years ago, repairing tendons and replacing limbs was also not more than just a vision.

2.2 What is a Nanomaterial?

In some respects, the XXI century might be then considered the "*age of nano*", because nanoparticles are more and more present in our everyday life in many different fields, from energy and environment, to electronics, construction, medicine, transport, but also packaging, paint and coatings, sport, textiles and more[7]. With nanotechnology, we have learned how to manipulate nanoparticles to make them functional, and although we have not yet reached the "molecular manufacturing" envisioned by Drexler, the field has made giant strides.

However, as it happens often, nanoparticles have not been created by humankind. In nature they can be found either as mere phase (salt nanoparticles from aerosol, volcanic particles, carbon black, etc.) or as complex hierarchical structures (in

---

[6]The main criticism concerns the fact that molecules and atoms are not rigid but endless moving (as pointed out by Smalley and Silby). Furthermore, if assemblers and replicators are made, will they be dangerous on a long range?
[7] See also: http://www.nanoandme.org/nano-products

marine shells, bones, tooth, wood, nacre, insect skeletons, etc). The presence and the featuring role of nanoparticles have been discovered in many medieval materials, in glasses (e.g. Au and Ag nanoparticles) and pottery (e.g. Cu and Ag nanoparticles [9]–[11], but also in earlier times such as in the well-known Damascus blades [12]. Even the so-called *elixir of life*, originally described by the alchemist Paracelsus, is believed by some to have been made of a colloidal gold dispersion [13]. However, nanoparticles in a featuring role was ascertained and employed with awareness only in the last 30 years.

But why does being "nano" make difference?

It´s known that "nanometre" is a unit of length equal to $1 \cdot 10^{-9}$ m. In figure 2.2 an idea about how small is a nanometre is given by comparing different "objects".

An apple of ~7 cm
is 70 million nm

An ant ~5 mm
is 5 million nm

A Bacteria
is ~1000 nm

A virus ~100 nm

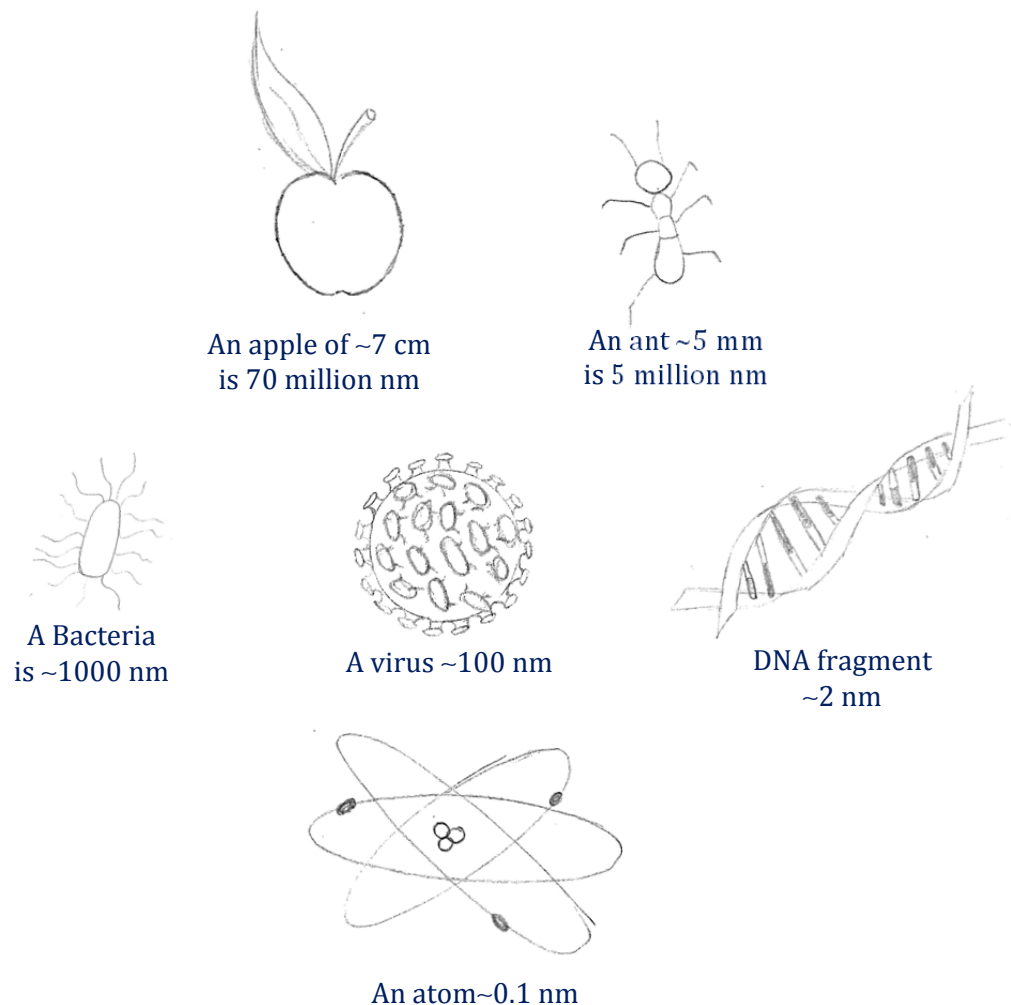DNA fragment
~2 nm

An atom~0.1 nm

Figure 2.2. An idea of nano: how big (or small) is a nanometre and what can we compare it with (courtesy of Ms. C. Nuglisch).

Materials with size in the 1-100 nm range show evident changes compared to the bulk. The electronic band gap increases, till the point that also conductors materials turn to insulators, Kubo effects are observed, crystal structures and electron arrangements can change, adding, for instance, catalytic activity to the material, but also optical properties are affected, and a change in colour can be observed.

Going down to the nanoscale, we literally enter a new world, the world of neglected dimensions, referring to Ostwald again [6], where the well-established concepts of classical physics are no longer valid and new laws and theories must be established. For instance, the concept of intensive properties, by definition independent from mass, are no longer valid, thus changes in melting point, conductivity, malleability, can be observed for nano-sized materials along with changes in catalytic activity, magnetic properties, crystal structures, etc.

Properties of nanomaterials are so peculiar that they can be considered a new state of matter. This peculiarity is due to the large number of surface atoms compared to atoms in the bulk. The smaller the size, the higher is this number and the more marked the difference; but there is obviously more. Nowadays nano-science is not anymore a mere question of reducing size; potential of nano-systems go beyond. With the increased knowledge about properties at the nanoscale, it is clear that the possibility to create tailored systems for specific applications is more than just a vision.

The key question is now: why despite the wide range of choices, is the inorganic research mainly focused on few selected classes of materials?

In the next chapter this question will be answered and properties and potentiality of transition metal carbides (MC) and nitrides (MN) will be discussed.

3. Transition Metal Nitrides and Carbides

In this chapter, a brief overview about properties of MN/MC is given. This step is fundamental to understand their chemical behaviour and problems related to their synthesis. An exhaustive and excellent treatise can be found in reference [14, 15].

Transition MN/MC possess many appealing duplicities. Already mentioned was their combination of properties that place them between classical ceramics and pure metals, having for instance good mechanical properties (hardness, strength, durability) like ceramics, and at the same time electrical conductivity (or even superconductivity), catalytic activity and, in some cases, magnetic properties (like metals). Another "weirdness" concerns the expectation that noble metals do not form compounds with nitrogen and carbon due to the filling of the anti-bonding region of their bands, but in fact the existence of nitride and/or carbide of almost all transition metals has been either observed or theoretically predicted [16].

Among the most "exotic" compounds are also known platinum nitride (PtN [17, 18]) and carbide (PtC [19]), palladium nitride (PtN$_2$ [20]), iridium nitride [15, 18] and iridium carbide [21], ruthenium nitride [22, 23], rhodium nitride (RhN$_2$ [24]), gold nitride and carbide (Au$_x$N [25], Au$_2$C$_2$ [26, 27]) silver nitride (Ag$_3$N [28]) and carbide [27], copper carbide (Cu$_2$C$_2$, known as Cu(I)acetylide [29]), and even osmium nitride (Os$_5$N$_2$ [30]), plutonium nitride [31] and uranium nitride [32].

A further weirdness for these compounds is that the ideal stoichiometry is not a rule, rather an exception, with a broad range of composition also for binary compounds, and a vacancy concentration up to 50% (atomic percentage) on the non-metal lattice sites. Interestingly, when a large fraction of non-metal sites are vacant, the vacancies tend to exhibit long-range order [14].

In fact, transition MN/MC are thermodynamically stable. However, the high energy needed to form the metal-non-metal bond requires the employment of strong synthetic conditions (high temperature, high pressure, strong nitrification/reducing agents, etc). For this reason, despite their high potential, the coverage in literature is still relatively scarce. In the last 10 years, however, there was a renewed interest in MN and MC due to the development of novel synthetic pathways for their production, but the percentage is still relatively low compared to other systems (see figure 3.1).
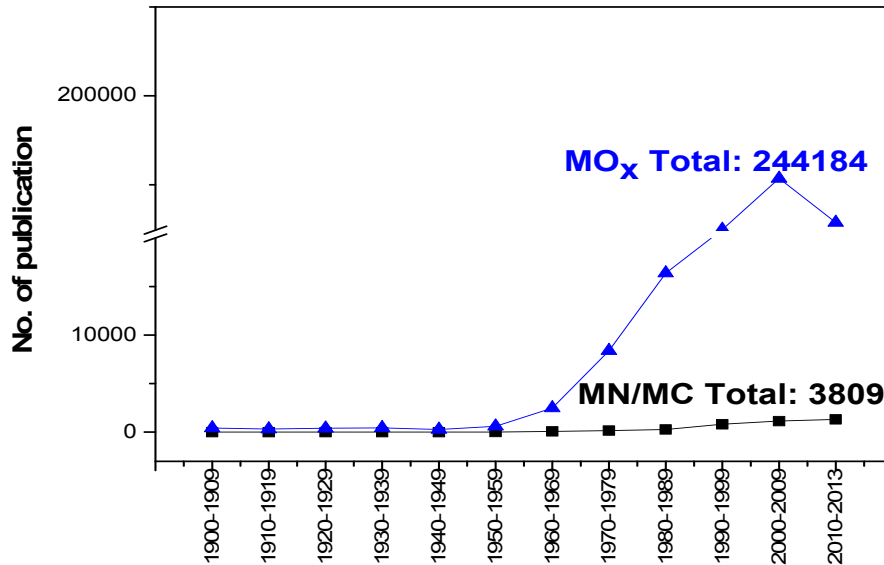
Figure 3.1. Comparison of the number of publications (rough estimation) concerning research related to metal oxide, metal nitride and metal carbides (source Web of Knowledge[SM]).

More than for other materials, properties of MN/MC (and therefore performance) are deeply related to their composition and structure, more specifically to the M/nM ratio and the presence of impurities, vacancies, defects, etc.

A good example of how the M/nM ratio can dramatically affect properties of these materials is given by the sub-class of metal oxy-nitrides (MON). In MON, N atoms are partially replaced by O atoms in the anion grid. It is worth mentioning that MON are not MO_x doped by N, but represent an "*out-and-out*" class of materials, whose properties can be different from both pure MO_x and MN. The band gap of MON is intermediate between that of MO_x and MN, so that while MO_x are oft insulators, MON can be a semiconductor, whereas MN might show metallic conductivity. The band gap difference affects also the optical properties. In TaON for instance, as showed by Domen et al. [33], a systematic increase of the N loading in the crystal structure of tantalum oxide significantly changes the final band gap. In simpler words, while Ta_2O_5 is a white insulator (3.9 eV), TaON and Ta_3N_5 are a yellow and a red semiconductor (2.5 and 2.1 eV) respectively [33] (see e.g. fig. 3.2). Due to their suitable band gap energy values, systems based on these compounds have been largely studied as visible light driven photo-catalysis and especially for the water splitting reaction under visible light [33–35].

Figure 3.2. Photographs of Ta_2O_5, TaON and Ta_3N_5 prepared as reported in reference [36].

More generally, oxygen forms a solid solution with both MN/MC and once it is dissolved in the lattice, it is almost impossible to remove. The dramatic effect of the presence of oxygen on the final properties of a material has been observed in the case of TiC. It showed a significant difference in TiC electrical conductivity as a function of the O amount; probably because oxygen might be ionically charged in the lattice and would hinder mobility of electrons [37]. This fact also explains why properties of compounds of supposedly equal composition and stoichiometry but prepared in different ways produced inconsistent results in the past. These differences can be ascribed to several factors. Most important are deviations from the expected stoichiometry, namely the effective metal/non-metal ratio, presence of impurities (or other interstitial elements), structural defects, different porosities, etc. These complications, together with the uneasy synthetic requirements (e.g. heat treatment at higher temperature for long time), have made MN/MC less appealing compared to their oxide counterparts.

In section 3.4 and chapter 4 several tailored routes for the synthesis of nano-sized MN/MC will be discussed.

3.1 Properties

Crystal structure

From a crystallographic point of view, MN/MC are *interstitial compounds,* with a complex and very different crystal structure. The situation can be even more complicated in the presence of a second metal (e.g. alkaline or alkaline earth), but these classes of compounds will not be discussed here.

For binary compounds, the geometry of the interstitial sites strongly affects the properties of the crystal and, from the left to right side of the periodic table, the crystal structure changes from a simple one, usually similar to that of the parental metals, to more complex ones.

This trend was rationalized by Hägg′s [38] with an empirical rule. Pursuant to this rule, the final structure depends on the non-metal/metal radii ratio:

$$r = \frac{r_{nM}}{r_M} \qquad \text{(Eq. 1)}$$

According to Hägg′s rule, for r < 0.59 the metal atoms form fcc, hcp or hexagonal structures with the non-metals in the corresponding tetrahedral or octahedral interstitial sites of the host metal structure [14].

The stability of the resulting structures is due to the fact that the interstitial sites are small enough to allow a sufficient bonding between the M and nM atoms without causing an expansion of the host lattice, which would destabilize the final structure [14]. For r > 0.59, to accommodate a larger number of non-metal atoms and sustain the metal-metal interaction without losing stability, the hosting metallic "cage" is contracted to a more complex structure. This structural distortion ensures that the atomic volume occupied by the metal atoms is smaller in the distorted structure compared to that expected in a hypothetical simple structure [14].

In general, most MN/MC have r < 0.59, exceptions are for instance ε-Ti_2N, Cr_3C_2, ε-TaN and WN (when prepared as film).

From a theoretical point of view, there are two main ways to describe the crystal structure in MN/MC [14]:

1) The interstitial model.

2) The coordination polyhedral model.

The first one is the simplest and most common approach and consists in identifying the crystal structure of the metal atoms among the simpler ones and then posing the N/C atom in this structure (including vacancies) in the interstitial sites.

Two examples are reported in table 3.1.

Table 3.1. Cristal structure displayed by WC and δNbN in terms of metal cage and non-metal positions [14].

Example	Hosting metallic structure	Non-metal positions
WC	Simple hex	Simple hex
δNbN	Hcp	Simple hex

The second approach is preferred for more complex structures and for a better structural comparison among different MN/MC crystals. This approach describes the lattice as constituted by coordination polyhedral, where the main polyhedral is made by metal atoms. As reported by Toth, the polyhedral model can be imagined in the same way silicates are described in terms of SiO_4 tetrahedra, and aluminium hydroxide (and related compounds) are described in terms of $Al(OH)_6$ octahedra [14].

The non-metal atoms can now be placed in the octahedral interstitial sites or in the centre of a trigonal prism, as reported in the figure 3.3. Often there are no clear interactions between the non-metal atoms to hold the structure but, as said, the occupied space is small enough (compared to the volume of the guest atoms) to allow sufficient bonding.
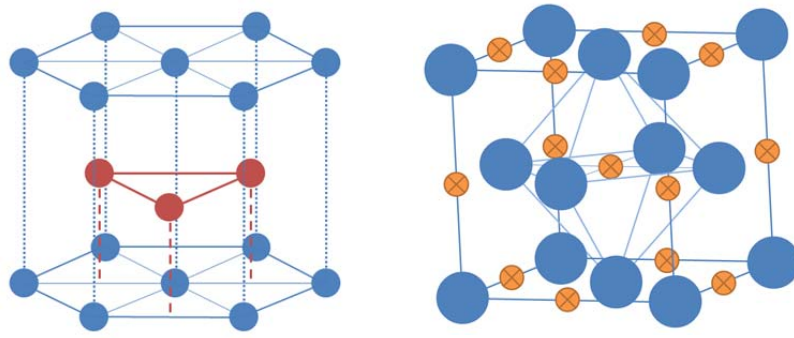
Figure 3.3. Two examples of interstitial sites in a hexagonal (left) and fcc (right) structure (namely trigonal sites, in red, and octahedral sites, in orange).

The differences between the crystal structures of the pure metals and those of the corresponding MN/MC can be also due to electronic properties. For pure transition metals, from left to right of the periodic systems, a change from bcc → hcp → fcc is observed, which depends on the number and types of valence electrons per atom, accordingly with the Engel-Brewer theory[8] [37, 39]. This trend, followed by the group VI of semi-nitrides and carbides (M_2X), depends on the valence electrons of N/C, and suggests an increase of sp electrons in the alloys.

The groups III-V also follow these trends but since they have a 1:1 stoichiometry (MX), i.e. a higher non-metal content (therefore a higher sp electron density[9]) the hcp structure is not observed, going directly to the fcc[10]. Stoichiometry changes from left to right in the periodic table too (see schema 3.1).

Left (early transition metals)		Right (late transition metals)
MX		M_3X
M_2X		M_4X
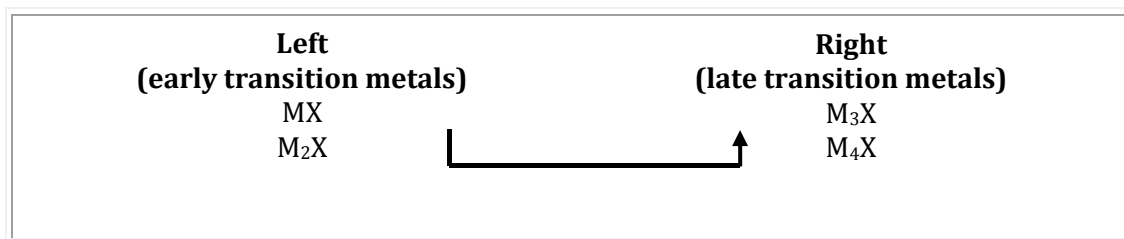
Schema 3.1. Expected stoichiometry for MN/MC from left to right on the periodic system.

---

[8] The crystal structure depends on the sp valence electrons (e) per atom (a): e/a.
[9] It is believed that the hybrid electrons (sp or dsp) are responsible of the structure, being outermost electrons, contrarily to the d electrons, which are deeper shell electrons and tend to be held closer to the nuclei [37].
[10] Bcc, hcp, fcc etc., for MN/MC refers to the "cage" of metal atoms.

The increase of the M/nM ratio is due to the repulsion of non-metal atoms by the metal ones. This increase of ratio reduces stability, which directly affects the melting point of the final material, especially for the nitrides, as shown in table 3.2. From this table, it can also be noted that, among all metals, the highest melting point belongs to tungsten. This is due to the filling of bonding and anti-bonding orbitals of the metallic band. The shift going to MN/MC is due to valence electrons of non-metal atoms (C, N) [14, 37].

Bonding in MN/MC (Electronic properties)

Most of the properties that make MN/MC so appealing arise probably from their chemical bond, where both an ionic and covalent character is present [14, 40]. It was stated in the previous section that the non-metal atoms are placed in the interstitial sites of the hosting metallic "cage", sometimes distorting the lattice in order to strengthen the metal/metal and non-metal/metal bonding. This bonding (i.e. the presence of these interstitial guests) dramatically affects the properties of the resulting material. For instance, the hardness of titanium carbide is improved by further addition of carbon [37 and reference herein]. Although a general trend cannot be extrapolated, this example proved the key-role of the non-metal part on the MN/MC final properties.

The study of the bonding and electronic properties of MN/MC and the comparison with those of the corresponding parental metals is especially interesting ever since Levi and Boudart in 1973 [41] discovered the similarities of the electronic properties of WC with those of Pt. Being cheaper and less inclined to undergo passivation, a MC would be an apt noble metal replacement in many key catalytic processes. However, in order to understand and anticipate their activity, either as active phase or as functional support, deeper investigations of their electronic structures is necessary. For instance, while it is known that the bonding in MN/MC is due to the interaction of the 2s and 2p orbitals of the non-metal atoms (N, C) with the d (e_g and t_2g) metal orbitals [42, 43], the direction of the electron transfer is still under debate[11].

---

[11]As explained by Oyama [37], in terms of structure and composition the non-metal atoms seem to increase the density of sp electrons in the final material as studies on chemical reactivity have shown. However, other studies (XPS, EXAFS, APW) showed that the negative charge is delocalized around the non-metal atoms.

Electrical and Magnetic properties

Electrical and magnetic properties of MN/MC are of the same order of magnitude of those of the corresponding metals (e.g. Hall coefficient, electrical resistivity, magnetic susceptibility, etc.). A partial list of several MN/MC properties and corresponding parental metals is included in Table 3.2.

Ceramics are commonly insulators (resistivity 10^{13}–10^{18} Ω·m) but for MN/MC, in contrast, the electric conductivity lies in the regime of metallic conductors (10^{-2}–10^{-3} Ω·m), and far from values observed for other ceramic materials. Among all interstitial carbides, WC has for instance the lowest electrical resistivity (10^{-5} Ω·m at r.t.) [44].

Rare earth intermetallic nitrides and carbo-nitrides are high performance magnets, with high Curie temperature and high saturation magnetization [45]. Among studies on novel materials, theoretical studies on $Nd_2Fe_{17}N_3$ have shown the important effect of the nitrogen loading, which leads to a material with higher Curie temperature compared, for instance, to the pure oxide [46, 47]. Other interesting ferromagnetic materials are $Fe_{16}N_2$ and some iron nitride based ternary compounds with $R_2Fe_{17}N_y$ composition (R=Sm, Ti, Mo, V, Cr).

Mechanical properties

Despite the several similarities among MN/MC and their parental metals in terms of structural and electrical properties, when it comes to mechanical properties, MN/MC are closer to ceramics than metals, with record melting points reflecting the high cohesive strength present in these materials (compared to the pure parental metal). This characteristic makes them suitable for application at high temperatures, as it will be discussed in section 3.3.

MN/MC Young´s modulus, i.e. the needed stress to create a *unit strain,* while changing sample length, are also higher than those for M° and closer to pure ceramics [37]. In general, mechanical properties are strongly affected by defects and porosity and to preserve hardness, the material must be prepared as compact (dense) phase. Exhaustive information about how to prepare a single MN/MC crystal today can be found in reference [14].

Table 3.2. Comparison of properties of some MN/MC with the corresponding parental metals.

	Melting point (K)	Micro-hardness (kg/mm²) r.t.	Young's modulus (GPa)	Magnetic susceptiblity (10^6emu/mol)	Electrical resistivity (µΩ·cm)	Hall Coefficient (m³/C·10^{11})
Ti	1933	55	120	153	39	-7.7
TiN	3220	2100	79	48	25	-6.7
TiC	2903	3200	370	6.7	68	-150
Zr	2120		95			
ZrN	3250	1500	460			
ZrC	3670	2700	348			-193/-94
V	2190	55	130	255	20.1	+7.9
VN	2619	1500	-	130	85	+4.2
VC	3103	2600	430	26.2	60	-4.8
Nb	2740	80	101	195	-	
NbN	2470	1400	-	31	-	
NbC	3870	2000	338	20	-	-13
Ta	3250	110	186	154	-	
TaN	3360	1050	-	-	-	
TaC	4070	1800	285	20	-	-11/-6.4
Cr	2130	230	250	180	20.8	36.3
CrN	1770	1100				
Cr_2N	2013	1100		16	79	-7.2
Cr_3C_2	2168	1300	390		75	-4.7
Mo	2883	250	320	89	5.47	+1.8
Mo_2N	2223	1700			19.8	+28.3
Mo_2C	2793	1500	230		71	-8.5
W	3670	400	345	59	5.39	+10.8
WN	873*				9	
WC	3049	2400	670	10	22	-218
Fe	1810	66	211	Ferromagnetic	9.9	+2.0
Fe_4N	943			Ferromagnetic		
Fe_3C	1923	840		Ferromagnetic		
Co	1767			Ferromagnetic		
Co_3N				Ferromagnetic		
Co_3C	2573*			Ferromagnetic		
Ni	1728			Ferromagnetic	7.1	
Ni_3N				Ferromagnetic	280	
Ni_3C	2373*			Ferromagnetic		
Mn	1517		191			+8.4
Mn_4N	1273					
Mn_3C	1793					

*Decomposes.
Data are extracted from reference **[14]** (in blue) and reference **[37]** (in green).

A good overview about mechanical properties on MN/MC is in reference [14] and references herein, but it must be anticipated that available data are too little to extract a general trend [14], and deeper investigations of the studied systems are still needed, to determine the exact composition and ensure better comparison.

In the present thesis, being interested in nanoparticles and systems with inherit porosity, mechanical properties of the prepared materials have not been tested. However, through proper refining of the synthetic conditions or simple post-synthesis treatments (annealing, sintering, etc.) of the prepared powders, the synthesis of a compact phase can be envisaged.

Catalytic properties

Bulk metal nitrides and carbides are principally known for their mechanical properties but as nano-sized materials they have been mainly investigated with regard to their catalytic properties. Compared to the M°, they have higher density of states[12] at the Fermi level, which reflects a potentially good catalytic activity. The interest of people working in catalysis is primarily due to their similarities with noble metals, as mentioned before [41]. In fact, Levi and Boudart observed a much lower activity of WC compared to Pt (in the formation of water from its components, in the reduction of tungsten trioxide by hydrogen and in some isomerization reactions). They also suggested that an increase of carbide porosity and/or surface area might have improved performance, which, together with their lower costs, can make these materials a real alternative to expensive and often scarce noble metal catalysts. Since then, many reactions have been tested and the best performances were shown in hydrogenation reactions [48, 49]. The catalytic activity of molybdenum carbide was found to be comparable to that of noble metals in the hydrogenation of cyclohexene [50] and CO [51]. Molybdenum alloys also showed comparable activity in isomerization of hydrocarbons [52, 53]. Several studies have also been addressed in the application of MN/MC in heteroatom removal (especially sulphur and nitrogen), key reactions in oil-refining. On the other hand, the activity in hydrogenolysis was found to be moderate and even scarce activity was found in oxidations reactions. A good overview about applications and potentialities of MN/MC in catalysis is

---

[12] Density of states are related and can be calculated via the heat capacities.

discussed in reference [54]. In table 3.3 a partial list of known reactions catalysed by MN/MC is reported.

Table 3.3. Partial list of some MN/MC tested as catalysts and electro-catalysts, corresponding reactions and classical catalyst(s) used.

Reaction type	Tested catalyst	Classical catalyst	Reference
Isomerization of hydrocarbons	Mo_2C, WC	Pt/Al_2O_3	[52] [53]
Low Temperature acid fuel-cells	WC	Pt	[55]
Hydrogenation of cyclohexene CO hydrogenation	MoC_{1-x} MoC_{1-x} TiN	Pd, Pt Ni, Pd and Pt Ru	[49] [56] [50] [51]
Oxidations reactions CH_4 oxydation to syngas	TiC, VC, WC	Pd, Au	[57] [58]
Hydrodesulfurization	MoC, Mo_2N	Co, Ni	[59] [60]
Hydrodenitrogenation	Mo_2N	Co, Ni	[61]
Fischer-Tropsch	Iron carbides	Fe, Ru, Co, Ni	[37] [62]
Ammonia synthesis and decomposition	Mo_2N, Mo_2C Co_3Mo_3N	Noble metal	[48] [63] [64]
Hydrodesulfurisation Hydrodenitrogenation Hydrodeoxygenation	MoC	Pt	[64] [65]
Hydrogenolysis (de)hydrogenation Isomerization reactions	MoC(O)	Pt	[53] [66][#] [52] [69]
Aromatization of CH_4	Mo_2C, MoC_{1-x}	Mo, Zn	[70]
Electrooxidation of Methanol	WC/Pt	20% Pt-Ru (1:1)	[71]
Selective Hydrogenation of C-C multiple bonds	TiC	Pd	[72]
Hydrotreating of coal-derived gas oil	Mo_2N, Mo_2C	MoS_2/Al_2O_3	[73]
PEMFCs*	Pt-Mo-N	PtMo alloy	[74]
PEM Fuel Cells (Anode)**	WC/W_2C	Pt	[44] [75] [76]
ORR***	Pt-WC/C	Pt/C	[76] [77]
CH_3OH and H_2/CO oxidation	WC/Pt	Pt	[78] [79]

[#]In this contribution all three reactions are tested.
*Proton Exchange Fuel Cells. **Polymer Electrolyte Membrane. *** Oxygen Reduction Reaction

A more interesting point about the usage of MN/MC as catalysts concerns their different selectivity. For instance, nitrides of group V show different selectivity from group VI (which, on the other hand, exhibits higher efficiency). This might be due to the difference in their electronic structures and their acid/base properties [67, 80].

Some interesting differences in selectivity of carbides compared to their parental metals will be presented in chapter 7.2. It is worth to mention that classical catalysts are subjects of improvement for about hundred years, while MN/MC have been just recently studied in catalysis, and already possess lower costs and higher chemical resistance.

Other properties

MN/MC are ***superconductive*** materials with relatively large critical temperatures, magnetic fields and current density [14]. NbN-based systems, for instance, possess one of the highest critical temperatures known ($T_c \sim 100K$) [14].

Their ***thermal conductivity*** does not depend on the temperature as is the case for corresponding pure metals [14].

Recently the ***elastic and optical properties*** of TiN, ZrN, and HfN were calculated, and it was found that their electronic properties are a combination of covalent, ionic, and metallic character and their elastic and optical properties change with metallic behaviour [14, 37].

Some metal nitrides are also considered new ***plasmonic materials*** [81].

From an electrochemical point of view, some MN possess high theoretical capacity, usually higher than that of graphite (~370 mAh/g), and they have been studied as a novel conversion electrode for lithium ion batteries. Applications of this kind are described in chapter 7 of the present thesis.

Finally, an exhaustive discussion on the thermodynamics of MN/MC and their phase diagrams can be found in reference [14].

3.2 Applications

As shown in the previous sessions, MN/MC possess superior mechanical properties, which have made them (as bulk materials or coatings) especially suitable for engineering/technical applications and for all those applications where durability and resistance to deformation, stress, abrasion, or usage in harsh conditions (such as high temperature, pressure, corrosive atmosphere, etc.) are desired. As for ceramics, their applications can also be extended to chemical barriers [82, 83] and medical implants [84]. Specific examples are reported in the following.

Iron nitride based systems are used as "fillers" to improve the strength of certain matrixes to form the so-called *cemented carbides*, while CrN, AlN and ZrN are used as long lasting hard coatings [85].

Titanium compounds, ranging from the pure nitride (TiN) to the pure carbide (TiC), including carbo-nitride (TiC_xN_y), oxycarbide (TiC_xO_y) and the oxy-carbo-nitride phases ($TiC_xN_yO_z$) are commonly used for coatings. Compared to TiN, TiC possesses a higher hardness (3200 kg/mm^2 vs 2100 kg/mm^2) and an extraordinary wear resistance; on the other hand, TiN shows particular resistance to corrosion. Titanium carbo-nitride (TiCN) is used to coat metals in order to increase hardness or reduce friction [86], but it is resistant only to moderate heat.

TiN and WC are largely used in cutting and working tools, e.g. drills (see figure 3.4). From this figure it can be seen that TiN has a gold-appearance and in fact it possess optical properties similar to gold. Due to its colour is largely used in decorative coatings (e.g. for jewellery). The colour can be changed from gold to red gold and even purple by partial substitution of nitrogen atoms with carbon (i.e. going to TiC_xN_{1-x}[13]).

Due to their high melting points, they also found applications as refractory materials [87 - 89]. In fact, at high temperatures they keep their strength but become ductile [14]. However, this disadvantage can be circumvented by properly alloying them, e.g. the addition of VC to TiC turned out to improve the yield strength of the latter [90].

---

[13] $TiC_{0.1}N_{0.9}$ is red golden while $TiC_{0.4}N_{0.6}$ is deep purple.

Figure 3.4. a) Cutting tools coated by TiN (source: http://www.titaniumexposed.com/titanium-nitride-coating.html); b) WC cutting tools source: http://www.tungsten-heavy-metal.com/tungsten-heavy-metal-carbide-cutting-tool.html)

Among finer applications, they are used for optical coating [91], electrical contacts [92] and as diffusion barriers [93] but also for hydrogen storage [94], as magnetic materials [95], gas barriers and sensors [37], or electrodes [96]. In particular, GaN, AlN and InN (band gap of 3.4 eV, 6.2 eV and 1.97 eV[14] respectively [99]), are studied as effective photodiode and in optoelectronic applications. Furthermore, to cover a wider spectrum, they can be simply alloyed (e.g. AlInN, GaInN and AlGaN) [100, 102]. Many metal oxy-nitrides are photoactive and thereafter studied as (photo)-catalysts [103]. The band gap of these materials can be adjusted, depending on the reaction involved, to exploit solar energy, to cleanse air and water from pollutants, etc. One important example is tantalum oxy-nitride, already discussed in chapter 2. Similar to TaON, also zirconium oxy-nitride presents interesting optical properties [104, 105].

In the case of magnetic nitrides and carbides, the range of applications can be extended to catalysis (as easily recoverable material [106, 107]), biomedicine (drug delivering, hyperthermia, contrast agents, etc.), electronics and more.

More exotic applications are those in aerospace devices [108] and in nuclear usages [109].

---

[14] The exact band gap value of InN is still under debate, especially for different temperatures. The value reported here is given by Guo and Yoshida [97] and it refers to r.t., while the calculated value at zero temperature is 0.78 eV [98].

3.3 Synthesis of MN/MC and related systems

Synthetic pathways to bulk MN/MC

As for many materials, preparation of MN/MC can be divided in two big synthetic classes, namely physical and chemical methods. An overview of the synthetic routes to prepare MN/MC is given in Scheme 3.2. Physical methods (e.g. physical vapour deposition [110], plasma and laser methods [111] including Laser-Heated Diamond Anvil Cell [112]) allow the production of well-defined and phase pure structures but they are optimized for specific target molecules and are more suitable for film and coatings. Furthermore, high price and the need of specific equipment make physical approaches non-suitable for large scale production. In contrast, chemical routes are more suitable for the preparation of a broad range of compounds by simple adjustments of the reaction conditions, and are thus more flexible.
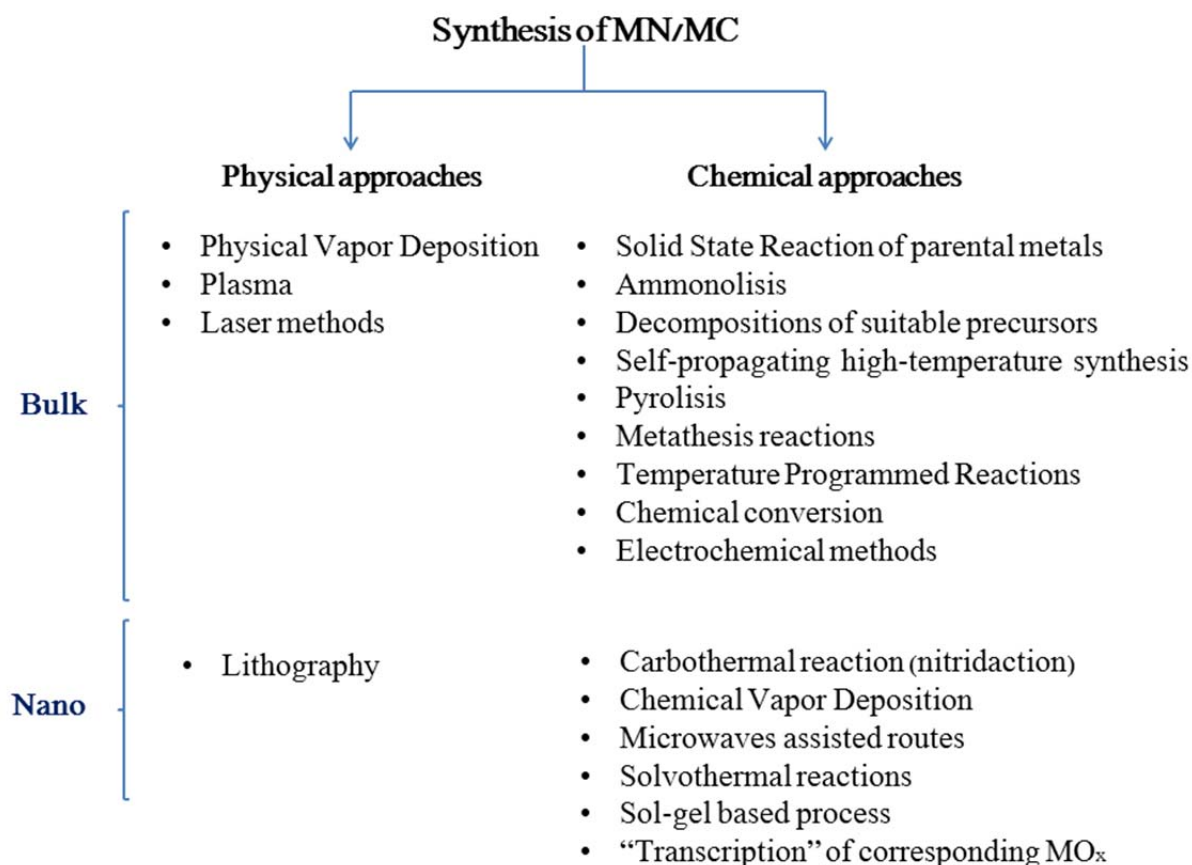
Scheme 3.2. Overview of some of the most used synthetic routes to prepare MN/MC.

The flip side of the coin when using chemical routes are poor size/shape control, as well as the presence of side products. This is especially problematic in MN/MC production, due to the high temperature requested, and related syntheses are often tailored only for certain products, trying to overcome or minimize these problems, also by preliminary or post-synthesis treatments.

In this section, the attention is focused only on chemical approaches. A partial list of common procedure to prepare MN/MC is presented in the following.

The classical way to produce MN/MC is via solid state reaction of the parental metals under inert or reductive atmosphere [37, 113] (also using H_2/CH_4) by heating up to ~2000 °C and using gaseous nitrogen or NH_3 as nitrogen source for the synthesis of nitrides, and pure carbon (also as coal or graphite) or various hydrocarbons, as carbon source for the synthesis of carbides. The carbothermal reduction of metal carbides is a well-known procedure (solid-gas reaction) but it usually produces impure, low surface area and often non-crystalline products. In this process, the carbon source is at first oxidized to CO_x, while the metal oxide is reduced to the corresponding carbide. When a source of nitrogen is also present, N atoms compete with C atoms in replacing the oxygen in the bond with the metal. In the latter case, the process is addressed as "*carbothermal nitridation reaction*" (eq. 2) [114, 115]. High temperatures are needed to form the metal- non-metal bonding but also to allow the diffusion of the gaseous reactants into the solid species.

$$MO_x + C \rightarrow M° + CO_x$$
$$2M° + C + \tfrac{1}{2} N_2 \rightarrow MN/MC$$

eq. 2
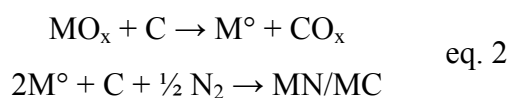
In some cases, the metal phase is obtained by reduction of the corresponding metal oxide or, when possible, is replaced by the metal itself. In both cases (with M° or MO_x) the reaction is favoured thermodynamically [116].

More recent routes involve *ad hoc* N/C sources such as in ammonolysis [117], thermal decomposition of suitable precursors (e.g. polymer [118] or metallic compounds, including complex amides [119, 120]) and azido compounds [121], self-propagating high-temperature synthesis (SHS) and combustion synthesis [122, 123], temperature programmed reactions (TPR) [124], chemical reduction and chemical conversion [118], liquid phase methods (using a metal salt and a reducing agent or in molten salts, metathesis [125], reaction with sodium amide [126], etc.) but also

electrochemical methods [127]. Most of these synthetic pathways are devoted to the preparation of MN/MC for engineering applications, i.e. with low surface area and almost no porosity, and are therefore unsuitable for the preparation of nano-sized materials.

Synthetic pathways to nano-sized MN/MC and related problems

As for many materials, a size reduction in MN/MC can bring to them additional benefits, such as higher catalytic activity, easier sculpting and possible quantum effects. However, the "extreme" conditions used by classical approaches are unsuitable for the preparation of smaller particles with high surface area and well-defined morphologies. High reaction temperatures, for instance, promote particles aggregation, preclude homogeneity and prevent the preparation of thermo labile materials (e.g. Cu_3N, Fe_3N and InN). Scalability is also often a sore point, especially when toxic compounds are involved.

Largely used for the successful preparation of nanoscopic metal oxides are sol-gel based syntheses, also known as Pechini-like process. This route involves the preparation of a colloidal solution (*sol*), which is then converted in a suitable network (or *gel*). During heating, the gel network controls the nucleation and growth of the metal oxide. This allows lower working temperatures still leading to crystalline phases. It leads to homogeneous products and ensures a higher surface area, dimensional and morphological control, simply by tuning reaction parameters.

The concept behind the sol-gel process can be transferred to MN/MC synthesis, by coupling the gel-preparation step with a following suitable heat treatment. This second step can be solvothermal [128 - 130] or carbothermal [115], for instance. Among other methods, the *hydrazide sol–gel process* [131], "*transcription*" of the MO_x nanoparticles into the corresponding MN/MC [132], microwaves assisted synthesis [133] and chemical vapour deposition [134].

In the next chapter, novel routes designed during this *habilitation* will be presented. The designed synthetic pathways were conceived especially to decrease the needed reaction temperature, to allow usage of non-toxic compounds and to minimize (or even avoid) post-synthesis purification, still bringing to phase pure and well-defined nanoparticles.

4. Novel Synthetic Strategies

Every scientist has a dream...

Physicists dream of finding a single law to explain the mechanism of the whole universe, while chemists dream of finding a single procedure to prepare complete classes of materials, preferably in a facile, inexpensive, green (i.e. also safe) and scalable way. Being a chemist, this was my dream while designing a new route to MN/MC.

To the same extend as for the synthesis of many nanomaterials the central point was to avoid uncontrolled (fast) growth and coalescence of the as-nucleated nanoparticles, which would lead to inhomogeneous products, polydisperse in size and with ill-morphology. Then, more specifically for the synthesis of nanosized MN/MC, there were three more points to be considered while outlining an ideal route:

 i) how to minimize the heat treatment, i.e. decreasing reaction temperature and heating time,

 ii) how to ensure scalability, for large scale production,

 iii) how to increase porosity and/or surface area.

The first point, the inconvenient but necessary heat treatment, is a sensitive step. Due to the impossibility to work at room temperature, the presence of a stabilizer during the synthesis of MN/MC nanoparticles is essential. Nevertheless, this step can be made less critical if the stabilizer is also the C/N source, and it is even better if it leaves before the end of the reaction, to avoid post-synthesis purifications. Lastly, the whole process has to be able to produce significant amounts of material to use the material in practical applications.

For all these reasons, it is clear that precursors play a crucial role. To ensure scalability, reagents must be easy to handle and stable until reaction ignition, but also non-hazardous and cost-effective; while on the other side, to ensure small sizes, it must be able to "protect" the nanoparticles during their synthesis, for instance by forming a *templating* network (better if organic), where the nanoparticles can nucleate and grow in a controlled fashion. To close the circle, this matrix needs to be unstable enough to decompose after nanoparticles have formed. The gases released during this decomposition will conveniently assist the formation of a more

homogeneous product with a higher surface area. Finally, all the steps must take place in a reasonable time span, to minimize reaction time and working temperature.

A schematic representation of the concept is shown in scheme 4.1.
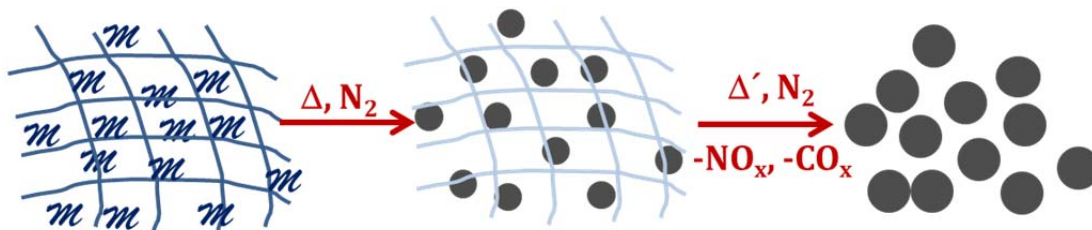
Scheme 4.1. From left to right: the metal precursor (𝓂) "entrapped" in the organic network converts to MN or MC nanoparticles nuclei, by heating it under nitrogen flow. Upon further increase of the temperature ($\Delta'>\Delta$), nucleation and growth of the nanoparticles occur, while the organic matrix simultaneously decomposes providing the N or C necessary to form the final MN or MC, and releasing the excess of N/C, mainly as NO_x/CO_x.

Clearly the chemical nature of the organic network must also play a big role, and one might expect that different precursors will bring differences in the final product.

In line with what was previously stated, different C/N sources have been tested. Results can be divided in three main routes:

1. The Urea-Glass Route

2. The Biopolymer Route

3. The Sugar Route

Quod erat demonstrandum, the choice of one of these routes over the others, although concept-wise very close, allows full control over composition, size and in some cases shape of the final nanomaterial. These routes will be discussed in detail in the following sessions.

4.1 The Urea-Glass Route [135] [136]

In the beginning was the Urea…

In order to prepare the "ideal" precursor described before, urea was initially considered as a suitable candidate for its key properties, which will be briefly discussed here. In addition, urea is a natural and readily available compound.

Urea or, accordingly with the IUPAC definition, diamino-methanone, is the diamide of carboxylic acid with the formula $CO(NH_2)_2$ (figure 4.1). It is also known as diaminomethanal. It is a small molecule, planar when solid, pyramidal as gas [137], at r.t. a white odourless and non-toxic powder. It was isolated for the first time in 1727 by Herman Boerhaave [138] and was the first organic compound to be prepared synthetically from inorganic materials [4].
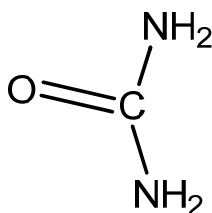
Figure 4.1. Molecular structure of urea.

Urea possesses two important types of functional groups, one carbonyl group and two amide groups. Due to the presence of both these groups, urea can be used as C or N source for the preparation of MN or MC, respectively, simply by adjusting the reaction conditions as will be shown in the following sections. In the urea molecule, the oxygen in the C=O group is considered basic (compared for instance to CH_2O), although no hydrolysis occurs in water, while the C-N bonding has a partially double bond character and the C is sp^2 hybridized.

An important property of urea is its ability to form H-bonds. In the solid phase, each oxygen atom is bound to two urea molecules via H-bonds (forming two NH-O bonds), resulting in an extended network with an open (porous) structure, which can conveniently host small molecules, resulting in systems called *clathrates* [139, 140]. The ability to form H-bond gives to urea also a high solubility in water and polar

solvents (121.0g/100g and 5.837g/100g in water and EtOH respectively at 25.5 °C [141]).

According to some authors (for example in reference [142]), urea can react with several substrates to produce urethanes. For instance:

$$CO(NH_2)_2 + EtOH \rightarrow 2HNC(O)OEt + NH_3 \qquad \text{eq. 3}$$
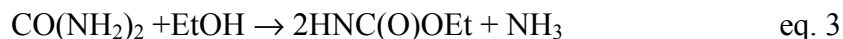
This reaction is sustained by high temperatures; however, during our study, no changes in urea/ethanol solutions were observed, even under heat treatment (90°C for one night). The IR spectra of urea/ethanol solution recorded after heat treatment, perfectly match with that of pure (untreated) urea (see figure 9.1 in the appendix).

Urea is known to form complexes with many metals, usually via the carboxylic group or in a few cases via the amide group, hardly with both simultaneously (i.e. urea acts mainly as monodentate ligand). In the solid complexes with Ti, V, Cr, Mn, Fe, Ni, Mo, Zn and Cu it coordinates through the C=O, while Pt and Pd through the NH_2. For some metals, the specific bonding was never reported, such as Nb [143 - 145].

Its capability to perform as N-source for the production of bulk MN was already observed by Podsiadło in 1995 for the preparation of GaN and InN [146, 147], but only in 2003 it was first used for the synthesis of MN as nanoparticles [148]. In this synthesis a solid complex between urea and a metal (namely Cr, Al, Ti, Nb) is prepared and then recrystallized/precipitated to obtain a solid complex, which is in a second step thermally treated. However, its usefulness to make MC was not reported in that study and related ones [149, 150].

In my study, in order to reach the targets discussed above, the substitution of a crystalline metal-urea precursor with a "glass"-like structure was considered, bringing significant differences. The glass is the result of the urea ability to form polymer-like arrangements, which are kept together by hydrogen bonds and electrostatic interactions, and can conveniently host the nanoparticle "seeds". The intermediate glass, formed by heating up a mixture of urea, a metal salt and a suitable solvent, is then converted (upon further heat treatment) into the final MN/MC nanoparticles. For this reason, the process is generally dubbed as "*Urea Glass Route*" (UGR). The UGR is a non-aqueous and surfactant free route and can be considered

as a combination of an atypical sol-gel based process and a carbothermal reduction/nitridation (eq. 2), where urea, during the particles formation, plays many roles (namely the anionic source, the intermediate solvent and the stabilizing agent).

The main advantage of this procedure is a closer contact of the C/N-source with the metal centres (i.e. the nanoparticles seeds), which is easier in a more fluid material rather than in solid, also allowing higher contact interfaces and therefore a better mixing. In this way the final product can be obtained at temperatures lower than those required in classical syntheses. Also, due to the decomposition of the organic matrix during the heat treatment and simultaneous gas release, template removal and post-synthesis purifications are not necessary. Additionally, properly tuning synthetic parameters, the amount of residual carbon can be adjusted (i.e. increased, reduced or even avoided), as needed for the desired product. Residual carbon can in fact be considered beneficial for specific applications, as discussed in chapter 7.

Finally, thanks to the use of a jelly starting material, several products can be prepared simply by changing the metal source. In scheme 4.2, products prepared up to now via the UGR are reported (left panel) together with the expected field of application (right).
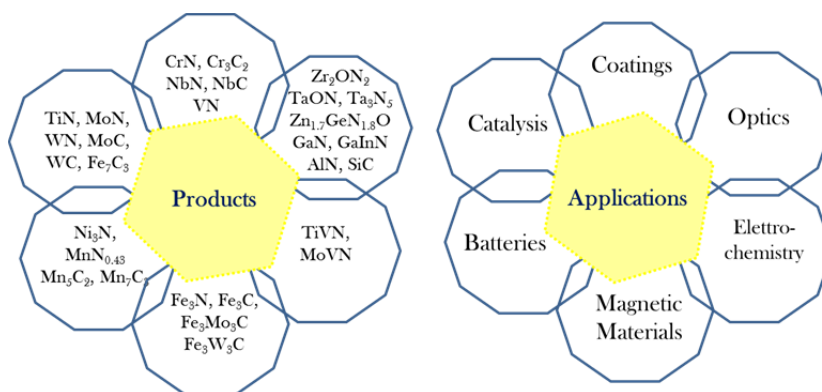
Scheme 4.2. Overview of synthetized compounds (left) and corresponding application field (right).

It is important to remark that having a glassy intermediate is particularly significant here since the final MN/MC materials, being ceramics, are difficult to shape or process further, i.e. are tough and not malleable material.

It might be mentioned that similar results are obtained when urea is replaced with derivatives of similar reactivity, similar results are expected. Some examples of

preparation of MN/MC using urea alternative molecules were exploited during our study and are reported in literature [136].

The UGR in the lab

As already commented, in the UGR the starting precursor makes the difference. This precursor can be more or less viscous, in some cases jelly (figure 4.2) or as a paste-like material. In any case, it comprises three components: a metal salt, the C/N source and a solvent (to facilitate the coordination of urea molecules with the metal atoms). The selected shortlist will be imposed in order to get a homogeneous starting material.
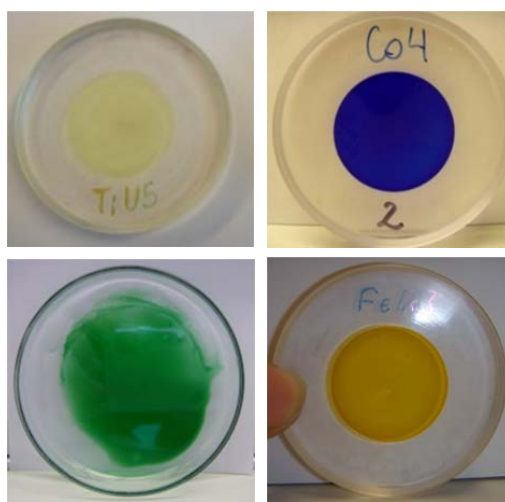
Figure 4.2. Some metal-urea starting materials (clockwise Ti, Co, Fe and Cr urea "jelly" precursors).

When possible, suitable choices are ethanol as a solvent and a chloride as metal source (either hydrate or anhydrous), in this way the corresponding metal-orthoesters are formed and a major part of chloride is released as HCl in this first step. Due to salt solubility problems, ethanol is sometimes replaced by methanol, while metal chloride can be replaced by nitrates or acetates to address selected targets. To be more specific, for some metals, such as nickel, the bonding between the metal and the chloride is so strong that a significant amount of chlorine can be found in the final product; in this case, other salts have to be considered (e.g. acetate). In any case, proper amounts of urea (or similar C/N source) are added to the alcoholic solution to reach the wished urea/metal molar ratio (R), let under stirring until dissolution is complete and the system appears homogeneous. A summary-overview of the synthetic conditions used for each system is reported in table 4.1.

Table 4.1. Experimental details for the preparation of MN/MC nanoparticles via the UGR.

Product	Metal source	C/N Source	Solvent	R	Additives	Reaction Temperature (°C), (HT)[#]
MN						
Mo_2N	$MoCl_5$	Urea	Ethanol	1	--	800
W_2N	WCl_4	Urea	Ethanol	1	--	800
NbN(O)	$NbCl_5$	Urea	Ethanol	3	--	800
np-CrN	$CrCl_3 \cdot 6H_2O$	Urea	Ethanol	3	--	800
np-CrN	$CrCl_3 \cdot 6H_2O$	DI	Ethanol	0.5/1	--	800
CrN_{fibers}	$CrCl_3 \cdot 6H_2O$	PAN	DMF	3	PUF	800
TiN	$TiCl_4$	Urea	Ethanol	3/4	--	800
GaN	$GaCl_3$	Urea	Ethanol	0.5	--	800
GaN	$Ga(NO_3)_3$	Urea	Methanol	5	--	800
Ni_3N	$Ni(CH_3COO)_2$	Urea	Ethanol	3/4	--	350/400
VN	$VOCl_3$	Urea	Ethanol	3	--	800
np-Fe_3N	$C_{10}H_{14}FeO_4$	Urea	Ethanol	3	--	600 (1+3)
np-Fe_3N_{trascr}	Fe_3O_4	Urea	Water	<8	Agar	800
Fe_3N_{fibers}	$C_{10}H_{14}FeO_4$	PVP	Methanol	1	--	600
$MnN_{0.43}$	$Mn(CH_3COO)_2 \cdot 4H_2O$	Urea	Methanol	7	--	800
Ta_3N_5	$TaCl_5$	Urea	Methanol	5	$CaCO_3$	775
MON						
TaON	$TaCl_5$	Urea	Methanol	2	$CaCO_3$	775
Zr_2ON_2	$ZrO(NO_3)_2 \cdot H_2O$	Urea	Methanol	9	NH_4Cl	800
$Zn_{1.7}GeN_{1.8}O$	$Zn(CH_3COO)_2/Ge(CH_3O)_4$	Urea	Water/Ethanol	*	NH_4Cl	800
MC						
MoC	$MoCl_5$	Urea	Ethanol	7	--	800
WC	WCl_4	Urea	Ethanol	7	--	800
np-Fe_3C_{trascr}	Fe_3O_4	Urea	Water	>8	Agar	800
np-Fe_3C	$FeCl_2 \cdot 4H_2O$	Urea	Ethanol	3	$Fe(CO)_5$	700 (1+2)
np-Fe_3C	$C_{10}H_{14}FeO_4$	Urea	Methanol	1	--	700
np-Fe_3C	$C_{10}H_{14}FeO_4$	Urea	Ethanol	3	--	800 (1+2)[#]
np-Fe_7C_3	$C_{10}H_{14}FeO_4$	Urea	Ethanol	5	--	700 (4+2)
ns-Fe_3C	$FeCl_3 \cdot 6H_2O$	DI	Ethanol	1	--	700
mp-Fe_3C	$FeCl_3 \cdot 6H_2O$	DI	H_2O	2	SiO_2	700 (4+2)
NbC	$NbCl_5$	DI	Ethanol	5	--	800
Cr_3C_2	$CrCl_3 \cdot 6H_2O$	DI	Ethanol	0.5	--	900
Mn_5C_2	$Mn(CH_3COO)_2 \cdot 4H_2O$	Urea	Methanol	7	--	900
Mn_7C_3	$Mn(CH_3COO)_2 \cdot 4H_2O$	Urea	Methanol	7	--	1000
TiC(N)	$TiCl_4$	Urea	Ethanol	10	--	800
NbC(N)	$NbCl_5$	Urea	Ethanol	10	--	800
VC(N)	$VOCl_3$	Urea	Ethanol	8/10	--	800

[#] HT=4+3 if not stated otherwise. * Solid mixture.

Homogenization time differs according to the initial composition and viscosity, and can last up to one night. Formation of a urea-metal salt is also confirmed by the higher solubility of urea in presence of the metal salt than in pure ethanol [141]. In general, when using higher R an increased amount of carbon and lowered amounts of nitrogen are found in the final product. In this way, composition and coordination state of the glass can be decided *a priori* and can be addressed to the synthesis of MN over MC (or *vice versa*), as discussed in section 4.1.1. In some special cases, to achieve specific targets (e.g. targeted morphologies), the use of some additives was considered (see Table 4.1).

Finally, the starting precursor gel is transferred into a furnace and heated under N_2 flow up to 800°C for a selected time (figure 4.3).
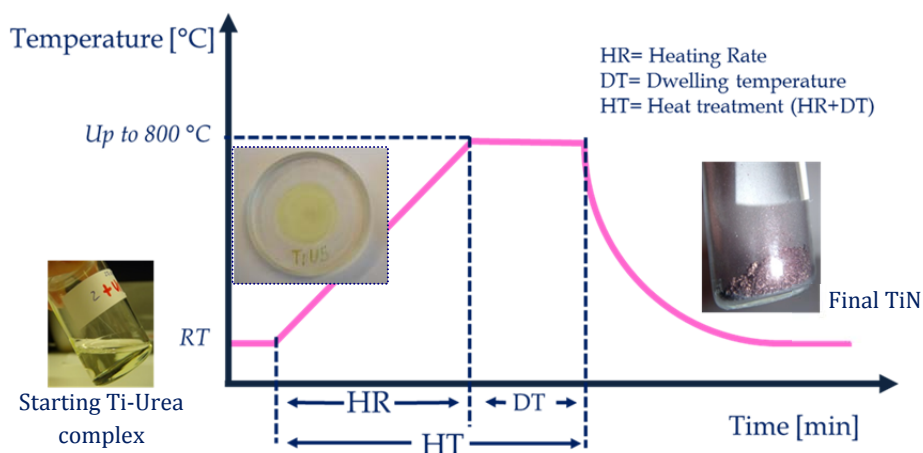
Figure 4.3. Schematic representation of the heat treatment using the preparation of TiN as an example.

After the requested heat treatment (HT=HR+DT), which usually must be optimized for each product, a solid powder is obtained (see figure 4.3 and 4.4).
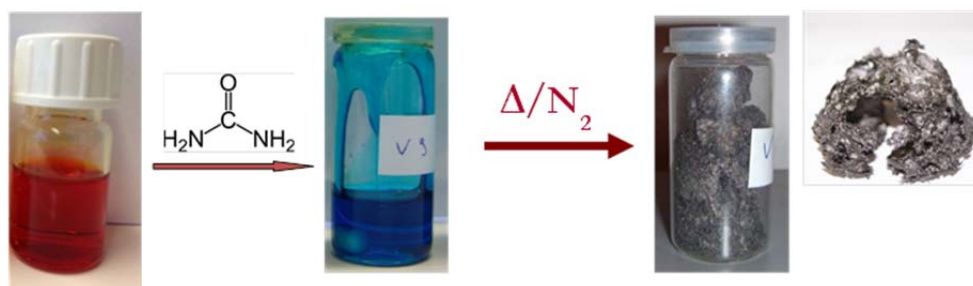
Figure 4.4. Schematic description of the urea-glass route using the VC(N) preparation. From left to right: starting VOCl$_3$/EtOH solution (orange), resulting solution after adding urea (R=9, blue) and final powder (grey) upon heat treatment at 800°C under N_2 flow. A zoom of a VN grain is also reported to show the metallic appearance of the final product.

Before the heat treatment: the starting complexes

In order to have information about complex formation and bonding between urea and the metal, IR investigation have been performed on the starting materials upon removal of residual solvent. Due to the several IR modes of urea and their further combination in the complex, a precise description about the structure of the complexes would remain rather speculative. However, there are two main points that can be addressed:

1) confirming the metal-urea complex formation;

2) deducing whether the metal-urea bridges are via NH groups or via the C=O group.

For an easier interpretation, it must be considered that urea can be represented by three resonance structures, schematically reported in figure 4.5, which equally contribute to the final structure in the pure phase.
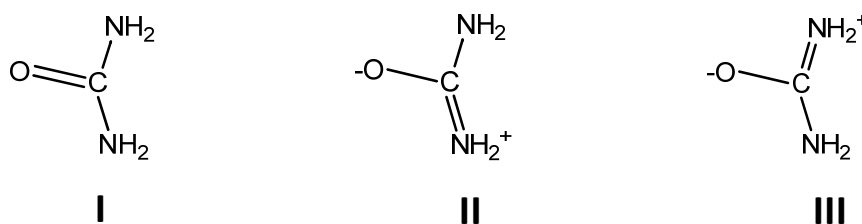
Figure 4.5. Resonance structure of the urea molecule [143]

In general, in solid complexes, distinguishing between the two types of linkage is easy, and key changes expected are listed below:

Coordination via N (less contribution from structures II and III) [143]

    I. NH_2 stretching frequency similar to those in amido complexes ($\nu_{(NH_2)}=$ ~3200-3180, $\delta_{(NH_2)}$ ~1530, ρ_w ~1000, ρ_r ~660 cm^{-1})[15], and together with the free -NH_2 mode of urea (shifted at lower frequency in the complex), two more modes appear due to bonded NH_2- ($\nu_{(NH_2)bonded}$ ~3100-3000 cm^{-1}).

    II.   CO stretching frequency increases ($\nu_{(C=O)}=1683$ cm^{-1} for the pure urea).

    III.   CN stretching frequency decreases ($\nu_{a(CN)}=1471$ cm^{-1} for the pure urea).

---

[15] For Hg-NH_2 complexes bands were observed at ~400-700 cm^{-1}.

Coordination via O (less contribution from structure I) [143]

I.   No appreciable changes in the NH stretching frequency ($\nu_{(NH_2)free}$=3500-3350 cm^{-1} for the pure urea).

II. CO stretching frequency decreases ($\nu_{(C=O)}$=1683 cm^{-1} for the pure urea).

III. CN stretching frequency (usually) increases ($\nu_{a(CN)}$=1471 cm^{-1} for the pure urea).

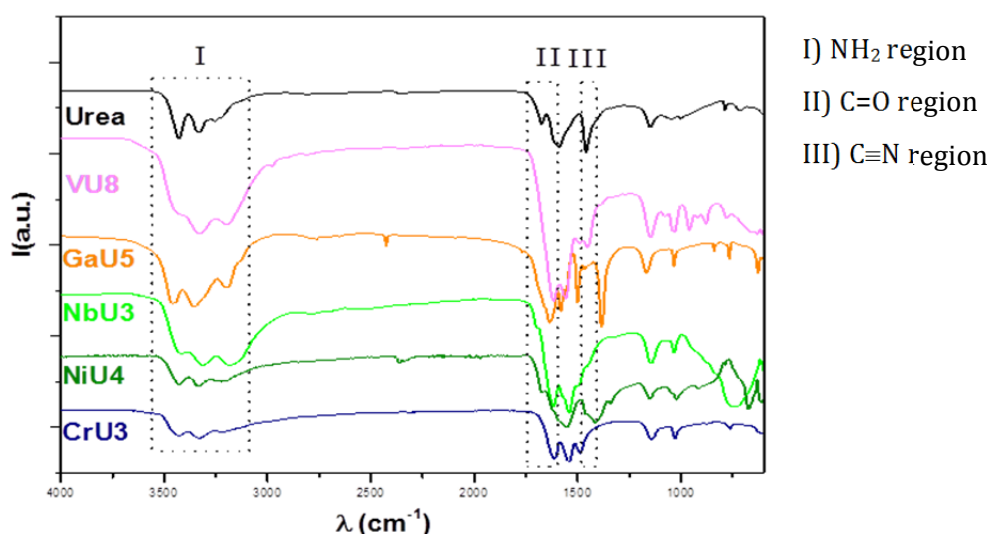IR-spectra of several metal-urea precursors are reported in Figure 4.6.

Figure 4.6. IR Spectra of several metal-urea starting complex dried to remove the excess of ethanol. The number in the acronym corresponds to the R value.

For better comparison of these differences, the IR spectrum of pure solid urea is also reported in figure 4.6, and peak positions/attributions are listed in table 4.2. Bands below 700 cm^{-1} are usually attributed to the metal bonds [143 - 145]. As shown in this figure, the coordination chemistry of the UGR starting "gels" seems to be more complex. Coupling/decoupling of several modes together with the appearance of new bands can be observed. In some cases the change in frequency (compared to pure urea) expected for some reported metal-urea complexes are not in line with what is observed in the UGR complexes. This effect could be due to the nature of the "gel" itself, where some urea molecules are coordinated with the metal centre and then, in turn, coordinated with a second shell of urea molecules. This observation seems to be somehow supported by the observation that often both peak intensity and position of the NH$_2$ bands (I) change independently whether the complex is linked via C=O or NH$_2$ bridges. Intrinsically, it cannot be excluded that urea could act as polydentate

ligand and that some residual ethanol molecules stay entrapped in the precursor structure. This point is currently under investigation.

Table 4.2. IR frequencies for the metal-urea starting precursors reported in figure IR. The frequency of pure urea and corresponding attribution are reported for comparison.

Assignment	Urea	NiU4	TiU5	GaU5	NbU3	CrU3	VU3
$\nu_{as}(NH_2)$	3425_m	3426	-	3458	3417	3428	-
$\nu_{as}(NH_2)$	3322_m	3328	3304	3356	3312	3329	3320
$\nu_s(NH_2)$	3250_w	3255	-	-	-	-	-
$\nu_s(NH_2)$	3220_w	3205	3163	3199	3182	3222	3211
$\nu_{as}(CH_3)$	-	-	2976	-	-	-	2991s
$\nu_{as}(CH_2)$	-	-	-	-		-	2852s
$\nu(NO_3)$	-	-	-	2764, 2426, 1768	-	-	-
$\delta_s(NH_2)$	1675_m	1674	1698	1635	1700	-	-
$\delta_{as}(NH_2)$	1620_{sh}	1625	1625	1581	1614	1613	1618
$\nu(CO)$	1587_{st}	1592	1545	1556	1539	1540	1549
$\nu_{as}(COO)$	-	1552	-	-	-	-	-
$\nu(NO_3)$	-	-	-	1466	-	-	-
$\nu_{as}(CN)$	1459_{st}	1461	-	-	1453	1488	1491
$\nu_s(COO)$	-	1415	-	1384	-	-	-
$\delta_s(CH_3)$	-	1342	-	-	-	-	-
$\rho_s(NH_2)$	1148_m	1150	1147	1167	1143	1142	1145
$\nu(TiO-C)$	-	-	1097	-	-	-	-
$\rho_s(NH_2)$	$1048_{w,br}$	1047	1037	1033	1032	1028	1029
$\rho(CH_3)$	-	1023	-	-	-	-	-
$\nu_s(CN)$	1004_w	-	-	-	-	-	-
$\tau_s(NH_2)/\pi(CO)$	786_w	785	-	765	735	874, 762	969, 761
$\delta_s(COO)$	-	673	-	-	-	-	-
$\nu(M-Urea)$	-	-	632	627, 533	595	606, 554	-

Legend: s, as, ν, δ, ρ, π and τ indicate symmetric, asymmetric, stretching, deformation, rocking, out of plane and torsion vibrational modes. st, m, w, sh and br stand for strong, medium, weak, shoulder and broad.

A deeper study on the exact coordination in the precursors is still in progress, since it requires more sophisticated techniques (e.g. XPS, EXAFS, NMR, HR-MAS, etc.)

and specialized data analysis. SANS techniques should also be used to ascertain a super-structuring in the network, since the PXRD performed on the starting glassy materials only showed amorphous patterns and, in few cases, just traces of the metal salts (figure 9.2 in appendix).

During the heat treatment: conversion to the final MN/MC

In order to study the conversion mechanism of the starting glass to the final product, a thermo-gravimetric investigation has been performed under nitrogen between r.t. and 1000 °C (figure 4.7). The thermo trace of pure solid urea was also recorded for comparison.

It is known that urea decomposes in three main steps [146, 147]:

I)   Decomposition starts with ammonia release followed by condensation reactions (with biuret and triuret formation) up to ~200°C.

II)   Further condensation reactions with formation of dicyandiamide and melamine up to ~300°C.

III)   Formation of bigger molecules (e.g. ammelide, ammeline, melame, meleme and melone), which decompose upon further temperature increase releasing CO_x, ammonia, and H_2CN_2.

The comparison of urea thermo-trace with the traces obtained for the complexes immediately shows marked differences (figure 4.7): the complete decomposition of metal-urea takes place more slowly and at higher temperature, supporting a relatively strong metal-urea complexation. Different than in pure urea, this decomposition does not occur in several sharp steps but in a rather smooth fashion, indicating the formation of an intermediate "glass-like" structure, stable up to 600-700°C (depending on the metal). Prior to the glass formation, residual solvent and small fragments are lost between 100-200 °C. Then the glass is transformed slowly to the final product under further mass loss.
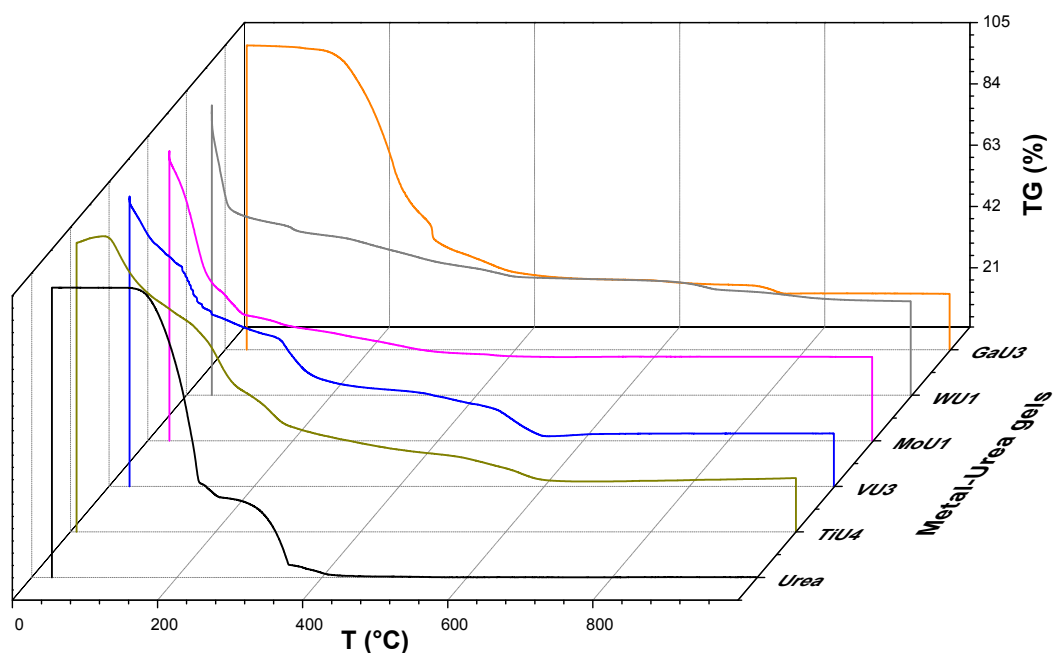
Figure 4.7 TGA thermotraces of several metal-urea complexes recorded under N_2 flow.

Elemental analysis and XRD performed on samples quenched at T<400 °C showed that the intermediate glass is rich in C, N, and O (table 9.1 in the appendix) and, unless the intermediate step involves a metal oxide formation, it has no crystalline structure (figure 9.3 in the appendix). In every case, for temperatures above 600°C, the matrix decomposes through-and-through, releasing strong nitrification agents (such as NH_3 and H_2CN_2), and the glass intermediate is converted into the final MN/MC, possibly involving in-situ formation of a transient MON and/or of MCN phase. This point was carefully studied in the case of iron and will be discussed in detail in section 4.1.2 and 4.2, together with the influence of the N_2 from the nitrogen flow on the material final composition. It was in fact ascertained that *both* sources of nitrogen (namely from the atmosphere and from the urea) are necessary for the formation of the final material.

Reaction is completed up to 800-900°C with release of most of the oxygen and carbon (for the nitride formation) or nitrogen (for the carbide formation). In section 4.1.1 it will be shown that, in some cases, an exceeding carbon phase forms a coating shell around the particles, either amorphous or graphitic depending on the metal used, thus featuring the final material.

Characterization

Chemical and surface characterization was performed via ICP, EA, N_2 physisorption and TGA. EA-ICP results are listed in table 9.2 in the appendix.

Identification of the crystalline phases was made by powder X-rays diffraction (wide-angle XRD). The use of the ICDD database (PDF4+) allowed phase attribution, while first crystallite-size estimation was made by the Scherrer´s equation [151, 152]:

$$d(nm) = 0.9\lambda/(FWHM\ cos\Theta) \qquad eq.\ 4$$

where Θ is the Bragg´s (diffraction) angle and λ is the X-ray wavelength ($\lambda = 0.154$ nm, for the used copper X-rays source). The FWHM (full width at half maximum) of the peak is sensitive both to the lattice disorder and to the nanoparticles size. For the FWHM calculation the main peak was used, unless differently specified. In figure 4.8, XRD patterns of some MN and MC prepared by the UGR are shown.
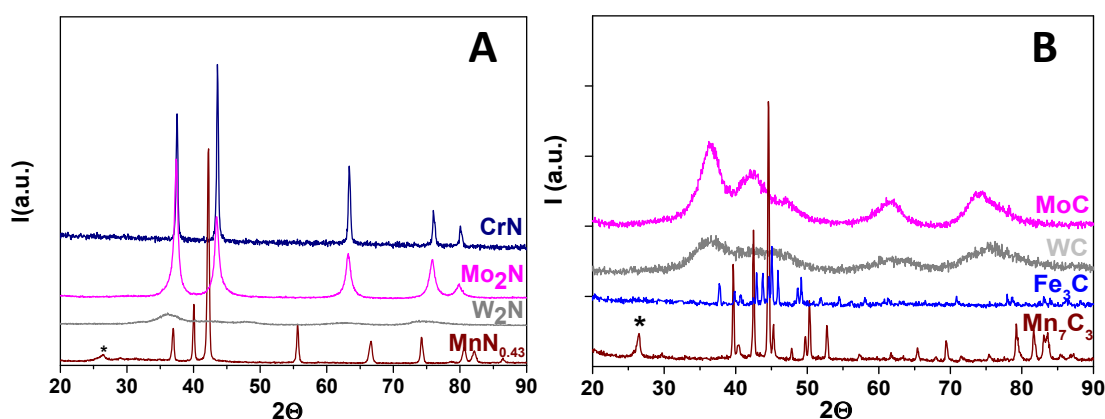
Figure 4.8. XRD patterns of some MN (A) and MC (B) prepared via the UGR. Marked peaks (*) are attributed to carbon (ICDD 04-015-2407).

In general, with the UGR the final product is made of small (5-10 nm in diameter) but already crystalline particles. However, the presence of an external passivation layer on the nanoparticles surface as well as the presence of molecularly dissolved oxygen in the MN/MC lattice and/or in the residual carbon phase, when present, cannot be excluded, since it is not be observed in the XRD pattern. On the contrary, oxygen substitution in lattice sites (as N or C replacement), as well as metal vacancies, would affect peak intensities and would possibly shift peak positions (usually to lower angle, i.e. to lattice expansion) [37, 153]. In some cases, a metal

oxide formation has been observed as intermediate step, which depends on the nature of the precursors used, as discussed in section 4.1.2.

Since titanium is an oxyphilic element, oxygen contamination was exemplarily investigated in a TiN sample prepared by the UGR. Corresponding XRD, EELS patterns and TEM/HR-TEM images are reported in figure 4.9. It can be observed that only traces of oxygen were found by EELS, while the XRD pattern very nicely matches with the one expected of pure TiN.
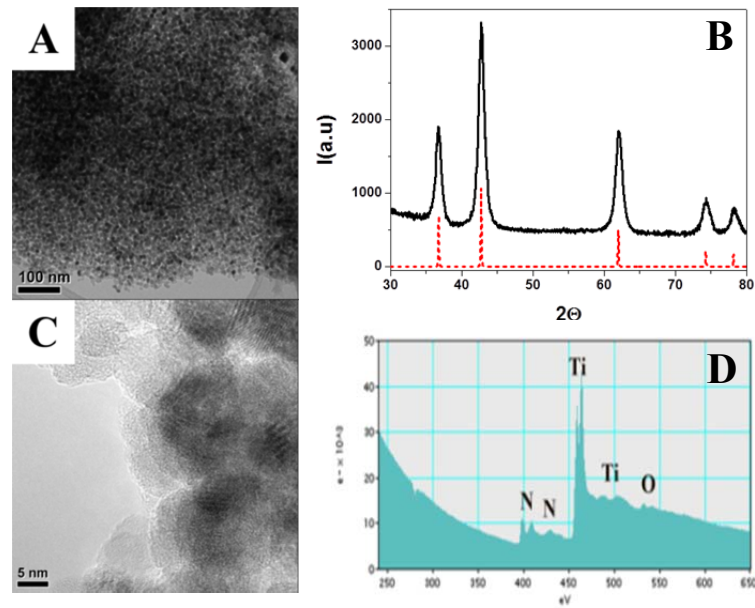

Figure 4.9. A) TEM image (overview) of TiN nanoparticles prepared via the UGR, B) corresponding XRD pattern (in red the expected pattern from database, ICDD 04-008-7173), calculated size: d~10 nm, both from eq. 4 and TEM images. C) HR-TEM image showing lattice fringes inside the TiN nanoparticles, with d_{exp}=2.18 corresponding to the 200 reflections (d_{th}=2.13) and D) EELS pattern.

In order to gain information about homogeneity on a larger scale, SEM investigation has been performed, and some representative images are reported in figure 4.10, where also small nanoparticles can be observed as well.
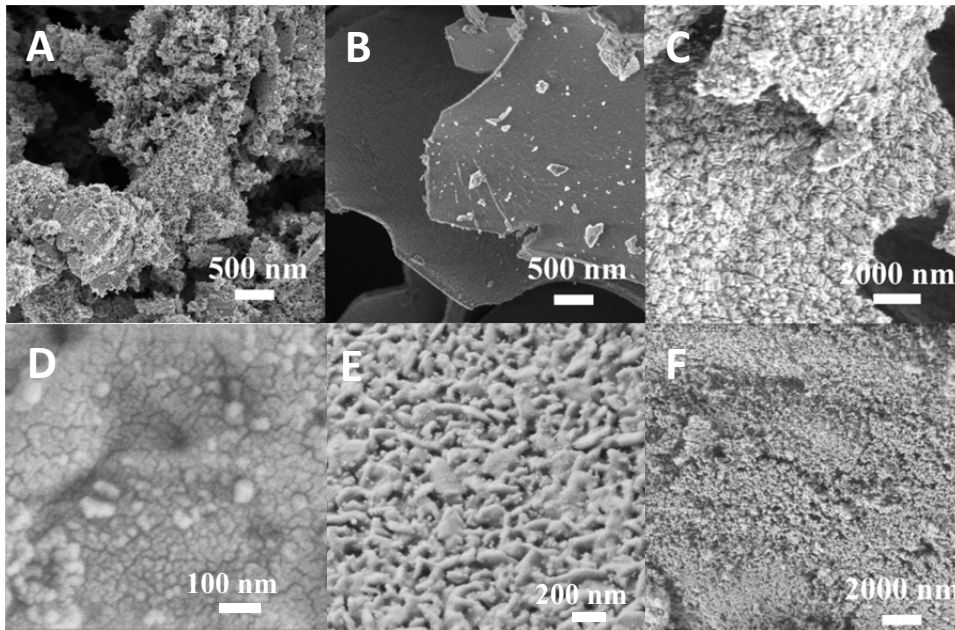
Figure 4.10. SEM images of several MN/MC nanoparticles (A, MnN$_{0.43}$; B, VN; C, Mo$_2$N; D, Fe$_3$C; E, MoC; F, WC).

Finally, to have better insight of the apparent size and morphology, TEM investigations have been performed (figure 4.11).
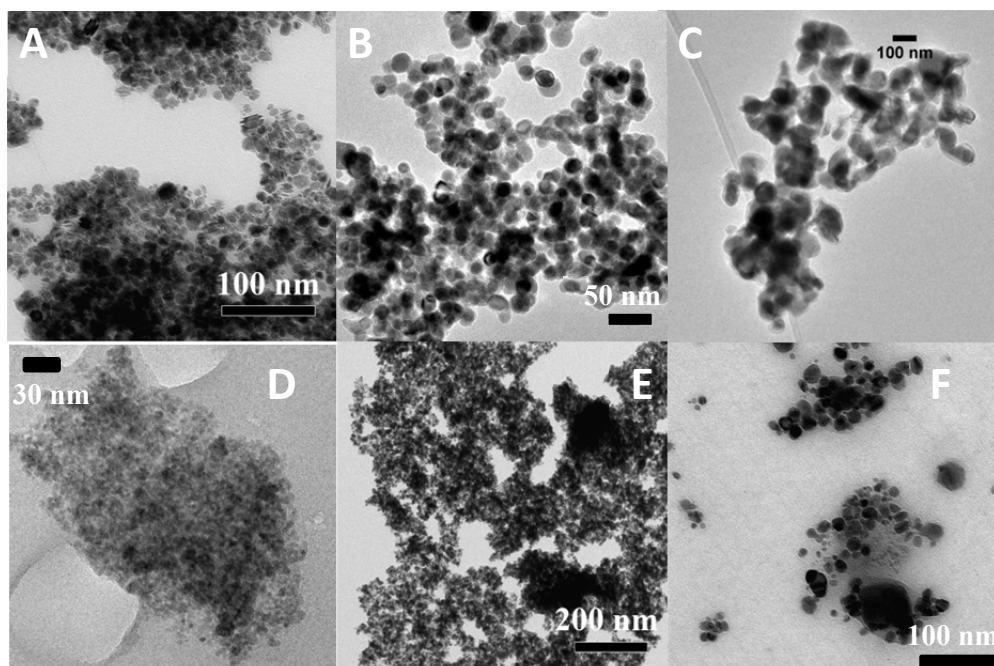
Figure 4.11. TEM images of several MN/MC nanoparticles. (A, Mo$_2$N; B, NbN; C, MnN$_{0.43}$; D, Fe$_3$C; E, WC; F, MoC).

Observed nanoparticles are usually well-defined, spherically shaped, and are interacting only weakly. Here it must also be considered that no dispersing agents have been used to separate the particles before image acquisition.

4.1.1 Advantage of the UGR route

In the previous sessions, it was shown how via the UGR several MN/MC could be obtained in a similar way, just by adjusting the precursor composition and/or reaction conditions (see table 4.1 and figure 4.8). In this session, it will be shown how further control over particle size and carbon/nitrogen contents can be obtained and how the synthesis can be tailored for the production of more complex systems, such as ternary, quaternary and alloyed systems.

Effect of the heating rate

An easier way to affect the nanoparticles nucleation and growth is to change the heat treatment. It was proved that reaction rate strongly influences the size of the final product. Representatively, the case of Mo_2C is reported here (figure 4.1.1.1).
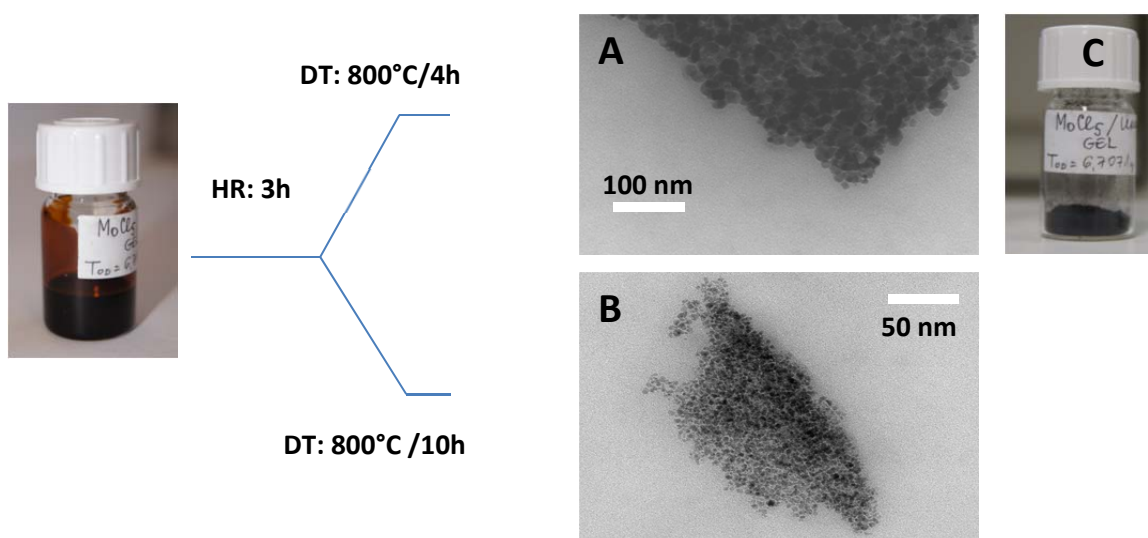
Figure 4.1.1.1 Mo-Urea precursor heated under different conditions and corresponding TEM picture showing the size difference of the final nanoparticles. Photo C corresponds to the final Mo_2C powder after higher heating rate.

For this system a significant reduction of nanoparticles size (from 30 nm to 10 nm in diameter) was obtained by increasing the dwelling time (from 4 hours to 10 hours). This is somehow surprising because in a classical crystallization process, and accordingly with LaMer [154], a rapid nucleation results in smaller size. In the present case, this apparently anomalous behaviour can be explained considering that a lower heating rate also slows down the decomposition of the organic matrix, which holds the nanoparticle nuclei altogether and protects them from rapid growth and

coalescence effects. It was in fact observed that nanoparticles are formed during the HR step, while they crystallize during the DT and following cooling down[16] (see figure 4.3).

Effect of the urea/metal ratio (R) [36] [155] [156]

It was observed that by changing the urea/metal molar ratio (R) the chemical composition of the final product can be changed, going for instance from the metal nitride to the metal carbide phase or from the metal oxide to the corresponding metal nitride phase, passing (when possible) by the corresponding intermediate metal oxy-nitride. This behaviour will be exemplarily shown in the following for the molybdenum and tantalum cases, respectively. Experimental details are reported in table 4.1. In figure 4.1.1.2 the case of molybdenum is described.
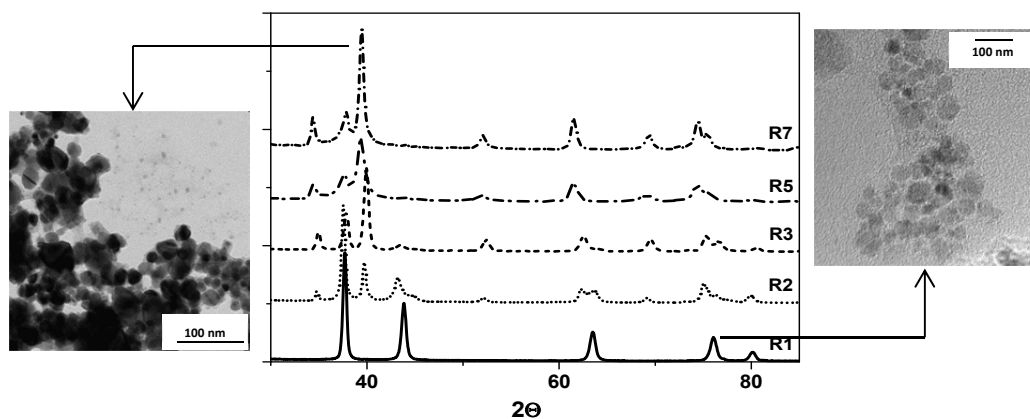
Figure 4.1.1.2. XRD patterns of Mo-Urea samples prepared with different R and treated at 800°C. Samples prepared with R=1 and R=7 were indexed as Mo_2N (ICDD 00-025-1366) and Mo_2C (ICDD 00-011-0680) respectively. a-b) TEM image of the sample prepared with R=1 and R=7 respectively.

In the transition from MN to MC, and depending on the metal, a mixture of the two phases (as in case of molybdenum) or a carbo-nitrides phase ($M_xN_yC_z$) can be observed (as in case of manganese). To better understand this transition, we have to consider that carbides are often structurally similar to their nitride counterparts (as discussed in chapter 3), and during the HT, nitrogen and carbon can either compete in bonding the metal atoms, or the carbon can simply be "solubilized" in the nitride phase in a second step, as shown by Jack in the case of iron [157], converting the nitride into a carbide. The nitride phase is usually the less thermodynamically stable

---

[16] In-situ XRD measurements have been performed via synchrotron radiation (KMC-2) and data analysis is still in progress.

phase. The effect of the metal-urea ratio in changing the final composition will also be shown in section 4.1.2 for the case of iron.

Contrary to the MN →MC transcription, the incorporation of N into a MO_x structure to form MON or MN is not at all trivial, and purity can be a big issue. This is especially important for those materials, whose band gaps lie in the visible range and find application as photo-catalysts. In chapter 3, it was mentioned that the complete or partial replacement of oxygen with nitrogen in some metal oxide structures has a strong effect on the electronic band gap of the final material (reflected also by the different color, as shown in figure 3.2), and it is a result of the combination of the 2p atomic orbitals of N and O. If the band gap value lies in the visible light range, the material is photoactive. Traces of carbon can therefore strongly compromise the performance of the material and for this reason, a classical UGR was ineffective to prepare phase pure TaON and Ta_3N_5. This is attributable to a prompt nitrification step. From the XRD patterns of Ta-Urea samples prepared with different R (Figure 4.1.1.3) it can be observed that all the products obtained for R<5 are constituted by TaON with traces of Ta_3N_5 and carbon and display dark colours. For R > 5.0, Ta_3N_5 percentage increases, TaON is still present, together with Ta_4N_5, a black (and therefore undesired) side product.
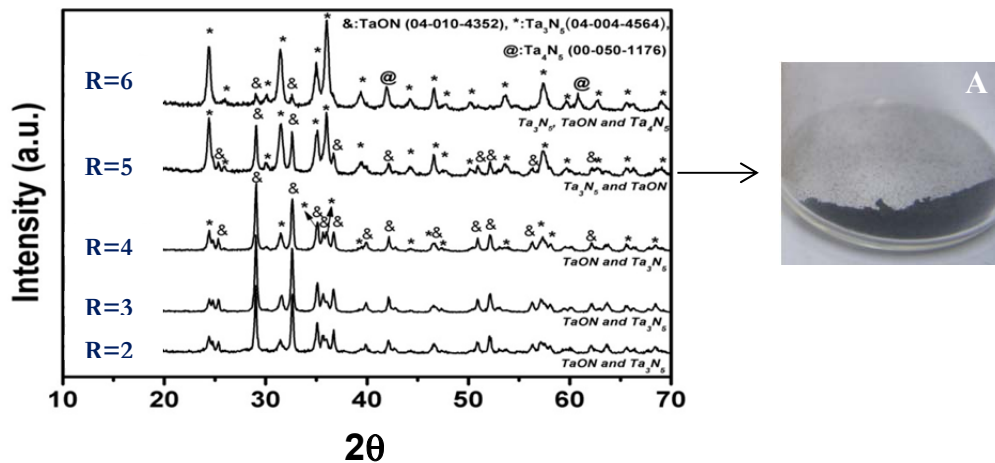
Figure 4.1.1.3. XRD patterns of Ta-Urea samples prepared with different R and treated at 800°C. A) Digital photo of the powder obtained from R=5 showing the black colour of the sample.

In order to slow down the nitrification step, a classical *escamotage* was considered: the use of a capping agent, i.e. a complexing agent able to bond urea and retard its decomposition. For this purpose, calcium ions first and silica nanoparticles thereafter were used. A complete description is reported in references [36] and [158] for the use of calcium ions and silica nanoparticles, respectively. In both these studies, urea, still employed as in-situ nitrogen source, is stabilized by complexation with Ca^{2+} ions or silica nanoparticles. This complexation leads to a slower nitridation step necessary to obtain well-defined TaON and Ta_3N_5. In the following, the case of the calcium ions assistance will be discussed.
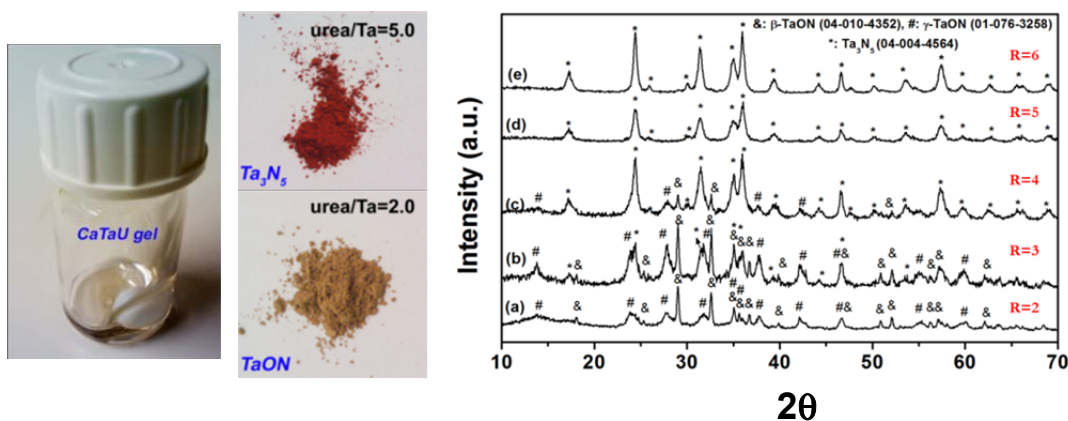
Figure 4.1.1.4. Left: digital photo of Ca-Ta-Urea precursor at R=2, before and after heat treatment (yellow powder). The material prepared at R=5 after heat treatment (red powder) is also reported. Right: XRD patterns of Ca-Ta-Urea precursors prepared at different ratio. Adapted with permission from reference [36] (© 2011 Wiley-VCH Verlag GmbH & Co. KGaA, Weinheim).

The presence of calcium affects not only composition, but also homogeneity of the final material. In figure 4.1.1.5, SEM images of a sample prepared with and without the addition of calcium ions are compared. In absence of calcium, polydisperse nanoparticles ranging from 30 to 200 nm in diameter are observed, while in presence of Ca^{2+}, higher homogeneity is observed.
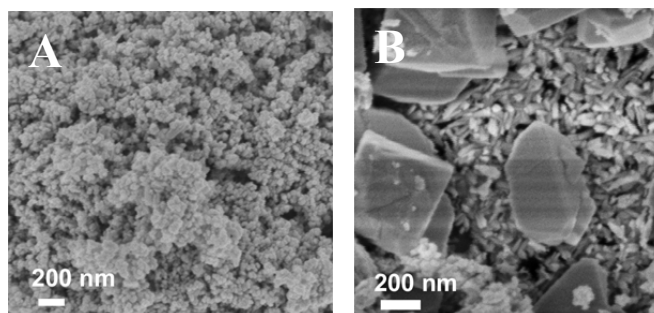
Figure 4.1.1.5. SEM images of Ta-Urea samples prepared with (A) and without (B) the assistance of calcium ions and treated at 800°C.

TEM investigation confirmed the formation of monodisperse and crystalline nanoparticles of ~30 nm in diameter (figure 4.1.1.6).
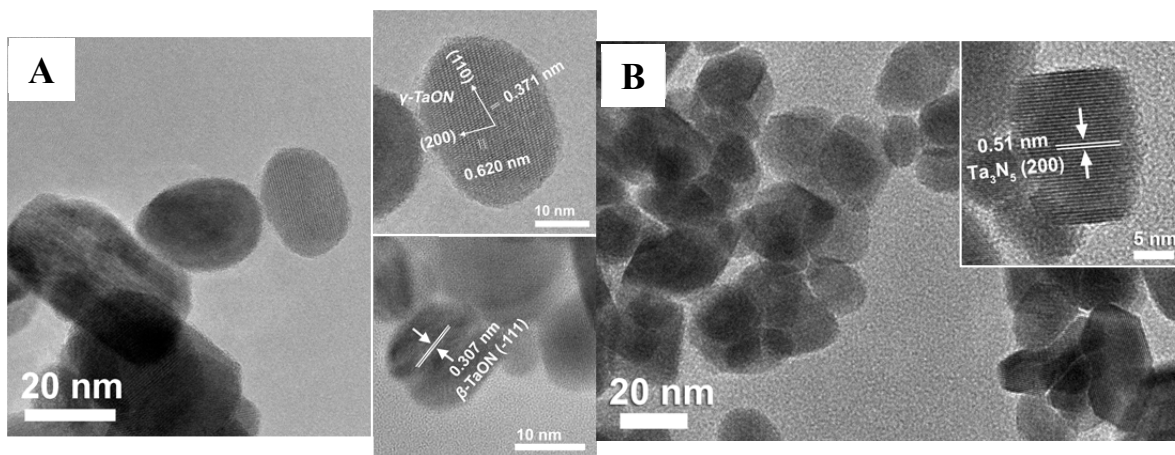

Figure 4.1.1.6. TEM images of samples prepared with calcium addition at R=2 (A) and R=5 (B), respectively. Adapted with permission from reference [36] (© 2011 Wiley-VCH Verlag GmbH & Co. KGaA, Weinheim).

In agreement with other authors [159 - 161] and as indicated by FT-IR investigation, Ca^{2+} bonds urea through oxygen bridges (red shifts for $\nu_{C=O}$ and δ_{NH}, blue shift for ν_{CN} in presence of calcium [36]). The C=O bonding is therefore weakened by the interaction with the calcium ion, which also increase the electron density around the carbon. This means that the C–N obtains a partial double-bond character and becomes more stable. In this way, urea decomposes slower with a consequently less eruptive ammonia release. TGA study confirmed that in presence of calcium, decomposition temperatures are shifted to higher values (figure 4.1.1.7).
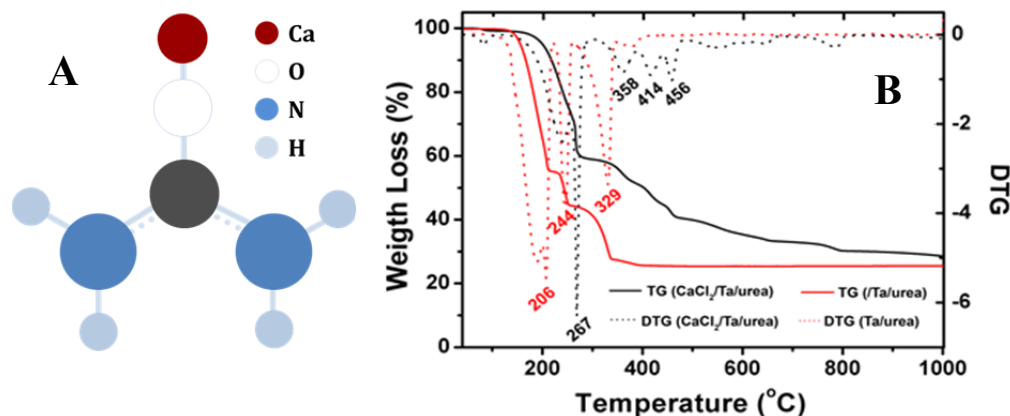
Figure 4.1.1.7. a) Schematic representation of the Ca-Urea bonding. B) TGA thermo-traces of Ta-Urea samples prepared without (red pattern) and with (black pattern) the assistance of Ca^{2+}. Adapted with permission from reference [36] (© 2011 Wiley-VCH Verlag GmbH & Co. KGaA, Weinheim).

In addition, the calcium product formed during the heat treatment could also have a surface-protecting role, i.e. it may act as a surface stabilizer, reducing surface tensions of the particles, as suggested by the shell-free surfaces (figure 4.1.1.6).

Similarly to the case of tantalum, also pure zirconium oxy-nitride could not be prepared simply applying the UGR, classically. For this system, too, the desired product was not phase pure. Massive carbon leftovers were found, which affected the colour of the final material (coloured in black rather than yellow). In this case, the addition of NH_4Cl was considered as "purifying agent". In figure 4.1.1.8, photos of the sample prepared with and without the addition of ammonium chloride are shown, together with the corresponding HR-TEM images of the sample prepared with NH_4Cl. The HR-TEM images nicely show the crystallinity of the nanoparticles.
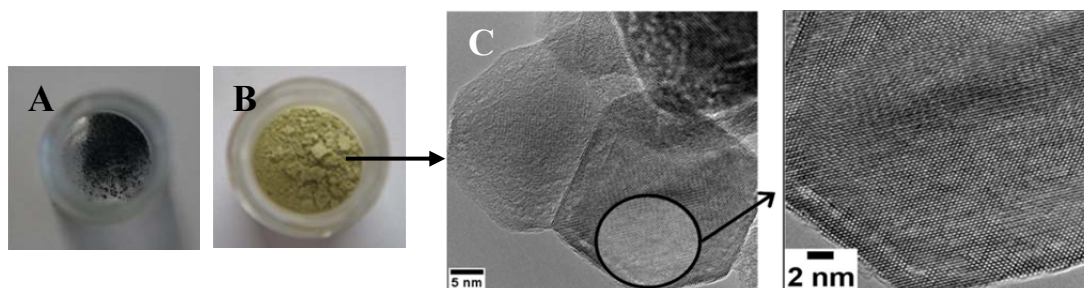

Figure 4.1.1.8. Digital photo of zirconium oxy-nitride samples prepared without (A, black) and with (B, yellow) the addition of ammonium chloride. C) HR-TEM images of the sample shown in B.

This study is, however, still in progress.

Effect of a second metal component: toward quaternary systems and alloys [162]

Motivated by the positive result obtained for ternary systems (namely tantalum oxy-nitride and zirconium oxy-nitride), our attention moved further to more complex compounds, such as quaternary systems and alloys. Still in the field of photoactive materials, we attempt to prepare $Zn_{1.7}GeN_{1.8}O$ and GaN@InN nanoparticles, both being semiconductors with appealing photo-catalytic properties. Using the UGR, the indium content in the final material can be adjusted simply by changing the initial ratio between the metal precursors. For each system, experimental details can also be found in table 4.1.

For both these systems, the available chemical synthetic pathways are rather limited. To the best of our knowledge, the UGR is one of the first reported bottom-up approach to prepare quaternary nitride [162].

From a compositional point of view $Zn_{1.7}GeN_{1.8}O$ is a heterogeneous solid state solution of $ZnGeN_2$ and ZnO. Also here, the classical UGR approach did not lead the desired material, and a massive presence of carbon as side product was observed, similar to the case of zirconium oxy-nitride. As already mentioned before, the presence of carbon renders the final material black, thus impairing its optical properties. To overcome this drawback, as for the case of zirconium oxy-nitride, ammonium chloride is added to the mixture of metal salts and urea [162]. The precursor appears in both cases (with and without ammonium chloride), colourless and "glassy". Upon heat treatment of the precursor, a solid powder is obtained: yellow when ammonium chloride is used, black otherwise. The yellow powder consists (as ascertained by TEM and XRD) of small but already crystalline nanoparticles (d~15 nm), stable and morphologically well-defined. A comparison of the XRD patterns and TEM images of the sample prepared with and without stabilizing agent is reported in figure 4.1.1.9.
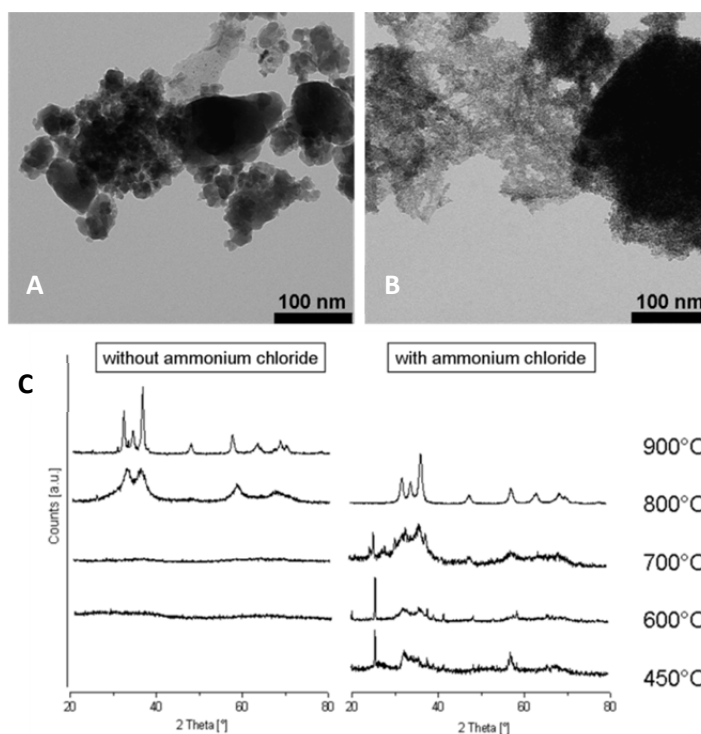
Figure 4.1.1.9. TEM images of Zn-Ge-Urea sample prepared without (A) and with (B) the assistance of NH$_4$Cl and treated at 800°C. C) XRD patterns of the Zn-Ge-Urea samples thermally treated at different temperatures with and without NH$_4$Cl. Final product is attributed to Zn$_{1.7}$GeN$_{1.8}$O (ICDD 00-024-1443). Adapted from reference [162] by permission of the Royal Society of Chemistry.

From this figure it can be observed that in absence of ammonium chloride no crystalline features can be detected at T< 800 °C. In contrast, with NH$_4$Cl alternative crystallization behaviour is observed and crystalline features are displayed at 450 °C already. The addition of NH$_4$Cl creates an atmosphere richer in ammonium that resulted in a decrease of the nucleation temperature, which consequently leads to uniform size and well-defined shape. In addition, the overall reaction temperature can be decreased by about 100 °C. Size observed by TEM (~15 nm in diameter) are in good agreement with that calculated by XRD (~10 nm, with eq. 4). HR-TEM study confirms nanoparticles crystallinity with lattice fringes of 2.77Å, corresponding to Zn$_{1.7}$GeN$_{1.8}$O [163].

TGA analysis of the systems is reported in figure 4.1.1.11. From the comparison of the thermo-traces recorded on the sample with and without the addition of NH$_4$Cl it can be seen, at about 300°C, a higher mass loss in presence of the additive, possibly due to the ammonium rich atmosphere[17]. Furthermore the in presence of NH$_4$Cl, the thermo-trace has a smoother (continuous) trend, while in absence of additive, the trend present defined steps.
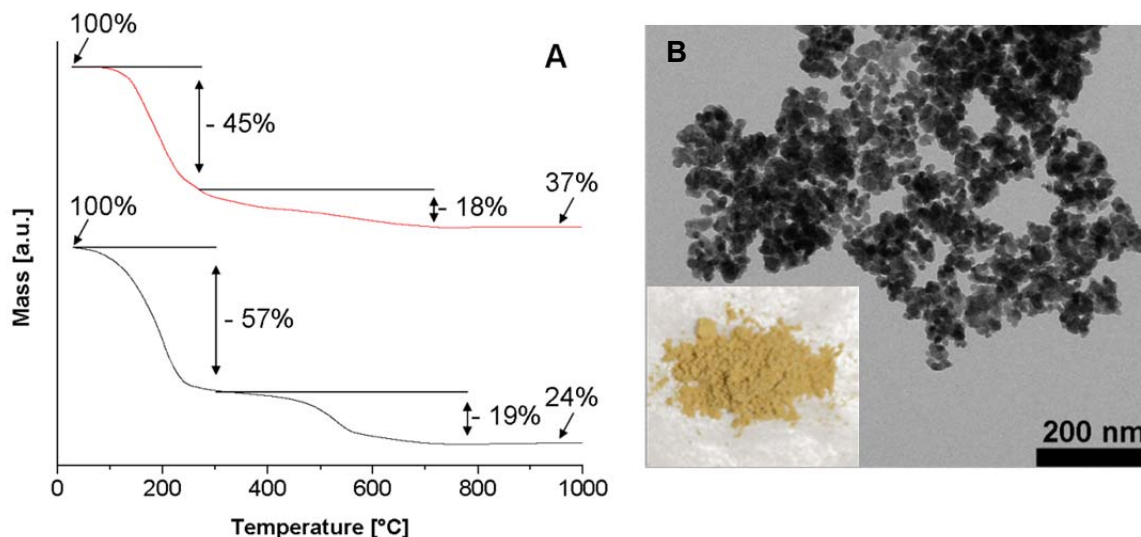

Figure 4.1.1.11. A) TGA thermo-traces of Zn-Ge-Urea sample prepared without (red pattern) and with (black pattern) the addition of NH$_4$Cl. C) TEM image of Zn-Ge-Urea sample prepared with the assistance of NH$_4$Cl and treated at 800°C. A digital photo of the product is also reported. Adapted from reference [162] by permission of the Royal Society of Chemistry.

Finally, photo-catalytic properties of our material were tested via a model reaction for the degradation of organic dyes, showing promising preliminary results as discussed in chapter 7.

---

[17] Decomposition of ammonium chloride is expected at~340°C.

As last example of this session, the preparation of $Ga_xIn_{1-x}N$ nanoparticles, with tuneable indium content will be presented. In a typical synthesis, gallium urea precursor with R=5 were prepared, then varying amounts of $In(NO_3)_3$ were added (see table 9.3). Upon solvent evaporation, a white crystalline powder is formed (a complex between the metal and the urea). The complexes formation in the gallium-urea, indium-urea and gallium-indium-urea samples was ascertained by IR investigation (figure 9.4 in the appendix). The IR spectra of the bimetallic urea complexes are different from the monometallic ones and from that of pure urea. The main differences concern CO and CN bands, while NH_2 bands undergo only small changes. This seems to suggest that one metal, presumably Ga (present in higher amounts), is bonded to urea through oxygen bridges (via C=O), while the other (In) binds urea through NH_2 groups. The bonding between the two metals probably occurs through urea molecules. However, as for other precursors, further analyses are in progress to establish the exact nature of the complex and the coordination shell.

The precursors, calcined at 750 °C under nitrogen flow, bring to fine solid powders (figure 4.1.1.12), and corresponding XRD patterns are reported in figure 4.1.1.13.

Figure 4.1.1.12. Gallium-Indium nitride samples prepared with R=5 and varying amount of In (table 9.3). The indium loading strongly affects the band gap of the final alloy and, as a consequence, different colours can be observed, from light yellow (colour of the pure GaN) to dark blue (colour of the pure InN).

Sizes calculated by the Scherrer equation (eq. 4) range between 5 and 10 nm in diameter. TEM investigation confirms the formation of small nanoparticles of ~10 nm in diameter (figure 4.1.1.13).
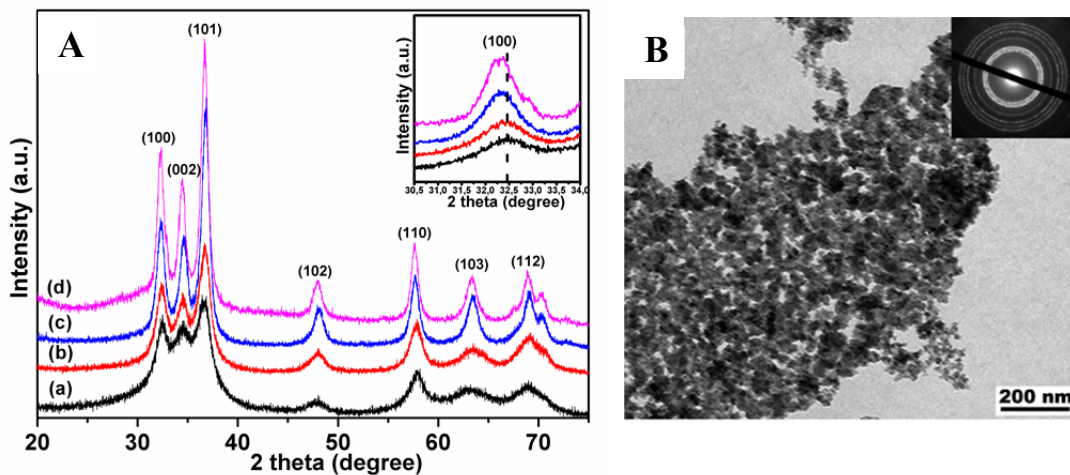
Figure 4.1.1.13. A) XRD patterns of the pure GaN and Ga-In-N samples with increasing indium content: (a) GaN, (b) GaInN-0.05, (c) GaInN-0.10, and (d) GaInN-0.2. B) TEM image (and corresponding SAED) of the GaInN-0.10 sample (c).

From the XRD patterns a shift to lower angles in the peak positions of samples containing indium can also be observed, compared to the positions of the hexagonal structure of pure GaN (ICDD 04-012-0444). This might be due to the increase of the crystal lattice as a consequence of the substitution of smaller Ga^{3+} with bigger In^{3+} ions. Similar effects were found in the systems of Al-Y-N, Al-Sc-N, and Al-Ga-N [164 – 166]. In addition, the progressive peak shifts (by increasing the indium loading) toward lower angle supports the ternary nature of the as prepared Ga-In-N samples, rather than the formation of GaN and InN mixtures. XRD findings seem to be supported by IR investigations on the final powders (figure 9.5). IR spectrum of the pure GaN shows a broad absorption at about 595.3 cm^{-1}, attributed to the Ga–N stretching mode [167], which is shifted to 588.1 cm^{-1}, 583.6 cm^{-1} and 574.5 cm^{-1} for GaInN-0.05, GaInN-0.10 and GaInN-0.2, respectively (figure 9.5 appendix). Considering that the absorption of the In–N stretch is expected at about 510 cm^{-1} [168], this shift supports further the indium loading into the GaN structure.

Finally, to confirm the simultaneous presence of In and Ga in the nanoparticle clusters, elemental mapping and EDAX measurements were performed and results displayed in figure 4.1.1.14. From this figure the presence and location of the different elements (marked with different colours) can be observed in a selected nanoparticles cluster (in white). It can nicely be seen that the carbon profile simply matches the holey carbon support film of the TEM grid.
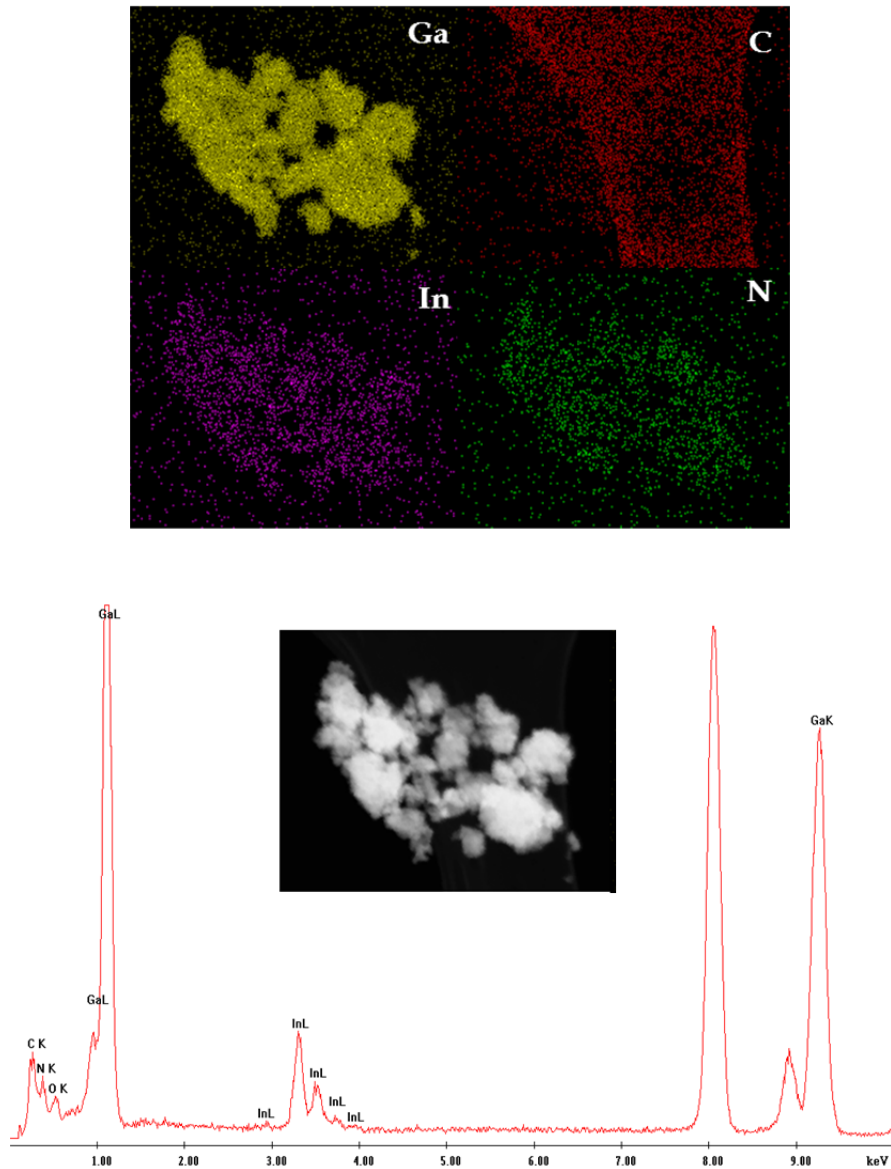
Figure 4.1.1.14. Atomic mapping of the GaIn-0.1 sample and corresponding EDAX pattern (unmarked peaks are attributed to the Cu lines from the Cu grid used).

From the EDAX pattern it can also be seen that the detected oxygen amount is close to the detection limit and mainly on the surface of the aggregates.

4.1.2 Magnetic Nitrides and Carbides: the case of iron

During the *habilitation* work, special attention was given to the study of iron based systems. As many iron compounds, iron nitrides and carbides are magnetic (in some cases exceeding saturation magnetization of iron oxide), but are also ceramic materials. Thus they are believed to be suitable replacements of iron oxide in many of its numerous applications. In addition, their expected lower toxicity makes them a suitable alternative also to metallic iron. Due to their magnetic properties, alongside the field of applications discussed in chapter 3, further employments can be expected. Magnetic nanoparticles are nowadays largely used in many different fields, for instance in electronics (as magnetic fluids [169], magnetic data storage and recording [170]), in biomedicine [171] (as contrast agents in medical imaging [172] (MRI), as drug delivery systems [173] or in hyperthermia treatment of cancer [174]), in environmental issues (e.g. for the purification of water [175, 176]) but also in catalysis (also as easily recoverable catalysts) [106, 107]. In the latter field, both iron nitride and carbide phases have shown activity in key-reactions, e.g. in the Fischer-Tropsch process [177, 62], and in ammonia decomposition and synthesis (Haber-Bosch process) [64].

Presently, one the most commonly used magnetic nanomaterial is iron oxide (both as γ-Fe_2O_3 and Fe_3O_4). The extensive use of this material is mainly due to the several and easy synthetic pathways to obtain it in form of well-defined nanoparticles, monodisperse both in size and morphology (usually spherical), often with the possibility to tune its size [178]. Additionally, its impact on biological systems has been widely studied, showing low toxicity, depending on the functional group used to stabilize them [179, 180]. On the contrary, pure iron ($Fe°$), although it possesses higher saturation magnetization (see table 4.1.2.1), it is also bio-toxic, as many metals are [181], preventing any use in biomedical applications. In this respect, the corresponding nitride and carbide could be a good compromise between iron oxide and iron. Although definitive studies to prove their biocompatibility are still in progress, it is clear that a first step to this outcome (namely the replacement of FeO_x with Fe-N/C systems) relies on a competitive preparation of these materials.

Table 4.1.2.1. Overview of some iron compounds and corresponding saturation magnetization values.

Compound	Molecular formula	C/N content (wt%) [157]	$M_{s,bulk}$ emu/g	Ref.	Note
Metallic iron	Fe°	--	200	[182] [183]	130-150 emu/g if nanosized
Magnetite Iron(II,III) oxide	Fe_3O_4	--	90	[184]	
Hematite Iron(III) oxide	Fe_2O_3	--	0.59	[185]	
Maghemite Fe(II) deficient magnetite	γ-Fe_2O_3	--	90	[182] [183]	40-70 emu/g if nanosized
Di-iron nitride	Fe_2N	11.4	0.74	[186]	Decomposes at 200°C
Iron nitride	Fe_3N	7.7	123	[187]	
Martensite (γ')	Fe_4N	5.9	190	[182] [183] [188]	Roaldite
Martensite (α'')	$Fe_{16}N_2$	3.0	240 315	[189] [190]	The reason for the high saturation magnetization observed for this compound is still under debate
Cementite	Fe_3C	6.7	140	[191]	Orthorhombic
Eckstrom-Adcock carbide	Fe_7C_3	8.4	120	[174] [175] [192]	Iron carbide
Hägg carbide (χ)	Fe_5C_2	7.9	100-140	[174] [175] [193] [194][195]	Monoclinic

In table 4.1.2.1 some common iron phases are reported, but the variety of iron based compounds is richer and surely one of the first exploited by humankind. Metallurgy employing combinations of iron and carbon dates back even to prehistory, when meteorites were used as first sources of iron [196]. Beads found in *tomb 67 at Gerzeh*, which were made by using meteoritic iron as the metal source, represent one of the earliest examples of exploitation of iron in Egypt [197]. Even the superior hardness of Damascus sabre seems to arise from iron carbide nanoparticles reinforcing iron metal [12]. According to legend, carburization of iron toward stronger cutting tools (including swords and blames) was developed by an Anatolian population called *Chalybes*, who might also have forged the sword of Julius Cesar [198]. This sword (called *crocea mors*) it might became, subsequently, the mythic King Arthur´s sword: *Excalibur* [199].

Mythology and novels aside, the featuring role of carbon (and recently also nitrogen) in the iron structure is well-recognized today, complementing the final material with additional properties.

From a structural point of view, both iron nitride and carbide are also interstitial compounds. In metal nitrides, nitrogen atoms are placed on the octahedral sites of the hexagonal crystal structure of iron, while, in metal carbide, carbon atoms occupy the trigonal prismatic sites of an orthorhombic iron structure. As observed from table 4.1.2.1, both iron nitride and carbide can exist in several stable forms. Interstitial vacancies can be filled further with anions, bringing to non-stoichiometric compounds. According with Fang et al., Fe_7C_3 presents both types of basic crystal structures, one orthorhombic and one hexagonal [200]. Interestingly, this material is not easily found in a standard phase diagram of iron and carbon and, in early studies, some authors have noted its production only as metastable phase, and attributed it to a rapid cooling rate of the particles after laser pyrolysis [37]. More recently, Fe_7C_3 was synthetized mechanically as bulk [201] and as nano-crystalline phase by CO_2 laser pyrolysis [202].

From a synthetic point of view, synthesis of Fe_3N and Fe_3C nanoparticles presents the same challenges as other MN/MC (see chapter 3), with a further issue: the high reaction temperature can bring to their decomposition into $Fe°$ and N_2/C. Originally, iron carbide phases were only found as side products in some processes, such as graphitization of carbon at lower temperature, in presence of iron-based catalysts. More recent syntheses are flame spray pyrolysis (Fe_3C) [203], CVD [204] or ammonolysis of pre-synthesized iron or iron oxide nanoparticles in presence of ammonia. These methods are unsafe and energy consuming and are therefore not ideal for large scale production [205, 206].

In this session, it will be shown how iron carbide and nitride phases can be prepared in a simpler way, based on the UGR. The influence of precursors and heat treatment in controlling final composition and morphology will also be discussed. At the end of the session, a "transcription method" from iron oxides to Fe_3N and Fe_3C nanoparticles (also based on the UGR) will be presented, while the use of other types of organic *gelators*, such as biopolymers and sugars, will be discussed in section 4.2 and 4.3, respectively.

Iron carbide nanoparticles (np-Fe₃C) [207]

More than for other MN/MC presented up to now, the preparation of phase pure Fe_3C nanoparticles required a careful study over reaction conditions. In particular, higher temperature or prolonged heat treatment caused carbide decomposition into elemental iron and carbon, while the use of solely iron (III) chloride (standard precursor in the UGR) brought bigger particles, ill-defined in shape, together with a high amount of residual carbon in the final product. After careful refining of the synthetic conditions, it was found that employing a mixture of Fe(II) and Fe° (namely a 2:1 alcoholic solution of $FeCl_2 \cdot 4H_2O$ and $Fe(CO)_5$), urea as C-source and short heating rate (i.e. 1 hour to reach the final temperature and 2 hours of dwelling time), well-defined, small but already crystalline Fe_3C nanoparticles could be obtained, as shown in the following. It was suggested by IR investigation (figure 4.1.2.2) that in the jelly-like starting material urea partially replaces water in the first coordination shell of iron, probably via C=O bridges [149, 208], as schematically reported in figure 4.1.2.2. The disappearance of the CO band (at ~1680 cm^{-1}) in the spectrum of the complex supports this idea somehow. Similar to what was discussed in the previous session, the high viscosity of the starting material also seems to indicate a linkage among urea molecules via secondary bounds (presumably H-bonds involving amide groups), forming a wider polymer-like network.
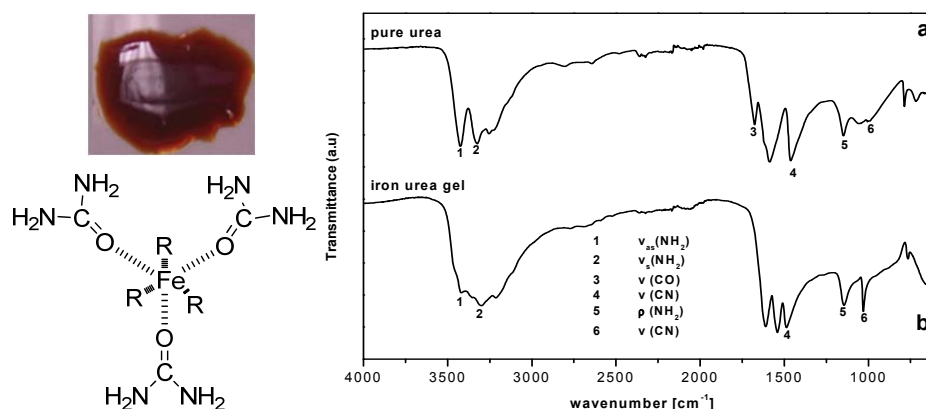

Figure 4.1.2.2. Left side: Digital photo of the starting iron-urea precursor (reddish) and proposed structure of the urea-iron complex. Right side: IR spectra of solid urea (a) and iron-urea precursor (b).

To have information about the formation mechanism of the final Fe_3C, TGA has been performed between r.t. and 1000°C under nitrogen flow (figure 9.6.A in the appendix) and results are similar to those of other urea-metal complexes. The decomposition of urea takes place at temperatures of up to 350°C, when a stable intermediate phase is formed. The IR spectrum of samples quenched at 200°C is very close to that of the starting material gel. At 400°C a disordered structure is observed, confirming the "glassy" nature of the iron intermediate (see figure 9.6.B in the appendix). As previously discussed, this phase is rich in N, C and O, as ascertained by EA (table 9.1), and is converted, upon further temperature increase (up to 700°C), into the final Fe_3C phase, with an overall mass loss of 50 wt%. It was observed that further temperature increases (over 700°C) only bring to a decomposition of Fe_3C into Fe° and C and the formation of a transient FeO_x intermediate phase was not observed in the corresponding XRD patterns (see figure 9.6.B in the appendix). The reaction is then completed at 700°C and samples were therefore calcined under N_2 flow up to 700°C (figure 9.6.A). The final product is a solid silvery magnetic powder (see photo in figure 4.1.2.3) made of orthorhombic Fe_3C, as ascertained by XRD (figure 4.1.2.3). From the XRD pattern of the sample heated at 700°C, the absence of any significant amount of crystalline metallic iron can be observed, an important prerequisite for the application in biomedicine.
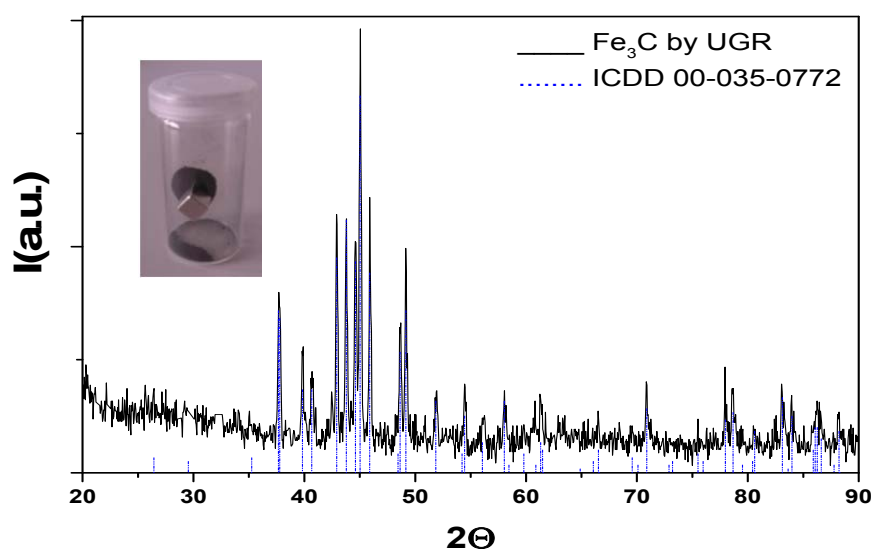

Figure 4.1.2.3. XRD of the final powder obtained upon heat treatment at 700°C for 1+2h. Reference pattern is also reported for comparison as dotted (blue) vertical lines.

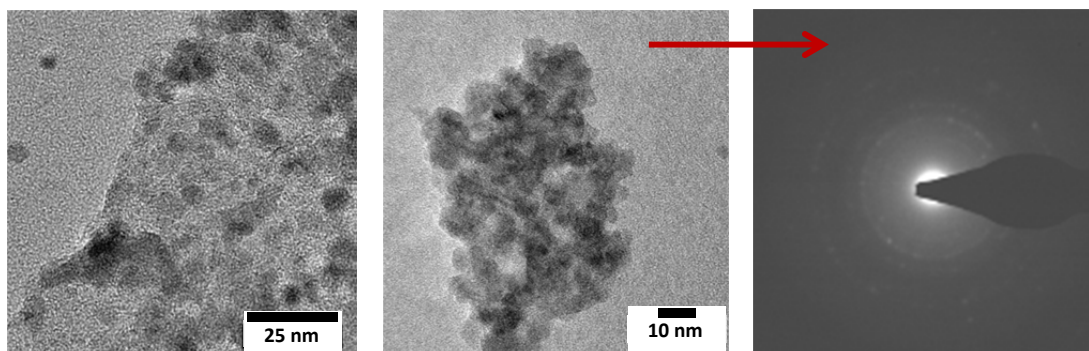Size and shape of the prepared system were investigated by TEM (figure 4.1.2.4).

Figure 4.1.2.4. TEM images (different resolutions) and corresponding SAED of Fe₃C nanoparticles.

The measured lattice fringe distance of d=0.20 nm can be attributed to the (031) plane of the orthorhombic Fe_3C (d_{calc}=0.2013 nm, ICDD 00-035-0772) in agreement with the XRD finding. In terms of size, the sizes calculated by XRD using the Scherrer equation (eq. 4) and those observed via TEM are, however, not in agreement. In fact, while the Scherrer equation gave a crystallite size of ca. 30-40 nm in diameter, TEM clearly shows smaller nanoparticles (5-10 nm in diameter). This apparent discrepancy can be explained by the presence of organized nanoparticle arrays, considering the high magnetic attraction between the particles. SAED performed on nanoparticles clusters shows crystalline patterns (figure 4.1.2.4). Similar magnetic arrays of Fe_3O_4 are also known [209] and analogous effects were observed for other nanostructures too [210]. From TEM study it was also observed that some nanoparticles lie down onto an amorphous phase, probably carbon. The carbon phase might also form a thin protective shell around the particles, improving their stability.

Magnetic measurements were performed on the Fe_3C powder at r.t., and the curve of the magnetization vs. applied field is shown in Figure 4.2.6, in comparison to the magnetic behaviour of the same system prepared via the Biopolymers Route (section 4.2). As expected, for particles smaller than 20 nm, the magnetization curve reflects the superparamagnetic non-hysteretic behaviour of the system. The calculated value of saturation magnetization normalized to Fe_3C[18] gives a specific value of 46.7 emu/g Fe_3C, one of the best reported in literature so far for nanosized iron carbide

---

[18] i.e. without taking into account the surplus of carbon in the final weigh of the sample. The carbon phase is not expected to contribute to the magnetization value.

free from iron [191, 207]. A reduced magnetization value, compared with the bulk (140 emu/g) [211] is expected for nanosized materials (see table 4.1.2.1). Further characterization and mechanistic details on this system are reported in references [207] and [212].

From Fe₃N to Fe₇C₃ and Fe₃C nanoparticles [212]

In order to gain control over composition and morphology of the final material, other iron- and C/N-sources were explored. In particular, it was found that replacing iron chloride with iron (II) acetyl acetonate (Fe(acac)$_2$), a broader range of composition could be obtained and, similarly to the case of molybdenum presented in section 4.1.1, Fe$_3$N and Fe$_3$C, but also Fe$_7$C$_3$, could be prepared adjusting R. On the other hand, replacing urea with DI, rather the spherical nanoparticles, a tubular morphology (namely wrapped nanosheets) is obtained. The use of DI implies the formation of a significant amount of carbon as side product, which can be, however, conveniently exploited to obtain mesoporous structure via hard template approach. All these findings are discussed in the following.

The replacement of iron chloride with Fe(acac)$_2$, still using urea and ethanol, leads to a red homogeneous dispersion rather than a "gel". IR spectrum of the dried precursor is mainly a combination of the IR bands of urea and Fe(acac)$_2$, with an important difference: the C=O band (1690 cm^{-1}) is still visible (figure 4.1.2.5).
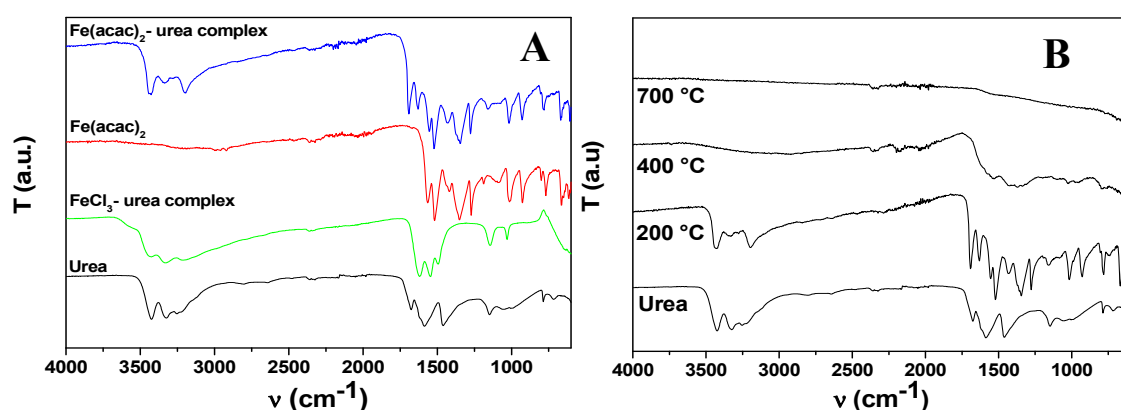

Figure 4.1.2.5. IR spectra of A) iron-urea starting complex using iron acetate and iron chloride as metal source (for comparison the spectra of the pure Fe(acac)$_2$ and urea are also reported). B) IR spectra of iron acetate-urea complex calcined at different temperatures. For comparison the spectra of pure urea is also reported.

In the CN region (1600 cm^{-1} – 1400 cm^{-1}) some differences can be observed, somehow indicating a bonding of iron with urea via its -NH$_2$ groups or a linkage between the C=O group of the acetil-acetonate with the amide groups of urea.

Suspensions prepared with different Fe-Urea molar ratio are thermally treated at 700°C under N$_2$ flow for 1+2h. In figure 4.1.2.6 the corresponding diffrattograms are reported showing the strong influence of the starting ratio on the final composition. In absence of urea (R=0) and for R<1, mainly pure iron is obtained. For R=3 reflections of Fe$_3$N and traces of Fe$_3$C are observed, while for R>3, the main product is Fe$_7$C$_3$, together with traces of the nitride.

From figure 4.1.2.6 it can be also observed that independently of R, no peaks of iron oxide and/or graphite are present.
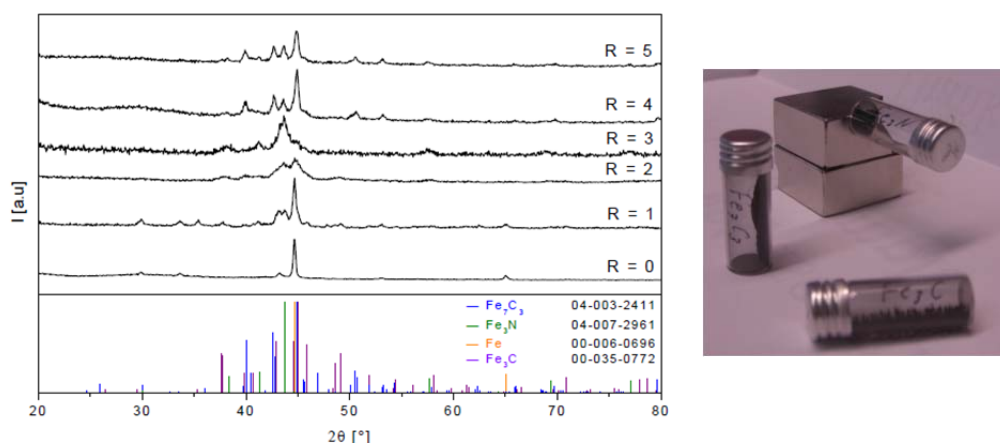
Figure 4.1.2.6. XRD pattern of iron-urea samples prepared at different R and treated at 700°C (1+2h).

By playing with the heating time it is possible to prepare pure Fe$_7$C$_3$ (see table 4.1.2.2 at the end of this chapter), while the preparation of phase pure Fe$_3$N is not possible with this route anyway. However, pure iron nitride can be obtained by replacing urea with macro- molecules, as discussed in section 4.2. The influence of a larger molecular weight on phase purity might be ascribed to a "protecting" role of the macromolecule, which shield the Fe$_3$N nanoparticles from excessive heating and therefore faster decomposition; in other words, the presence of the macromolecule can retard nitride decomposition and carbon diffusion into the nitride structure.
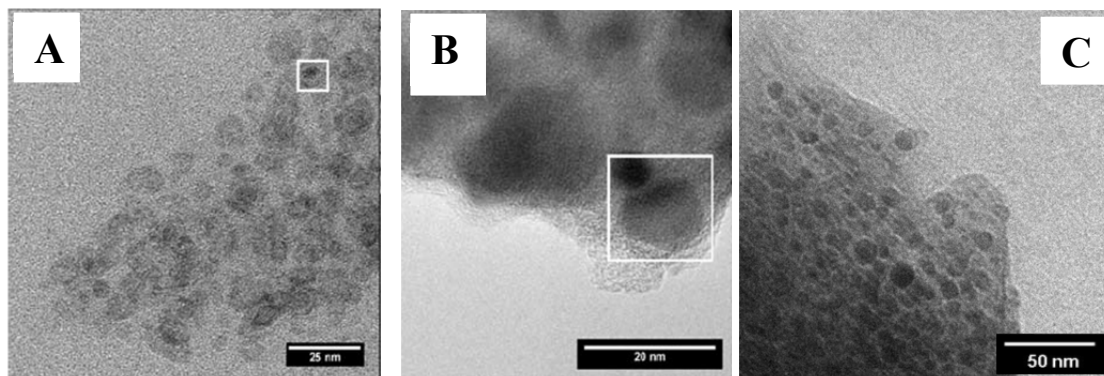
Figure 4.1.2.7. TEM images of Fe$_3$N (A), Fe$_7$C$_3$ (B) and Fe$_3$C (C) nanoparticles.

From a mechanistic point of view, in accordance with GS-MS analysis, the Fe(acac)$_2$ decomposes releasing acetone and acetyl-acetone [213], together with the decomposition of urea up to 350°C (as described in section 4.1). The intermediate material is amorphous and rich in C-N-O and, in contrast to the previous case, a Fe$_3$O$_4$ intermediate is formed up to 400°C [212]. Between 400°C and 600°C, nitrification of iron oxide into iron nitride occurs. Here, the NH$_3$ released from the decomposition of urea is the strong nitrification agent. Furthermore, it is known that iron phases catalyse the decomposition of ammonia [214, 215], which in turn decomposes releasing H$_2$, thus providing a reducing atmosphere. Finally, at 800°C, due to the diffusion of carbon (still partially present in the compound as an amorphous side product) to the nitride structure and the conversion into iron carbide is observed. It must also be said that experiments performed under argon did not lead to iron nitride but directly to iron carbide phase. The influence of the N$_2$ flow is discussed in section 4.2.

The whole process is schematically reported in scheme 4.1.2.1.
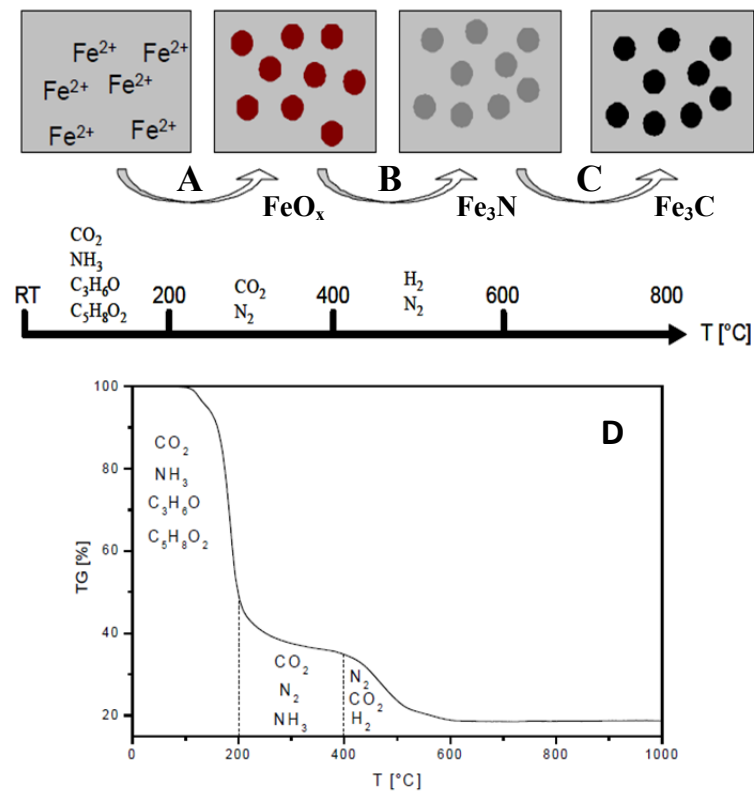
Scheme 4.1.2.1. A) The homogeneous iron-urea precursor starts decomposing and forms an N-C rich matrix, simultaneously the nucleation of iron oxide nanoparticles begins. B) Iron oxide reduction to iron and following iron nitride formation. C) Decomposition of the nitride phase with conversion to the corresponding carbide. D) Thermo trace of the iron-urea precursor. Adapted from reference [212].

Iron carbide based nanosheets (ns-Fe₃C) [216]

In the present section the influence of the carbon source on the final morphology is discussed. Replacing urea with 4,5 di-cyaniomidazol (DI), rather than spherical nanoparticles, long tubular structures could be obtained. Sample characterization shows that the final structure is made of N-rich carbon nanosheets, where small nanoparticles (~5 nm) are loaded onto. Since these results have been already discussed in reference [216], only a short description will be given here, as a comparison with the previously discussed findings.

The preparation of the iron carbide based nanosheets involves the use of iron (III) chloride in ethanol but, as anticipated, urea is replaced by DI (experimental details are reported in table 4.1, entry "ns-Fe₃C"). The starting material is still "glassy" (as with the use of urea) and the coordination of iron with DI molecules, in agreement with other authors [217], is believed to be via the nitrogen atom of the aromatic ring of DI (as reported in figure 4.1.2.8). This assumption is also supported by IR investigation as previously discussed [216].
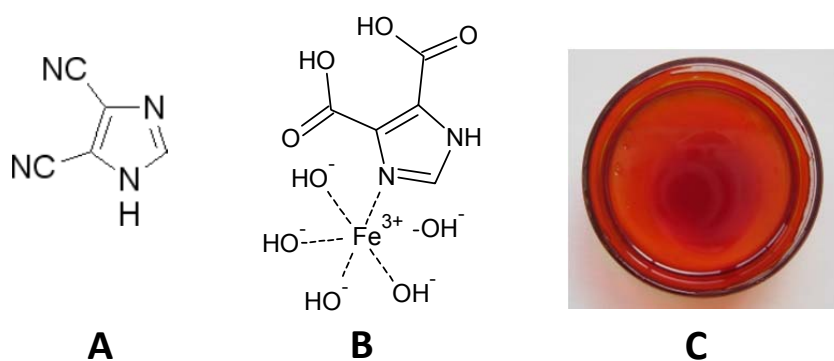

Figure 4.1.2.8. A) DI molecular structure; B) suggested iron-DI coordination involving hydrolysed DI. C) Iron-DI „glassy" precursor.

In order to get the final material, the glass is calcined at 700 °C under nitrogen flow (TGA study shown that the reaction is completed at this temperature [216]). XRD investigation confirmed that the final magnetic powder consists of a carbon rich iron carbide phase (figure 4.1.2.9).
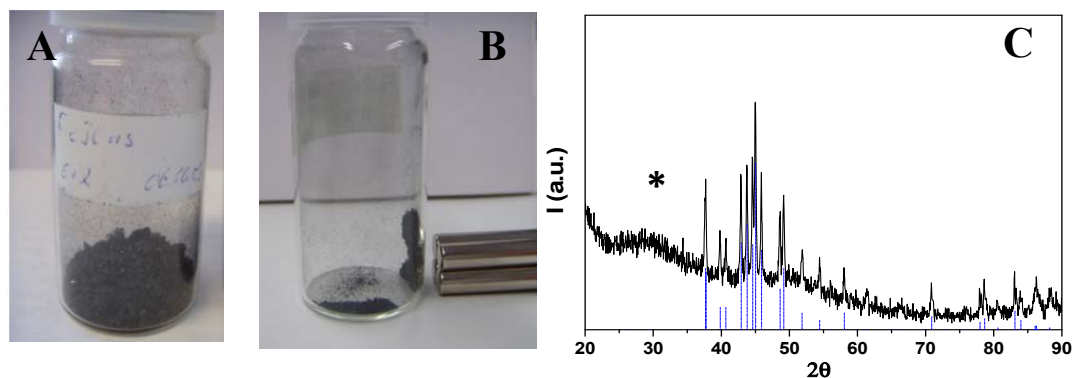
Figure 4.1.2.9. A-B) $Fe_3C@C$ final powder (prepared at 700°C), in B) a portion of the sample under the action of an external magnet. C) Corresponding XRD. The expected pattern for the orthorhombic Fe_3C is also reported as dashed blue vertical lines (ICDD 00-035-0772); marked peak (*) is attributed to carbon (ICDD 04-015-2407).

The uneven baseline indicates the presence of a secondary amorphous phase, which disappears upon temperature increase (figure 9.7 in appendix). Experiment performed at different temperature shown the formation of an amorphous intermediate, where also no iron oxide peaks are present (figure 9.7 in appendix). On the other hand, heat treatment at higher temperature (T>700°C) leads to the decomposition of the material into iron and carbon. The iron phase can be now observed in the XRD pattern (figure 9.7) and elemental analysis shown a dramatic carbon increase (up to 60%).

HR-SEM and HR-TEM investigations show that the system is constituted by tubular structures made of smaller nanoparticles (figure 4.1.2.10).
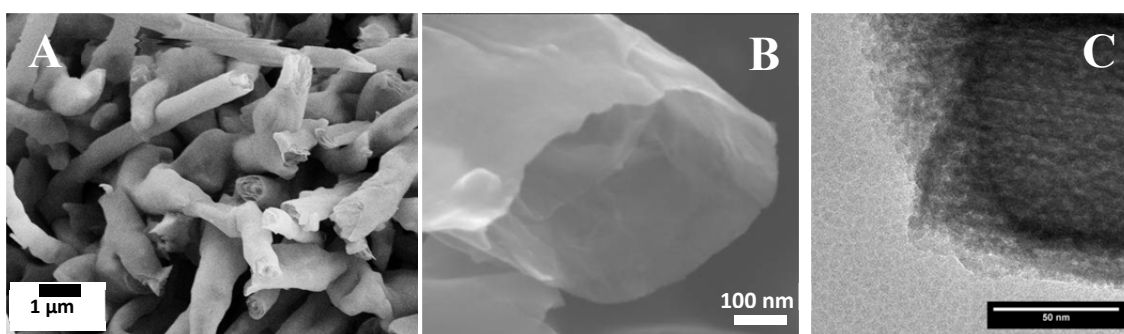

Figure 4.1.2.10. A) SEM image overview of the wrapped nanosheets. B) HR-SEM image on a single "tube". C) HR-TEM on a "tube" after few minutes of explosion under electron beam (i.e. when the organic matrix starts to decompose).

From the analysis of the lattice fringes, two crystalline components are observed. One of those can be safely attributed to iron carbide (2.7 and 5.5 Å), but the second set (2.0, 2.3 and 3.0 Å) belongs neither to any known iron carbide plane, nor to

standard graphite. This observation somehow suggest the formation of a hybrid material, made of Fe_3C and, accordingly with elemental analysis finding, a nitrogen-rich carbon phase. The N-rich carbon layers formed, due to the presence of the iron carbide nanoparticles, are magnetic and obviously unstable, therefore roll up. The formation of tubular structures is never observed using urea as anionic source, probably because urea leads to system with minimal amounts of residual carbon, obviously not enough to form extended sheets. Using urea, the Fe_3C nanoparticles are usually assembled in small isolated clusters, which obviously do not roll up (figure 4.1.2.4).

In the present case, to have more information about the carbon structure formed, Raman investigation was performed with and without iron carbide removal (the iron phase can be washed away with concentrated HCl). In the Raman spectrum before iron removal, only a band a 1270 cm^{-1} is present (attributed to C-N stretching mode [218] and no bands of structured carbon are present. On the contrary, after acidic treatment the typical D and G bands of carbon are the only observed (figure 4.1.2.11.A), suggesting that the elimination of the iron phase causes the decomposition of the N-rich carbon matrix into a "standard" graphitic structure. It must also be mentioned here that the powder obtained after acidic treatment is no longer magnetic. The complete removal of iron carbide can be ascertained by XRD investigation (Figure 4.1.2.11.B)
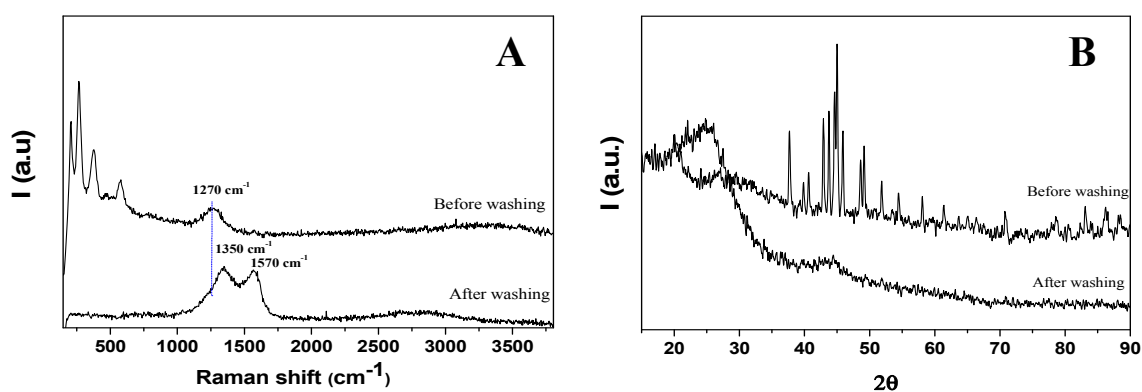

Figure 4.1.2.11. Raman spectra (A) and XRD patterns (B) of the $Fe_3C@C$ nanocomposite before and after acidic treatment (washing).

Mesoporous iron carbide nanocomposite (mp-Fe₃C) [214]

In the previous section it was showed that the use of DI over urea leads to the formation of $Fe_3C@C$ nanocomposite. The presence of this second carbon phase can be conveniently exploited for the preparation of nanocomposites with higher surface area. To be more specific, the carbon can represent a suitable matrix, which can conveniently host guest nanoparticles (e.g. used as hard template). After proper treatment, the guest nanoparticles can be removed, leaving a negative replica of the template. The $Fe_3C@C$ nanocomposite was prepared mixing iron chloride (the metal source) with proper amount of a water suspension of colloidal silica with size of ~22 nm in diameter[19]. Then DI is added to get a molar ration R=2, leading to a homogeneous mixture (synthetic details are reported in table 4.1, entry "mp-Fe₃C"). The precursor mixture was then heat treated at 700°C under N_2 flow. The resulting black powder and magnetic material was washed twice with a sodium hydroxide solution (1M), for two nights totally, and several time with pure water to remove any residual. The powder was dried at 80°C in air.

The process is schematically represented in scheme 4.1.2.2.
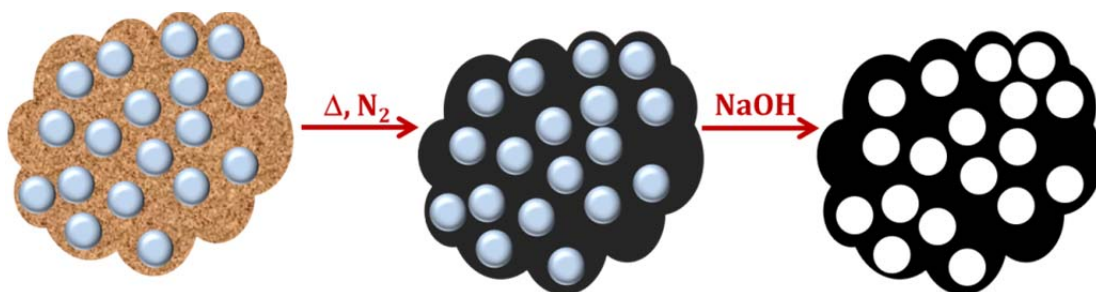
Scheme 4.1.2.2. Schematic representation of the process used to prepare the mesoporous iron carbide based nanocomposite. From left to right: silica nanoparticles (in light blue) are mixed with the metal-DI precursor. The mixture is treated at 700°C leading to the formation of Fe₃C@C, as discussed in the previous session. The material contains the silica nanoparticles, which are unaffected by the heat treatment. Upon washing of the sample with NaOH, the silica can be completely removed, leaving a porous structure (white spheres), where pores are a negative replica of the hard template silica nanoparticles.

The complete removal of silica was ascertained both via IR and XRD measurements. In figure 4.1.12 the XRD patterns of the nanocomposite before and after silica removal are reported. A photo of the magnetic powder is also reported for comparison.
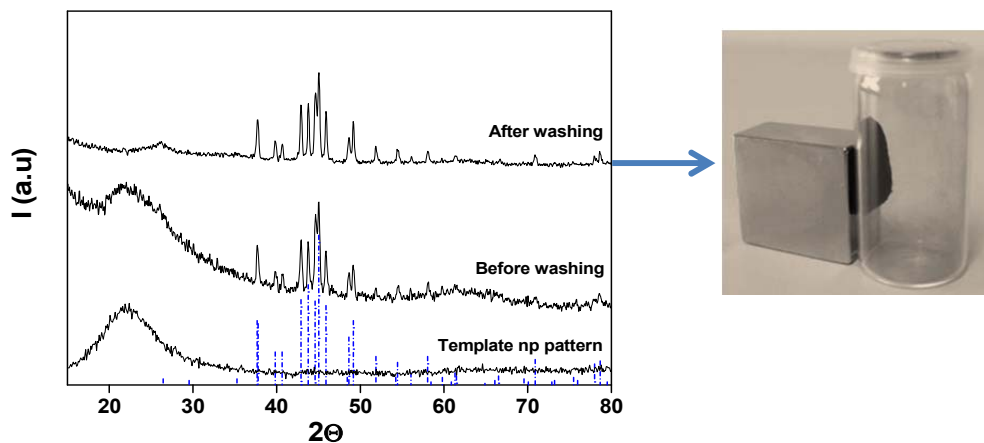
---

[19] Ludox AS40 (see also table 10.1).

Figure 4.1.12. XRD patterns of the of Fe$_3$C@C powder before and after silica removal (washing). The pattern of pure ludox (template) and the expected pattern for Fe$_3$C (blue vertical lines, ICDD 00-035-0772) are also reported for comparison. A digital photo of the sample after the washing step is also reported.

The porous nature of the nanocomposite can nicely be seen from SEM and TEM investigations (figure 4.1.13).
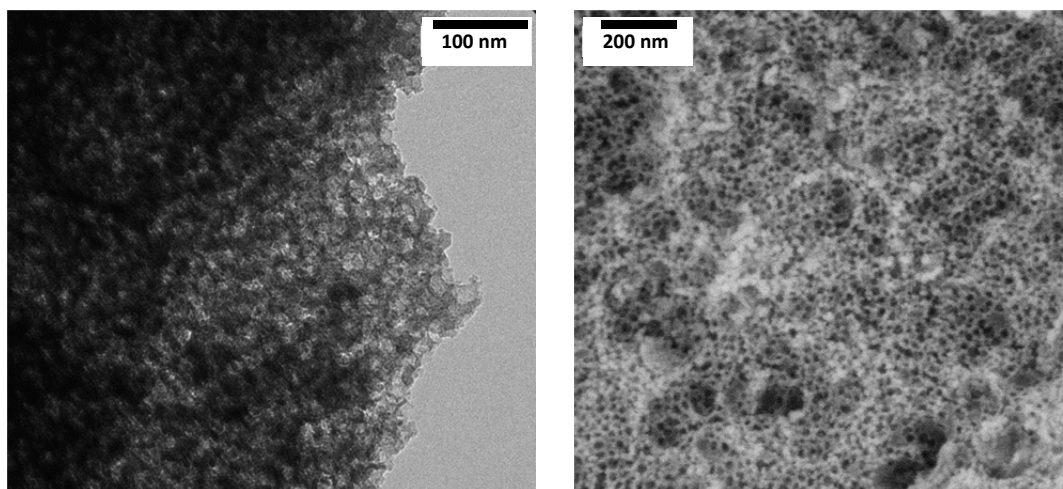

Figure 4.1.13. TEM (left) and SEM (right) images of the Fe$_3$C@C powder after silica removal showing the porous inner structure of the material. Pore sizes calculated by TEM/SEM are ~20 nm, which nicely match with the original silica nanoparticles sizes.

Surface area and pore size distribution measured for this material via nitrogen physisorption analysis gave a value of ~400 m^2/g and 20 nm pores respectively [214].

Catalytic activity of this nanocomposite was tested in ammonia decomposition reaction. Performance was also compared with the activity of bare Fe$_3$C nanoparticles, showing a higher and complete ammonia conversion at lower temperature, as discussed in chapter 7.

Fe₃C and Fe₃N from FeO_x: a transcription route [219]

By the UGR small (~10 nm in diameter and superparamagnetic) iron nitride and carbide nanoparticles can be synthesized, and final composition could be adjusted by varying metal-urea molar ratio and heat treatment. In section 4.2, it will be shown how to prepare larger and thus ferromagnetic particles (~30 nm in diameter) replacing urea with macromolecules (the *Biopolymer Route*). In the present session, a "transcription" route for the preparation of "middle-size" nanoparticles will be introduced. The particles prepared with this route have an average size of 20 nm and their corresponding magnetic properties place them at the border between superparamagnetic and ferromagnetic nanoparticles [219].

This route slightly differs from the classical UGR, since iron oxide particles are used both as template and iron source, while urea is still used as C/N source. The transcription of other kinds of metal oxide into nitrides previously investigated, with a special focus on the composition of the final material [132]. In the present case, more attention was given to the preservation of the sizes of the original template particles.

The structural transcription of oxide into the corresponding nitride/carbide has to overcome two challenging steps: 1) at first reduction to metal iron and, more difficult, 2) a crystal structure rearrangement from cubic (iron oxide) to hexagonal/orthorhombic (iron nitride/carbide).

The template nanoparticles (15-20 nm in diameter) were synthesized via the procedure of Park et al. [178]. Reaction conditions are reported in table 4.1.1 (entry "np-Fe₃N$_{trascr}$" and "np-Fe₃C$_{trascr}$") and in reference [219].

During this study, it was found that urea could serve as C/N source but the final nanoparticles are highly aggregated, probably due to a reduced amount of gasses released during the heat treatment. To circumvent this problem, agar can be used to isolate the nanoparticle nuclei during the heating step. Agar is chosen because it forms a gel with water [220], which can disperse the template nanoparticles and keep them separated, while urea still provides the C/N. Here it must be said that using agar alone, i.e. performing the reaction in absence of urea, the final product only consists of iron and iron oxide and formation of a nitride and/or carbide is not observed (independently of the amount of agar used). This result is, however, not surprising considering the oxygen rich structure of agar. On the other hand, in presence of urea,

a ratio 1 of agar/iron oxide is enough to get spatial separation among the particles, with minimal amounts of residual carbon. In fact, although on one hand the carbon structure is a key factor in conserving the shape and size of the particles during the heating step, it might be undesired in some applications. At the end of the section it will be shown how to remove this excess. Here it can be anticipated that, considering the absence of the carbon peak at 26° in the XRD, the amorphous nature of the residual carbon phase can be safely assumed. XRD and TEM images of the samples prepared with and without agar are reported in figure 4.1.2.14.
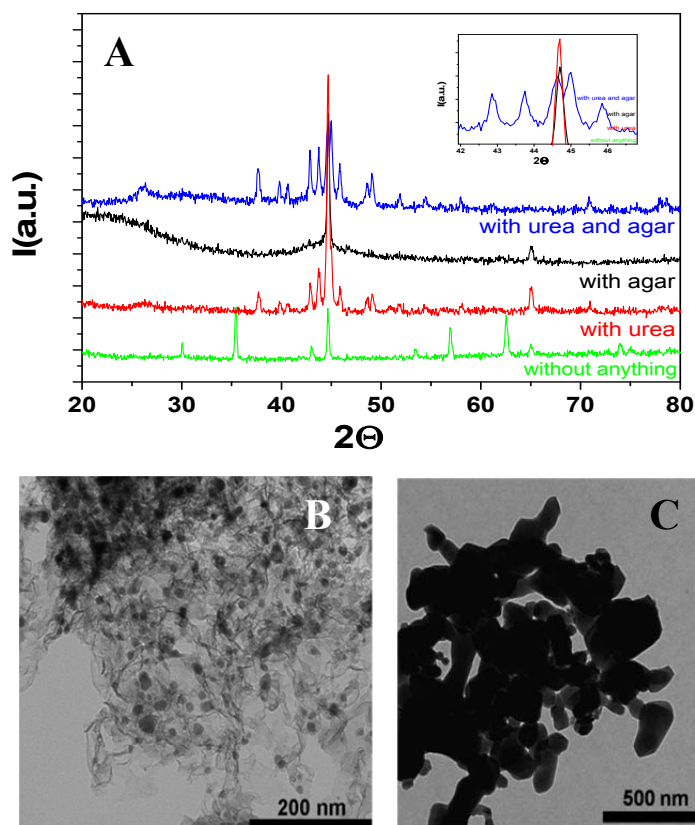

Figure 4.1.2.14. XRD pattern (A) and TEM images (B-C) of the product with and without the addition of agar, respectively. In (A) the XRD patter of the iron oxide nanoparticles heat treated at the same temperature but without the addition of agar and urea is also reported for comparison.

Size analysis from several TEM images of the particles shows a small size reduction (compared to the iron template) from ~20 nm to ~17 nm. This can be explained with the higher density of the MN/MC compared to MO_x, which might cause a contraction of the particle volume during the reaction (figure 4.1.2.5).
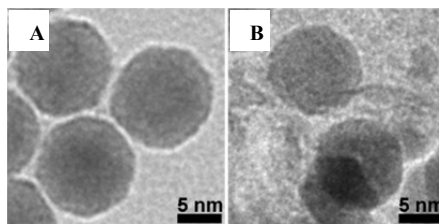
Figure 4.1.2.15. TEM images of iron oxide template particles (A) and corresponding Fe₃C particles after transcription (B). Adapted with permission from reference [219](© 2012 American Chemical Society).

Also in this case, by varying R, the final composition could be adjusted, going from iron oxide (R<1), to metallic iron (R<5), to Fe_3N (R<10) and Fe_3C (R>15). XRD investigations on quenched samples show that the conversion of the material starts at 700 °C, while for T<700°C the material still consists of iron oxide. Up to 700 °C only a mixture of different phases is achieved, while for T>700°C, the wished-for composition is obtained [219]. From a mechanistic point of view, the transcription mechanism from iron oxide to nitride and then carbide is assumed to be similar to that discussed in the previous session.

As mentioned before, the products always contain a residual amount of carbon, mainly amorphous. However, a closer look at the systems (via HR-TEM) showed a more ordered structure around the nanoparticle. This is in line with the fact that iron can catalyse the graphitization of carbon [221]. In the present study, this important structural difference was conveniently exploited by using H_2O_2 (30%) to remove the amorphous carbon. Hydrogen peroxide it is known to react selectively with amorphous carbon, without affecting ordered carbon [222]. Particles were then washed with water and separated from the solution with a magnet. TEM images of the "washed" samples show nanoparticles covered with a shell of ordered carbon (~1 nm thick, figure 4.1.2.16), while XRD patterns remain unaltered by the washing step (figure 9.8 appendix). Oxygen amount in the washed sample was also measured and found to be less than 4%.

Thanks to the thin carbon shell around the particles, stable dispersion of these nanoparticles (in water) was possible using poly-ionic liquid as dispersing agent. Results are discussed in chapter 5.
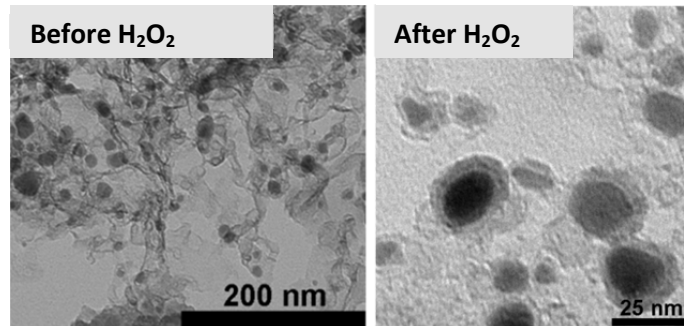
Figure 4.1.2.16. TEM image of particles before and after treatment with hydrogen peroxide. Adapted with permission from reference [219] (© 2012 American Chemical Society).

~

Table.4.1.2.2. Summary-overview of some results obtained for systems presented in this section.

Main product	$M_{s,exp}$ emu/g	Size* (Ø nm)	Side product	Best reaction conditions	Reference
Fe$_3$N	34.8	5-25 (9#)	Fe$_3$C, C	Fe(acac) ·6H$_2$O, urea, R=3, 600°C (1+2)	[212]
Fe$_3$N	n.m.	16	C	Iron oxide, urea, agar, R>10, 800°C	[219]
Fe$_7$C$_3$	33.5	20-100 (27#)	C	Fe(acac) ·6H$_2$O urea, R=5, 700°C (4+2)	[212]
Fe$_3$C	46.7	5-10 (9#)	C	FeCl$_2$·4H$_2$O, Fe(CO)$_5$, urea, R=3, 700°C (1+2)	[212]
Fe$_3$C	39.3	5-10	C	Fe(acac) ·6H$_2$O urea, R=3, 800°C (1+2)	[212]
Fe$_3$C	88	18	C	Iron oxide, urea, agar, R>15, 800°C	[219]
* From TEM images. # Calculated by XRD with eq. 4.					

4.2 The Biopolymer Route (BpR) [215][223]

The ability of urea (and structurally similar small molecules) to form suitable precursors, together with a metal salt, for the preparation of MN/MC with tuneable composition spontaneously lead to the idea to extend the choice of precursor compounds, especially with the aim to change size. In this respect, biopolymers can be considered suitable C/N sources and stabilizing agents for the preparation of nanosized MN/MC because they are mainly made of carbon and hydrogen (possibly nitrogen and oxygen) and decompose at high temperature, but can still be stable at moderate temperatures (up to 300°C under N_2, e.g. Chitosan [224]). Similarly to the UGR, biopolymers can firmly bind metal ions through their functional groups while, during heat treatment, can restrain nanoparticles growth and create spatial separation between nanoparticles seeds (as in the case of agar, reported in section 4.1.2). This control inevitably affects size of the final product and well-defined nanoparticles are obtained. The use of biopolymers to prepare morphologically refined metal oxides nanostructures is also known [225].

In this session, the synthesis of Fe_3N and Fe_3C nanoparticles using biopolymers will be discussed and results compared with those obtained via UGR. Further details of this study can be found in [215, 223].

To explore the potential of the biopolymer route (BpR), two different iron salts (namely iron nitrate and iron acetate) and three different polymers (namely gelatin, chitosan and alginate) have been employed. Experimental details and molecular structures of used macromolecules are reported in table 4.2.1 and figure 4.2.1, respectively.

Table 4.2.1. Summary-overview of some results obtained for systems described in this session.

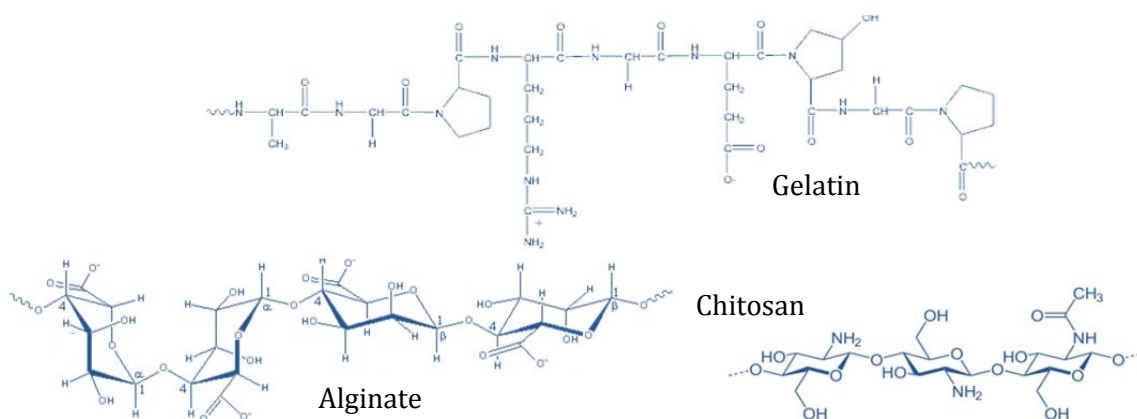| Metal salt	Biopolymer	Solvent	Product	Temperature	Ref.
$Fe(NO_3)_3 \cdot 6H_2O$	Gelatin	Water	Fe_3N	700°C	[215]
$Fe(CO_2CH_3)_2$	Gelatin	Water	Fe_3C	650°C	[223]
$Fe(CO_2CH_3)_2$	Chitosan	Water	Fe_3C	650°C	[223]
$Fe(CO_2CH_3)_2$	Alginate	Water	Fe_3C	650°C	[223]

Figure 4.2.1. Molecular structures of three biopolymer used as C/N source for the preparation of iron nitride and carbide via the BpR.

The interaction between iron cations and the biopolymer is suggested through the carboxylate groups in the cases of gelatin and alginate (for the latter, forming cross-linked arrays with the metal cations [226]), while for chitosan through its amine functional groups (via ligand interaction with the amine lone pair electrons).

In each case, nanoparticles are prepared from aqueous solutions of the iron salt mixed with aqueous solution of the selected biopolymer. Differently than in the UGR, here the precursor inherits the polymer structure and, more interesting, the porosity of the starting material can be changed by changing the iron salt. Using iron acetate for instance, a "plastic" film is formed, while using iron nitrate a "foam-like" structure is obtained (figure 4.2.2). This behaviour is probably due to the oxidation of the biopolymer in presence of the nitrate precursor, with consequent release of gases.
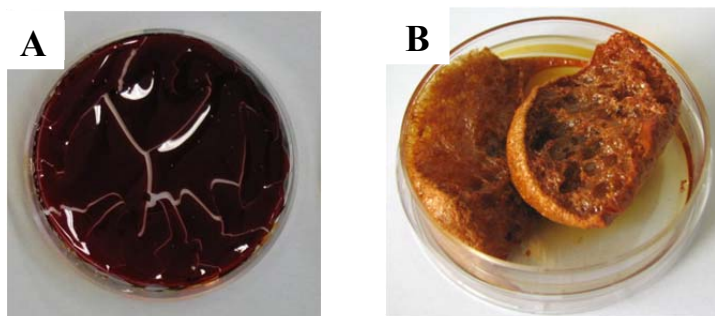

Figure 4.2.2. Fe-gelatine precursors prepared starting from iron acetate (A) and iron nitrate (B), respectively.

As for the UGR case, upon heat treatment of the precursor under nitrogen, the biopolymer decomposes to form an intermediate C-rich matrix, where nanoparticles are first loaded into. However, unlike that in the UGR, using biopolymers, well-defined iron oxide nanoparticles are always observed as intermediate phase[20], probably due to higher oxygen content of the starting precursor. The oxide intermediates convert (above 600°C) to the corresponding nitride or carbide. Due to the C-rich composition of the biopolymer, amorphous carbon is always present in the final sample as a side product (wt 20-25%).

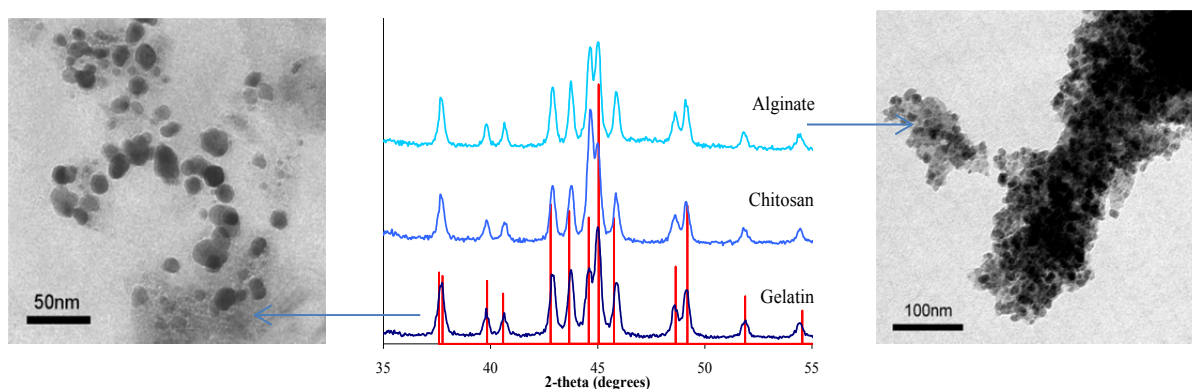In figure 4.2.3 XRD patterns and TEM images of iron carbide prepared via the BpR are reported.

Figure 4.2.3. XRD pattern of iron carbide prepared using iron acetate and gelatin, chitosan or alginate as C source. The expected pattern for the Fe_3C (ICDD 00-035-0772) is also reported as red vertical lines[21].

Replacing iron acetate with iron nitrate, Fe_3N is obtained still using gelatin as nitrogen source. Corresponding XRD pattern and TEM images are reported in figure 4.2.4.

---

[20] By quenching samples at lower temperatures.
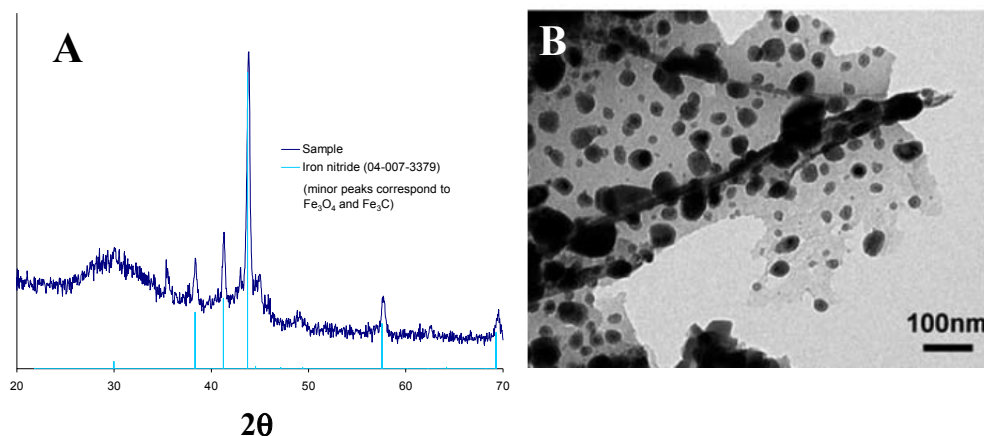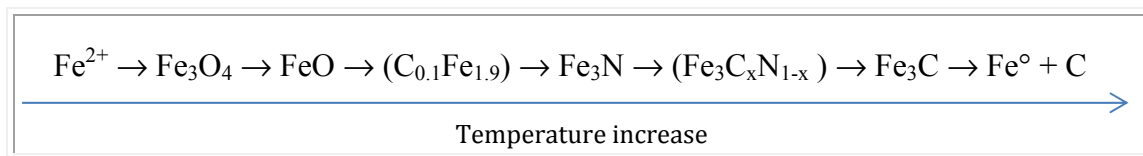[21] The sample synthesized from chitosan also contains metallic iron as side product.

Figure 4.2.4. XRD pattern (A) and corresponding TEM image (B) of iron nitrite prepared using gelatin as N source. The expected pattern for the ε-Fe$_3$N (ICDD 04-007-2962) is also reported as light-blue vertical lines.

The study of the formation mechanisms of iron nitride and/or carbide (TGA-MS), indicates that the decomposition of the biopolymer and the metal precursor involves the releases of CO_2, HCN, H_2O and NH_3 below 300°C (when the formation of the C-N rich matrix starts), while the main loss of nitrogen occurs at higher temperatures (500-600°C) as NO_x (matrix decomposition). The formation of intermediate iron oxide nanoparticles occurs simultaneously with the formation of the C-rich matrix [223]. In a second step, iron oxide reacts with the C/N matrix to form the final nanoparticles, with final mass loss up to 600 °C and further release of carbon and oxygen as CO_x. It was observed that all tested biopolymers decompose in a similar way and both intermediates and final products are similar, as observed from the XRD patterns of the quenched samples [215, 223]. This confirms that, despite the different composition and structure of the starting polymer, similar mechanism of nanoparticles nucleation and biopolymer decomposition takes place. As in the UGR, the synthesis can be directed toward the formation of the nitride or the carbide phase by adjusting precursor composition and heating rate. Additionally, in the BpR, also particle sizes and surface area seem to influence the final composition, as discussed below. The iron nitride phase is obtained as an in-situ intermediate during the conversion of the iron oxide nanoparticles into the most stable carbide phase, up to 800°C, possibly passing by an iron carbo-nitride phase. As previously reported,

further increase of the temperature only leads to the decomposition of iron carbide in iron and carbon.

The conversion steps are reported schematically in scheme 4.2.1.

$$Fe^{2+} \rightarrow Fe_3O_4 \rightarrow FeO \rightarrow (C_{0.1}Fe_{1.9}) \rightarrow Fe_3N \rightarrow (Fe_3C_xN_{1-x}) \rightarrow Fe_3C \rightarrow Fe^\circ + C$$

Temperature increase

Scheme 4.2.1. Iron intermediate sequence in the formation of iron carbide via the BpR.

A study on samples prepared with different biopolymer/metal molar ratio (R) show that a higher R supports the carbide formation, as for the UGR (figure 4.2.5).
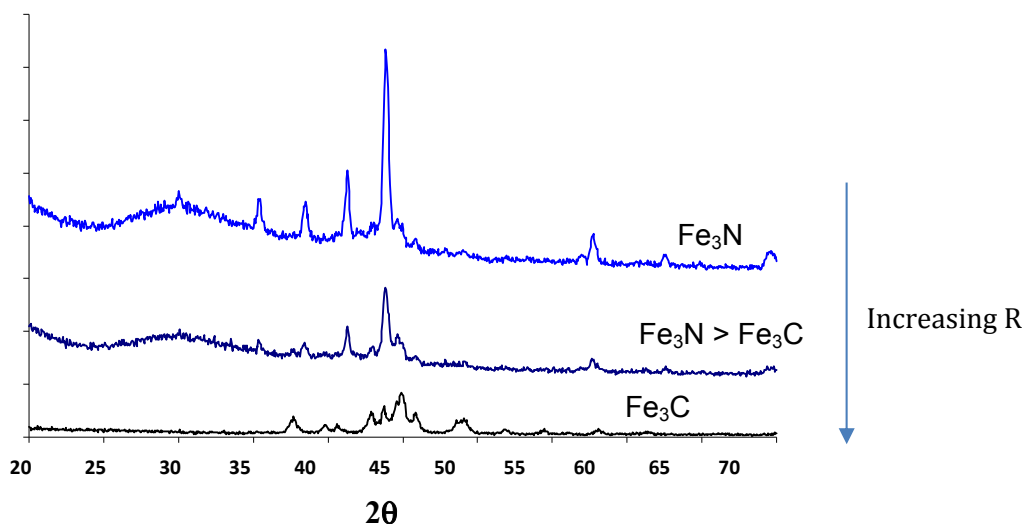

Figure 4.2.5. Iron-gelatin samples prepared with different amount of iron and heat treated at 700°C.

However, for the formation of the nitride phase, the reaction temperature plays here the main role within a certain composition range. In other words, the choice of the precursor composition affects the temperature range at which the iron nitride (known to be a metastable phase) is formed. The main difference between the use of iron acetate and nitrate as metal salts lies in the formation of larger oxide nanoparticles in the case of acetate than in the case of the nitride; i.e. a sample prepared with acetate shows a lower surface area than one using nitride salt. This finding is confirmed by the use of iron acetate/gelatine precursors with different mechanical structure: one as film (prepared in the standard way) and the other one as foam (by freeze drying). The

former brought to iron carbide only (upon heat treatment), while the latter to iron nitride. This dependence of Fe_3N formation and stability on the surface area of the Fe_3O_4-np intermediate is consistent with related reports of the ammonolysis of iron oxide nanoparticles, where the degree of nitridation was dependent on the surface area [227].

Finally, in order to gain information about the influence of the nitrogen flow on the formation of the Fe_3N, a focused study was undertaken. This study shows that heat treatment under N_2 atmosphere is a *conditio sine qua non* for the nitride formation, but still not sufficient. In fact, XRD pattern performed on samples calcined under argon showed phase-pure Fe_3C while, iron acetate/agar gels (agar because is a nitrogen-free source) only brought to a mixture of iron oxide phases (figure 4.2.6), even at higher temperature (up to 800°C). To understand the role of the N_2 atmosphere, one must remember that iron can catalyse ammonia decomposition and therefore it is likely that the ammonia released during the decomposition of the biopolymer can further decompose on the surface of the iron oxide nanoparticles, leading to nitridation and formation of Fe_3N. Assuming that the synthesis and decomposition of ammonia on iron nanoparticles are equilibrium processes, this could explain why the use of nitrogen atmosphere supports the nitride formation. It can then be suggested that when the partial pressure of N_2 is lower (as when argon is used), the formation and subsequent release of molecular N_2 is favourable, preventing diffusion of atomic nitrogen into the iron-rich nanoparticle. Interestingly, when agar is used as C-source neither iron nitride nor carbide are formed.
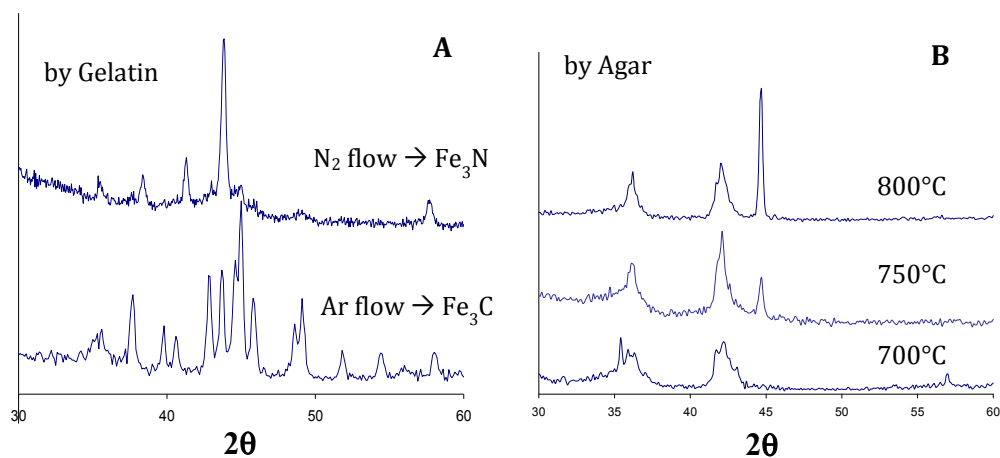

Figure 4.2.6. A) Iron-gelatin samples treated under different atmosphere and B) iron-agar sample calcined under N_2 at different temperatures.

Finally, as observed from figure 4.2.3, Fe_3C nanoparticles prepared via the biopolymer route have an average diameter of 25-30 nm, i.e. three times larger than nanoparticles diameter obtained by the urea route (~8 nm). The size increase implies higher saturation magnetization (~130 emu/g), comparable to that of bulk Fe_3C (~140 emu/g) [191]. Especially interesting is the comparison of the magnetic properties of Fe_3C nanoparticles prepared via the two routes (figure 4.2.6): via the UGR, small, superparamagnetic nanoparticles are prepared, while via the BpR, bigger (~25 nm) ferromagnetic nanoparticles are obtained. For the small nanoparticles, the superparamagnetic character and the absence of metallic iron and residual carbon could lead to applications in bio-medicine, and for bigger nanoparticles, applications where higher magnetization is needed, for instance for magnetic membrane, or miniaturised loudspeakers could be considered.
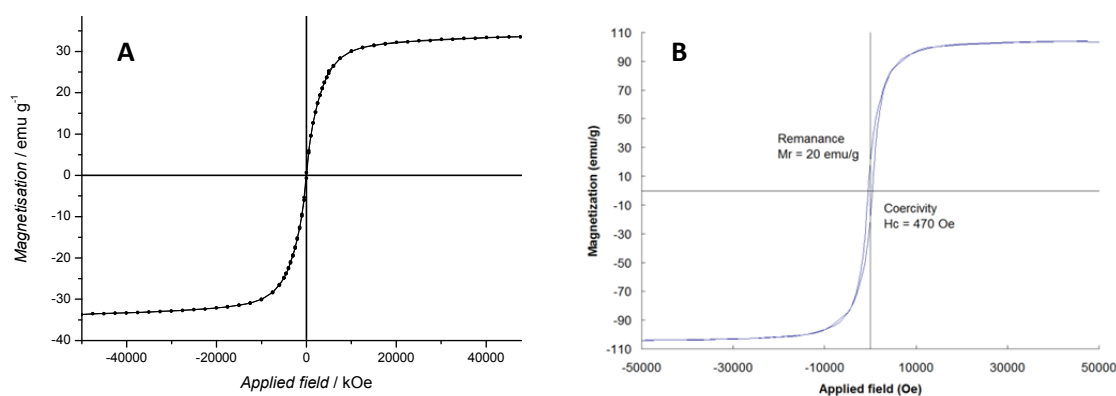

Figure 4.2.6. Magnetic hysteresis loop of the powdered iron carbide obtained via UGR (A) and BpR (B) recorded on a superconducting quantum interference device (SQUID) at 298 K. The values of the saturation magnetization normalized to pure Fe_3C are ~47 and ~130 emu/g respectively.

4.2.1 Ternary Systems via the BpR[22]

The BpR is also suitable to prepare ternary systems in an easy way, due to the possibility to start with a "gel-like" starting precursor, where the two metal cations can be dispersed homogeneously into the polymer structure (as schematically reported in scheme and figure 4.2.1.1 for the preparation of Fe_3Mo_3N). The attention has been mainly addressed to the synthesis of η-carbides/nitrides with the form A_3B_3C (with A= Fe, Co, Ni and B= Mo, W). Experimental details of prepared ternary systems are reported in table 4.2.1.1.
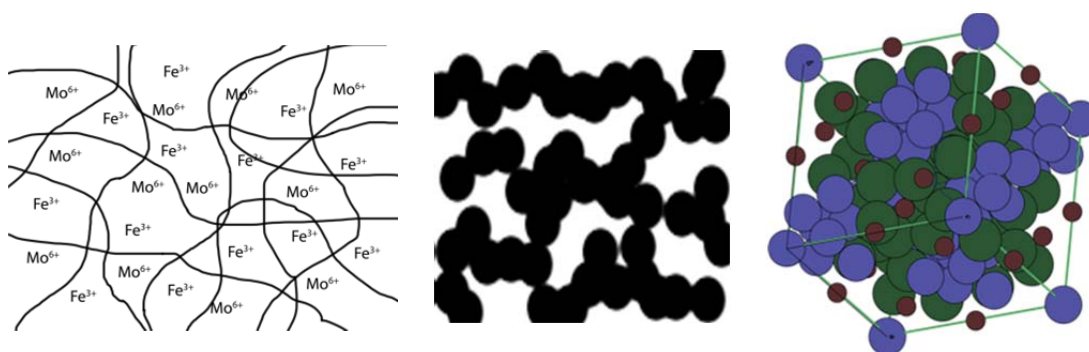
Scheme 4.2.1.1 Schematic representation for the preparation of molybdenum iron ternary nitride. From left to right: precursor metal ions are dispersed in the polymer matrix. The matrix decomposes upon calcination under N_2 flow forming nanoparticles. Expected crystalline structure for the ternary nitride (iron positions in lilac, molybdenum positions in green, nitrogen position in dark red).
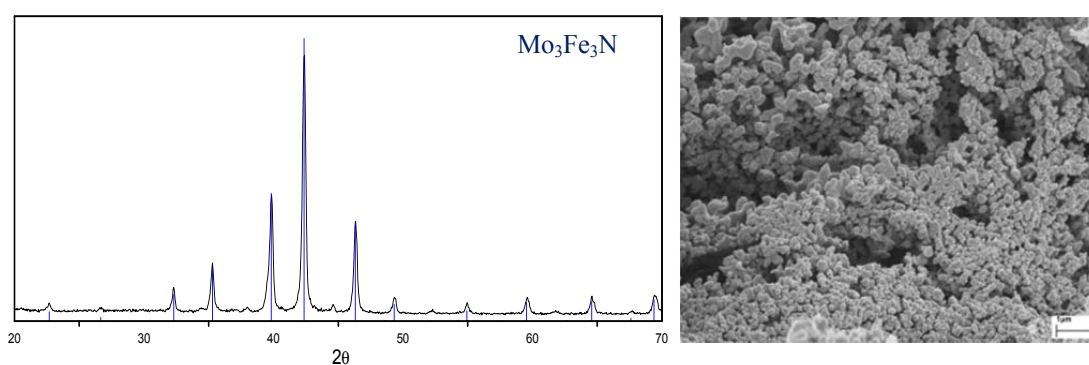

Figure 4.2.1.1 XRD pattern and SEM image of Mo_3Fe_3N prepared starting from ammonium molybdate tetrahydrate and iron nitrate as metal salts, and ammonium alginate as N-source. Expected XRD pattern from database is reported as vertical blue lines (ICDD 04-008-1300).

---

[22] Private Communication (Regina Hafner, Diploma thesis).

Table 4.2.1.1. Experimental results overview.

Product	Metal salt	Biopolymer	Solvent	Metal mmol	T(°C)
Mo_3Fe_3N	$Fe(NO_3)_3 \cdot 6H_2O$	Ammonium alginate (8g)	Water	1	800
	$(NH_4)_6Mo_7O_{24} \cdot 4H_2O$			1	
Fe_3W_3C	$Fe(NO_3)_3 \cdot 6H_2O$	Ammonium alginate (6g)	Water	2	800
	$(NH_4)_2WO_4$			1.7	
Co_3W_3C	$Co(NO_3)_3 \cdot 6H_2O$	Ammonium alginate (5g)	Water	2	800
	$(NH_4)_2WO_4$			1.7	
Co_3Mo_3C	$Co(NO_3)_3 \cdot 6H_2O$	Ammonium alginate (8g)	Water	2	800
	$(NH_4)_6Mo_7O_{24} \cdot 4H_2O$			1.7	

A study on quenched samples has shown that the formation mechanism from precursor to final nitride still passes through an oxidic intermediate, as is the case for the formation of iron carbide and nitride discussed in the previous section. In figure 4.2.1.2 XRD patterns of samples calcined at different temperature is reported.
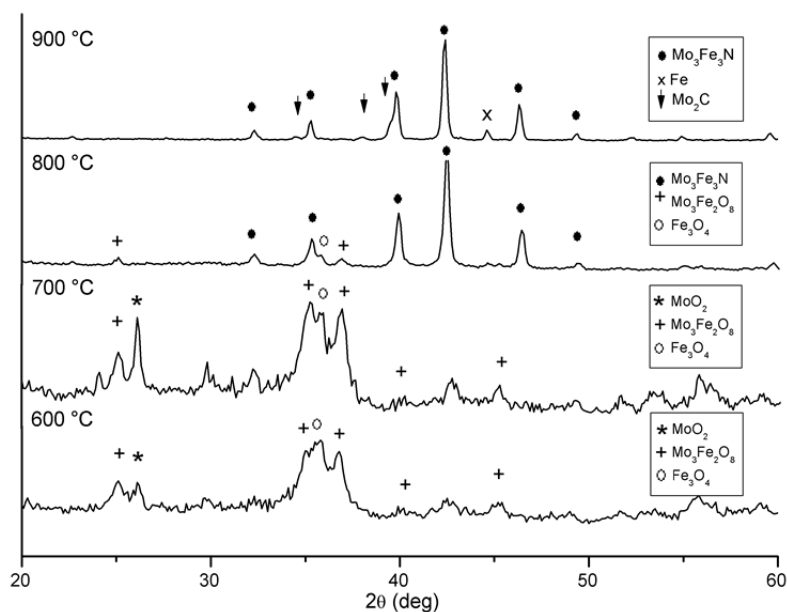

Figure 4.2.1.2 XRD patterns of samples prepared starting from ammonium molybdate tetrahydrate and iron nitrate as metal salts and ammonium alginate as N-source and then calcined at different temperatures.

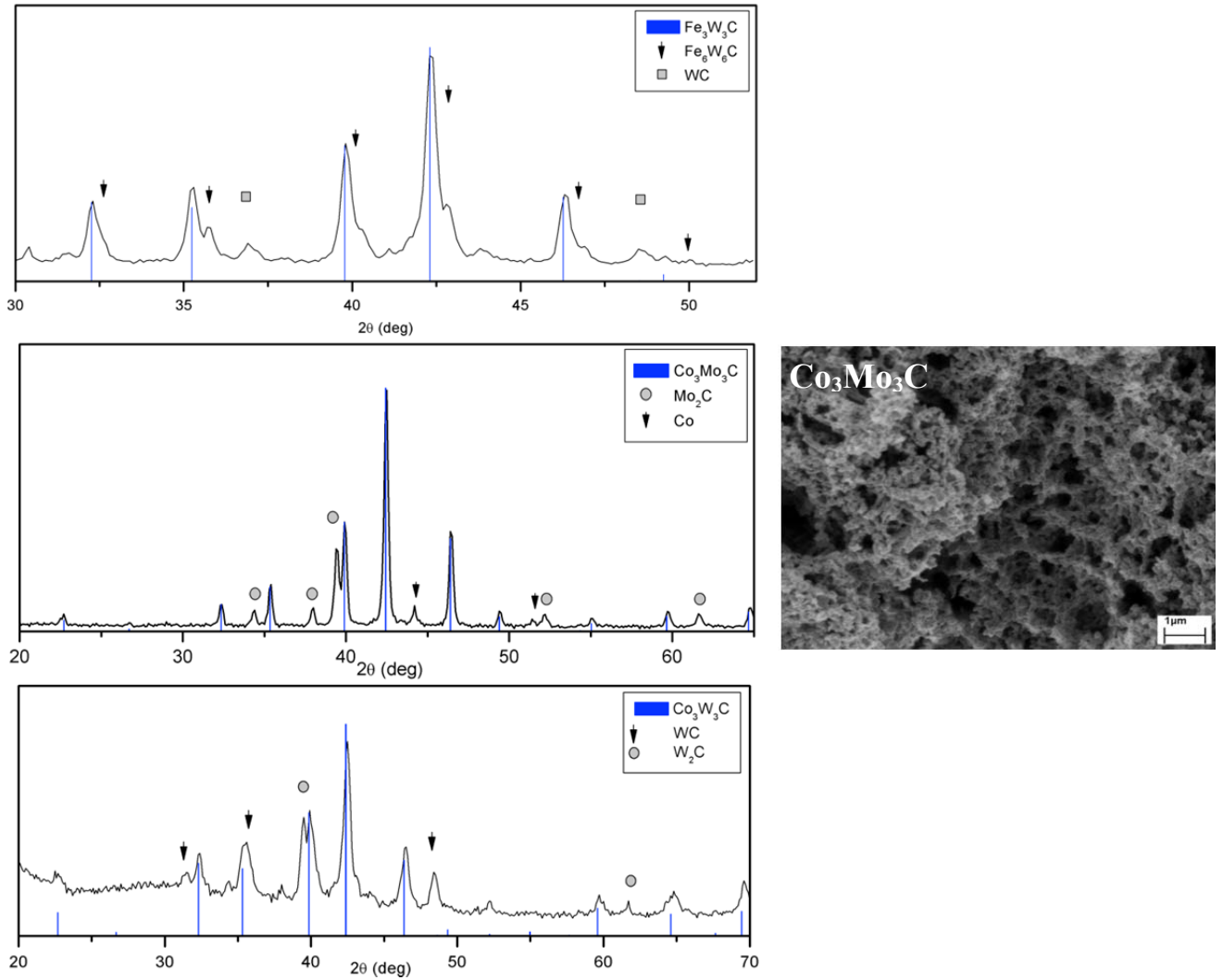Following this route, also Fe_3W_3C, Co_3Mo_3C and Co_3W_3C have been prepared (figure 4.2.1.3).

Figure 4.2.1.3 XRD patterns of Fe_3W_3C, Co_3Mo_3C and Co_3W_3C. Reference patterns (from database) are reported as vertical blue lines (ICDD 04-010-7446, 04-005-5150 and 01-078-4940 respectively). SEM image of Co_3Mo_3C is also shown.

It can be observed, from the XRD patterns that prepared materials are not pure phases and residual amount of pure metals or metal oxides are present. Purity is still an issue and research in this direction is in progress.

4.3 *La Via dello Zucchero[23]* (*The Sugar Route*)

Inspired by the results obtained with the UGR first and the BpR route then, but also to employ renewable resources, the synthesis was modified to a *"Sugar Route"*, where sugar-base molecules are used as N/C-source for the production of MN/MC. It will be shown that, due to the C-rich structure of these molecules, mainly MC@C nanocomposites are obtained[24]. Two of the main advantages of this route are: i) the use of water as solvent and ii) an easy scaling (up to several grams in the lab) of the process. It must be said, however, that this is a very recent approach and the related research is, to a large extend, still in progress. For this reason, only preliminary and partial results can be reported here, although promising. In figure 4.3.1 some of the tested compounds are reported.
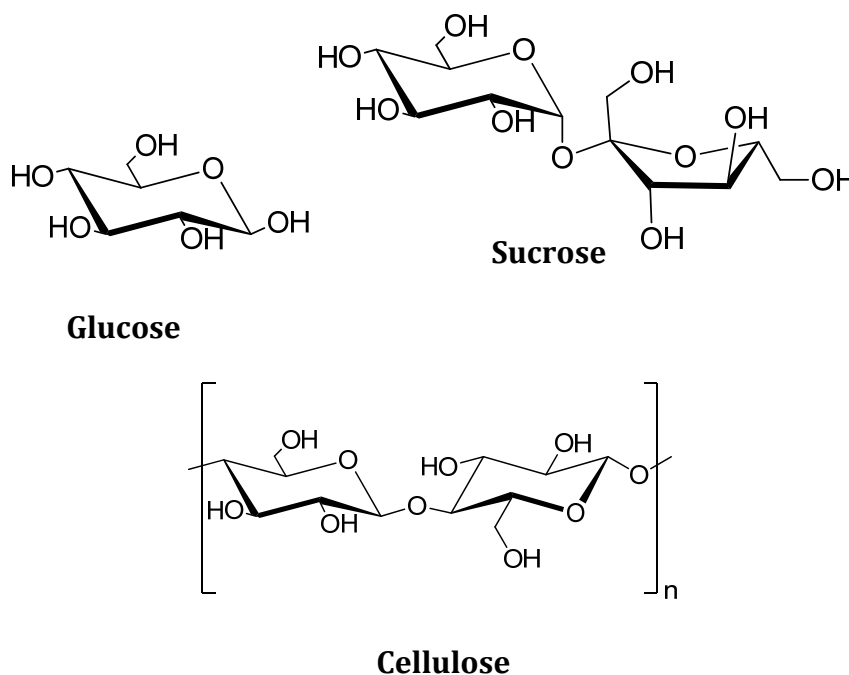

Figure 4.3.1. Some molecules employed as C/N source for the preparation of MN/MC based systems via the Sugar Route. The bonding between the metal ions and the molecules is believed to be through oxygen bridges.

In contrast to the UGR, but similarly to the BpR, the use of sugar-based polymers leads to a massive carbon excess in the final products (up to 70% in some cases), which obviously can be no longer considered a side product but rather an integral part of the final system. Far from being a disadvantage, the carbon phase features the

---

[23]Title inspired by "The Sugar Street" from "The Cairo Trilogy" by Naguib Mahfouz.
[24] The preparation of other types of MN/MC based nanocomposites is discussed in Chapter 5.

material. It is still a "green" compound and can nicely serve as functional matrix, where the nanoparticles are loaded into; and it adds further properties to the resulting system. Thus, the final material can possess properties, which are not observed in the two phases separately (such as electrical conductivity, enhanced catalytic activity, magnetic properties, etc.) but also porosity and larger surface area. In chapter 7, it will be shown how this combination of properties can be properly exploited toward selected applications.

The use of sugar base precursors, which are also reducing agents, also allows the preparation of pure metal and metal alloys based nanocomposites. Depending on the metal, the graphitization degree can be tuned going e.g. from turbostatic carbon (in presence of nickel) to almost perfect graphitic layers (in presence of Fe or Mn). It is known that some metals can catalyse the formation of ordered or partially ordered graphitic-like structure, usually obtained at higher temperature (T>1000°C) [228].

The systems prepared via the sugar route and related experimental details are reported in table 4.3.1, however, since the present thesis focuses on MN/MC, the results concerning pure metals and metal alloys will not be discussed here. Part of this research has been reported in reference [229].

Table 4.3.1. Experimental details for the preparation of nanocomposites via the *Sugar Route*.

Product	Metal precursor(s)	C-source	Temperature (°C)	Ref.
$Fe_3C@C$	$Fe(NO_3)_3$ /Fe° in acetic acid	Cellulose	800°C	[230]
$Fe_3C@C$	$Fe(NO_3)_3$	Glucose	800°C	*
$Pd_{0.9}Ni_{0.1}@C$	$Pd(NO_3)_2 \cdot xH_2O$ $Ni(NO_3)_3 \cdot 6H_2O$	Cellulose	700 °C	[231]
$Fe_{0.5}Ni_{0.5}@C$	$Fe(NO_3)_3 \cdot 9H_2O$ $Ni(NO_3)_3 \cdot 6H_2O$	Cellulose	900 °C	[231]
$Mn_{0.75}Fe_{2.25}C@C$	$MnAc_2 \cdot 4H_2O$ $FeAc_2$	Cellulose	1000 °C	[231]
$Pd_{0.5}Ni_{0.5}@C$	$PdCl_2$ $Ni(NO_3)_3 \cdot 6H_2O$	Cellulose	800 °C	[229] [231]
Ni@C	$Ni(NO_3)_3 \cdot 6H_2O$	Cellulose	800 °C	[229]
Ni@C	$Ni(NO_3)_3 \cdot 6H_2O$	Sucrose	800 °C	[229]
Ni@C	$Ni(NO_3)_3 \cdot 6H_2O$	Glucose	800 °C	[229]
$Cu_{0.5}Ni_{0.5}@C$	$CuCl_2 \cdot 2H_2O$ $Ni(NO_3)_3 \cdot 6H_2O$	Glucose	800 °C	[229]
$W_{0.15}Ni_{0.85}@C$	$(NH_4)_6H_2W_{12}O_{40} \cdot xH_2O$ $Ni(NO_3)_3 \cdot 6H_2O$	Glucose	800 °C	[229]

*Private Communication (unpublished results).

Cellulose [230] [231]

Cellulose was initially tested as C-source for the preparation of iron carbide. Cellulose is one of the most abundant (and therefore cheap) polysaccharide available, made of -$(C_6H_{10}O_5)_n$- repetitions (figure 4.3.1).

In a typical synthesis, an iron salt (e.g. iron(III) nitrate non-hydrate) is at first dissolved in water and then mixed with the cellulose. Alternatively, synthesis can be made even "greener" using a solution of scrap iron dissolved in glacial acetic acid (dissolution takes about a week). In both cases, the resulting solution is impregnated into the cellulose source (either laboratory grade filter paper or micro-crystalline cellulose). It must be said that cellulose is not soluble in the aqueous iron solution but forms a homogeneous mixture. This mixture is, in a second step, heat treated under nitrogen flow up to 800°C. The process is schematically reported in figure 4.3.2.
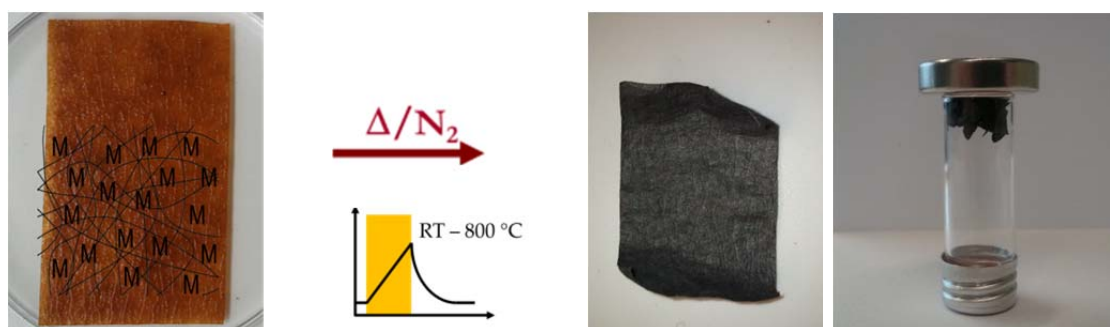

Figure 4.3.2. Iron carbide preparation using the cellulose of a filter paper as C-source. From left to right, filter paper impregnated with the iron salt aqueous solution (orange), the same filter paper after heat treatment under N_2 flow up to 800°C (black). Being magnetic, the filter paper can be attached to an external magnet.

The final black, brittle (when paper filter is used) and magnetic material consists of iron carbide nanoparticles (~50 nm in diameter) dispersed in a structured carbon matrix, as ascertained by XRD and TEM investigations (figure 4.3.3). Metallic iron is not observed in the XRD pattern of the final material.
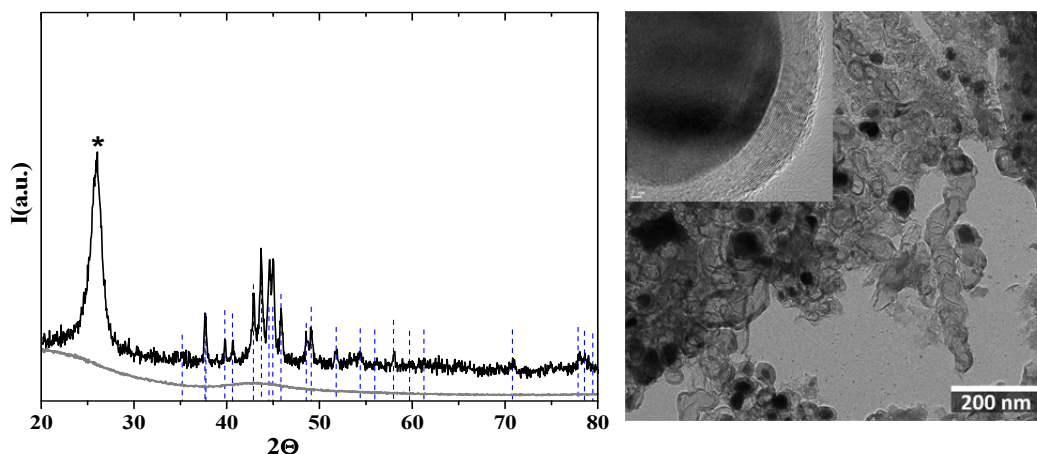
Figure 4.3.3. Left: XRD pattern of iron carbide prepared using cellulose (black) and calcined cellulose (grey) at the same temperature but without addition of iron. For comparison, Fe_3C reference pattern is also reported as blue vertical lines. Marked peak (*) is attributed to graphitic carbon (ICDD 04-15-2407). Right: TEM image of Fe_3C nanoparticles embedded in the carbon matrix. In the inset, a HR-TEM image shows the core-shell nature of the particles.

Interestingly, the shape retention observed for the filter paper can be transferred to any intended shape, including "origami" (folded papers) as shown in figure 4.3.4.

Figure 4.3.4. A filter paper folded as a "crane" (A) then soaked with the iron precursor solutions (B) and finally heat treated under N_2 flow up to 800°C (C). Adapted with permission from reference [230] (© 2013 Wiley-VCH Verlag GmbH & Co. KGaA, Weinheim).

Shape retention is not only retained at the macro-scale, but also down to the micro-scale. In figure 4.3.5, SEM images of cellulose calcined with and without the presence of iron are shown. Beside a small shrinkage, no remarkable differences are observed. On the contrary, the change at the nanoscale is dramatic (TEM image in figure 4.3.5): while in absence of the iron precursor the carbon does not present any structure (it is amorphous), in presence of iron a ribbon-like structure is observed. The inorganic nanoparticles are loaded into that structure. These "ribbons" were identified as graphite layers by HR-TEM. A mechanistic study has shown that the formation of iron carbide still passes through an iron oxide intermediate phase, as for

the case of the BpR [230] but when the iron oxide nanoparticles shrink and disappear, a Fe@C eutectic is formed, i.e. Fe@C "droplets" are observed. These droplets are able to diffuse along the matrix and they "etch" parts of the carbon phase. The "etching" leads to the transformation of amorphous carbon in graphite, which is left behind the droplets as the observed "ribbons". This behaviour has been observed by HR-TEM performed at the reaction temperature and documented in a short movie [230]. HR-TEM performed on microtomed samples shows that, in some cases, the ribbons form right angles, indicating that they are made of piled graphite layers, rather than forming carbon nanotubes (figure 9.9 in the appendix).
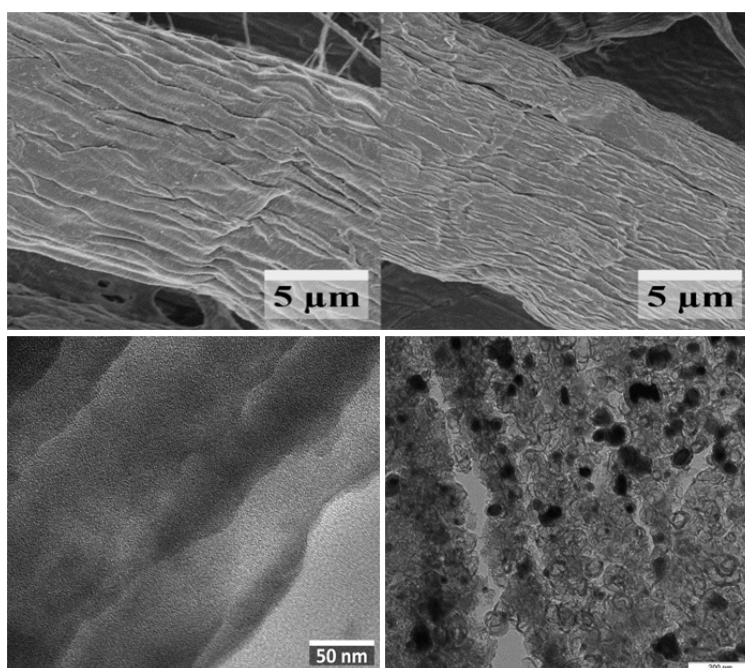

Figure 4.3.5. SEM (up) and TEM (down) images (by microtomy) of cellulose calcined in absence (left) and in presence (right) of iron.

In figure 4.3.6, result of nitrogen sorption measurement on the nanocomposite is reported, showing a type IV isotherm and surface area of 270 m^2/g. Isotherms of calcined cellulose in absence of iron and uncalcined cellulose are also reported for comparison. In all cases, data were analysed with a quenched solid density functional theory (QSDFT) model [232] on the adsorption branch of the isotherm.
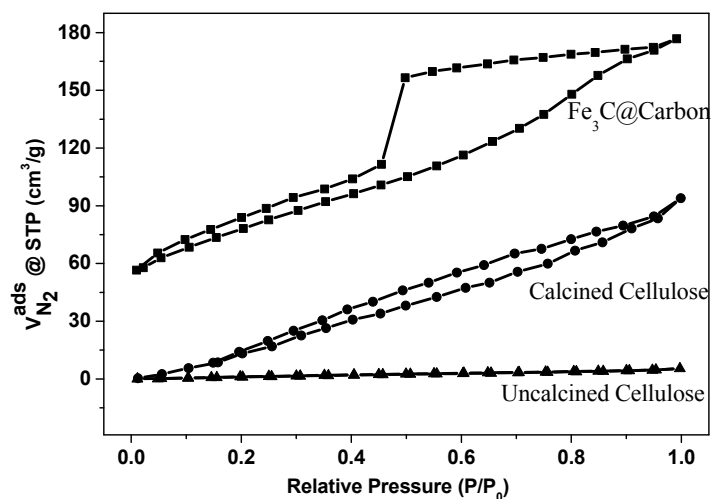
Figure 4.3.6. Nitrogen sorption isotherms and related surface area values of $Fe_3C@C$, calcined cellulose in absence of iron and uncalcined cellulose.

Similarly to the BpR, the use of cellulose allows the preparation of ternary systems, e.g. $Mn_{0.75}Fe_{2.25}C@C$ (figure 4.3.7). Solutions of the two metals can be prepared separately and mixed, then a selected amount of cellulose can be added.

Table 4.3.2. Experimental results on samples prepared with cellulose as C-source.

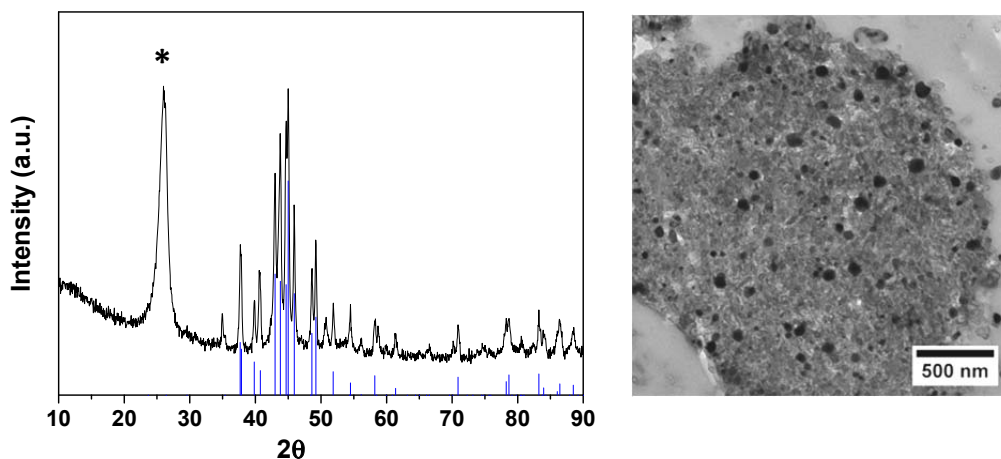|	Elemental analysis (wt%)			Ratio $M_1:M_2$	Surface area (m^2g^{-1})	Average size (nm) by TEM
	M_1	M_2	C			
$Fe_3C@C$	30	--	70	--	up to 270	~50
$Mn_{0.75}Fe_{2.25}C@C$	4.8	17.8	73	0.75:2.74	194	~30

Figure 4.3.7. Left: XRD pattern of manganese iron carbide prepared using cellulose. The reference pattern is also reported as blue vertical lines (ICDD 04-002-8999), while marked peak is attributed to graphitic carbon (ICDD 04-15-2407). Right: corresponding TEM image.

Glucose and Sucrose [229]

Iron carbide based nanocomposites prepared using cellulose as carbon source possess magnetic behaviour due to the presence of the iron carbide phase, while the carbon phase provides high surface area. These properties make the material especially suitable as filtration agent and absorber (related tests are reported in chapter 7). However, the performance employing the nanocomposite as catalyst was far below expectations (data not shown). Thinking back, one can explain this lack of activity: the active phase (the iron carbide nanoparticles) is deeply enwrapped into the carbon phase, making the nanoparticle surface almost inaccessible to the substrate. In order to overcome this problem, smaller molecules have been tested, and in particular glucose and sucrose are considered valid alternatives to cellulose, for the preparation of systems more suitable for catalysis. The replacement of cellulose with glucose leads, for instance, to iron carbide nanocomposites with minor amounts of carbon and nanoparticles more exposed on the surface (i.e. less embedded into the matrix). To confirm this point, it must be said that TEM images of the sample are acquired in the classical way and there was no need of microtomy. The XRD results seem to indicate that nanoparticles prepared using glucose are also smaller than those obtained with cellulose, while the carbon phase is less structured (very broad carbon peak observed at ~30°), as shown in figure 4.3.8.

The sample is prepared adding suitable amount of glucose to an aqueous solution of iron nitrate (R=16). Here, it must also be stated that one important difference to the

use of cellulose is that glucose is fully soluble in water and the starting precursor is a clear and homogeneous solution rather than a mixture. The solution (either as such or dried to remove the excess of water[25]) is then heat-treated up to 800°C, without dwelling temperature (after reaching 800°C, the oven is immediately left to cool down).

A mechanistic study is currently in progress also to understand the lower grade of graphitization of the final carbon phase compared to that obtained with cellulose. This behaviour is possibly also related to the reducing properties of glucose.
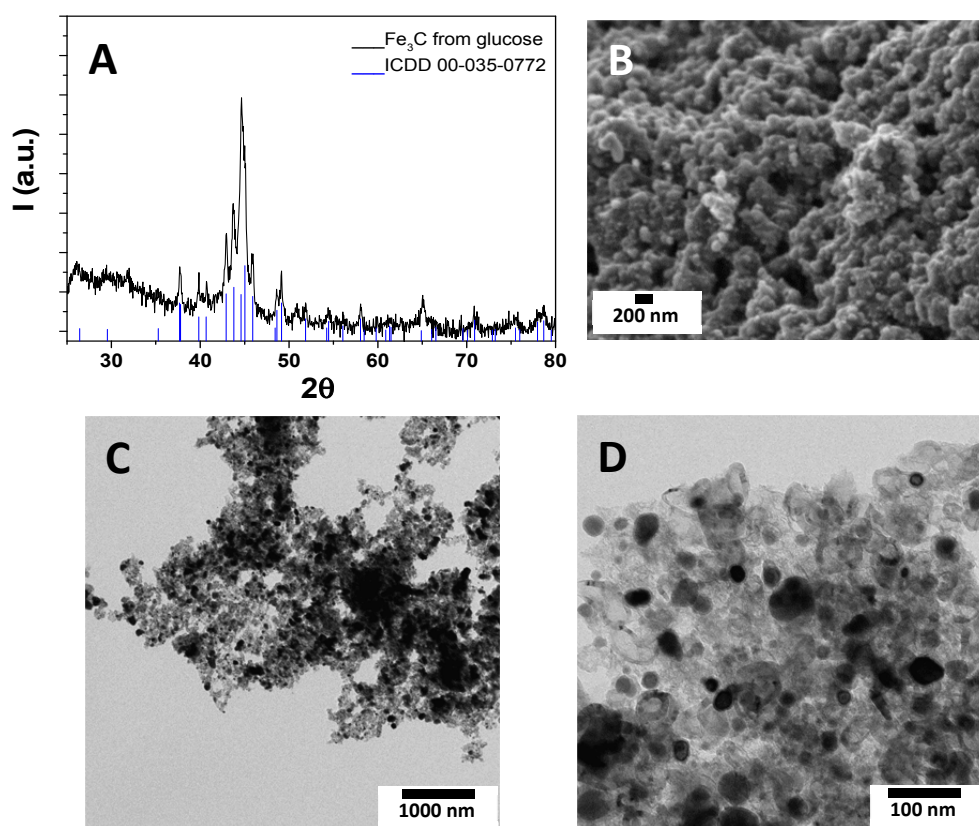

Figure 4.3.8. A) XRD pattern of iron carbide prepared using glucose. The reference pattern is also reported as blue vertical lines. B) corresponding SEM and C-D)TEM images, at different resolution.

---

[25] After drying, a crystalline compound is obtained, with the same color of the starting iron nitrate solution.

5. MN/MC based Nanocomposites

In the previous session, it was shown that when macromolecules are employed, the final sample contains significant amount of carbon as side product. This excess of carbon forms a matrix where the MN/MC nanoparticles are loaded into, and gives additional properties to the final material. Therefore these systems were addressed as "nanocomposite". Analogously to composites, nanocomposites are constituted by two (or more) phases: a matrix (sort of scaffold) and a filling phase. The close contact between these phases results in an overlap of the properties of both materials, leading to a multifunctional system. Different to composites, nanocomposites can be considered homogeneous systems also from a microscopic point of view, due to the smaller (nano) sizes of the fillers. Phases can be combined according to the final application and the number of possible combinations is limitless.

However, once again, while extensive studies have been performed on metal oxide-based nanocomposites [233 - 236], the research related to MN/MC is still scarce and mainly focused on silicon based systems [237].

In this chapter, the preparation of some MN/MC nanocomposites, based on the synthetic procedure presented in chapter 4, will be discussed. This preparation can be performed *"in-situ"* or after nanoparticles synthesis (post-synthesis approach), depending on the final product.

5.1 Manganese and Nickel Nitride based Nanocomposite

Employing the UGR (see chapter 4.1), $Ni_3N@C$ and $MnN_{0.43}@C$ nanocomposites can be prepared (experimental details are reported in table 4.1). For the nickel system, small nanoparticles (~25 nm) are found homogeneously dispersed in the carbon phase. On the contrary, for the manganese system core-shell nanoparticles are formed. Analogously to the case of iron discussed in section 4.3, both nickel and manganese can catalyse the graphitization of carbon during the formation of its nitride.

i. MnN₀.₄@C nanocomposites [156] [238]

In the search for alternative/novel anode materials, manganese nitride based systems represent attractive candidates due to high theoretical capacity (e.g. $MnN_{0.4}$ has 531 mAh/g), compared for instance with commercial graphite (370 mAh/g), and exhibits less polarization than several previously reported metal nitrides.

The manganese nitride has been prepared accordingly to the classical UGR and in figure 5.1.A digital photos of the sample, before (colourless, glassy precursor) and after (black powder) the heat treatment, are reported.

XRD investigation confirms that the system is made of manganese nitride (a non-stoichiometric phase) and carbon (figure 5.1.B). TEM study shows that particles partially agglomerate forming clusters (figure 5.1.D), but the shell around them can be observed in some isolated particles (figure 5.1.C).
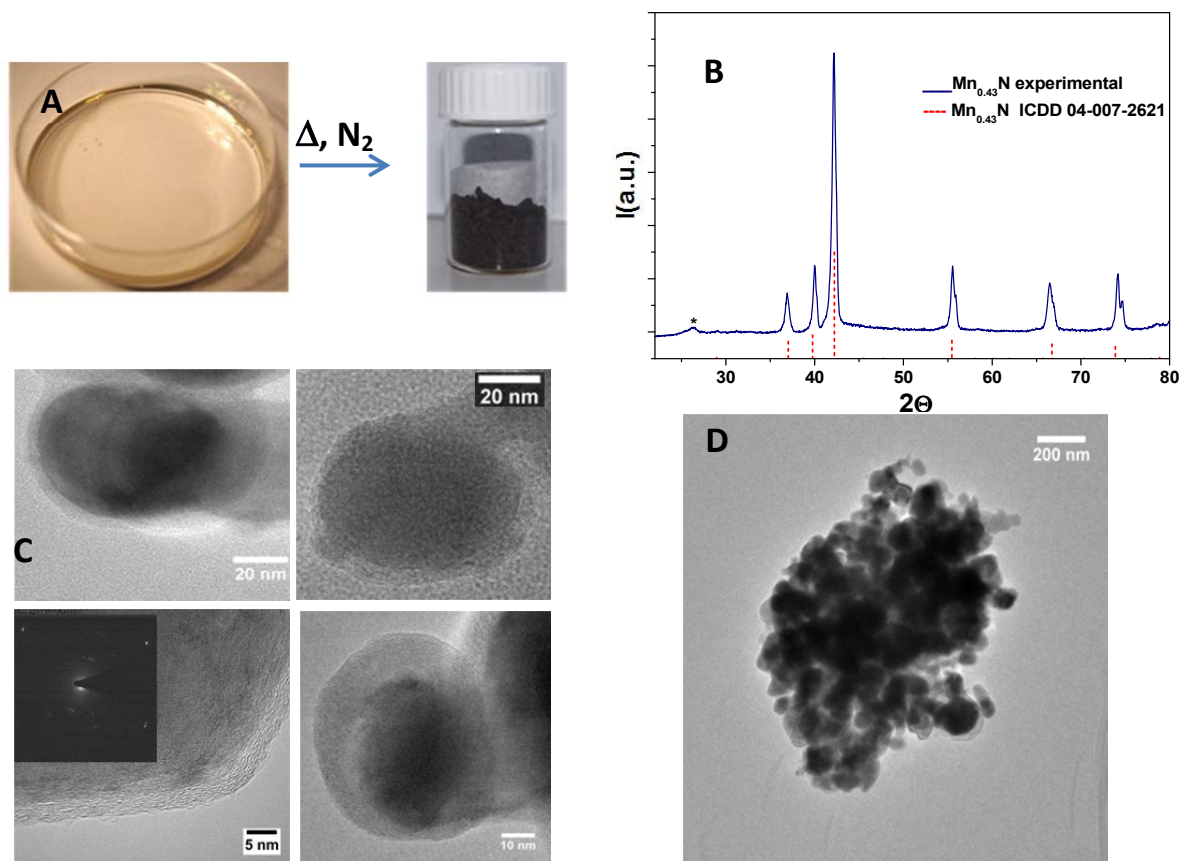

Figure 5.1. A) Mn-urea gel-like precursor (colourless and transparent) and corresponding product after heat treatment under nitrogen at 800°C (black powder). B) XRD pattern of the sample after heat treatment ($MnN_{0.43}$ reference pattern is also reported as red vertical lines for comparison); marked peak (*) is attributed to graphitic carbon (ICDD 04-015-2407). C- D) corresponding TEM images.

As observed from the TEM image, nanoparticles are polydisperse in size with diameters between 20 and 50 nm (in line with the calculated particle sizes from XRD

data ~30 nm). The HR-TEM study shows clear lattice fringes in the shell ($d = 3.33$ Å) attributable to graphite (ICDD 00-056-0159, $d_{002} = 3.35$ Å). Further analysis of lattice spacing allows the identification of the core as $MnN_{0.43}$ ($d = 2.50$ and 2.28 Å; ICDD 04-007-2621 $d_{130} = 2.43$ and $d_{002} = 2.26$ Å). In some particles, a low contrast interface of few nanometres is observed with lattice distances of ~2.65 Å, possibly residual MnNCN (ICDD 04-011-7543, $d_{012} = 2.69$ Å), an intermediate product.

N_2 physisorption measurement on the final powder shows a type IV isotherm (data not shown), with corresponding BET surface area of 79.3 m^2/g, one of the highest reported so far for manganese-based nanomaterials.

The formation mechanism was also investigated by quenching samples at different temperature and performing both XRD and FT-IR investigations. This study showed that the formation of the final manganese nitride (up to 800°C) passes through the formation of a MnNCN phase, as also suggested by HR-TEM findings and similar to other cases previously discussed. The nitride converts to the carbide phase (a mixture of Mn_7C_3 and Mn_5C_2) at higher temperature (figure 5.2).
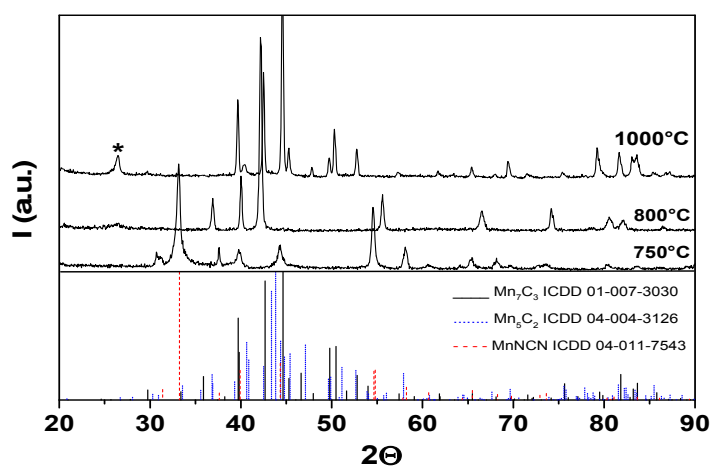

Figure 5.2. XRD patterns of Mn-Urea samples quenched at different temperature showing the formation of MnNCN (750°C), MnN (800°C) and a mixture of Mn_7C_3 and Mn_5C_2 (reference patterns are reported as vertical lines for comparison). Marked peak (*) is attributed to graphitic carbon.

Interestingly, FT-IR studies (figure 9.10) show that, for lower temperature, MnNCN formation is accompanied by the formation of $C_xN_y(NH_2)_z$ polymers (possibly catalysed by the metal [239]) upon urea decomposition (up to 600°C), forming a yellow powder. The polymers and the MnNCN phase further decompose to N-doped

graphite together with the formation of the nitride. At higher temperature a more defined graphite peak is also observed (figure 5.2).

As anticipated, the presence of carbon gives the system additional properties, i.e. it improves the electrical conductivity of the final material, and it contributes to the Li storage capacity in its battery applications. This nanocomposite was tested as anode material vs Li° (as counter electrode), showing excellent cyclic stability (230 mAh/g) and Coulombic efficiency close to 100%, as shown in section 7.3.

ii. $Ni_3N@C$ nanocomposites [240]

Nickel based materials have been receiving more and more attention as suitable alternative materials to more expensive catalysts. However, nickel nitride is hardly considered, due to its thermal instability, which makes its synthesis difficult, especially as nanoparticles. However, with the UGR, the intermediate matrix stabilizes the nanoparticles during their crystallization step. The presence of the carbon phase in the final material stabilizes the nitride further without affecting its catalytic properties, as it will be shown in chapter 7. In this chapter, results on catalytic tests will be shown, in particular $Ni_3N@C$ was studied for the first time for hydrogenation reactions with H_2, showing good catalytic activity. Interesting, a different selectivity compared to the Ni@C nanocomposite (prepared in similar way and tested in the same conditions) was observed.

Digital photos of the Ni-Urea complex, before and after calcination, are reported in figure 5.3. In this figure the XRD pattern and TEM images of the final product are also reported. From XRD figure can also be seen that for T > 450°C, cubic metallic nickel is formed and elemental analysis on this sample shows a loss of nitrogen.

To have information about the formation mechanism, TGA and FT-IR studies have been performed (figure 9.11 appendix). From IR spectra the complexation of urea with the metal through C=O was observed (due to the change in the the C=O vibration position, compared to pure urea, at 1587 cm^{-1}). Beside this shift, the spectrum of the precursor is mainly a combination of vibration mode of urea and the nickel acetate (the metal precursor).
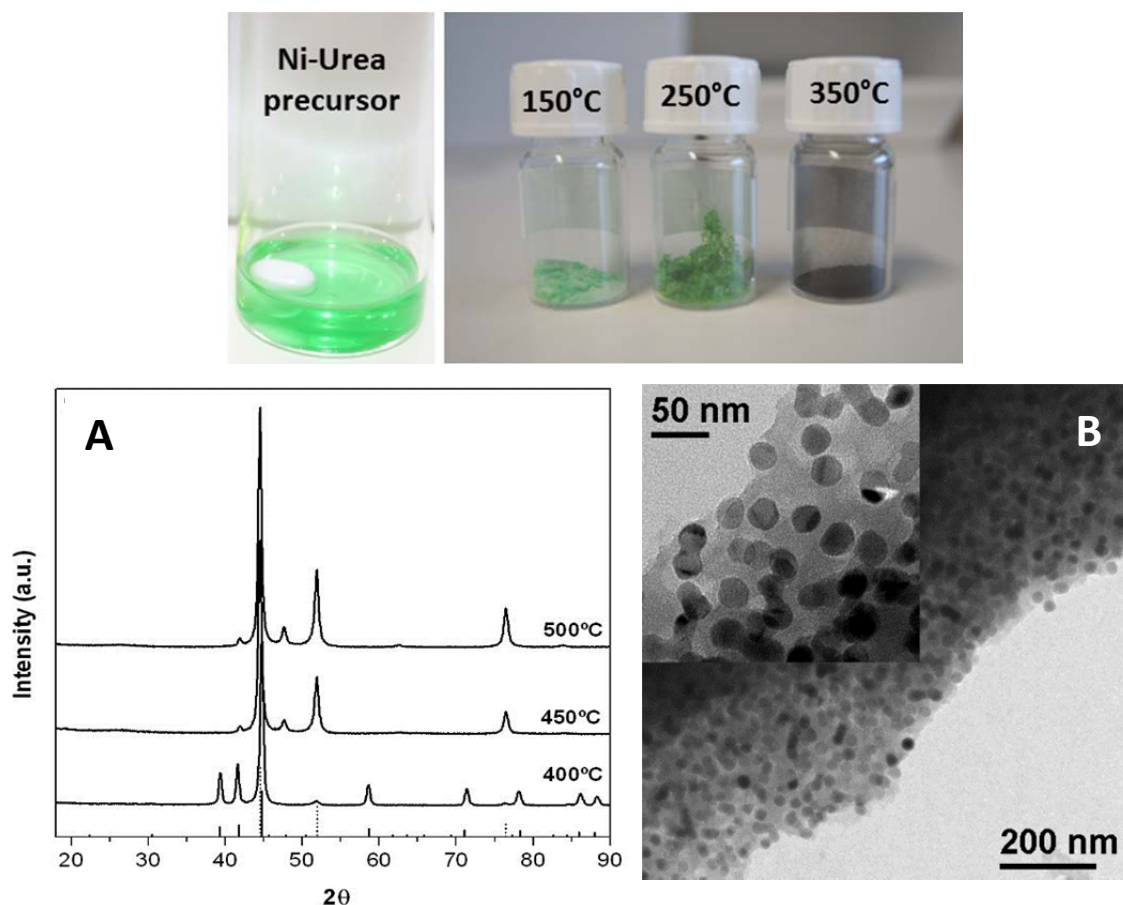
Figure 5.3. Up: Ni-urea gel-like precursor (green and transparent) and corresponding product after heat treatment under nitrogen at different temperature). Down: A) XRD patterns of sample prepared with R=4 and treated at different temperature (reference pattern is also reported as vertical lines for comparison, ICDD 04-011-7280). B) TEM images at different magnification.

TGA on the precursor shown that the decomposition starts at 130°C, followed by two main decomposition steps at 300 and 380 °C respectively. The decomposition step at 300 °C corresponds to the formation of the N-rich carbon matrix, with a first mass loss of ~50%. IR showed, at this temperature, the formation of intermediate cyano-type complexes (appearance of a band at ~2193cm^{-1} [241, 243]. At higher temperature, the decomposition of the intermediate cyano-product takes place (see IR figure) till, at 350 °C, the nitride is formed (as ascertained by XRD). At T > 350 °C, Ni$_3$N decomposes to metallic nickel, as observed in the TGA pattern (mass loss between 350 and 400°C) and confirmed by XRD (peaks shift to higher angles, where Ni° peaks are expected).

5.2 MN/MC in Liquid Media: post-synthesis preparation [212] [219] [244] [245]

Along with many advantages of the synthetic pathways reported in chapter 4, there is one disadvantage, i.e. the prepared material is always obtained in form of a powder. Depending on the featuring metal, the powder can appear more or less fine (TiN), or fluffy (VN), or hard (WC), or magnetic (Fe_3C) or even nicely coloured (Ta_3N_5), but in each case always as a solid phase. For many applications the possibility to work with a fluid phase might be necessary (e.g. in coating, casting, applications as electrode, films testing, etc.) or simply desired (e.g. for the preparation of magnetic-fluids). The dispersion of metallic ceramics in liquid media can be achieved by coupling the nitride/carbide phase with a second phase (possibly water soluble), such as a surfactant, a polymer or a poly-electrolyte. For the incorporation of the second phase, the classical in-situ functionalization (largely used for the preparation of metal oxide hybrids) is not suitable here since no organic moieties survive during the heat treatment required for the MN/MC synthesis (T>>300°C).

To overcome this problem, the final system must be prepared in two steps (as schematically reported in scheme 5.1):

1) preparation of nanoparticles (e.g. as described in chapter 4),

2) addition of the second suitable phase, which can be firmly attached on nanoparticles surface.
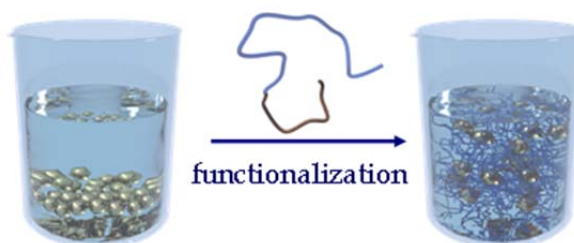
Scheme 5.1. Concepts of post-synthesis stabilization of solid nanoparticles. Reprint with permission from reference [237](© 2013 Springer).

This approach might not be easy, especially in the case of magnetic particles dispersion. Furthermore, there is still a lack of studies on MN/MC surface compatibility and functionalization (some attempts are described in reference [237]). However, while for MC reactivity close to that of carbon based structure (e.g. CNTs) might be expected, for MN there are no closer correspondences, and a dedicated study has yet to be conducted. As the interaction between the nanoparticle surface and the organic component is preferred to be chemical (rather than physical), the

second phase might also play more than a mere dispersing agent role, providing the MN/MC nanoparticles additional functionality (e.g. stimuli-responsivity, water solubility, etc.). That is why these systems are also addressed as nanocomposites.

As it is known that ILs and PILs can stabilize carbon structures, e.g. via a cation-π interaction [246, 247], some systems have been tested as dispersing agents for MC nanoparticles.

One of the first dispersing agents tested was an imidazolium based poly(ionic liquid), with the monomeric structure reported in figure 5.4.A. It was observed that both the imidazolium and the bromide groups have high affinity for carbon surfaces (related nanolatexes have been used to prepare concentrated CNT dispersions [249]). Furthermore, nanolatexes incorporating this IL possess stimuli responsiveness, based on the interaction between the imidazolium moiety and some anions [250, 251] .

This nanolatex, prepared by microemulsion polymerization using a bromide based ionic liquid surfactant [250, 251], were mixed with a powder of highly aggregated tungsten carbide nanoparticles of ~4 nm (see table 4.1 for experimental details on nanoparticles preparation), resulting in stable water-borne dispersions. WC was chosen with the intention to prepare hard and abrasive-resistant coatings in a simpler way. However, further applications can be envisaged.
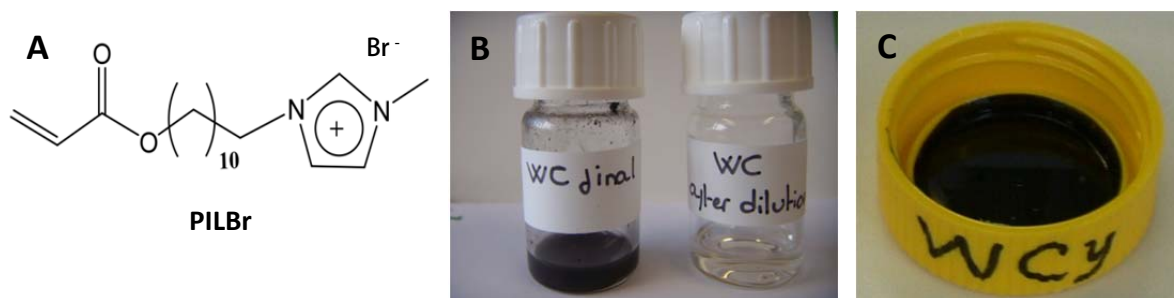
Figure 5.4. A) Molecular structure of the monomer. B) WC/nanolatex dispersion obtained by medium sonication treatment (5 min @ 50% amplitude in 30s doses, with micro tip) with aqueous nanolatex and C) corresponding casting.

Nanoparticles dispersions were obtained by mixing the solid nano powder with different amounts of nanolatex and shacked using a Sonifier with a 4 mm microtip for a total of 300s (in several steps) at the same amplifier amplitude (50%). A concentration of WC of 3.03% (w/w) was found to be optimal to get dispersion stable for days, without noticeable sediment. This means that, despite a WC density

of 15.8 g cm^{-3}, thermal Brownian motion forces exceed gravitational effects, where the driving force for the nanolatex–WC interactions might be the imidazolium group. The dispersion mechanism is possibly related to the separation of the original carbide nanoclusters embedded and therefore stabilized in the nanolatexes.

In a second time a portion (~1g) of the dispersion was dropped into a polypropylene mold and left to dry overnight. The dried film (173±2µm thick) appears shiny and glazed.
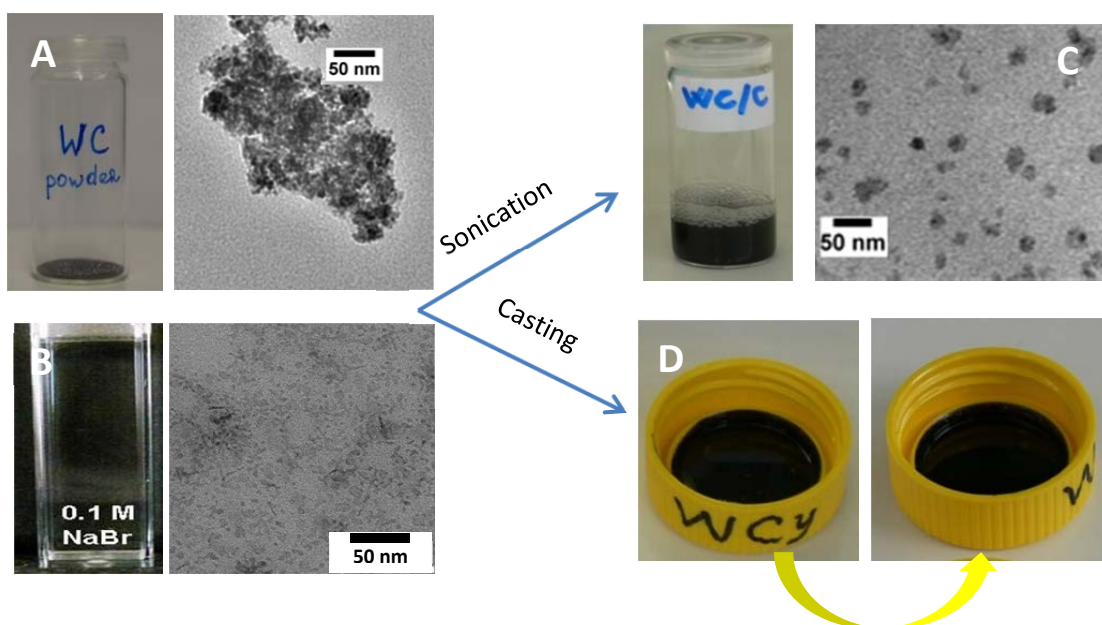

Figure 5.5. A) WC powder and corresponding TEM image. B) Latex/water solution and corresponding TEM image. C) WC/Latex dispersion and corresponding TEM image. D) Casting of the WC/Latex dispersion.

A second portion was diluted heavily for UV-Vis and from this analysis a 39.8 OD/cm path-length was found indicating that the dispersion is actinically black (absorbs all incident photons in the visible range) [244]. Thermal diffusivity and dielectric loss of the casted material were also investigated, and through-plane thermal diffusivity was measured at r.t., resulting in thermal diffusivities of 0.11 mm^2/s. This means that for low nanoparticles loading (here <<1 volume %), the WC does not perturb the heat transfer [244]. However, thanks to the observed intense actinic effect, we consider these nanocomposites as a new class of photo-thermal materials.

A drop of the diluted dispersion was used to perform TEM investigation. From TEM images (figure 5.5. and 5.6) it can be observed that clusters of smaller nanoparticles

are dispersed in/on the hydrogel nanolatex particles, similarly to what was observed for the intra-dendrimeric stabilization[26] of noble metal nanoparticles [253]. The nanolatexes are hydrogel particles that seem to possess similar effective high surface area, when water swollen. SEM images show a silkier structure compared with that of naked nanoparticles (figure 5.6).
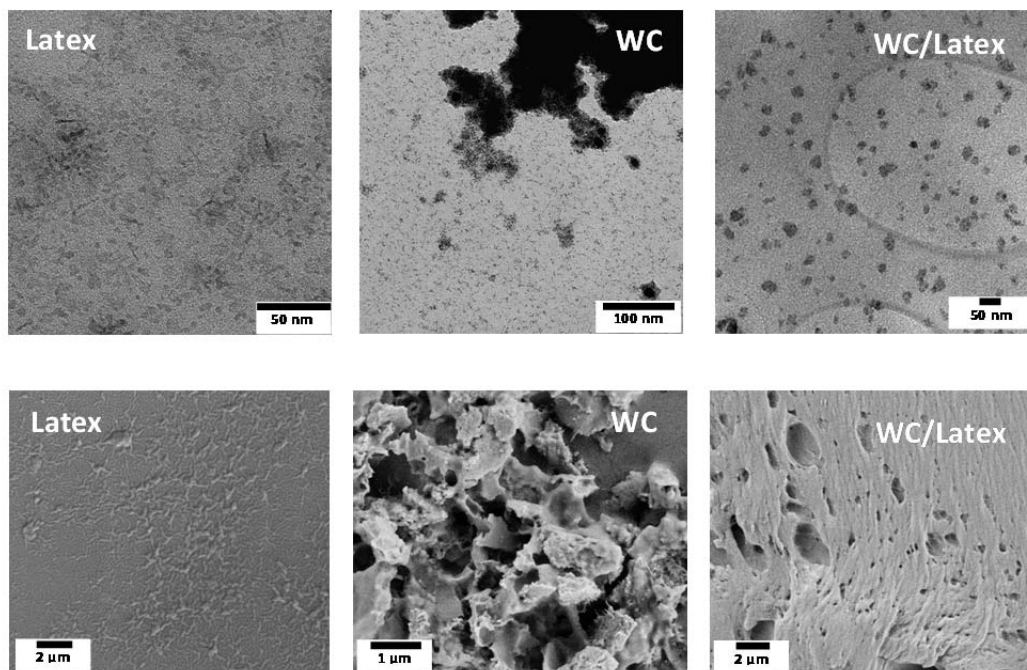

Figure 5.6. TEM images (up) and SEM images (down) of WC nanoparticles before and after dispersion in PILBr. Images on the pure latex are also reported for comparison.

Based on these positive results, the PILBr nanolatex was also used to disperse Fe_3C nanoparticle. The overall behaviour was however, on preliminary tests, not completely satisfactory, since it did not bring to long-term stable dispersion. Based on a more recent experience, this might be attributable to a negative effect of the strong sonication treatment rather than to the dispersion ability of the PIL. For magnetic nanoparticles it was in fact observed that, although the use of ultrasound seems to initially help the homogenization by disaggregating the nanoparticle clusters, on the other hand it supports the reorganization of the dispersed particles into bigger and more stable clusters (where probably the nanoparticles are aligned along low energy orientations). They are impossible to re-disperse stably, with the same conditions. For this reasons, new experiments have recently been planned, starting from a new synthesis of the PILBr system.

---

[26] Dendrimers are "all surface" and optimal for coordinating noble metal ions and the subsequently formed reduced nanoclusters.

Meanwhile, other dispersing agents have been investigated. A further system tested in order to firmly disperse magnetic nanoparticles in water media, toward the preparation of alternative ferrofluids, is a NitroDOPA-PEG molecule. As the name suggests, this molecule is made of two different parts (see scheme 5.2), where the dopamine part can be attached to the nanoparticle surface, while the PEG tail ensures the dispersion in water.
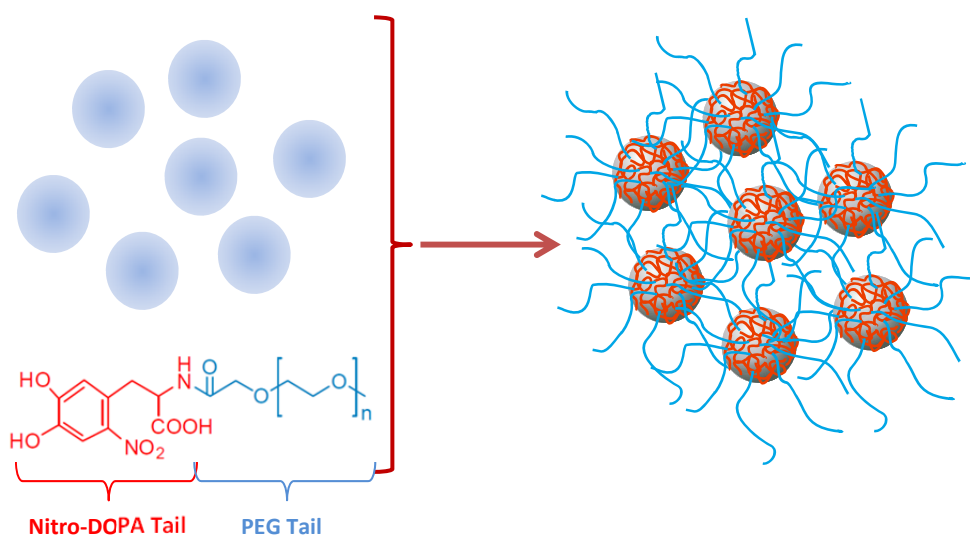
Scheme 5.2. Schematic representation of the dispersion process of nanoparticles with Nitro-DOPA-PEG molecules.

This molecule was previously used to disperse iron oxide nanoparticles, creating a system with high colloidal stability [254] and proven biocompatibility [248].

Fe_3C nanoparticles (prepared as reported in section 4.1.2) were then dispersed in a Nitro-DOPA-PEG water solution. The final solution has a dark-grey colour (indicating no iron etching from nanoparticles surface) and was stable for several weeks. XRD performed on the dispersion shows both peaks of iron carbide (although of reduced intensity compared to that of pure uncoated iron carbide) and the Nitro-Dopa-PEG system (figure 5.7). In order to perform a FT-IR study, a portion of the dispersion was dried and then washed several times to remove the excess of surfactant and then dried again. The IR spectrum recorded on the washed powder (coated with NitroDOPA/PEG) still shows all IR-bands of the reference measurement (NitroDopa-PEG without particles), confirming the presence of the coating material on the particle surface. The two absorption bands at 1490 cm^{-1} and 1280 cm^{-1} arise from the Nitro-Dopa coated particles. These can be assigned to the C-C-ring vibration and NO_2^- stretching vibration of the Nitro-Dopa.
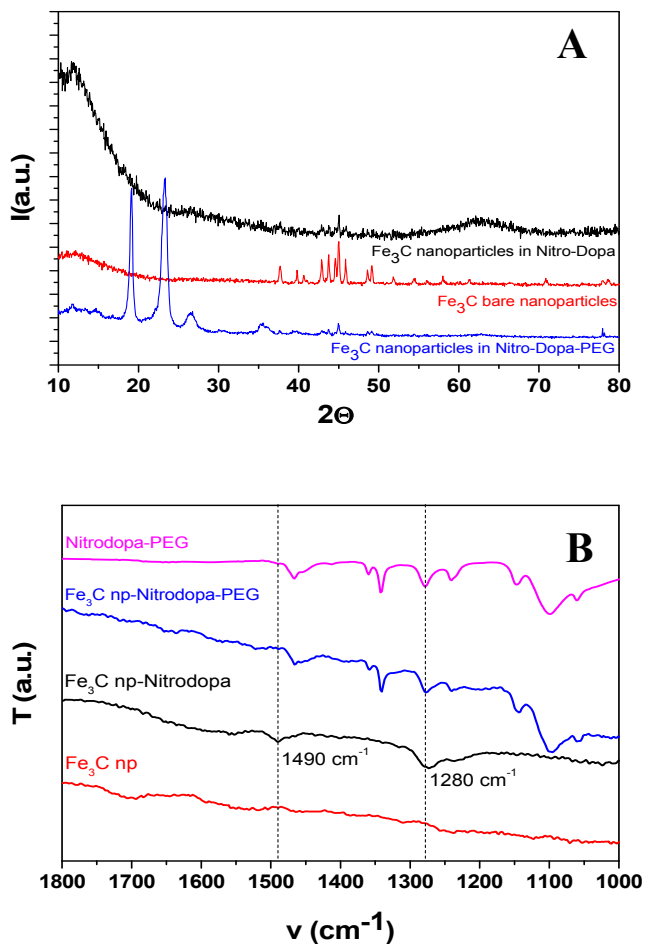
Figure 5.7. A) XRD patterns and B) FT-IR spectra of the iron carbide nanoparticles bare and dispersed with the Nitro-DOPA-PEG molecules.

TEM investigation (figure 5.8) shows that after dispersion nanoparticles are found mainly isolated rather than in clusters (as found before dispersion, figure 5.8.A).
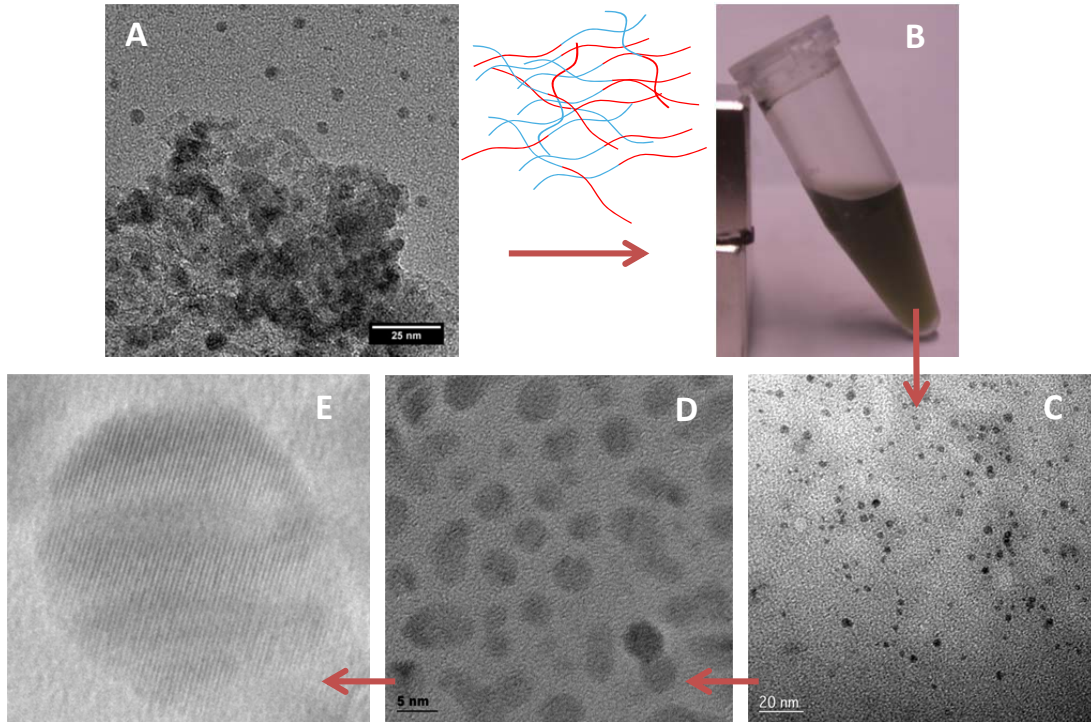
Figure 5.8. TEM images at different magnification of the Fe$_3$C nanoparticles prepared from UGR (see section 4.1.2) after dispersion in water with the Dopa-PEG surfactant (C-E). TEM image of nanoparticles without the addition of the surfactant is also shown (A). In B) Digital photo of the iron carbide/dopa-PEG/water dispersion.

Analysis on lattice fringes gave a value of d$_{spacing}$=0.20 nm in good agreement with the expected value for iron carbide (d= 0.2013 plane 031 of the orthorhombic Fe$_3$C). On the other hand, the amount of iron carbide, which could be dispersed in this way, is still too small to see any magnetic effect on the solution.

In order to increase the nanoparticles concentration of the dispersion, other materials have been investigated. In particular a monomeric Emim (1-ethyl-3-methylimidazolium) based ionic liquid with different counter ions, such as tetrafluoroborate [BF$_4$], dicyanamide [N(CN)$_2$], trifluoromethylsulfonate (triflate) [TfO], ethylsulfate [ES], methanesulfonate [MS], and thiocyanate [SCN] were tested. Among these ILs, the [Emim][SCN] and [Emim][N(CN)$_2$] systems shows the best capability as dispersing agent, while the other investigated systems always shows sedimentation of the nanoparticles powder. Despite the absence of sedimentation, a colour change can be observed, from grey to orange and light yellow using [Emim][SCN] and [Emim][N(CN)$_2$], respectively (figure 5.9). Considering that XRD studies performed on these dispersions still show the characteristic pattern of iron carbide (similar to that of the bare Fe$_3$C nanoparticles [245]), the colour change

might be due to a partial leaching of iron from the nanoparticles surface, which probably leaves a carbon-rich surface. The C-rich surface might also be the reason of the stabilization effect in these ILs, i.e. the ILs possibly bonds the nanoparticles surface over C-bridges via the polarizable imidazolium groups of the ILs.
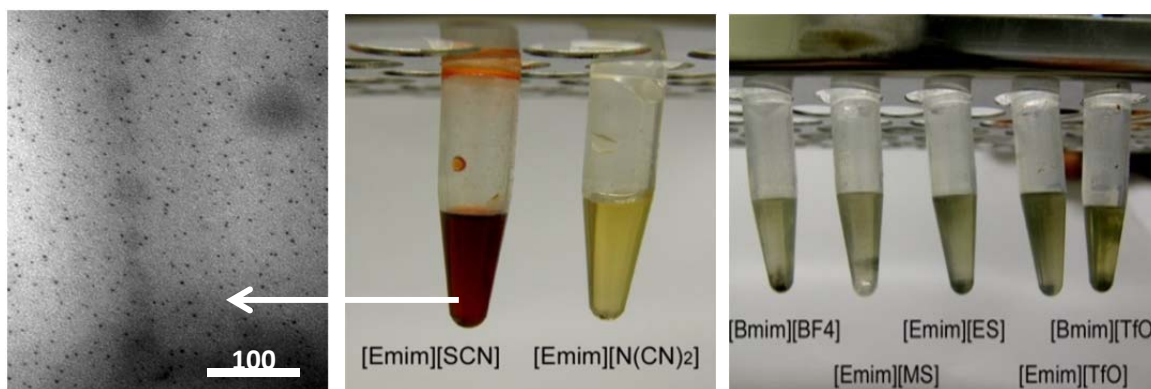

Figure 5.9. Fe₃C@Emim-based dispersions and TEM images of Fe₃C nanoparticles dispersed in [Emim][SCN]. Adapted with permission from reference [245] (© 2010 American Chemical Society)

This study provides evidence that the presence of carbon on the nanoparticles surface can favor the nanoparticle dispersion. The stabilization through the carbon might be improved by the presence of a thicker shell around the nanoparticles, without affecting the magnetic properties of the final system in any way. The preparation of iron carbide nanoparticles with a well-defined carbon shell is possible through the transcription route discussed in section 4.1.2. In this session, it was shown that the wash treatment used to remove the excess of carbon leaves the graphite shell around the particles intact. Thanks to the presence of this shell, nanoparticles can be stabilized, for instance using poly(1-ethyl-3-vinylimidazolium bromide: PVImBr), a water soluble poly-electrolyte [219]. This polymer was directly mixed with the nanoparticles powder, using only a very small amount of water to facilitate homogenization[27]. After dispersion, the mixture was shortly sonicated in an ultrasonic bath (low intensity), then separated by ultracentrifugation and washed several times to remove the excess of carbon. The washed nanoparticles powder, now functionalized with the PVImBr, was finally dispersed in water.

---

[27] 30 mg of powder were added to 100 mg of PVImBr and 10 mL of water.

The dispersion was homogeneous, black in colour and stable for weeks. In figure 5.10 dispersions of iron carbide in pure water and in a PVImBr/water solution are shown.
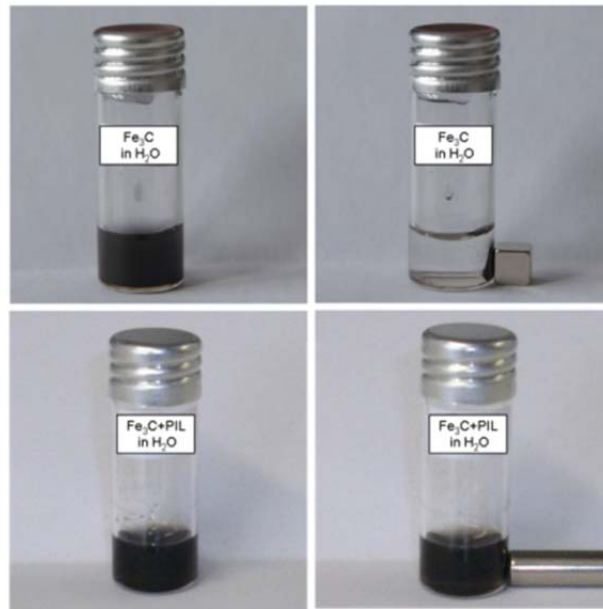
Figure 5.10. Fe$_3$C nanoparticles dispersed in pure water are immediately attracted by the presence of an external magnet (top). In Fe$_3$C@PVImBr dispersion (bottom) the particles are well dispersed in aqueous PIL dispersion and appear they have been stabilized in such a small particle state that the individual nanoparticles probably cannot sustain a magnetic moment. Reprint with permission from reference [219](© 2013 Springer).

Based on findings obtained by these studies, focused experiments will be performed in the future to obtain highly concentrated dispersions of MN/MC (see chapter 8 for outlook).

6. Processing: beyond spherical nanoparticles

The possibility to arrange nanoparticles with preferred orientations, together with the option of changing shape and hierarchy in a systematic way, is surely one fundamental aspect in nanotechnology. Control over morphology and type of assemblies can add to the final material additional features, e.g. changes in magnetic [255] or optical [256] properties, different selectivity in catalysis, improved conductivity, etc.

Alongside the difficulties related to the synthesis of metallic nanoceramics, successful pathways toward MN/MC processing are scarce in technology compared to the wide set of routes known for metal oxides.

In this chapter, it will be shown how, based on the routes presented in chapter 4, the structure of the final product can be adjusted, e.g. going from mesoporous materials with higher surface area to more complex hierarchical structures, such as fibres and bio-replicas. Spin-coating and printing will also be presented as easier ways to obtain MN/MC nanoparticle layers, compared to the most common but uneasy CVC processes[28].

In general, three main strategies are followed (schematically reported in schema 6.1):

I) ***Post-synthesis processing***, nanoparticles powder is dispersed in a proper medium, eventually with the assistance of a functionalization agent (see also chapter 5), and then casted via dip, spin or spray-coating.

II) ***In-situ processing***, the starting jelly precursor is processed via dip, (electro)spin or spray coating (including ink-jet type printing and aerosol process) in presence of a stabilizing agent and then thermally treated to get the final MN/MC. During the heat treatment, the stabilizing agent decomposes and transforms into a functional auxiliary phase.

III) ***Use of hard template***, the starting jelly precursor is combined with a hard template (e.g. silica nanoparticles), which is removed after calcination leaving a negative replica (this method is suitable for the preparation of mesoporous materials).

---

[28] CVC processes usually require high temperatures (up to 1000°C) and costs, and are difficult to scale.
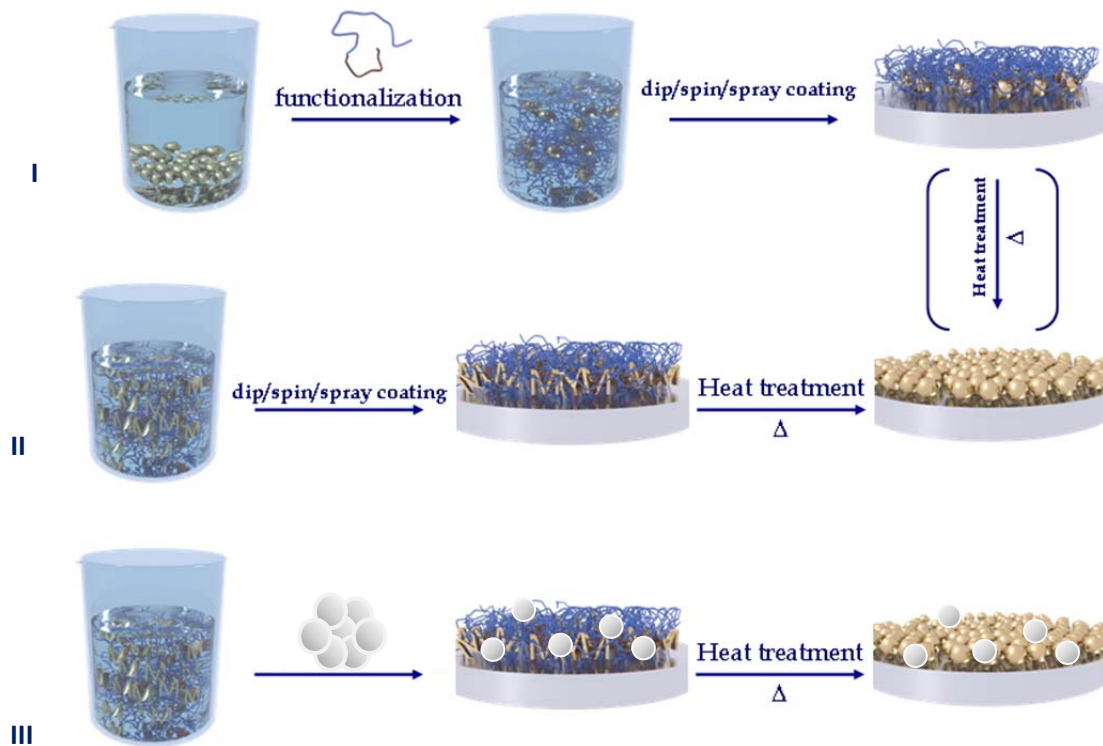
Scheme 6.1. Schematic representation of the route used to process MN/MC nanoparticles (see text for details).

One advantage of these routes is the possibility to make homogeneous and, when properly refined, defect free films, coating and casting. In the following, some specific examples for route I and II will be presented, while route III has been already discussed in section 4.1.2.

6.1 Spin-coating [156]

i. Spin-coating of powder mixtures

In order to prepare homogeneous and relatively thin nanoparticle layers, a spin coating device can be employed. A spin coater is a well-known and simple machine for dispersing a substance on a flat substrate. The substrate is rotated at high speed, spreading the dropped material by centrifugal force. The higher the angular speed of spinning, the thinner the resulting film. Thickness depends also on the viscosity and concentration of the solution and the solvent.

Rotation is continued until the desired thickness of the film is achieved, while the solvent (usually a volatile compound) evaporates. In figure 6.1 a scheme of the

procedure is reported. The film obtained simply by dropping the nanoparticles dispersion on a glass substrate is also reported for comparison.
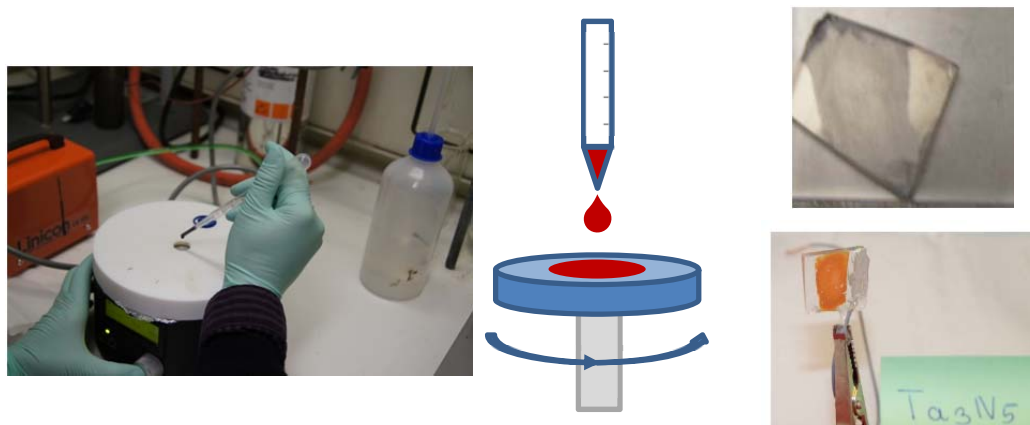
Figure 6.1. Preparation of Ta$_3$N$_5$ layers via spin-coating. The powder is firstly dispersed in nafion and spread onto a FTO substrate. The film (orange) obtained without the assistance of a spin-coater is also shown.

Although the process was found to be effective to reduce layer thickness and improve homogeneity at the macroscale level, the SEM investigation shows a high degree of inhomogeneity (figure 6.2).
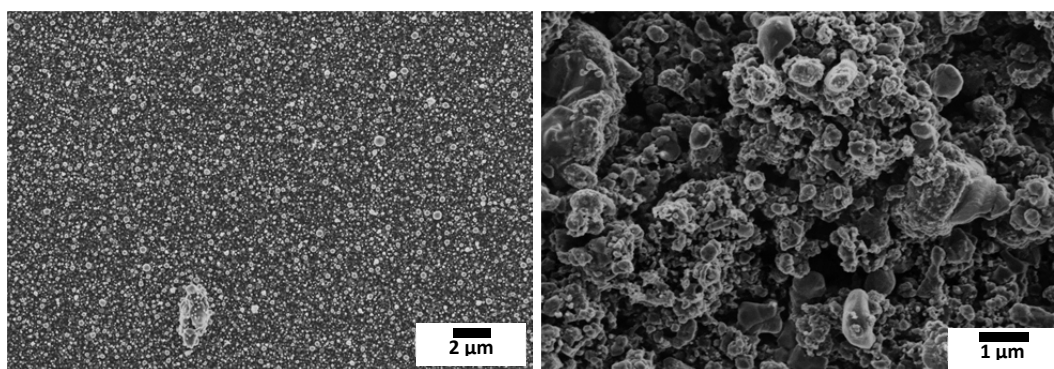
Figure 6.2. SEM images (different magnifications) of Ta$_3$N$_5$ nanoparticles after spin-coating of the corresponding powder.

Better homogenization can be obtained exploiting route II, i.e. via spin-coating of the precursor gels, which are calcined in a second step.

ii. Spin-coating of starting gels

In order to prepare thinner and homogeneous nanoparticle layers for direct application in electrochemistry processes, the spin-coating of the jelly starting materials was considered. The precursors were prepared as reported in chapter 4. A few drops of the precursor, previously mixed with a suitable structuring polymer

(e.g. PEG), were placed on the substrate and left rotate until solvent evaporates. The layer was then directly calcined under N_2 at 700°C. At this temperature, the polymer decomposes and leaves before the end of the reaction. In figure 6.3 and 6.4 SEM images of some films prepared with this approach are reported.
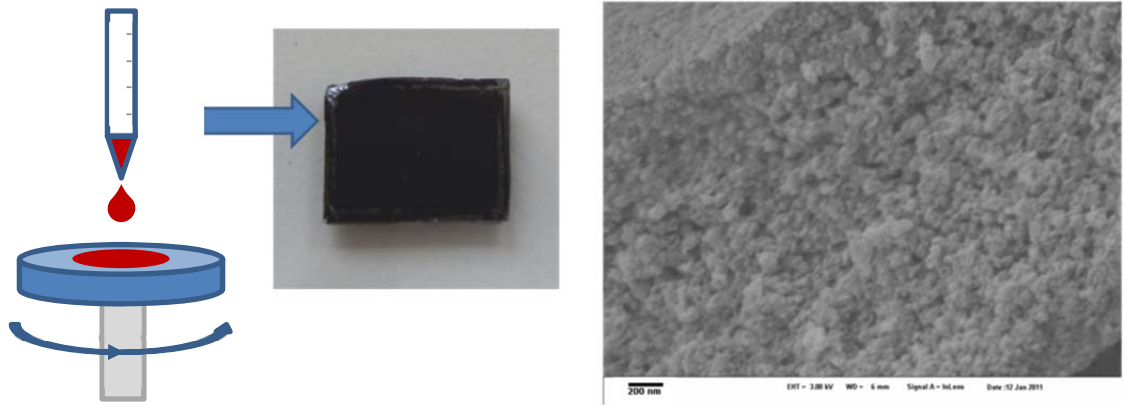
Figure 6.3. $MnN_{0.43}$ layer obtained spin-coating the starting gel and then calcining the layer under N_2. On the right the corresponding SEM image showing high degree of homogeneity.

Figure 6.4. SEM image of GaInN (left) and CrN (right) nanoparticle layers obtained by spin-coating the corresponding starting gels and then calcining them under N_2. In the inset on the right image, the corresponding film after calcination. On the right side, the "scratch" is intended to give an estimation of the layers deepness.

6.2. Printing [230] [231]

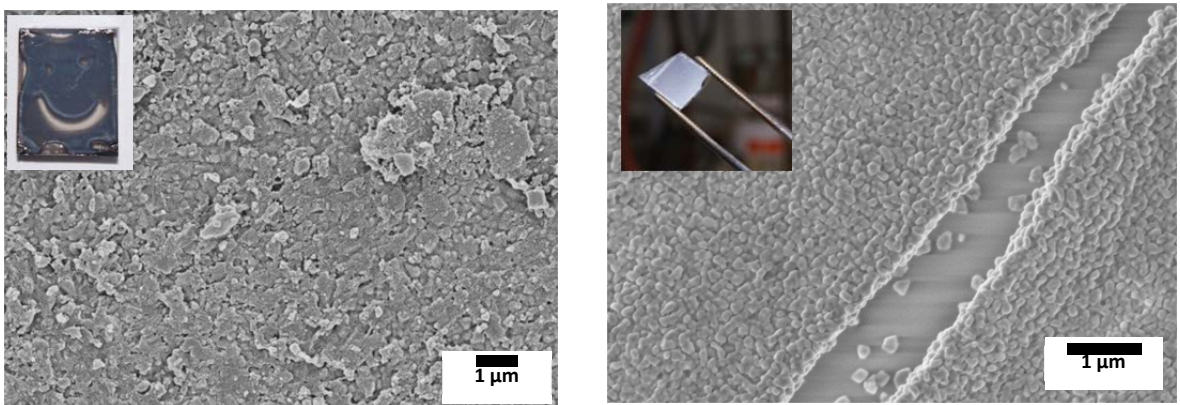The spin-coating technique was shown to be a useful tool to create relatively thin and homogeneous nanoparticle layers in a fast and easy way. It is however clear that neither control over layers arrangement nor the possibility to create multi layers can be envisaged with this technique. To achieve these targets without sacrificing simplicity and still aiming at high precision/selective patterning, an ink-jet printing process was coupled with the sugar route (see section 4.3). During the preparation of iron carbide via the sugar route (using cellulose as C-source), the iron precursor catalyses the formation of microstructured graphene nano-assemblies, which load the final Fe_3C nanoparticles. Thus, the precursor can be considered a sort of "catalytic ink" that can be used to design patterns of nanoparticles in a controlled fashion via printing techniques. In this way, ordinary cellulose can be converted, for instance, into a working electrode, using a simple and inexpensive set-up. It must also be pointed out that one of the main improvements of this methodology, compared with similar printing techniques, is the possibility to work at high temperatures.

In a typical experiment, a printer cartridge was filled with the iron solution, then a selected subject was printed on a paper support. The subject of this printing can be as diverse as the imagination can suggest. Here the Minerva head[29] was chosen as an example. The printed paper can be directly calcined resulting in an embossed pattern, perfectly corresponding with the initial draw (figure 6.5). The embossed appearance is due to the small shrinkages undergone by cellulose during the thermal treatment (as shown in figure 4.3.5).
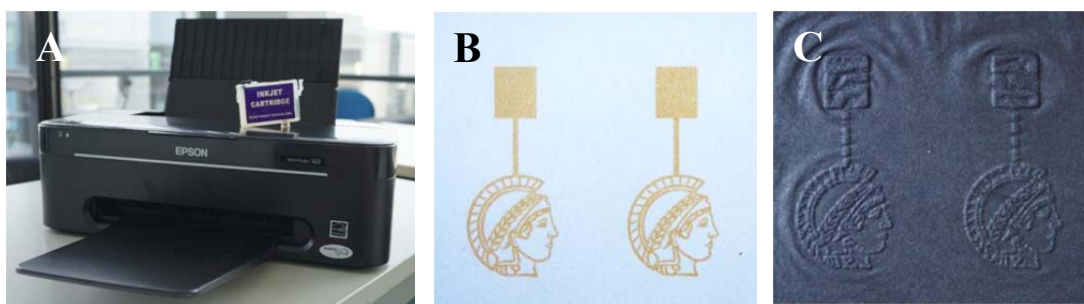
Figure 6.5. Preparation of the patterned electrode: a) standard printer used; b) printed iron based ink on paper before and c) after thermal treatment to convert the ink into carbon/ceramic arrays.

---

[29] Symbol of the Max-Planck-Society.

The key point here is that, while the regions where the iron-ink was deposited are converted (upon calcination) into a nanocomposites made of iron carbide and graphite (i.e. a crystalline and conductive phases), the non-printed regions have been only converted into amorphous carbon. This difference is crucial and can be conveniently exploited using the calcined sample as an electrode, for instance for the selective electro-deposition of copper (Figure 6.6).
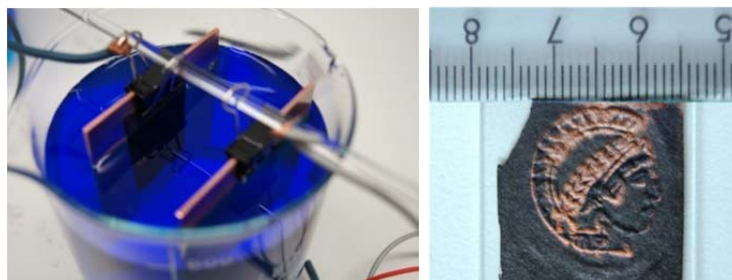
Figure 6.6. Copper deposition on the printed Minerva electrode: on the left the used set-up and on the right the final product.

Similar concepts can be applied to 3D structure (figure 6.7).

Folded

Soaked

Calcined

Coated
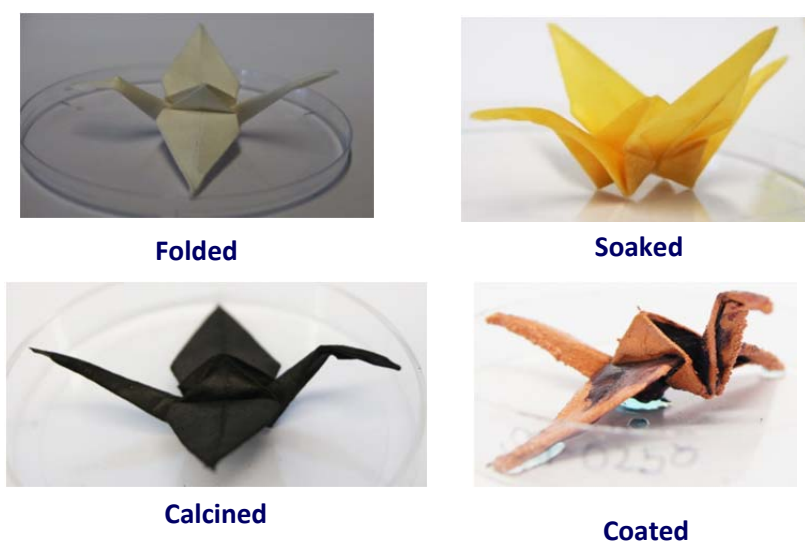
Figure 6.7. Steps of the electrodeposition of copper on an origami-crane prepared as described in section 4.3. Reprint with permission from reference [230] (© 2013 Wiley-VCH Verlag GmbH & Co. KGaA, Weinheim).

6.3 Electrospinning

UGR meets electrospinning

In order to go beyond spherical morphologies, the UGR was complemented with an electrospinning (ES) process. Electrospinning is a versatile technique for the production of a variety of complex organized structures such as fibres (with diameters below the micrometre scale), ribbons, core-shell composites, hollow tubes, etc. The process consists in the application of an electrical field to a capillary containing a suitable polymer solution, held on the tip by its surface tension. As the intensity of the electric field is increased, the hemispherical surface of the solution at the tip extends to form a polarized conical shape called *Taylor cone*. When the electric field reaches a critical value, at which the charge density overcomes surface tension, a jet is ejected. Then, solvent evaporation occurs along the trajectory and leads to a polymer based fibre on a collecting plate, forming a non-woven fabric. Fibres diameter can be adjusted by changing viscosity of the solution, conductivity, applied electrical potential, distance between the tip and the collecting plate, etc.

Different to a standard ES process, where preformed nanoparticles dispersions are used, the process here is divided in two steps: in the first step, a suitable precursor solution is electrospun to form fibres, which are, in a second step, thermally treated under N_2 flow to convert the metal-organic precursor in the final nitride or carbide based fibres (scheme 6.2).
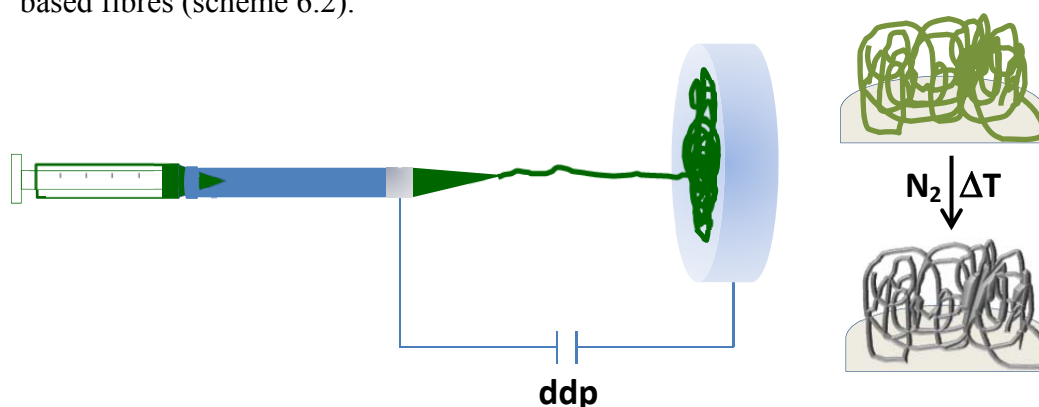
Scheme 6.2. Schematic representation of an electrospinnin set-up to produce fibers. The electrospun fibers are, in a second step, calcined under N_2 flow.

In the present study, special attention was devoted to optimize the electrospinning conditions to obtain nano-sized fibres (rather than usual micrometre ones) and to keep size and morphology of the electrospun fibres during the heat treatment. The

procedure here was applied to chromium and iron based fibres, and it is believed to be suitable for the production of other metallic ceramics.

Conditio sine qua none to get the wished-for morphology is that the electrospun precursor must provide enough mechanical stability to allow the fibre formation as well as keeping fibre strength to prevent collapse, above all during heat treatment.

The usual UGR precursor (metal salt mixed with urea and a proper solvent) was found to be unsuitable to be electrospun, confirming the short range order discussed in chapter 4. Therefore, the use of an auxiliary polymer was considered. At first, methylated poly(urea-*co*-formaldehyde) resin (PUF) was tested. Although a stable coordination compound with the metal chloride (the metal source) was obtained leading to the expected nitride phase, the precursor could not be electrospun, probably because of its tight cross-linking and a resulting resin-like structure. On the other hand, the use of poly-2-ethyloxazoline leads to precursor easy to be electrospun but mechanically not stable enough, so that the prepared fibres melted during the heat treatment. In this respect, polyacrylonitrile (PAN) turned out to be a perfect fibre scaffold (already used for carbon fibres formation [257]) but *alas* a poor nitrogen and carbon source. The winning strategy involved again a tandem approach, where PUF and PAN were used jointly to play the N/C source and the fibres scaffold respectively. It must be said however that also PUF contributes to the structure scaffold, since samples treated at 900°C in absence of PUF show a fused network structure composed of fibres with knob-like particles on their surface, while PUF-containing fibres present well defined rod-like shapes, confirming the stabilization effect of the PUF resin during the calcination process. In this way, while PUF provides resistance to the moisture and also acts as the main C/N source, the PAN plays the structure stabilizer. This finding was confirmed by performing experiments on the PAN/PUF mixtures, as well as using PAN and PUF separately [258]. For the iron based sample, PVP (rather than a PAN/PUF mixture) was sufficient to bring to the final products, due to its high compatibility with the chosen iron precursor. Experimental and technical details are reported in table 6.1.

Table 6.1. Experimental details of the electrospinn process to produce Cr- and Fe-based fibres.

Metal solution	Auxiliary Polymer	R	Solution flows (mL·h⁻¹)	Voltages (kV)	Collector distance (cm)	Heat treatment (°C)	Product
$CrCl_3·6H_2O$ in DMF	PAN/PUF	3:1*	0.25-0.5	12-14	12-16	800	$CrN+Cr_3C_2$
						>1000	Cr_3C_2
$Fe(C_5H_7O_2)_2$ in methanol	PVP	1:1**	0.25-1.0	10-18	8-12	600	Fe_3N
						700	Fe_3C
* PAN:Cr; **PVP:Fe							

As previously experienced, also in this study, it was found that calcination temperature has a strong influence on composition, carbon scaffold organization and texture. Furthermore, independently from the final morphology, the formation mechanism both for MN and MC was found to be that one observed using the classical UGR (chromium based products) or the BpR (iron based products).

6.3.1   Chromium based fibres [258]

Preparation of chromium based nanoparticles fibres was achieved as reported in [258], starting from a solution of $CrCl_3·6H_2O$ in a PAN/PUF/DMF solutions (see table 6.1). The polymeric solution was electrospun at r.t. in accordance with the conditions reported in table 6.1 and left to dry, then thermally treated at various temperatures (800-1400°C) under N_2 flow. The main change is observed between 800-900°C, when a phase change from CrN to Cr_3C_2 is observed. For T>900°C no significant changes are observed (the product is chromium carbide), while at lower temperature (800°C) a mixture of CrN and CrC is obtained (figure 6.8). From this figure, an increase of the graphite peak at about 26°C can also be seen. The catalytic effect of chromium based particles on graphite layer formation was previously observed [136].
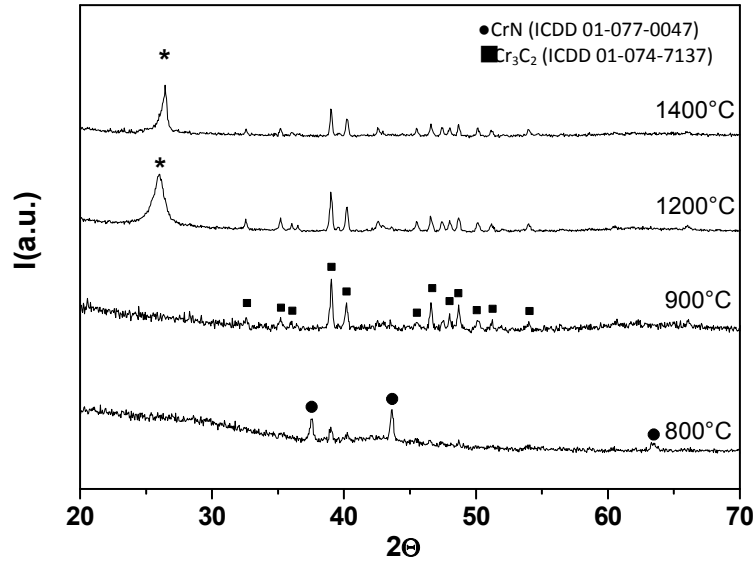
Figure 6.8. PAN-PUF-Cr based fibres annealed at different temperatures. Marked peak (*) is attributed to graphite (ICDD 04-15-2407).

To have information about fibre sizes and shape retention during the thermal treatment, SEM investigations were performed before and after the heat treatment, showing that electrospun fibres are made of homogeneous mats and have diameters from 200 to 500 nm. Fibres treated at 800°C have similar diameter and a closer look at their texture highlight a particle-based composition (Figures 6.9).
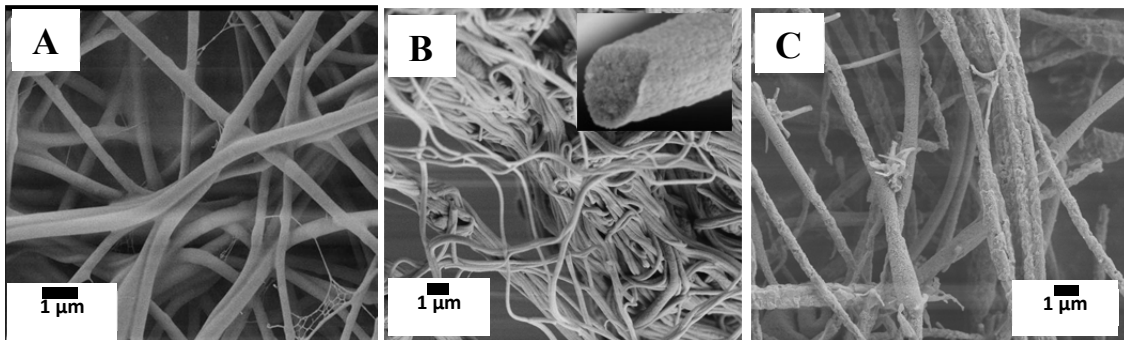
Figure 6.9. SEM images of as-spun amorphous fibres of PAN-PUF-Cr: (A) before and (B-C) after heat treatment at 800°C and 1400°C, respectively.

TEM investigation just confirmed the fibrous nature of the sample and the graphite presence and chromium carbide (via SAED), while CrN reflections were not observed probably due to its low amount inside the fibres (~10%) [258]. Nitrogen sorption experiments show a lower specific surface area for samples obtained below 900 °C (25 m^2/g calculated by the BET method), while for samples treated at T>1200°C the specific surface areas was up to 110 m^2/g (figure 9.12 in the appendix)

and the corresponding pore diameter evaluated by non-linear density functional theory (NLDFT) calculation varies from 4 to 8 nm.

6.3.2   Iron based fibres

Iron nitride and carbide based fibres were prepared starting from a solution of iron (II) acetylacetonate in poly(N-vinylpyrrolidone) (PVP). The choice of the acetylacetonate over the usual chloride is due to a higher stability towards iron alcoholate formation[30] [259]. On the other hand, the high molecular weight of PVP presented high compatibility with the iron precursor due to its capability for cation complexation. The ES process leads to bead-free fibres at any of the electrospinning conditions tested, producing bimodal fibres (80 nm and 300 nm). This effect is known in ES and (at controlled humidity) it is due to the instabilities of the jet polymer. At higher voltages the jet is stable enough to form a minimum of secondary jets with well-defined diameters producing two average fibre sizes. Fibres were thermally treated under nitrogen atmosphere at different temperatures ranging from 400 to 700 ℃ (2h+1h of dwelling time). The resulting products were black fibre mat structures with a brittle aspect and were stable at room temperature.

XRD study shows that, similar to what was previously observed (sessions 4.2 and 4.3), the iron nitride/carbide fibres formation passes by the formation of iron oxide nanoparticle up to 500 °C (figure 6.10). At 600 ℃, the conversion of the iron oxide in nitride occurs and Fe_3N is the only crystalline phase present. At higher temperature (700 °C) only elemental iron and iron carbide are found. Surprisingly and differently than previously observed, no crystalline carbonaceous species can be observed, indicating that the iron phase, here, does not act as a graphitization catalyst. The formation of nitride over the carbide phase depends on the heating rate and final temperature, and follows a similar nitridation/carbidization mechanism discussed in section 4.2.

---

[30] The use of acetylacetonate as capping ligand for metal alcoxydes formation is known [260].
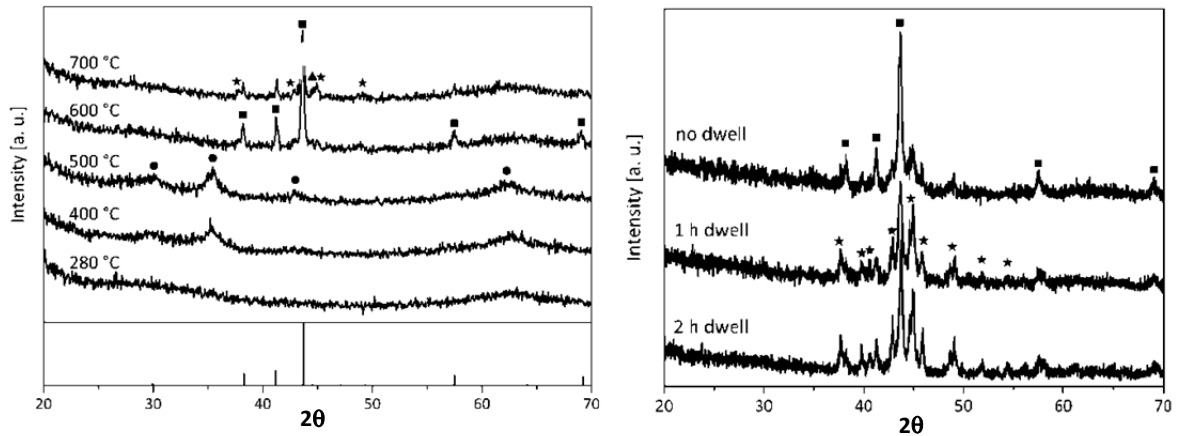
Figure 6.10. A) XRD patterns of iron oxide (circles), iron nitride (squares) and iron carbide (stars) containing electrospun fibres treated at different temperatures. The reference pattern expected for iron nitride is also reported for comparison as vertical lines (ICCD 04-007-2250). B) XRD patterns of iron carbide fibres prepared with different dwelling time.

XRD diffractograms of samples treated at 700 ºC with different dwelling times revealed the formation of iron nitride and a minimum amount of iron carbide for fibres without dwelling, while the content of iron carbide increased with increasing dwelling time. The intensity of the signals of iron nitride decreased and broadened, suggesting a partial transformation of the nitride into carbide by simple reaction of the iron with the fibre scaffold. Elemental iron was also observed in any case and it increased with heating time (or temperature), due to the iron carbide decomposition [261].

SEM investigation (figure 6.11) confirms the bimodal sizes of the electrospun fibres, which is preserved also after heat treatment. With increasing temperature however, it was observed that the roughness of the fibre surface increased gradually over the whole temperature range. At 600 ºC particles with an average diameter of 60 nm were observed on the surface of the fibres (Figure 6.11C). These blossoming branch-like mats suggest that the iron nitride particles grow from the inside of the fibre structure. Based on previous observations (see section 4.2), it can be assumed that the transformation from the oxide to the nitride phase is a local surface nitridation between the nitrogen from both the polymer and the reaction atmosphere.
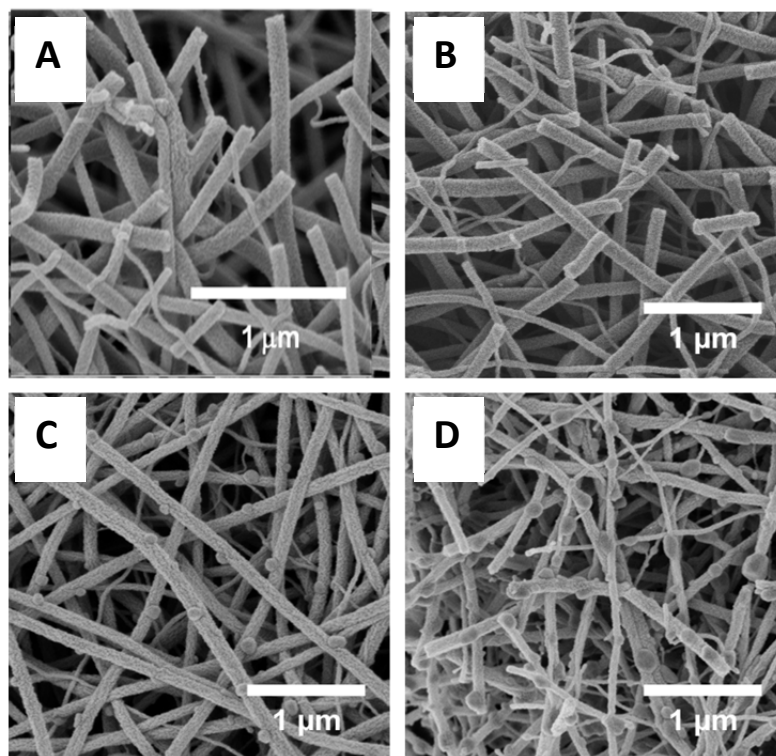
Figure 6.11. SEM images of the precursor fibres before (A) and after heat treatment at 500 (B), 600 (C) and 700 °C (D), respectively.

TEM investigation (data not shown) confirms fibres morphology and shows nanoparticles with larger sizes (20-30 nm) embedded in the carbon fibre scaffold for samples treated at 600°C. The formation of aggregates was rarely observed. SAED studies showed the planes (211), (112), (111) and (113) of iron nitride particles. No planes corresponding to graphite were observed, indicating that the fibre scaffold is made of amorphous carbon. The ultramicrotomography of these fibres indicates that iron nitride species are both outside and inside the fibres.

6.4 Bio-templating and the cyber-leaf [262]

In material chemistry there are two main strategies to achieve complex morphologies. One is based on nano-engineering, the art of creating structure using molecules as building blocks. The other one is the use of template (more or less complex) to produce replicas. In the study presented in this session, biological structures have been employed as templates for the preparation of complex morphologies, still keeping "simplicity" as *Leitmotiv*. Bio-templating is not only a relatively simple way to get hierarchical structure otherwise difficult to achieve but

also an easier way to transfer key biological features to inorganic materials (e.g. porosity, high surface area, improved transport pathways, cellular functions, etc). The use of bio-template is well-known in oxides synthesis but not yet fully exploited for the preparation of other materials.

In chapter 4, it was discussed how even large molecules such as biopolymers (gelatin, chitosan, cellulose, etc.) can be successfully used for the preparation of metallic ceramics. It is then not hazardous to think that other, similar molecules could play a similar role, for instance *lignin*. Lignin is an abundant and robust biopolymer, and together with cellulose, gives mechanical strength to the plants. Exemplarily, a *Ficus religiosa* skeleton leaf was chosen as lignin rich substrate for the preparation of hierarchical Fe_3C based structures [262]. As the other source previously presented, here the lignin-rich leaf skeleton acts as both, a template and a carbon source for formation of an iron carbide based composite, by carbothermal reduction of the iron precursor ($Fe(CH_3CO_2)_2$ in water, 10 wt%). Leafs were soaked in the iron acetate solutions for a few minutes, removed by the liquid surplus and dried in air (40°C) for several hours. The pre-treated leaf was then transferred in a crucible and heat-treated at 700°C under N_2 flow. An image of the leaf and corresponding SEM after the heat treatment is reported in figure 6.12.
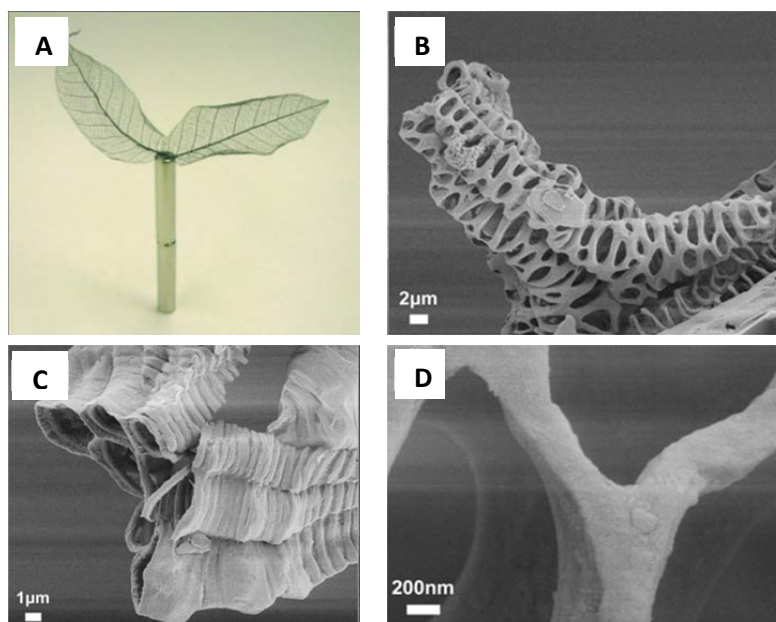

Figure 6.12. Digital photo and SEM images (different magnifications) of the *Ficus religiosa* replica. Adapted with permission from reference [262] (© 2010 Wiley-VCH Verlag GmbH & Co. KGaA, Weinheim).

From this figure it can be nicely observed that the leaf skeleton completely retained the network-like structure from the macroscopic down to the nanoscale (figure 6.12). On the other hand, the composition of the leaf is now completely changed and has been completely converted to a nanocomposite constituted exclusively of iron carbide, iron (minor phase) and carbon, as ascertained by XRD investigation (figure 6.13.A), which turn the leaf into a magnetic material (figure 6.13.B).
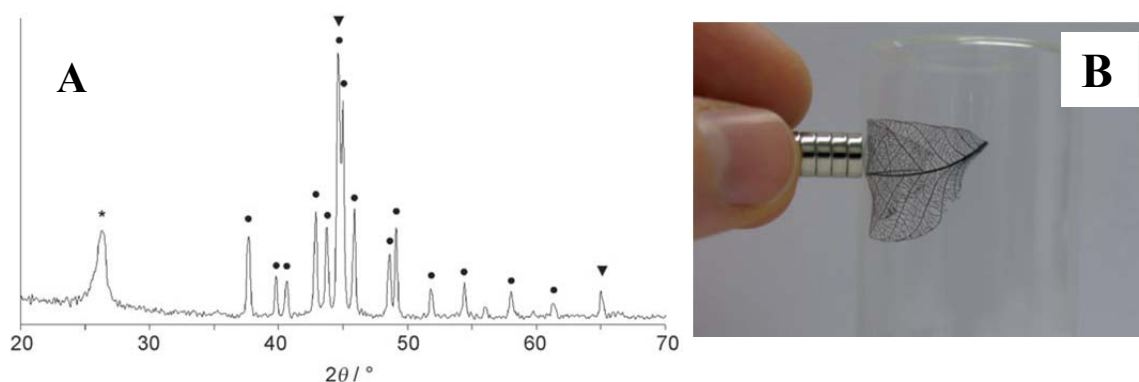
Figure 6.13. A) XRD pattern of the leaf after heat treatment at 700°C showing reflection of Fe_3C (•, ICDD 04-010-7474), Fe (▼, ICDD 04-008-1441), and graphite (*, ICDD 01-075-1621). B) digital photo of the magnetic leaf attached to an external magnet. Reprint with permission from reference [262] (© 2010 Wiley-VCH Verlag GmbH & Co. KGaA, Weinheim).

The magnetic leaf is not only a beautiful example of unconventional ceramic structure, but it is also a highly functional material. This intricate network can be used, for instance, as an electrode. A leaf is indeed an evolutionarily optimized structure, light and robust at the same time, gifted by an optimal system to transport nutrients. In the cyber-leaf metabolites can be substituted by electrons. The leaf´s potential as electrodes was demonstrated using the leaf in water splitting and metal deposition (platinum) test. The success of these experiments confirmed the homogeneity of the conducting network. In figure 6.14, two images of the water splitting experiment are reported. In figure 6.14.B the evolution of oxygen (bubbles) from the cyber-leaf can be nicely observed, in a sort of artificial photosynthesis process. The images of the leaf before and after the electrochemistry test are also reported in this figure. The leaf structure is unaffected, showing its robustness.
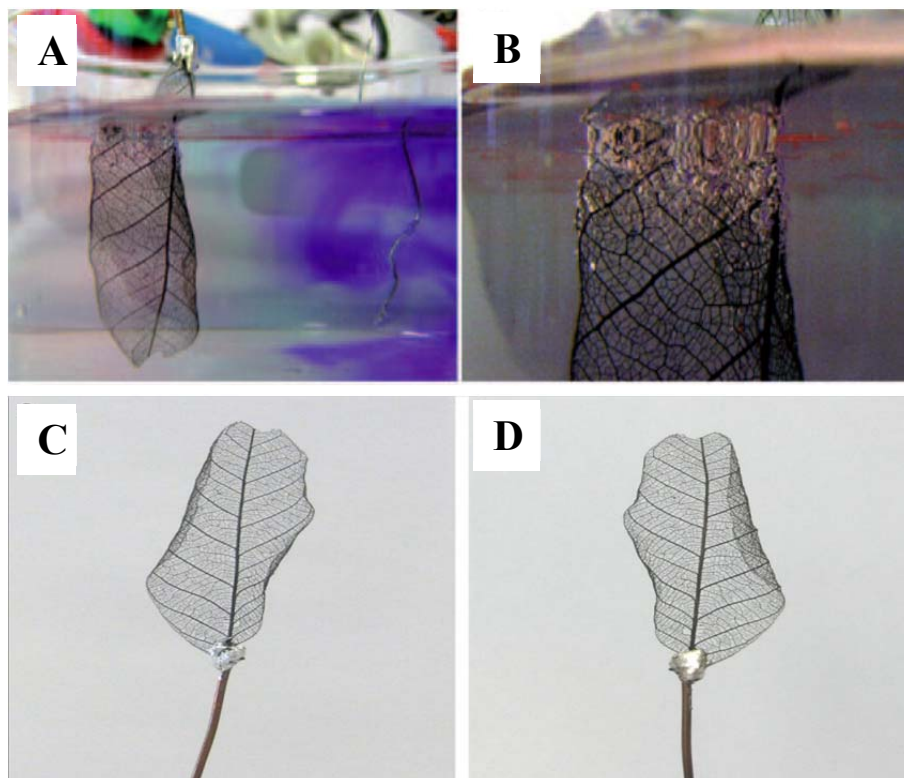
Figure 6.14. Application of the cyber-leaf as electrode in the electrolysis of water. A) The leaf and a Pt wire are immersed in an aqueous solution of sodium sulfate containing phenolphthalein and act as anode and cathode respectively. B) At the anode the oxidation of water takes place and oxygen is released as small bubbles. C-D) Photographs of the leaf before and after the electrolysis, respectively, showing the stability of the leaf structure (no changes are observed). Adapted with permission from reference [262] (© 2010 Wiley-VCH Verlag GmbH & Co. KGaA, Weinheim).

A similar approach can be used to template wood, which possesses intrinsic high porosity and is made of micro-sized channels, which makes this material especially interesting in applications based on diffusion and mass transport (such as filtration and gas separation). A piece of raw wood can be simply soaked with an iron nitrate aqueous solution and heat treated at 800°C under N_2 flow. SEM and TEM investigations confirm that the complex channels structure can be nicely replicated (figure 6.15).
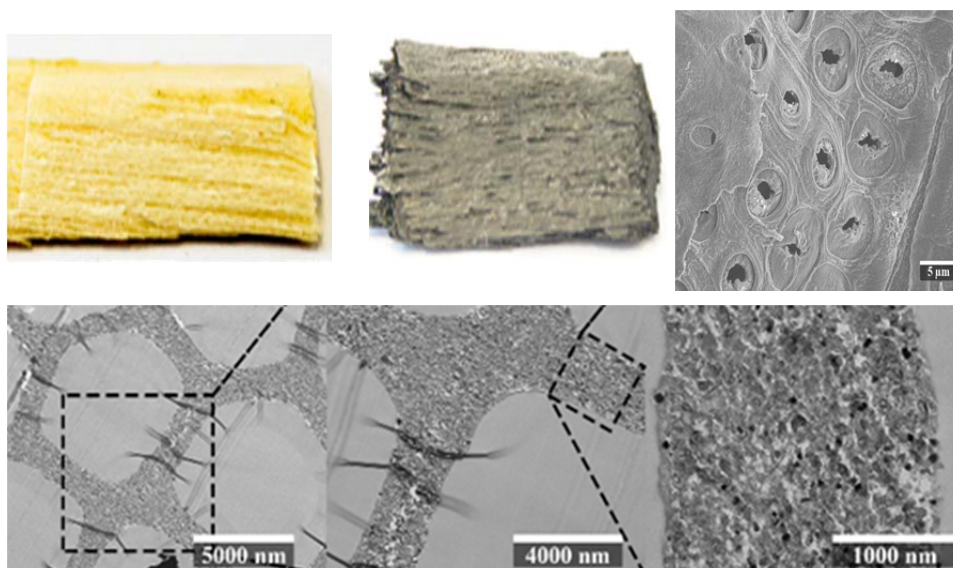
Figure 6.15. Piece of wood soaked with an iron/water precursor solution and then calcined under N_2. SEM (up) and TEM images (down) of the wood after calcination at different magnification, showing the conversion of the inner structure into a nanocomposite of iron carbide nanoparticles in a carbon matrix, as for the case of nanocomposite prepared with cellulose as C-source (see text for details).

6.5 Aerosol Spray Process [263]

As discussed in chapter 3, one of the most promising applications of MN/MC based systems is surely in the field of catalysis. Regardless whether they play the active phase or the catalyst support, one important prerequisite is a higher surface area. Obtaining material with high aspect ratio is surely one of the main reasons pushing researchers "to go to nano". However, for ceramics, due to their nature, a preparation of material with inherited porosity is not a trivial problem. Even though nanoparticle-based systems possess higher surface area (compared to the corresponding bulk phase), this does not always mean dealing with homogeneous porous distribution and/or homogeneous structure. This is especially true for MN/MC partially due to the relatively high temperature needed for their synthesis. For an ideal catalytic process, however, homogeneity can make the difference. To reach this target, the UGR was coupled with an aerosol spray technique, allowing the manipulation of materials otherwise not easily processable. Aerosol techniques have been currently used to produce porous and non-porous oxide particles [264, 265] but hardly applied to non-oxide ceramics. In this study, titanium nitride based material has been considered at first as model system, but the procedure can be extended to other materials as will be shown at the end of the section. Also in this route, the formation of a suitable starting complex is fundamental to get the right N/C ratio and to minimize residual products

(mainly oxygen). Interestingly, the woven porous final material is made of small nitride nanoparticles, with primary crystal size of ~6 nm, homogeneously loaded into a carbon matrix. As for the classical UGR, the first step is to prepare the precursor solution by mixing the metal source (namely titanium chloride) and urea (as nitrogen source) in a proper solvent. The solution is then sprayed to form an aerosol that is subsequently pyrolysed at different temperatures. After the pyrolysis step, the particles are collected on a filter and found to be made of an amorphous coordination "polymer" rich in carbon and nitrogen (a "glassy" phase). The "glassy" phase is then further heated under N_2 flow, up to 800°C. In scheme 6.3, a schematic representation of the spray process is reported.
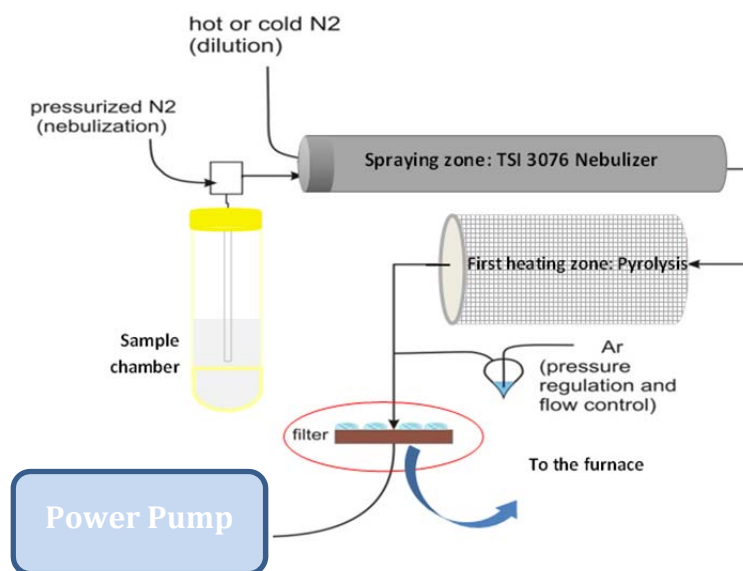
Scheme 6.3. The precursor solution made by dissolving $TiCl_4$ (1g) in dry acetonitrile (ACN, 50 mL) and adding 4,5-dicyanoimidazole (DI, 300 mg) and urea (300 mg), is stirred until complete dissolution of the solids, then injected in the sample chamber. The spraying gas is Argon at a flow rate of 2 L/min. The aerosol flow is carried through the spraying zone, where the droplets are pre-dried by natural evaporation. Finally, the particles enter a quartz tube furnace (first heating zone) heated to various temperatures. The residence time in the first heating zone is about 15s. After the spray pyrolysis, the particles are collected on a filter and heat treated in an oven under nitrogen at 800°C for 3h.

The second thermal treatment promotes the crystallization of the particles and releases a major part of the carbon, without affecting the original particle sizes, while carbon loss and density increase during the crystallization step, leading to the observed porous structure. Elemental analysis indicates a 50% mass loss (both in C% and N%) after the second step.

A scheme of the whole procedure is also reported in figure 6.13.
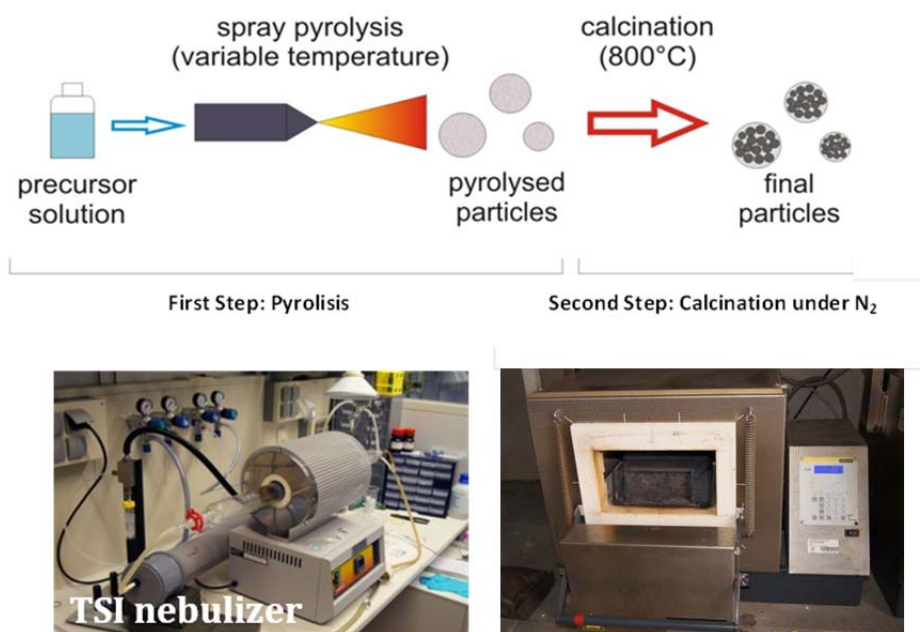
Figure 6.16. Steps of the aerosol process. Down the set-up is shown. The first heat treatment is made with a tubular oven under inert atmosphere, while the second heat treatment is made using a Nabertherm® furnace under N_2 flow.

However, a significant amount of oxygen and titanium oxide was found in the final product. To reduce this side phase, acetonitrile instead of ethanol can be used as solvent and di-cyanoimidazole, an oxygen-free nitrogen source, instead of urea as N-source. The addition of the aromatic heterocycle was found to be effective in reducing the amount of oxygen in the final product, however the formation of the nitride phase still gave unsatisfactory results (i.e. a mixture of titanium oxide and nitride was obtained). Following a strategy already reported for the synthesis of quaternary systems, the stratagem of coupling urea with DI turned out to be successful. The tandem work of urea, playing the N-source, and DI, sinking the residual oxygen (possibly serving as C-source, i.e. providing a higher reducing atmosphere) was found to be effective for obtaining amorphous intermediate species (after the first heat treatment, the pyrolisis step). The amorphous intermediate can be converted in the final crystalline nitride phase during the second heat treatment. It must be pointed out that the formation of TiN was never observed after the pyrolysis step probably because the residence time in the first "heating zone" (see scheme 6.3) is too short to allow its crystallization. On the other hand, a poorly crystallized

anatase phase is observed after pyrolysis. In figure 6.17 XRD patterns of the product obtained after pyrolis using urea, DI and both organic molecule (DI+Urea) are reported.
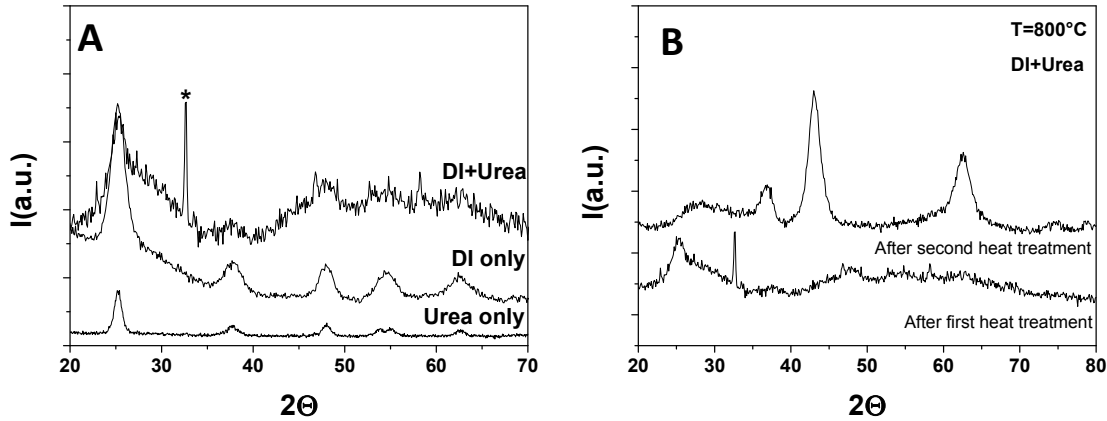
Figure 6.17. A) Comparison of the XRD pattern of products obtained after pyrolysis using urea, DI and Urea + DI respectively. B) Comparison of the product obtained using both DI and urea at 800°C, before and after calcination under N_2.

From these patterns it can be observed that after the calcination step (second heat treatment) and independent from the pyrolysis temperature, only one crystalline phase is present resembling the cubic structure expected for TiN, indicating that the amorphous carbon/nitrogen matrix has worked both as nitrogen source and reducing agent to convert the titanium oxide to nitride, as previously observed for the classical UGR.

TEM studies on samples after pyrolysis (i.e. the first heat treatment) show spherical and polydisperse particles (~100 nm in diameter), independently from the temperature used. The observed interplanar distances (~0.34 nm, measured on different spots) can only be tentatively attributed either to anatase (d_{101}= 0.35 nm) or to a nitrogen doped titanium oxide[31]. After the calcination step, TEM images visibly show a structure inside the aerosol sprayed spheres. A closer look could ascertain that the spheres are made of smaller nanoparticles, which are held together in the carbon matrix. Furthermore, the formation of interstitial void between the smaller nanoparticles is also observed. The void formation is due to the significant mass loss after the second heat step and the increase in density throughout crystallization. Therefore, porosity is created inside the aerosol spheres.

---

[31] The distance expected in case of presence of a rutile phase does not match (d_{110}= 0.32 nm).

Since it was expected that the pyrolysis temperature has influence on the porosity and/or surface area of the final material, samples were pyrolized at different temperatures and then calcined at a constant temperature (i.e. 800°C). This temperature is the lowest temperature at which a crystalline nitride product, free from oxide, is obtained. In figure 6.18, TEM images of the samples treated at different temperature are reported, while table 6.2 reports size and surface area of the corresponding samples.
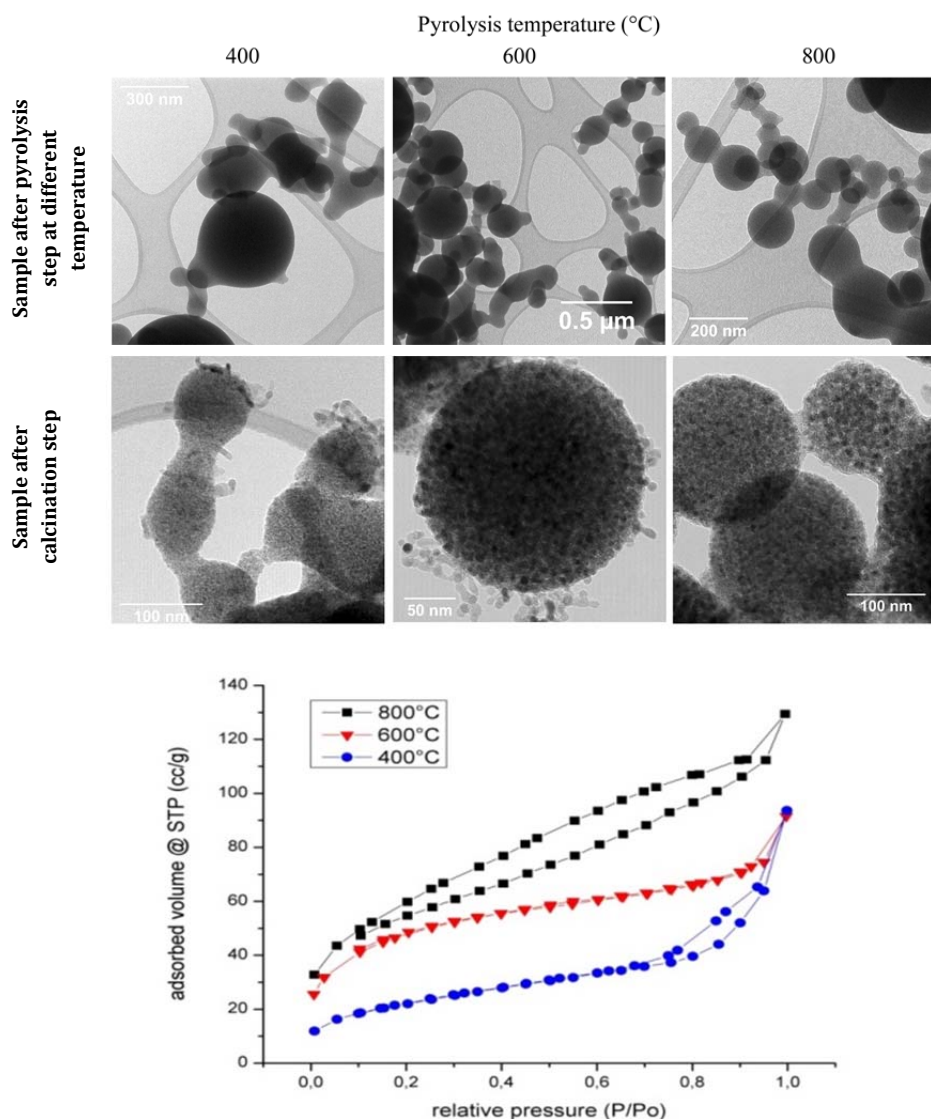
Figure 6.18. TEM images of the aerosol sprayed sample after the first (pyrolysis) and the second (calcination under N_2 flow) heat treatment. The N_2 physisorption curves obtained for samples pyrolized at different temperatures but calcined all at 800°C is also reported.

From table 6.2, it can be observed that crystal size is independent from the pyrolysis temperature (~6 nm in diameter), while, as mentioned above, the temperature of the second heating step has a significant effect on the final surface area.

Table 6.2. Experimental results overview of the aerosol sprayed sample.

Pyrolysis temperature (°C)	400	600	800
Average crystal size by TEM (nm)	~5	~6	~5
Average crystal size by Scherrer (nm)*	5.6	6.1	5.8
Surface area after calcination at 800°C (m²/g)	79	164	187
Pore volume after calcination at 800°C (cc/g)	$9.5 \cdot 10^{-2}$	$1.3 \cdot 10^{-1}$	$1.7 \cdot 10^{-1}$
*Eq. 4 section 4.1			

For all the prepared samples, surface area value is over 70 m²/g, confirming porosity inside the bigger particles[32]. Likely, the pyrolysis temperature influences the advancement of the organic precursor decomposition, which indirectly allows controlling the porosity of the produced particles. This effect can be attributed to the strong organic character of the particles obtained after the pyrolysis step. In each case, the final heat treatment allows rearrangements of the structure, but at lower temperatures the structure has a more organic character and the release of major part of carbon and nitrogen causes pore collapse and following sintering. On the other hand, for samples pyrolyzed at higher temperatures, the matrix has a stronger inorganic character. It is rather rigid, and during the calcination step, rearrangements are impaired by the carbon, which firmly holds the structure together, and keeps it when the matrix reacts. The pore size distribution (estimated by nitrogen physisorption technique) shows a pore size of 3-8 nm, as expected for the interstitial pores of nanoparticles with the described size.

---

[32] Non-porous spheres of the same size would have a surface area of 11 m²/g

In order to gain information about the reaction mechanism, the products obtained after the first heating step was analysed by IR. IR spectra recorded on samples treated at different temperatures are reported in figure 9.13 in appendix. These spectra show a progressive decomposition of urea and DI toward intermediate to cyanide and carbo-diimide products, which likely coordinate the titanium atoms (figure 9.13 and reference [263]).

As mentioned above, the process can be used for the preparation of other porous metallic ceramic, e.g. VN and W_2N. In these cases, vanadium oxy-trichloride and tungsten(IV) chloride have been sprayed, under the same conditions used for the titanium precursor. Spraying and pyrolysis was done at 600 °C, and the final heating treatment performed at 800°C. The XRD showed that in both cases the nitrides of the respective metals are obtained (Figure 6.16).

A
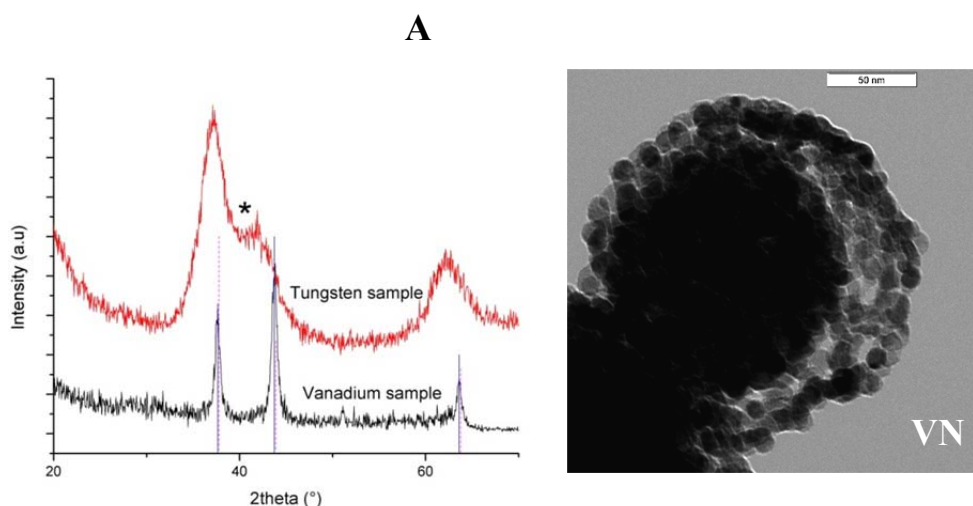
Figure 6.19. XRD patterns of vanadium nitride and tungsten nitride produced by aerosol synthesis. Reference patterns of expected VN (as continuous line, ICDD 00-035-0768) and W_2N (as dotted line, ICDD 00-025-1257) are also reported. Marked peak (*) is tentatively attributed to W_2C. B) TEM image of the VN sample prepared via aerosol spray process.

7. Testing

A chapter about possible applications is a suitable end for this long path through the world of metallic ceramics, which started by presenting their properties, discussing classical and novel synthetic pathways, encompassing simple and less simple ways to shape them into functional materials. Not by chance, the *Leitmotiv* of this research was "*simplicity*". A revolutionary material produced in negligible amounts has the same applicative importance as massive amounts of a material with no functionality. Their contribution to society will be the same: none. Therefore, reproducibility and scalability are of utmost importance.

In this final chapter, an overview of applications of some of the systems presented in previous chapters will be given. It is important to stress that each performed test represents a "*model test*" and further investigations must be undertaken to optimize both material and reaction conditions.

The tests are divided in categories and the following sessions will be devoted to:

1) Applications related to environmental issues.

2) Catalytic applications.

3) Battery applications.

7.1 Applications for Environmental Issues

$Fe_3C@C$ and $Zn_{1.7}GeN_{1.8}O$ prepared via the cellulose routes (section 4.3) and the UGR (section 4.1) respectively, were tested as wastewater filters and in the degradation of organic dyes.

Filtration of pollutants [231]

$Fe_3C@C$ filtration capabilities were tested, using methylene blue (MB) and methyl orange (MO) in aqueous solutions as model systems, while a mixture of heptane and water was used for the *oil-from-water* separation. A fast and efficient dye uptake was observed, also due to the high surface area of the material, with filtration performances comparable to that of commercial activated carbon (e.g. 165 mg MB per g nanocomposite vs 220 mg MB per g of carbon). Some steps of the filtration process are reported in figure 7.1 together with the photospectrometric analysis of the same samples. Thanks to the magnetic nature of the nanocomposite, both removal and recovery of the filtrating agent are simple and fast. Also the recovery of the MB from the composite can be simply made by washing the loaded nanocomposite with alcohol. For comparison, a "white test" was also performed by adding pure powdered (non-calcined) cellulose to 125 mg/L of MB aqueous solution. This test led to no change, proving that the nature of the final nano-composite itself is the crucial factor for this property to emerge.
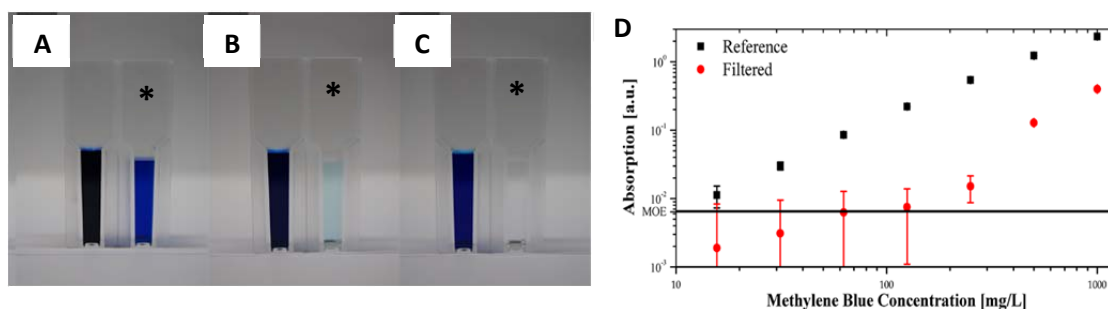
Figure 7.1. A-C MB stock solutions (dark blue) of 500, 250 and 125 mg/L MB and corresponding solution treated with 5 mg of the nanocomposite (*). D) Photospectrometric analysis of the samples.

To ensure that the filtration is not based merely on electrostatic interaction, experiments were repeated with the anionic dye methylene orange (while MB is cationic), leading to similar results. To ensure that the colour change is not

due to pH variations, the pH was tested before and after the filtration process, giving a constant value of 7.
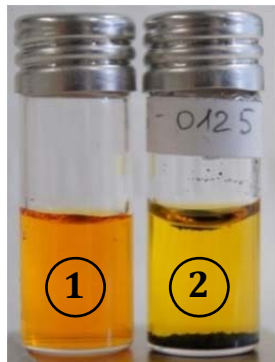
Figure 7.2. Stock solution containing 500 mg/L MO (orange, 1) and the corresponding filtered solution (yellow, 2).

The Fe₃C@C nanocomposite was also tested as oil-recovering agent (figure 7.3). It was indeed already shown that magnetic powders in oil spillages present several advantages compared to classic washing with surfactants: their action is faster, less stressful for the wildlife and easier to be removed [266, 267]. For this test, 5 mg of the nanocomposite was added to the mixture of heptane and water (0.5 mL of each).
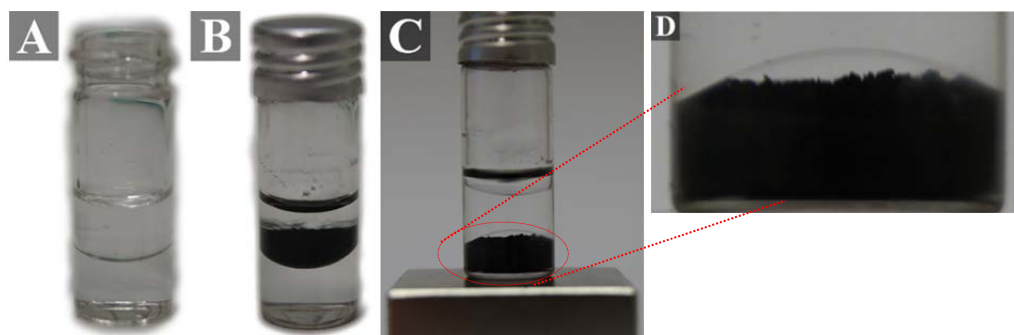
Figure 7.3. (A) Starting heptane/water mixture. (B) Mixture after the addition of the nanocomposite. (C) Vial with the mixture is placed on an external magnet. The nanocomposite loaded with the heptane phase is pushed to the bottom of the vial.

Immediately after mixing, the nanocomposite uptakes the organic phase almost completely. The fact that the nanocomposite can be completely removed with a magnet in a final step makes this material more interesting than activated carbon, because in the latter case the problem of removing the finely dispersed powder after pollutants uptake represents an issue itself. The mechanism

behind the filtration ability of the iron carbide nanocomposite must still be clarified.

Degradation of pollutants [162]

$Zn_{1.7}GeN_{1.8}O$ was tested as photo-catalyst for the degradation of rhodamine B (a model system miming water pollution), under Hg-lamp irradiation. The photo-catalyst powder was added to an aqueous dye solution (5 ppm rhodamine B in 50 mL water) and placed under the lamp. At regular intervals (~1h), a portion of the mixture was taken, separated from the powder by centrifugation and analysed by UV-Vis spectroscopy (figure 7.4).

The calculated reaction constant was 0.14 h^{-1}, assuming first order reaction kinetics [268]. It is worth to mention that the exposure to water and UV-light for several hours did not affect catalyst stability, as shown from the comparison of XRD pattern of the sample before and after testing (see Figure 7.4B).
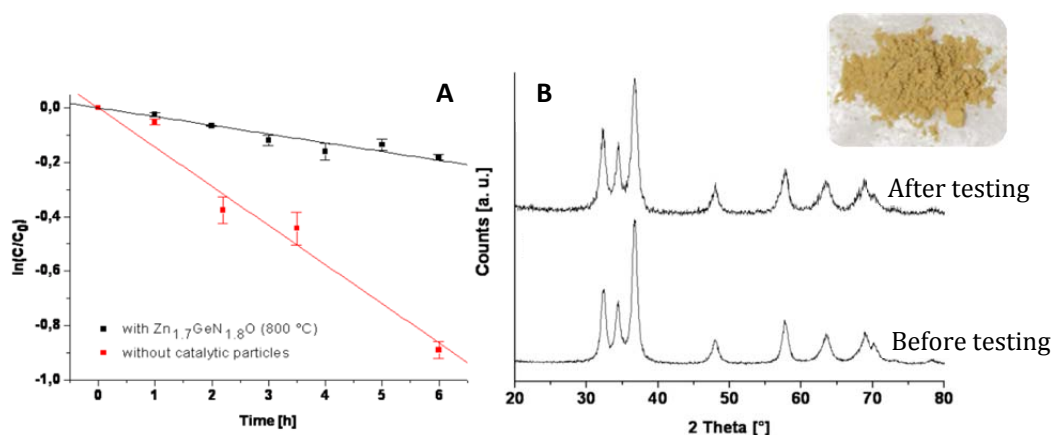
Figure 7.4. Photocatalytic degradation of rhodamine B. A) Plot of log(C/C$_0$) over the time in hours (C$_0$ is the initial concentration). B) XRD patterns of the powder sample (in the inset a digital photo) before and after the catalytic test. Both show the typical reflexes of $Zn_{1.7}GeN_{1.8}O$ (ICDD 00-024-1443). Adapted from reference [162] by permission of the Royal Society of Chemistry.

7.2 Applications as catalysts

As discussed in chapter 3, many MN/MC possess catalytic activities, in some cases showing isoelectronic structure with Pt group elements. They are thus considered a cost-effective alternative to noble metals. However, finding alternative catalysts is not just a cost-related issue. Waste and related environmental problems should be also considered, including groundwater contamination and toxic gas emissions (e.g. Cl_2, HCl, NH_3, SO_2) etc. In this respect, a further advantage of using MN/MC based catalysts concerns their relative high resistance towards poisoning. This is especially important in the field of oil refining and petrol-chemistry, due to the nitrogen- and sulphur-rich feedstock.

The use of early-transition-metal carbides and nitrides in catalysis for heavy industrial processes (e.g. hydroprocessing) is well-known. Surprisingly, though, not the same effort has been made for testing their activity in fine chemical synthesis, such as, for instance, ammonia decomposition, epoxidation reactions, the use of alcohols as alkylation agents (a typical green chemistry issue), activation and conversion of alcohols, hydrogenolysis and hydrogenation reactions, etc., all reactions typically catalysed by noble metals (see also table 3.3 in chapter 3).

The use of MN/MC in these processes will be discussed in the following. All tested catalysts were prepared with the routes described in chapter 4.

Details related to these reactions and corresponding results (overview) are reported in table 1 and 2, respectively.

Table 7.1. Overview of the tested reactions.
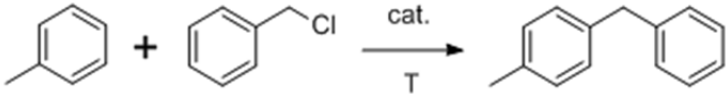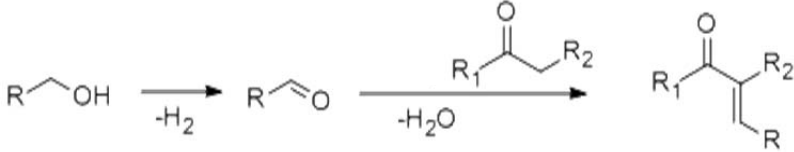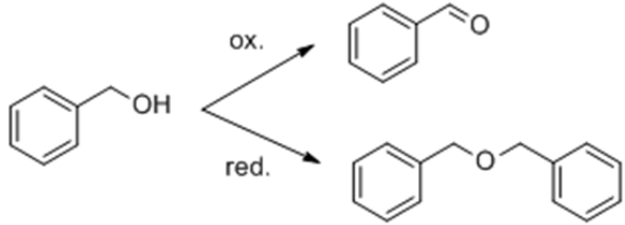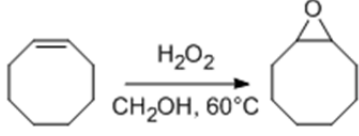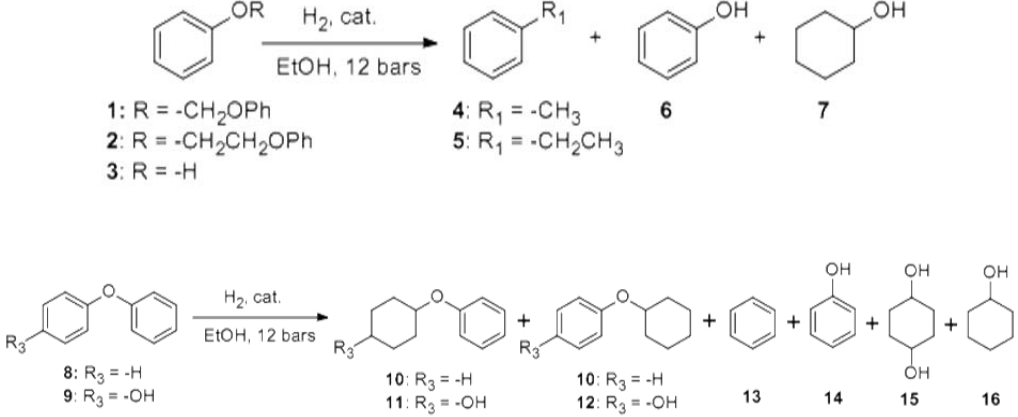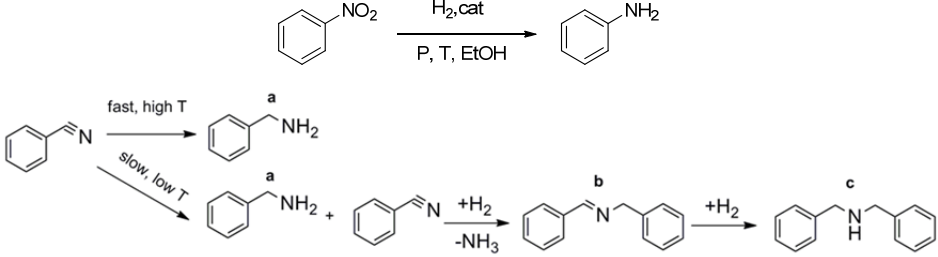
	Reactions	
1	Ammonia decomposition	$2NH_3 \rightarrow 3H_2 + N_2$
2	Alkylation Reaction	
3	Activation of alcohols	
4	Conversion of alcohols	
5	Alkene Epoxidation	
6	Hydrogenolysis of Aryl Ethers	
7	Hydrogenation Reactions	

Table 2. List of the tested catalysts and some experimental conditions and results

Catalyst*	Reactions (see table 1)	SSA m²/g	Conversion (%)	Temperature (°C)
mp-Fe$_3$C	1	145	95	700
np-Fe$_3$C	1	58	50	700
Mo$_2$N	1	68	100	650
	3	12	30	150
Mo$_2$C	1	13	92	650
	3	10	94	150
	4	25	85	100
W$_2$N	1	64	100	700
	3	64	100	150
WC (W$_2$C)	1	31	80	700
	3	84	100	150
	4	78	62	100
Fe$_3$N	1	39	100	800
Mn$_{0.75}$Fe$_{2.25}$C	2	194	98	110
TiN	3	200	95	150
NbN	3	23	90	150
NbC$_x$N$_{1-x}$	3	140	15	150
TaON	5	20	96-97	60
Ta$_3$N$_5$	5	20	96-99	60
TiN@Ni	6	116	100	125-150
Ni$_3$N	7	20	100	75

*The synthesis of these materials has been reported in chapter 4 (see table 4.1 for synthetic details).

i.i Ammonia decomposition [214] [215]

Ammonia decomposition (table 7.1, entry 1) is an industrial process that has attracted increasing attention for clean-up of syngas from coal [269], biomass gasification [270] and, most importantly, for on-site production of CO_x-free hydrogen for fuel cell applications [271]. Several metal nitrides and carbides (Mo_2N, Mo_2C, W_2N, WC/W_2C, Fe_3N, mp-Fe_3C, np-Fe_3C) were tested as catalysts for this decomposition and results are summarized in figure 7.5.
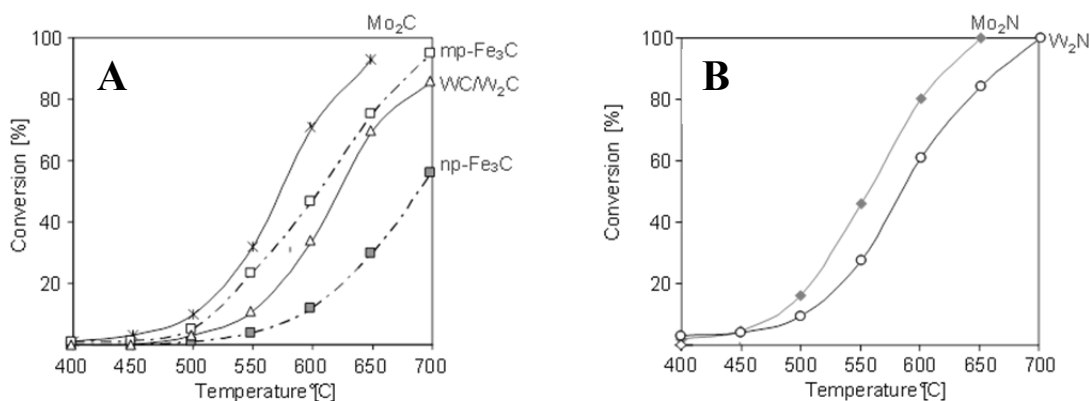
Figure 7.5. Catalytic activity of the different carbide (A) and nitride (B) materials in ammonia decomposition as a function of reaction temperature (GHSV = 15 000 cm^3 g_{cat}^{-1} h^{-1}, 25 mg catalyst).

From these figures it can be seen that all tested materials led to an ammonia conversion above 50% for a reaction temperature of 650°C. Mo_2N appears to be the most active material, reaching 100% conversion, followed by Mo_2C with 92% conversion at the same temperature, then WC/W_2C and mp-Fe_3C with 70 and 75%, respectively. Overall, the activity decreases in the order Mo_2N > Mo_2C > W_2N > mp-Fe_3C > WC/W_2C > np-Fe_3C, suggesting a higher activity for the nitrides than the carbides. However, a strong influencing factor seems to be the specific surface area of the material. In this study, two iron carbides were tested (both prepared by the UGR), namely mere spherical nanoparticles (np-Fe_3C, with SSA=58 m^2/g) and the mesoporous phase (mp-Fe_3C, SSA=145 m^2/g), showing a significant difference in catalytic activity, i.e. the ammonia conversion increased from 30% to about 75% at (650°C). Furthermore, the mp-Fe_3C reaches comparable ammonia conversion at lower temperature than np-Fe_3C [135]. This finding opens new rooms for the optimization of these catalysts, e.g. by structural modifications, by increase of porosity and/or surface area, also by proper dispersion of the active phase on suitable high surface area supports.

In Figure 7.6 the ammonia conversion over of the most promising carbides and nitrides at 600°C during a 16h time-on-stream is reported, showing stable catalytic activities for all materials. Only the WC/W_2C system displays a slight decrease of the catalytic activity, while, on the other hand, all the other systems do not show significant changes over time. Surprisingly the W_2N even shows an increase in its activity, from 55% to 61% of ammonia conversion.
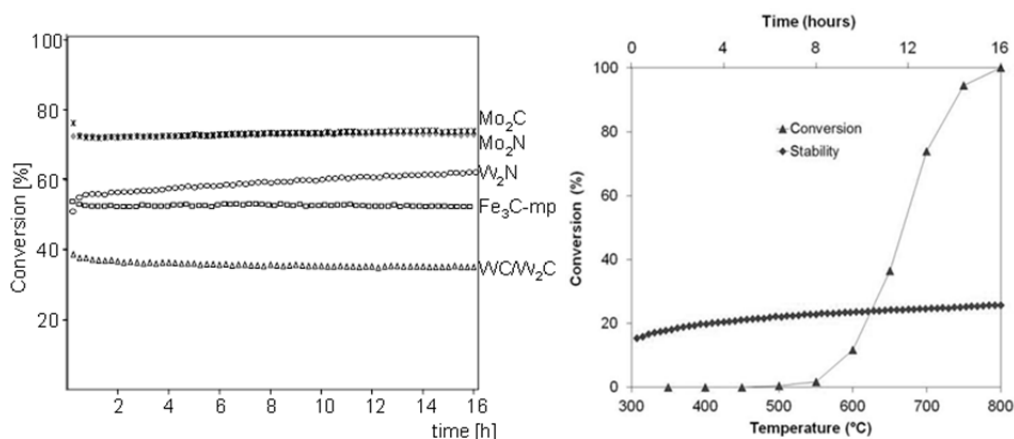
Figure 7.6. A) Stability of the catalytic activity of molybdenum and tungsten carbides and nitrides in NH_3 decomposition at 600°C (GHSV = 15 000 cm^3 g_{cat}^{-1} h^{-1}). B) Catalytic activity of Fe_3N as a function of reaction temperature (GHSV = 15 000 cm^3 g_{cat}^{-1} h^{-1}, 25 mg catalyst) and corresponding stability of the catalytic activity in NH_3 decomposition at 600°C (GHSV = 15 000 cm^3 g_{cat}^{-1} h^{-1}).

Despite the stable, or even increased catalytic activity exhibited by the tested materials, XRD studies performed after testing show that the carbide phases are converted into nitrides during the ammonia decomposition, while nitrides are converted into even N-richer phases (data not shown).

Since it was found that Fe_3C converts into the nitride, pure Fe_3N (prepared as reported in section 4.2) was also tested. Its temperature dependent activity is reported in figure 7.6. The decomposition reaction starts at about 500°C and it is completed with 100% conversion at 800°C [215].

This study shows that although MN/MC are not yet competitive compared to highly active supported ruthenium catalysts, there is surely room for improvements. These first results can be then considered already promising, above all for Mo_2C and W_2N, which have shown both high activity and higher stability. Besides, the lower costs of these systems, together with the easiness of the synthetic route and the usage of readily available precursors must also be considered.

i.ii Alkylation reaction [229]

Catalytic activity of $Mn_{0.75}Fe_{2.25}C$ prepared via the sugar route (chapter 4.3) using cellulose as C-source was tested in the alkylation reaction of toluene with benzyl chloride toward benzyl toluene (Table 7.1, entry 2), and the corresponding results are shown in table 7.3.

Table 7.3. Results of the catalytic alkylation of toluene with benzyl chloride using $Mn_{0.75}Fe_{2.25}C$ (110°C).

Time	Conversion (%)	Selectivity (%) benzyl toluene		
		meta	ortho	para
30 min	-	-	-	-
60 min	18	9	42	49
90 min	22	8	43	49
120 min	27	9	43	48
180 min	38	7	43	50
4 h	54	7	44	49
6 h	79	6	45	49
9 h	98	6	45	49
24 h *(blank)*	5	10	40	50

From this table, it can be seen that in absence of catalysts, only 5% of conversion was observed over 24 hours. In contrast, in presence of the catalyst (100 mg), full conversion is reached within 9 h [229].
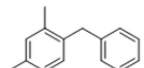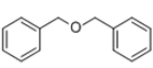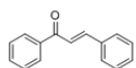
The same reaction was also tested under microwave irradiation, showing a 95% conversion within 10 minutes. Remarkably, 80% selectivity toward the meta-product (the thermodynamically not favoured product) was observed in this case. The reaction mechanism is currently under investigation.

i.iii Activation of alcohols [272]

TiN, NbN, Mo_2N, W_2N, NbC_xN_{1-x}, Mo_2C and WC were tested in alkylation reactions with alcohols (table 7.1, entry 3) using benzyl alcohol and acetophenone in xylene as a solvent [272]. TiN, NbN and NbC_xN_{1-x}, catalysed the formation of 1,3-diphenyl propenone, while Mo_2N, W_2N, Mo_2C and WC brought to Friedel-Crafts reactions of

benzyl alcohol on xylene. TiN shows the highest activity, with almost 90% yield[33]. Mo_2N, W_2N, Mo_2C and WC were also investigated in Friedel-Crafts-type alkylation of aromatics. It was found that, depending on the metal used, high selectivity is achieved for the alkylation of ketones or the alkylation of aromatics [272].

Table 7.4. Detailed analysis of the reaction mixtures obtained from benzyl alcohol and acetophenone at 150°C after 20 h. Reprint with permission from reference [272] (© 2009 Wiley-VCH Verlag GmbH & Co. KGaA, Weinheim).

Catalyst	Conv. (%)[*]	Results (%)			
TiN	95%	x	x	5%	94%
NbN	90%	x	x	17%	83%
Mo_2N	30%	20%	64%	14%	X
W_2N	100%	x	94%	x	6%
NbC(N)	15%	x	x	37%	63%
Mo_2C	94%	x	88%	11%	X
WC	100%	x	80%	20	X

[*] Amount of formed products as compared to the initial amount of benzyl alcohol (estimated by GC-FID)

TiN, NbN and NbC_xN_{1-x}, (Table 7.4) show strong tendency to 1,3-diphenyl-1-propanone. The most active and selective compounds toward Friedel-Crafts alkylation of xylene were W_2N, WC and Mo_2C, while Mo_2N, surprisingly the less active, only led to a complex reaction mixture.

i.iv Conversion of Alcohols [273]

Mo_2C and WC nanoparticles were also tested in the oxidation of benzyl alcohol in liquid phase, an important process in green chemistry (table 7.1, entry 4). Interestingly, tuneable selectivity was observed, depending on the reaction media.

---

[33] It was found to be even more active than TiN produced with higher surface area through similar route, showing higher yields in less than half of the reaction time, probably due to its high purity.

At first, tests were made in absence of solvent, with an amount of catalyst of 0.1% mol compared to the starting material. A comparison with the catalytic activity of platinum and ruthenium (classical catalysts for this reaction) is reported in figure 7.7.
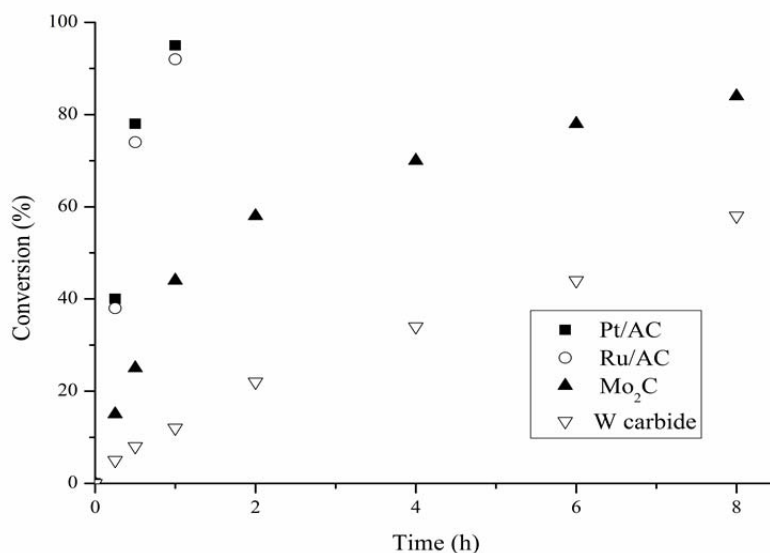
Figure 7.7. Catalytic activity of Mo_2C, WC, Pt/AC and Ru/AC in the solventless benzyl alcohol oxidation (T= 100 °C, P_{O2}=2 atm). Reprint with permission from reference [273] (© 2013 American Chemical Society).

After 10h a conversion of 85% and 62% for Mo- and W- carbide, respectively, was observed. Mo_2C presented higher initial activity than WC but undergoes deactivation. The noble metals reach almost full conversion after 2 h, showing a higher activity, but the much lower cost of carbides (10 times lower compared to noble metals) makes these results very promising. XRD study performed on the samples after catalysis shown that in the WC pattern, W_2C (a side product) disappears [273]. However, since no deactivation was observed for this material, it can be safely said that only the mono-carbide is the active phase. Furthermore, recycling reactions made with WC confirmed the stability of this catalyst under the tested reaction conditions [273]. Concerning the XRD pattern of Mo_2C after catalysis, a clear change phase was observed, with the formation of oxo-complexes. This conversion might then be responsible for the deactivation of molybdenum catalysts during the reaction. To ascertain that Mo_2C is in any case the only active phase, the activity of commercial molybdenum oxide (MoO_3) was also tested, showing a very low activity [273].

Surprisingly but more interesting, selectivity of the carbides is different than that of the tested noble metals (Table 7.5). For both catalysts, selectivity is addressed to benzyl ether formation (70−72%).

Table 7.5. Selectivity in the solventless benzyl alcohol oxidation. Reprint with permission from reference [273] (© 2013 American Chemical Society).

Catalyst	Selectivity at 60% conversion				
	Toluene	Benzaldehyde	Benzoic acid	Benzyl benzoate	Benzyl ether
W carbide	2	19	4	5	70
Mo carbide	1	18	3	6	72
Pt/AC	15	70	3	11	1
Ru/AC	12	74	7	7	0
Reaction conditions: solventless, alcohol (10g)/metal, 1000/1, T = 100°C, pO$_2$ = 2 atm					

On the other hand, when cyclohexane was used as a solvent, a drastic change in the selectivity was observed (table 7.6): up to 93% selectivity to benzaldehyde was reached, while the production of benzyl ether is avoided.

Table 7.6. Effect of solvent. Reprint with permission from reference [273] (© 2013 American Chemical Society).

Catalyst	Selectivity at 60% conversion				
	Toluene	Benzaldehyde	Benzoic acid	Benzyl benzoate	Benzyl ether
W carbide	-	90	4	6	-
Mo carbide	1	93	3	3	-
Pt/AC	4	90	2	4	-
Ru/AC	2	89	5	4	-
Reaction conditions: benzaldehyde/cyclohexane 25/75, alcohol/metal, 1000/1, T = 100°C, pO$_2$ = 2 atm					

Under the same conditions, Pt and Ru show a selectivity up to 90% to benzaldehyde. This finding would suggest that the MCs nicely act as *bifunctional* catalysts, where possibly acidity surface of these materials can play an important role[34]. This also means that choosing proper experimental conditions, they can be considered promising alternative to more expensive noble metal catalysts.

---

[34] The generated pH of the metal carbides was calculated to be 2.8 and 3.2 for Mo and W carbide, respectively.

i.v Alkene Epoxidation [158]

TaON and Ta$_3$N$_5$ nanoparticles were tested in cyclooctene epoxidation (table 7.1, entry 5) [158], since epoxides are important intermediates, e.g. in polymer synthesis [274]. For comparison, the activity of tantalum oxide nanoparticles of comparable size and surface area (20 nm in diameter and 20 m^2/g) were also tested. Results are summarized in the table 7.7.

Table 7.7. [158]

Entry	Catalysts	Conversion (%)	Selectivity (%)
1	Ta$_2$O$_5$[a]	57.1	95.9
2	TaON	96.8	96.1
3	Ta$_3$N$_5$	99.0	85.4
4	Blank test	12.8	99.0

[a]Ta$_2$O$_5$ prepared via traditional reverse homogeneous precipitation [158].

The Ta$_2$O$_5$ NPs exhibit lower conversion (57.1%) compared to TaON (96.8%) and Ta$_3$N$_5$ (99.0%). Considering that all systems possess similar surface area, the higher activity of TaON and Ta$_3$N$_5$ can be attributed to an increased electron density on the metal, due to the presence of the nitrogen atom(s) [158]. In fact, the activity of Ta in this reaction is associated with the formation of a [Ta$^{\cdot}$O*] intermediate, which reacts with the alkene to form the epoxides. The activity can then be improved with a more effective electron-donor ligands around Ta atom [275,276]. The N atoms in TaON and Ta$_3$N$_5$ can promote the O* transfer from [Ta$^{\cdot}$O*] to cyclooctene, thus improving the activity (Step I in Scheme 7.1).
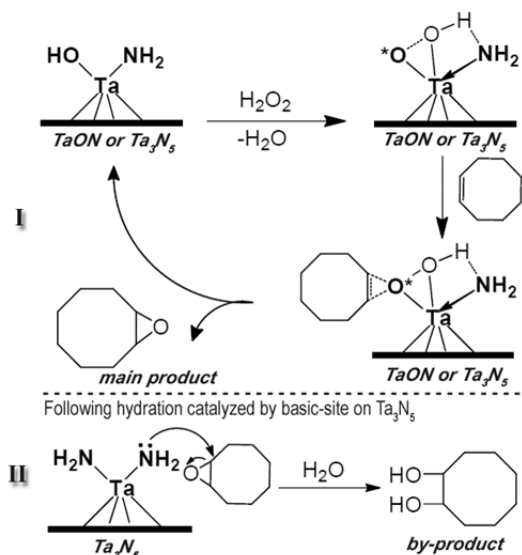
Scheme 7.1. Schematic illustration for (I) epoxidation of cyclooctene by TaON and Ta_3N_5 NPs, and (II) overreaction to diol-products catalysed by basic-site on Ta_3N_5. Adapted with permission from reference [158] (© 2012 Wiley-VCH Verlag GmbH & Co. KGaA, Weinheim).

.

The presence of nitrogen also affects selectivity. Ta_2O_5 and TaON exhibit high selectivity (95.9% and 96.1%, respectively), while Ta_3N_5 has reaches 85.4% only (Table 7.7). In fact, GC-MS study show that the product catalysed by Ta_3N_5 also contains a ~20% of cyclooctane-(di)ol [158], possibly as overreaction products, indicating the formation of these products [277]. Considering the lower electronegativity of N over O, a higher basicity of the catalyst can be expected when enough N is introduced [278], as for the case of Ta_3N_5. With the hydration of as-formed epoxide catalysed by base sites, the decreasing epoxidation selectivity is showed by Ta_3N_5 (Step II in Scheme 7.1).

In simpler words, the introduction of nitrogen atoms modifies the basicity of the nanoparticles, affecting the selectivity and improving activity over the pure tantalum oxide.

i.vi Hydrogenolysis of ethers [279]

Ni@TiN nanocomposite was tested for hydrogenolysis of aryl ethers (table 7.1, entry 6), as model molecules of lignin structure. The nanocomposite activity was compared to that of pure nickel and pure TiN separately.

Ni@TiN was obtained mixing TiN (prepared accordingly to the UGR) with an alcoholic solution of nickel acetate tetrahydrate, followed by solvent evaporation.

The resulting homogeneous bronze mixture was calcined under nitrogen at 500°C, leading to the final nanocomposite of Ni@TiN [279]. XRD pattern of the as prepared nanocomposite is reported in figure 7.8. The patterns of pure TiN and Ni are also reported for comparison. The simultaneous presence of nickel and titanium in the nanocomposite was confirmed by EDX investigation [279].
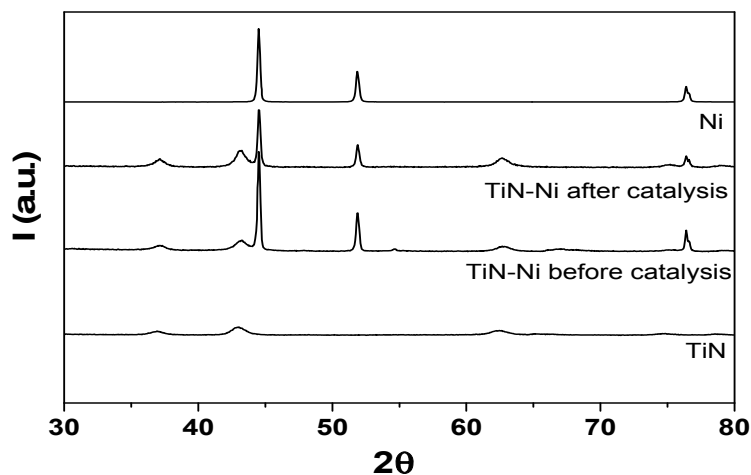
Figure 7.8. XRD patterns of the TiN@Ni nanocomposite before and after the catalytic test (see text for details. The patter of the pure TiN and pure Ni are also shown for comparison.

Catalytic tests show that the presence of TiN enhances the activity of nickel. A comparison of this material with pure TiN and pure Ni nanoparticles for the same reactions was also performed. Results are summarized in Table 7.8 and 7.9. TiN@Ni composite shows superior activity compared to the systems separately and leads to full conversion also toward diphenyl ether. On the contrary, TiN alone shows no activity for this reaction, while Ni particles possess only low activity for the cleavage of ether bonds.

1: R₁ = -CH₂OPh   **4**: R₂ = -CH₃
2: R₁ = -CH₂CH₂OPh   **5**: R₂ = -CH₂CH₃
3: R₁ = -OH
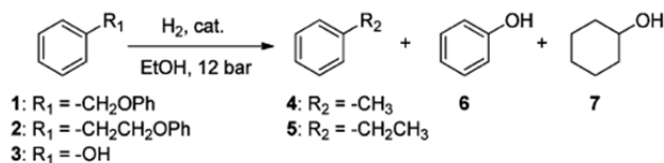
Table 7.8. Adapted with permission from reference [279] (© 2014 American Chemical Society).

Entry	Cat.	Substrate	T[°C]	Conversion[c] [%]	Selectivity [%] [c]				Productivity
					4	**5**	**6**	**7**	[mmol h^{-1} g$_{cat}^{-1}$]
1 [a]	TiN	1	150	0	-	-	-	-	-
4 [a]	Ni	1	150	90	57	-	43	-	0.962
6 [a]	TiN-Ni	1	125	>99	54	-	46	-	1.013
7 [a]	TiN	2	150	0	-	-	-	-	-
8 [b]	Ni	2	150	0	-	-	-	-	-
10 [b]	TiN-Ni	2	150	>99	-	54	-	46	0.608
11 [b]	TiN-Ni	3	150	55	-	-	-	100	0.620

Conditions: 0.05M solution of starting material in EtOH, 12 bars (a). 0.5 mL min^{-1}.
[b] 0.3 mL min^{-1}. (b) Determined by GC-MS analysis (c).

8: R₃ = -H   **10**: R₃ = -H   **10**: R₃ = -H
9: R₃ = -OH   **11**: R₃ = -OH   **12**: R₃ = -OH
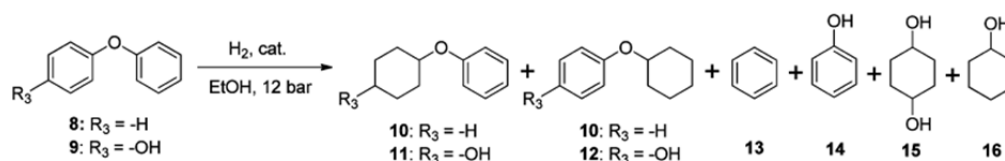
Table 7.9. Adapted with permission from reference [279] (© 2014 American Chemical Society).

Entry	Cat.	Substrate	T[°C]	Conversion [%][c]	Selectivity [%] [c]							Productiv.
					10	**11**	**12**	**13**	**14**	**15**	**16**	[mmol h^{-1} g$_{cat}^{-1}$]
12[a]	TiN	8	150	0	-	-	-	-	-	-	-	-
13[a]	Ni	8	150	<5	-	-	-	-	-	-	-	-
15[b]	TiN-Ni	8	150	99	5	-	-	46	-	-	49	0.259
16[b]	TiN-Ni	9	150	65	-	22	-	49	-	25	4	0.179

Conditions: 0.025M of starting material in EtOH, 12 bars. (a) 0.5 mL min^{-1}. (b) 0.3 mL min^{-1}. (c) Determined by GC-MS analysis

The promising results of Ni@TiN activity lead us to believe that the conversion of real lignin samples might be possible with MN/MC based systems, when properly alloyed.

i.vii Hydrogenation reactions [240]

The catalytic activity of nickel nitride nanocomposites have been studied for hydrogenation reactions, where usually noble metals are employed. Being thermo labile, the stability of the as prepared Ni_3N was at first tested under the reaction conditions (up to T=100°C), showing no changes (as ascertained by XRD and EA investigations) [240].

The $Ni_3N@C$ prepared by the UGR (see table 4.1 and chapter 5 for synthetic details) was tested for the hydrogenation of nitrobenzene, benzonitrile and 4-nitroacetophenone (table 7.1, entry 7) showing good catalytic activity at low temperature for all tested reactions. For comparison, $Ni@C$ nanocomposite was also tested in the same reactions and conditions. The $Ni@C$ sample was also prepared via the UGR, calcining the "gel" precursor to higher temperature (T>400°C). At this temperature the Ni_3N decomposes bringing to pure Ni [280].

Interestingly, it was found once more that nickel nitride has a different selectivity than nickel. Experiments on nitro-benzene show that Ni_3N has similar activity as Ni, while the hydrogenation of alkene (namely cyclohexene) was not achieved with the nitride. Of more interest for the hydrogenation of nitrile groups, a completely different behaviour between Ni_3N and Ni was observed, which leads to different products. The nickel nitride affords a full conversion of the benzonitrile already at low temperatures, leading to the formation of dibenzylimine. On the contrary, metallic nickel in the same condition does not catalyse the reaction. At higher temperature, the amine is the main product, probably due to the fast ratio of the reaction. With the nickel catalyst, amine formation was never observed. An overview of the obtained results is reported in table 7.10. In figure 7.9 the XRD patterns of the sample before and after catalysis are reported.

Table 7.10. Hydrogenation products for several substrates catalysed by Ni$_3$N@C and Ni@C. a, b and c represent benzylamine, dibenzylimine and dibenzylamine, respectively (see table 1 entry 7) [240].

Substrate	Catalyst	F (mL.min^{-1})	T (°C)	X (%)	S		
Nitrobenzene	Ni	0.5	50	>99	Aniline		
	Ni$_3$N	0.5	75	>99			
p-Nitroacetophenone	Ni	0.3	75	>99	4-Aminoacetophenone		
	Ni$_3$N	0.3	75	>99			
Cyclohexene	Ni	0.3	25	>99	Cyclohexane		
	Ni	0.5	50	90			
	Ni$_3$N	0.5	50	0			
	Ni$_3$N	0.5	75	<10			
					a	b	c
Benzonitrile	Ni	0.3	55	0	-	-	-
	Ni	0.5	75	48	-	92	8
	Ni	0.5	135	>99	8	-	92
	Ni	0.5	150	>99	-	-	>99
	Ni$_3$N	0.3	55	>99	-	>99	-
	Ni$_3$N	0.3	75	>99	22	69	8
	Ni$_3$N	0.5	135	>99	88	9	4
	Ni$_3$N	0.5	150	>99	94	-	6

F: volumetric flow, T: temperature, X: conversion, S: selectivity. Concentration reactant in ethanol: 0.05 M, 12-25 bar H$_2$.
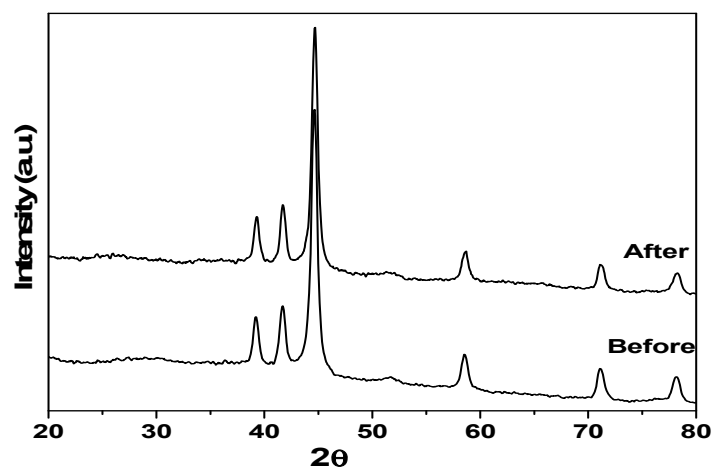
Figure 7.9. XRD pattern of Ni$_3$N@C nanocomposite before and after the catalytic test (see text for details).

7.3 Applications as batteries

More than two centuries after the Galvani and Volta studies about electricity, electrochemistry still represents a fascinating branch of modern science. Most of the related research is devoted to the study of energy storage and employment, in simpler words: batteries. In the last decades, after the Leclanché prototype of a "portable battery" (1866), the field has progressed enormously.

Figure 7.10. A) Vintage advertisement for Leclanché battery (source www.delcampe.net).
B) Li-ion battery damages a laptop (source:
http://batteryuniversity.com/learn/article/lithium_ion_safety_concerns)

A real revolution surely came with the invention of lithium batteries (1970´s), which brought several improvements, including high voltage, slow charge loss (5% in months) and no memory effect. On the other hand, the effect of bad usage of these batteries and related safety issues are also well-known (figure 7.10).

Nowadays, among the main targets in battery related research there are: 1) finding novel electrode materials with higher theoretical capacities and 2) increasing the energy density of a battery.

In current lithium ion batteries, Li ions move from anode to cathode (discharge) and back (charge). During charging, the lithium ions migrate from the positive to the negative electrode, where they become embedded in the porous electrode material in a process known as *intercalation* (lithium ions are stored by their intercalation into the electrode material lattice). Classical negative electrodes (anode) are made by carbon, usually graphite, while positive electrodes (cathode) are made by a metal oxide. An alternative path is, however, represented by the so-called *conversion reactions*, which might allow producing electrodes with higher storage densities of

lithium. In such reactions, lithium reacts with a transition metal compound, as schematically reported in equation 5:

$$M_mX_n + (ny)Li^+ + (ny)e^- \leftrightarrow mM° + nLi_yX \qquad \text{(eq. 5)}$$
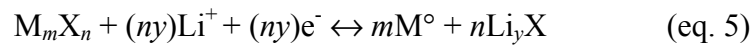
The conversion reaction is accompanied by structural changes of the electrode material. For this reason, special nanocomposite morphologies have to be synthesized to achieve cyclic stability of the capacity at satisfying charge and discharge rates. By reducing the particle size to the nanoscale, diffusion lengths can be minimized, which may allow faster charging and discharging of the battery [281, 282]. Conducting agents like carbon enable the conduction of electrons between the particles and the current collectors. By embedding the active material in a carbon matrix, the integrity of the electrode morphology and thereby the capacity of the electrode can be better maintained during cycling, despite the structural changes mentioned above [283 - 285].

On the other hand, to increase the energy density of a battery, the potential difference between the anode and the cathode can be increased. For that, the electromotive force of the reaction at the anode should be as low as possible. This is achieved when the free enthalpy ΔG of the anode reaction is low. As the latter is observed for the reaction of some transition-metal-oxides and -nitrides with lithium, these compounds may be attractive anode materials. Because of its abundance, low price and low toxicity, oxides and nitrides of manganese are especially interesting for the commercial application at larger scales. In the following session, tests on manganese nitride based systems as novel material for conversion reactions will be presented, while tests on more exotic, very promising, materials are still in progress.

Conversion reaction with MnN$_{0.43}$@C nanocomposites [238]

The manganese nitride in carbon nanocomposite, prepared as described in chapter 5, has been tested as anode material versus lithium metal as counter electrode.

It is known that manganese nitride can reversibly react with lithium to form LiN_3 and Mn [286]. As not only the nitride but also graphite can contribute to the electrochemical storage below 1V, determined capacities refer to the whole mass of the electrode material excluding the PVDF binder. In the first discharge two sloped

plateaus starting from 0.8 and 0.4 V respectively and a capacity of 341 mAh/g were observed. In the first charge, a capacity of 189 mAh/g was measured. In the subsequent cycles the capacity increased slightly and stabilized at a value of 230 mAh/g, with Coulombic efficiencies close to 100%. The voltage profile is steady in shape showing a plateau at 1.2 V in the charge and at 0.5 V in the discharge (figure 7.11).
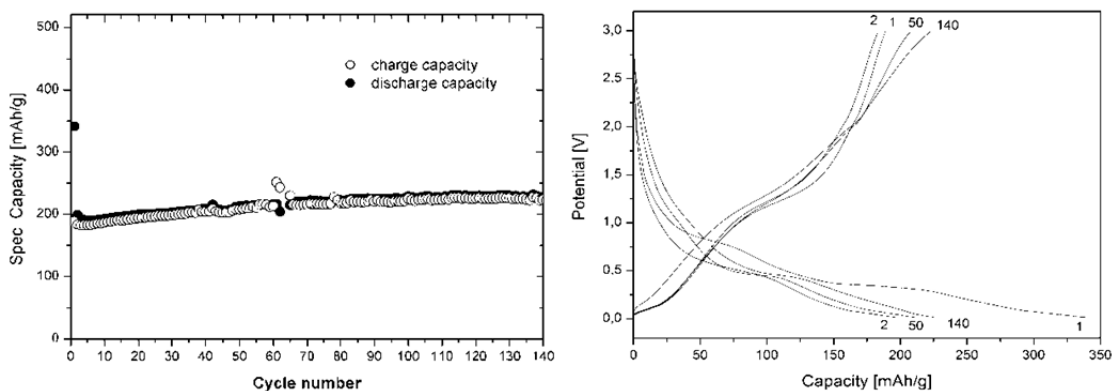
Figure 7.11. A) Charge/discharge capacity as a function of cycle number and B) potential versus specific capacity profile of $MnN_{0.43}$@C electrodes (voltage range 3-0.01 V, current density 10 mA/g).

Although the cyclic stability was very good, the obtained capacity was smaller than the theoretical capacity of $MnN_{0.43}$. Based on the theoretical capacity of graphite (371 mAh/g) and the carbon content of the electrode (overall 33 wt%), it can be calculated that the carbon can contribute to 122 mAh/g of the observed capacity at an outside estimate. This implies that the surplus capacity can be attributed to a reaction of Li with $MnN_{0.43}$. It must also be pointed out that MnNCN, which was found in minor amounts in the sample, is not electrochemically active, as a devoted battery test has revealed [238].

The discharged sample was then carefully characterized. The comparison of the XRD patterns before and after discharge (figure 7.12) show no remarkable changes in the $MnN_{0.43}$ peaks position, neither the formation of different crystalline phases.
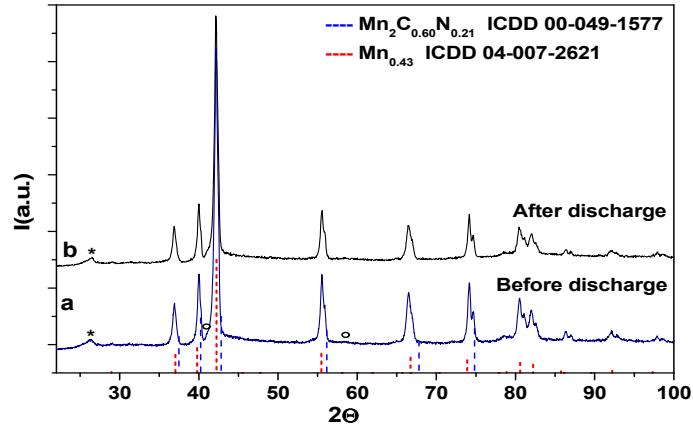
Figure7.12. XRD pattern of MnN$_{0.43}$@C before (a) and after (b) discharge

From these findings, it could be supposed that amorphous products are formed during the discharge steps, which are therefore not observed in the XRD pattern, in agreement with what was observed for other conversion type electrode materials before [284, 287]. In fact, this finding is not a surprise, since the formation of very small and amorphous crystallites in the conversion reaction Li$_3$N and Mn is often observed. This might also suggest that only a very small MnN$_{0.43}$ particles/surface fraction reacts, but as the intensity of X-ray reflexes is proportional to the volume, the residual "large" MnN$_{0.43}$ crystallites may be responsible for almost all the intensity we see in the pattern. More detailed investigations are currently in progress in order to understand the processes occurring during the discharge step. Here, it can easily be anticipated that preliminary tests have already shown an increase of the material capacity when the size of the MnN$_{0.43}$ particles are reduced.

8. Conclusions and Outlook

The research herein described was dedicated to explore alternative paths for an easier synthesis of nanosized MN/MC, keeping simplicity as the *Leitmotiv*. In spite of simplicity and reliability, the designed synthetic processes allow the production of functional materials, with the desired size and morphology in a well-controlled manner. The goal was achieved exploiting classical and less-classical precursors, ranging from common metal salts and molecules (e.g. urea, gelatin, agar, etc.), to more exotic materials, such as leaves, filter paper and even wood, with precise macro- and microscopic shape retention, while at the nanoscale MN/MC based nanocomposites can be created. It was shown that the choice of precursors and reaction conditions make it possible to control composition (going for instance from MO to MON to MN, or from MN to MC, up to quaternary systems), size (from 5 to 50 nm) and morphology, ranging from mere spherical nanoparticles to rod-like shapes, fibres, layers, meso-porous and hierarchical structures, etc. The nature of the mixed precursors also allows the preparation of MN/MC based nanocomposites, thus leading to multifunctional materials (e.g. MN/MC@C, MN/MC@PILs, etc.).

The designed routes are - concept-wise - similar and they all start by building up a secondary metal ion-N/C precursor network, which converts into an intermediate "*glass*". This *glass* stabilizes the *nascent* nanoparticles during their nucleation and impairs their uncontrolled growth during the heat treatment. One of the main problems related to the synthesis of MN/MC, i.e. the need for very high temperature, could be overcome this way. The prepared systems have been tested in many different fields, e.g. in batteries ($MnN_{0.43}@C$ shown a capacity stabilized at a value of 230 mAh/g, with Coulombic efficiencies close to 100%), as alternative magnetic materials (Fe_3C nanoparticles were prepared with different size and therefore different magnetic behaviour, superparamagnetic or ferromagnetic, showing saturation magnetization value up to 130 emu/g, i.e. similar to the value expected for the bulk), as filters and for the degradation of organic dyes (Fe_3C and $Zn_{1.7}GeN_{1.8}O$), as catalysts (both as active phase but also as active support, leading to high turnover rate and, more interesting, to tuneable selectivity).

With this research, the goal to simplify MN/MC nanoparticles production was achieved, making these systems now readily available in suitable amounts, both for fundamental and applied science.

This is a new starting point, a beginning, which discloses the tip of an iceberg of further possibilities, some of which will be presented in the following.

Development and Future perspective

Once the production of these materials can be made straightforward, any further modification, combination, manipulation is in principle possible and new systems can be designed according to the target application.

However, there are still many open questions, and its answers will allow complete control over the final structures.

More exhaustive mechanistic, theoretical and structural investigations of the systems are still needed. In this sense, collaborations with recognized experts in different fields of physical chemistry have already been established. These studies are also indispensable for understanding properties at the nanoscale (compared to the corresponding MN/MC bulk material), for controlling their reactivity, for improving performance (e.g. in catalysis, where stability is in some cases still an issue) and having a precise dimensional and morphological control. In this sense, the use of *ad hoc* prepared macromolecules, already containing, for instance, the selected metal or suitable functional groups is already planned, once more in collaboration with experts in the field of functional macromolecules.

A big part of the future research will be dedicated to the synthesis of more MN/MC based hybrids/nanocomposites, and in order to achieve this goal, fundamental research must be undertaken again (e.g. studying the chemical surface of the prepared nanoparticles) for a tailored surface functionalization. The concept behind the chemical stabilization of nanoparticle surfaces can already be conceived:

1) Nanoparticles preparation.

2) Surface functionalization with a compatible agent, which can possess more than one kind of moiety (e.g. X-F in scheme 8.1).

3) Moieties can be used for further processing, such as dispersion in polar/apolar media, changing nanoparticle polarity, polymerization, etc. The nature of the nanoparticle shell can also be changed by proper coating with carbon or silica.
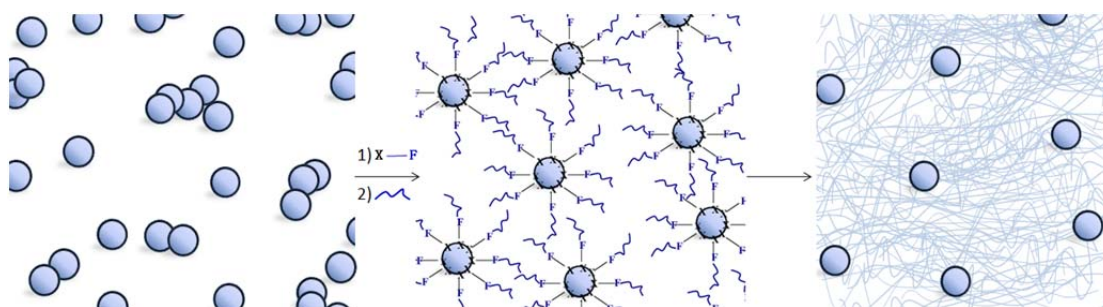
Scheme 8.1. Concept behind surfaces stabilization of nanoparticle. Reprint/Adapted with permission from reference [237](© 2013 Wiley-VCH Verlag GmbH & Co. KGaA, Weinheim).

The second component can be a responsive material, thus creating "smart" MN/MC based materials (still not available). This kind of research will also involve the preparation of novel ferrofluids and stronger contrasting agents, the preparation of suitable core-shell structures, incorporation of the as-prepared nanoparticles onto suitable support (e.g. graphene) and/or into large hierarchical systems in order to fully exploit their potential.

From the application point of view, future research will increasingly be focused on energy related processes, including photo- and electro-catalysis (e.g. with the production of new types of electrodes), photovoltaics, and energy conversion/storage (e.g. batteries, fuel cells). It will be intended both for designing tailored systems and it will aim to limit the impact of the production of these materials by reducing cost and energy consumption.

More efforts will go into the preparation of film and thin layers, also with the possibility to control the thickness. The catalytic "ink" presented in chapter 6 can, for instance, be used to design arrays of catalytic nanoparticles in a controlled fashion, where different steps of a single reaction can take place in the same working area, differently functionalized (thanks to the selected coating). But the production of selected (multi-)layers can be also conceived via the aerosol procedure presented in the same chapter, for instance by deposition of the aerosol particles on proper substrates.

As shown in chapter 4 and 6, the shape retention observed when using cellulose or wood immediately implies that any shape can be reproduced by folding cellulose or by wood refining, prior to the heat treatment. This would allow the production of more intricate, hierarchical structures. At the same time, the design of an alternative set-up for further temperature reduction will be considered.

9. Appendix

List of Abbreviations

Δ	Heat Treatment
λ	Wavelength
BpR	Biopolymer Route
CNTs	Carbon Nanotubes system
DI	(4,5) Dicyano-imidazole
DT	Dwelling Time
ES	Elettrospinning
fcc	cubic face centered
FWHM	Full Width at Half Maximum
hex	Hexagonal
HT	Heat Treatment
ICDD	International Centre for Diffraction Data
ILs	Ionic Liquid systems
M	Metal
MC	Metal Carbide
MN	Metal Nitride
MON	Metal oxy-nitride
MO_x	Metal Oxide
mp	mesoporous structure
nM	non-metal
np	Nanoparticles
ns	nanostructures
OD	Optical Density Units
PAN	Polyacrylonitrile
PEG	Poly(ethylene glycol)
PILs	Poly-ionic Liquid Systems
PUF	Poly(urea-co-formaldehyde) methylated resin
PVP	Poly(N-vinylpyrrolidone)
R	Molar ratio (usually Metal/C-N Source)
r.t.	Room temperature
UGR	Urea Glass Route
XRD	X-Rays Spectroscopy
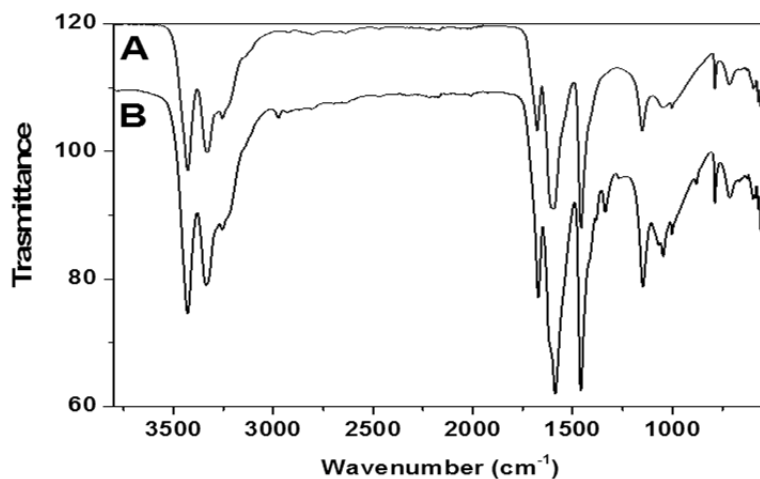
Figure 9.1 IR spectra of (A) pure urea and (B) dried urea from a solution of ethanol treated at 90°C one night and then dried. No significant changes can be observed, indicating that urea does not react with ethanol also under sustained heating.
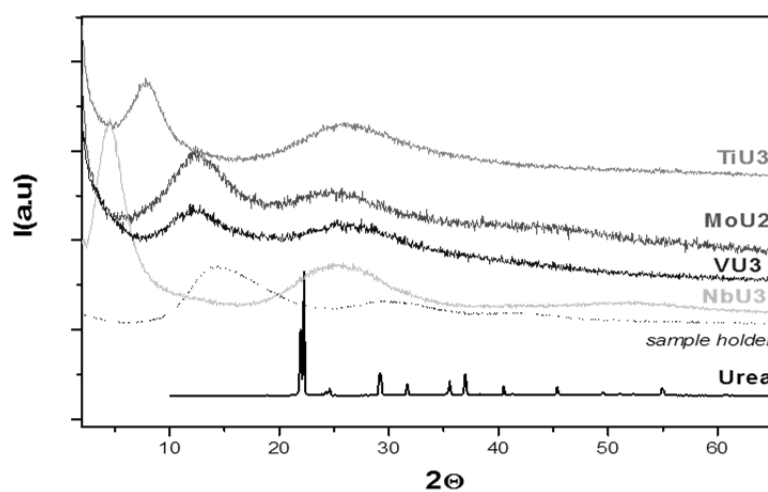
Figure 9.2 XRD patterns of some gel-like starting materials. The XRD patterns of urea and of the sample holder were also recorded (and here reported) to exclude their potential contribution in the sample patterns.

Table 9.1. Elemental analysis results of some intermediate glasses (T = 300-400°C).

Metal precursors	R	N%	C%	T (°C)	Final Product
Ti/urea	4	23.4	12.2	350	TiN
V/urea	3	15	9.75	350	VN
Nb/urea	3	17.0	7.6	350	NbN(O)
Ni/urea	4	20.5	21.7	250	Ni_3N
Fe/urea*	3	20-30	20-30	350	np-Fe_3C
Fe/DI	1	11.8	21.5	400	ns-Fe_3C

*Average obtained by several samples

Table 9.2 Experimental details for the preparation of MN/MC based nanoparticles with the UGR.

Product	%M	%N	%C
MN			
Mo_2N	91	6.7	<0.5
W_2N	87	2.9	<0.5
NbN(O)	n.m	11.4	0.4
CrN	n.m	5.9	4.9
TiN	n.m	15	3.2
GaN	85.4	12.8	2.6
Ni_3N	40	17.5	16.5
VN	46	13.3	14.5
Fe_3N	46.1	9.2	33.3
$MnN_{0.43}$	68	4.5	25
Ta_3N_5	n.m	10.9	0.4
MN(O, C)			
TiC(N)	n.m	14	21
NbC(N)	n.m	5.4	7.3
VC(N)	35	11	26
TaON	n.m	6.5	0.4
Zr_2ON_2	n.m	8.6	0.3
$Zn_{1.7}GeN_{1.8}O$	n.m	15.7	0.9
MC			
Mo_2C	91	<0.5	6.3
WC	85	<0.5	4.8
np-Fe_3C (da acac)	51.7	4.5	37.9
np-Fe_3C(da chloride)	67.9	1.8	22.9
ns-Fe_3C	56.1	11.8	28.3
mp-Fe_3C	40.9	7.4	42.9
Fe_7C_3	34.7	9.4	37.6
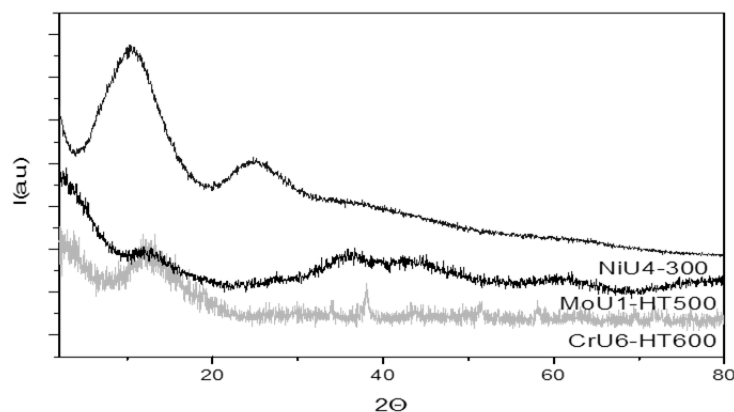
Figure 9.3 Samples quenched at temperature lower than the reaction temperature.

Table 9.3. Results overview for GaInN samples.

sample	In wt %	Ga wt %	N wt %	C wt %	Molar ratio In/Ga (precursor)	Molar ratio In/Ga (powder)	Molar ratio Ga/N (powder)	Molar ratio C/N (powder)
GaN	--	85.36	12.8	2.63	--	--	1.34	0.24
GaInN-0.05	5.83	73.17	14.35	1.85	0.05	0.05	1.02	0.15
GaInN-0.10	11.99	69.15	15.64	2.85	0.11	0.10	0.89	0.21
GaInN-0.20	11.77	79.66	14.82	0.96	0.25	0.09	1.09	0.08
GaInN-0.30	15.24	70.55	13.37	1.05	0.43	0.21	1.05	0.091
It must be said that with the same reaction conditions (just in absence of gallium) the formation of pure InN cannot be obtained. The sample prepared using In(NO3)3 in methanol and an In/urea molar ratio of 5, only brought to a non-stoichiometric phase, tentatively attributed as InxNCNy.							
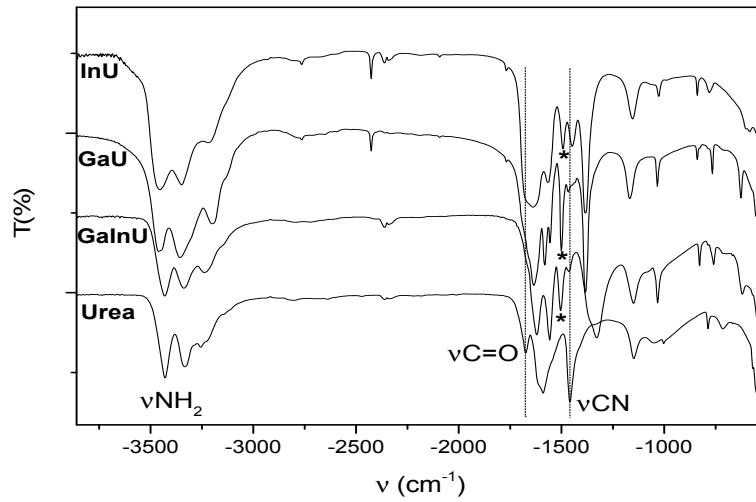
Figure 9.4. IR spectra of the bimetallic urea complexes
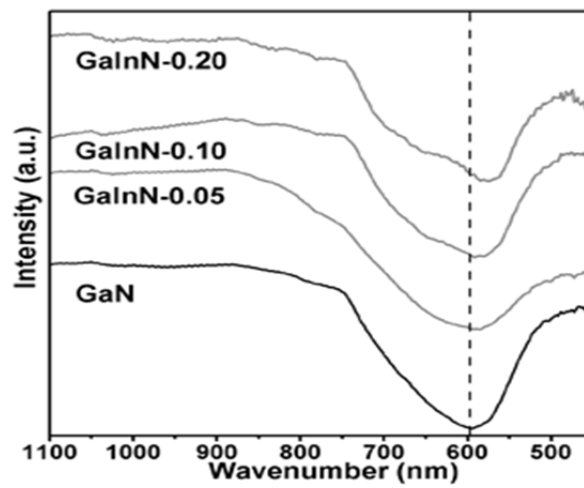
Figure 9.5. FTIR spectra of pure GaN, GaInN-0.05, GaInN-0.10 and GaInN-0.20.
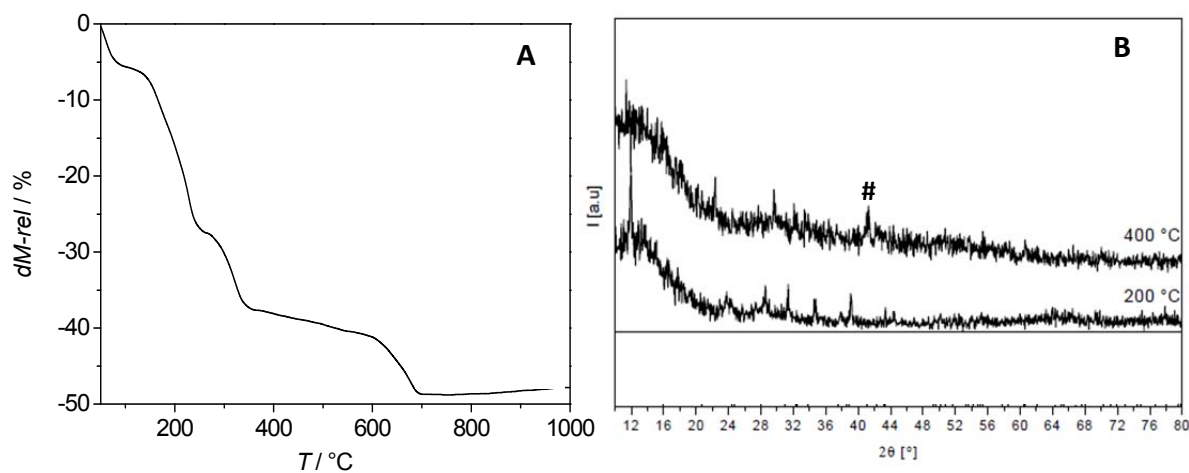
Figure 9.6. A) TGA pattern of the iron-urea sample (see section 4.1.2). B) XRD of the urea-iron samples quenched at different temperature. In the XRD the peaks of pure iron (#, ~45, ICDD 00-006-0696) and carbon (26°, ICDD 00-041-1487) can be observed.
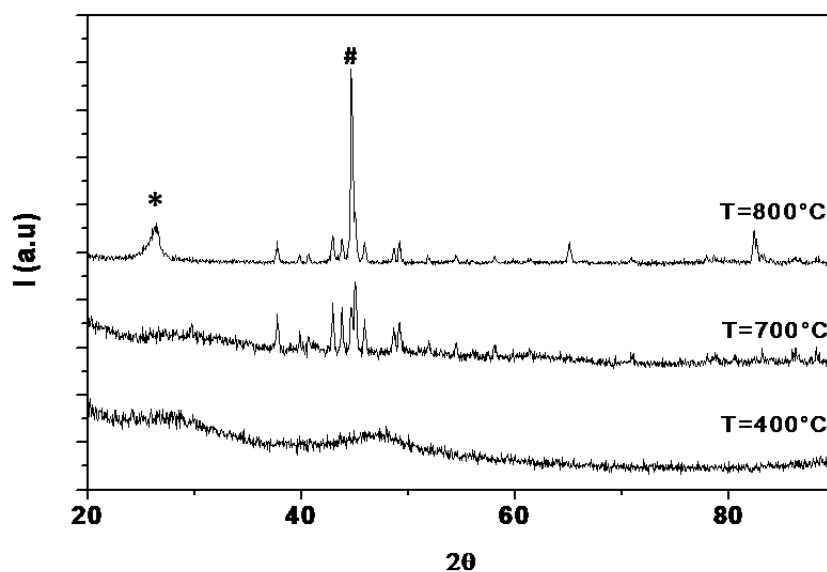
Figure 9.7. XRD patterns of Fe-DI derived samples (R=1) treated at three different temperatures. The main peak of pure iron (#, ~45, ICDD 00-006-0696) and pure carbon (*, ~26°, ICDD 00-041-1487) can be also observed
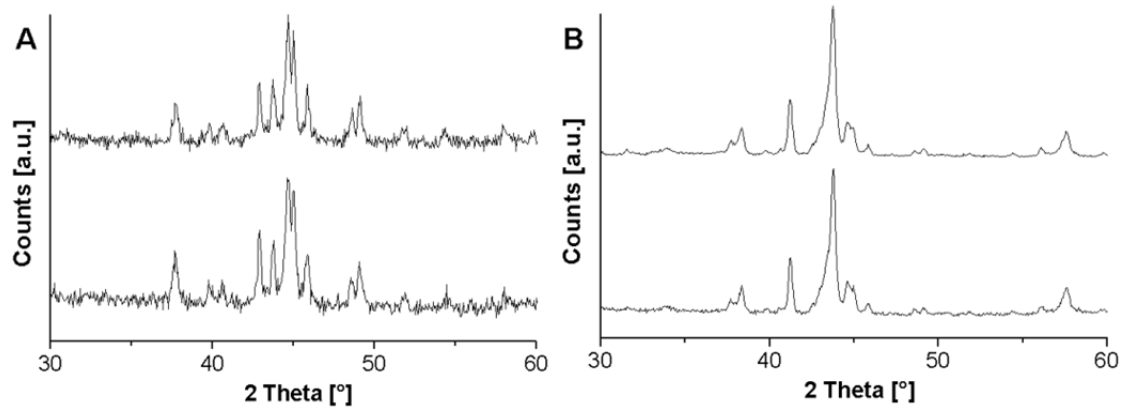
Figure 9.8. XRD patterns of the particles A) iron carbide and B) iron nitride particles before (up) and after (down) washing with H_2O_2.
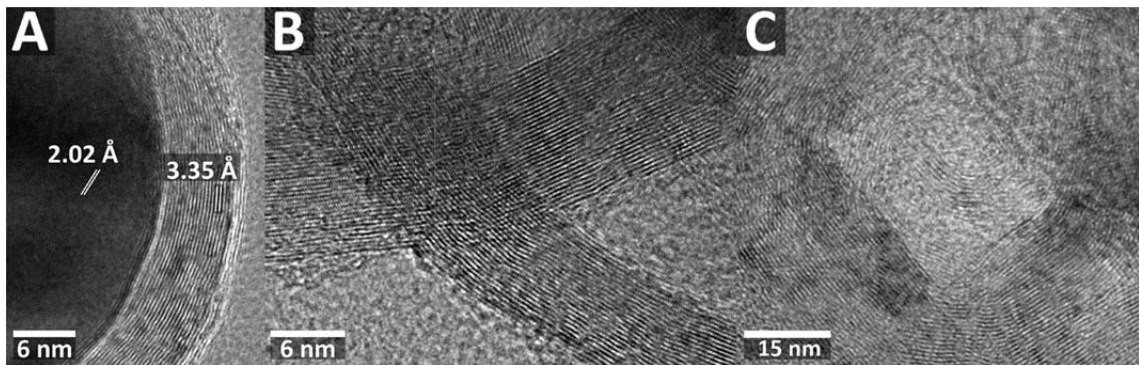
Figure 9.9. HR TEM images. A) Micrograph with labelled lattice fringes for iron carbide and graphite. B) free graphite. C) Sharp bends in the carbon layers, which confirm the graphene nature of the bends, rather than the formation of simple tubular carbon structure.
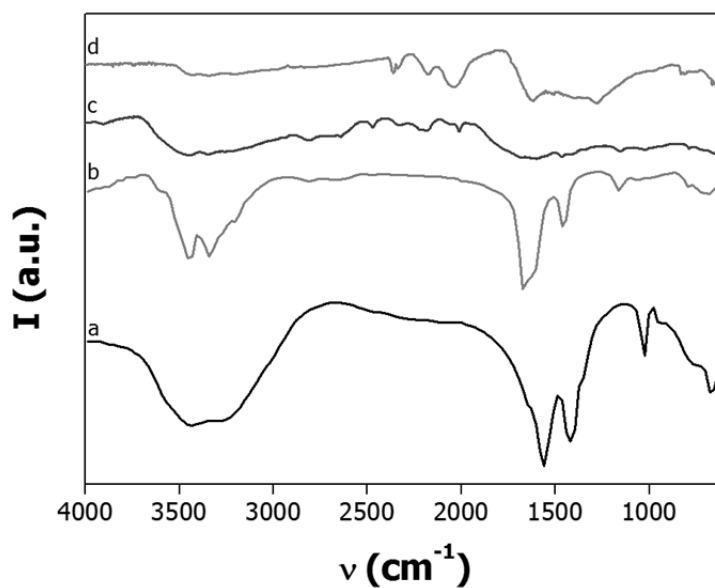
Figure 9.10. FT-IR spectra of (a) pure manganese acetate (b) urea (c) Mn-urea complex (d) Mn-urea sample calcined at 600 °C identified (by XRD) as MnNCN.
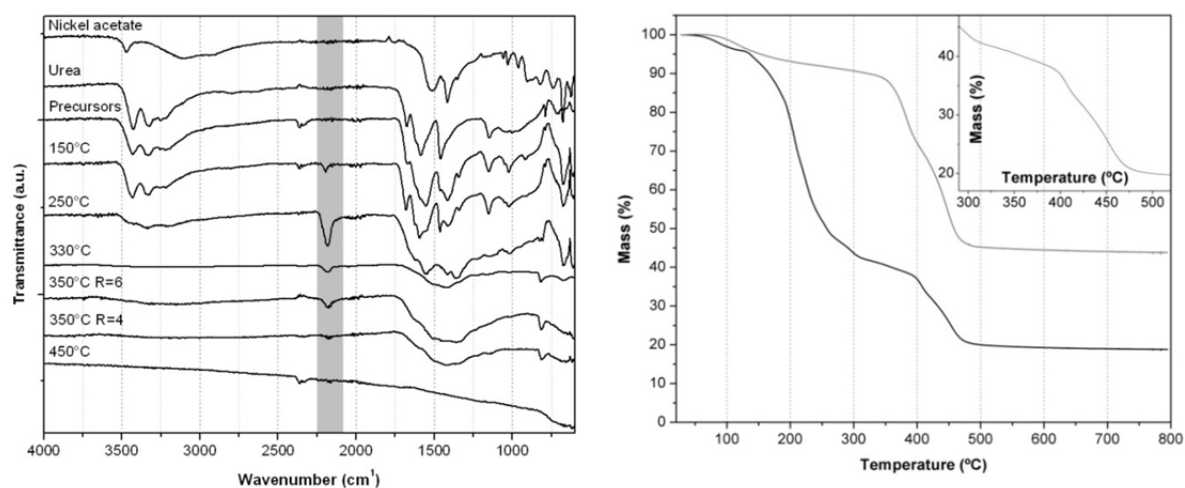
Figure 9.11 FT-IR (left) and TGA pattern of Ni-Urea precursors calcined at different temperature.
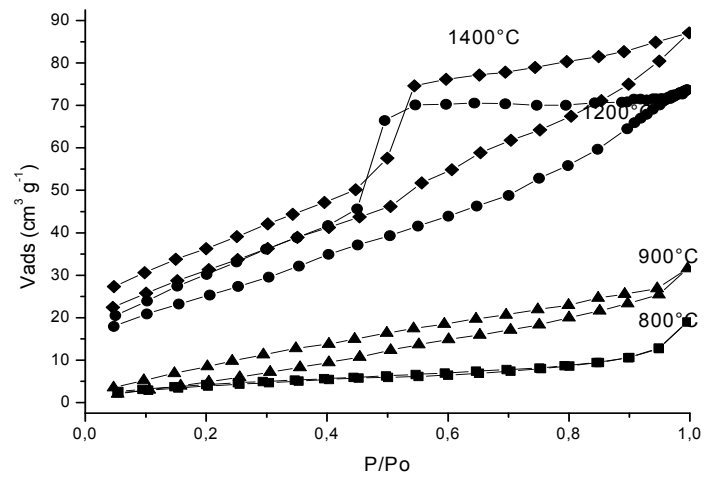
Figure 9.12. Nitrogen sorption isotherms from PAN-PUF-Cr fibres treated at different temperatures.
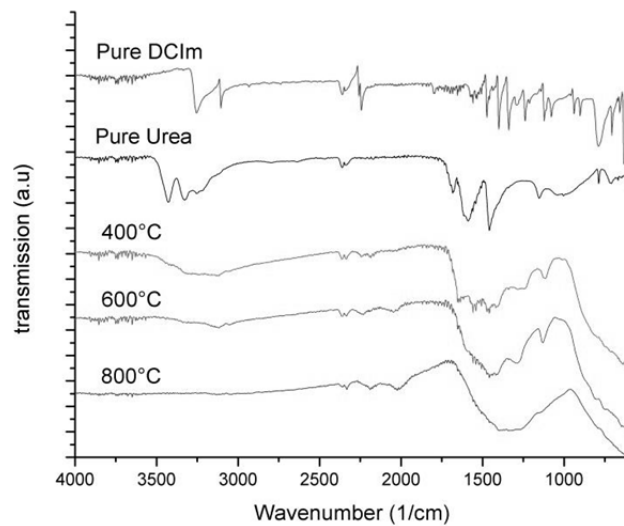
Figure 9.13. IR spectra of iron-DI samples heat treated at different temperatures. For comparison the spectra of pure DI (DCIm) and pure urea are also reported.

10. Chemical details and Techniques

Chemicals

Compound name	Purity	Provider	CAS
Alginic acid (PROTACID F120NM)		FMC Biopolymer, Norway	9005-32-7
Ammonium hydroxide	~25% NH_3 basis, puriss p.a	Sigma Aldrich (30501)	1336-21-6
Ammonium metatungstate hydrate	99,9%-w, powder	ABCR (AB119690, 25g)	12028-48-7
$CaCO_3$	>=99% (KT)	Fluka (21060-1kg)	471-34-1
Chitosan flakes		Aldrich (448869-50g)	9012-76-4
Chromium (III) chloride, sublimed	99% flakes	Aldrich (200050-25g)	10025-73-7
Copper Cobalt(II) nitrate hexahydrate	99 %	Strem Chemicals (93-2730 100g)	10026-22-9
Copper(II) nitrate hemipentahydrate	98%, ACS reagent	Sigma Aldrich (223395)	19004-19-4
Dicyanoimidazole (4,5)	99+% for analysis	Acros Organics (368530250), Merck (8.16101.0025)	1122-28-7
Ethanol	>=99,8% absolute (GC)	Sigma Aldrich (32205-1L)	64-17-5
$FeCl_3 \cdot 6H_2O$	p.A, > 98%	Fluka	10025-77-1
$FeCl_3 \cdot 6H_2O$	99+% for analysis	Acros (217091000, 100g)	10025-77-1
Filter paper	laboratory grade, MN 615	Macherey-Nagel	
Galium (III) chloride	99,999% ultra-dry, metals basis, 10 mesh beads	Alfa Aesar (35698)	13450-90-3
Galium (III) nitrate hydrate	crystalline, 99,9% trace metals basis	Aldrich (289892-25g)	69365-72-6
Gelatin Type A from porcine skin		Sigma (G2500-100g)	9000-70-8
Germanium (IV)methoxide	liquid	Aldrich (396362-5g)	992-91-6
H_2O_2	50wt-% in water; 35wt-% in water	Sigma Aldrich (516813-500ml) Sigma Aldrich (34988-7, 500ml)	7722-84-1
Indium (III) nitrate hydrate	99,99% metals basis, Lump/powder	Alfa Aesar (40185-10g)	207398-97-8
Iron (II) acetylacetonate	99,95% trace metals basis	Aldrich (413402-10g)	14024-17-0
Iron (II) chloride tetrahydrate	>= 99,0% puris p.a.	Sigma-Aldrich (44939-250g)	13478-10-9

Iron (III) chlorid hexahydrat	99+% for analysis	Acros Organics (217091000)	10025-77-1
Iron(II) acetate	97%	ABCR (AB117439, 5g)	3094-87-9
Iron(II)acetate	95%	Aldrich (339199)	3094-87-9
Iron(III) nitrate non-hydrate	>=98%, ACS reagent	Sigma Aldrich (216828, 500g)	7782-61-8
Ludox AS40 (particle diameter ~24 nm)	(40% water suspension of colloidal silica)	Sigma Aldrich (420840, 1L)	7631-86-9
Manganese (II) acetate tetrahydrate	>=99,0%, crystalline	Sigma-Aldrich (63537, 250g)	6156-78-1
Manganese(II) nitrate tetrahydrate	98%	Alfa Aesar (A18521, 250g)	20694-39-7
Methanol	>=99,9% (GC) LiChrosolv, for liquid chromatography	Merck (1.06007.1000)	67-56-1
Microcrystalline cellulose	Powder, ~20 micron; microgranular	Sigma Aldrich (310697;C6413)	9004-34-6
Molybdenum (V) chloride	95%, powder, 99,6% Crystalline, metals basis	Aldrich (208353-25g) Alfa Aesar (11832)	10241-05-1
N,N-dimethylformamide (DMF)	99,8% puriss p.a., ACS reagent	Sigma Aldrich (33120-1L)	68-12-2
Nickel (II) acetate tetrahydrate	98%	Aldrich (244066-100G)	6018-89-9
Nickel(II) nitrate hexahydrate	≥ 99 %, p.a.	Carl Roth (4395.1)	13478-00-7
Niobium (V) chloride	99,9% (metals basis), 100 mesh powder	Alfa Aesar (011548)	10026-12-7
Poly(urea-*co*-formaldehyde) methylated resin (PUF)		Sigma Aldrich (418536, 250ml)	68071-45-4
Polyacrylonitrile (PAN)	Powder, average Mw 150,000 (Typical)	Sigma Aldrich (181315-50g)	25014-41-9
Tantalum (V) chloride	99,99%, powder	Aldrich (400475-5G)	7721-01-9
Titanium (IV) chloride	99,90%; >=99,0% (AT); puriss	Acros Organics (197231000); Fluka (89545)	7550-45-0
Tungsten (IV) chloride	95% powder	Aldrich (263974-25G)	13470-13-8
Urea	ACS reagent 99,0 - 100,5%	Sigma-Aldrich (U5128)	57-13-6
Vanadium (III) oxychloride	99%, liquid	Aldrich (200891-100G)	7727-18-6
Zinc acetate	99,99%, trace metals basis	Sigma-Aldrich (383317-25G)	557-34-6
Zirconyl nitrate hydrate (white)	99%	Aldrich (24349-3)	14985-18-3

Techniques

HR-SEM

JEOL JSM-7001F field emission scanning electron microscope with an Oxford energy dispersive detector.

SEM

Field Emission JEOL JSM-7500F SEM LEO 1550 Gemini. The sample are loaded on carbon coated aluminium stubs and measured without any coating if it is conductive, otherwise the sample is coated by sputtering Au/Pd or Pt/Pd alloys prior to imaging.

TEM

Zeiss EM 912Ω operated at an acceleration voltage of 120 kV. Samples were ground, suspended in ethanol sonicated for 2 minutes in an ultrasonic bath. One drop of this suspension is put on carbon-coated copper grid and left to dry in air.

For microtomy, samples are embedded in LR White Resin (Medium Grade, Agar Scientific) and cut with a Leica Ultracut UTC to yield ultramicrotomes of the samples. An ultramicrotome cut was put on a 400 mesh carbon-coated copper grid.

HR-TEM

JEOL JEM-2100F 200kV Field Emission equipped with STEM (dark field imaging) and STEM-EDS, Philips CM200 FEG (Field Emission Gun) and LaB6, both operated at an acceleration voltage of 200 kV.

In-situ **TEM:** JEOL JEM-2000FXII with heating holder and video camera.

Ink-Jet Printing

HP DeskJet 710C™, HP Deskjet 5900C™ and an Epson™ Stylus S22. Initially, tests with different commercial printers were performed, bringing to similar (quality-wise) results. Thus the least expensive printer (Epson™ Stylus S22, costs approximately 25 €) was employed to conduct the following experiments.

FT-IR

FTIR spectrometer equipped with an attenuated total reflection (ATR) setup, Varian FTS 1000 between 600 and 4000 cm^{-1}. BIORAD FTS 6000

Nitrogen Sorption

Quantachrome Autosorb-1 or Quadrasorb at liquid nitrogen temperature (77 K). Data analysis performed by Quantachrome QuadraWin software (version 5.05). All the samples were degassed at 150 °C for 20 hours before measurements. Specific surface area was determined using the BET method.

Digital Photos

Sony SLT-A55 equipped with a SAL-1855 lens.

Raman

WITec 532 nm Nd:YAG with optical resolution diffraction limited to 200 nm laterally and 500 nm vertically, spectral resolution down to 0.02 wavenumbers. The laser beam is focused down to a micrometer size spot on the sample through a confocal Raman microscope (CRM300, WITec, Ulm, Germany) equipped with piezo-scanner (P-500, Physik Instrumente, Karlsruhe, Germany). The spectra were acquired using an air-cooled CCD detector (DU401-BV, Andor, Belfast, UK) behind a grating (600 g/mm) spectrograph (UHTS 300, WITec, Ulm, Germany). The ScanCtrlSpectroscopyPlus (version 2.02, Witec) was used for measurement setup and data processing.

Infrared Raman

Infrared Raman micro-spectroscopy, was performed by focussing a continuous laser beam down to a micrometer size spot on the sample through a confocal Raman microscope (CRM200, WITec, Ulm, Germany) equipped with piezo-scanner (P-500, Physik Instrumente, Karlsruhe, Germany). The diode pumped linearly-polarized 785 nm near infra-red (NIR) laser excitation (Toptica Photonics AG, Graefelfing, Germany) was used in combination with × 20 (Nikon, NA = 0.4) microscope objective. The spectra were acquired using an air-cooled CCD (PI-MAX, Princeton Instruments Inc., Trenton, NJ, USA) behind a grating (300 g/mm) spectrograph (Acton, Princeton Instruments Inc., Trenton, NJ, USA) with a spectral resolution of 6 cm−1. The ScanCtrlSpectroscopyPlus (version 1.38, Witec) was used for measurement setup and spectra processing.

TGA-MS

Thermo-gravimetric analysis was performed with a Netzsch TG-209 F1 Libra and a connected Pfeiffer ThermoStar GSD301-T2 mass spectrometer.

PXRD and Reference Database

Bruker D8 diffractometer using Cu-Kα radiation (λ = 0.154 nm) and a scintillation counter (or a KeveX Detector) and Advance diffractometer (Copper K-alpha radiation) equipped with a LynxEye detector. Species identification was performed according to ICDD-PDF4+ database

SQUID

Field-dependent magnetization curves were obtained using a Quantum Design Magnetic Property Measurement System (MPMS) SQUID (Superconducting Quantum Interference Device) magnetometer at room temperature in the field range of ±5 kOe.

Aerosol Spray set-up

TSI 3076 nebulizer, with argon as spraying gas and flow rate of 2 L/min. The aerosol flow is carried through a 1 m long tube of 100 mm diameter, where the droplets are pre-dried by natural evaporation. Quartz tube furnace with 300 mm length and 60 mm. in diameter. The residence time in the heated zone is about 15 s.

UV–vis diffuse reflection

Shimadzu UV-2045 PC at room temperature.

Catalytic tests performed at the MPI-KG

For section 7.2 (ii), in a typical reaction, the sample was placed in a SCHOTT screw-capped glass tube (160 mm length, about 10 mm inside diameter); after solvent addition, the solution was heated to 150 8C for 48 h.

For sessions 7.2 (vi-vii) all the reactions were performed using a H-Cube Pro reactor equipped with a hydrogen feed (generated in situ) and a liquid feed.

GC–MS

Agilent Technologies 5975 gas chromatograph equipped with a MS detector and a capillary column (HP-5MS, 30 m, 0.25 mm, 0.25 micron).

Electrospinning Set-up

Electrospinz, New Zealand with a 30 kV max. acceleration voltage. Polymer solutions were extruded from a 1 mL plastic syringe with 0.5 mm of diameter needle in an automatized injector at different flows. The fibres were collected in a round-shaped aluminium foil of 12 cm diameter. The temperature of the process was kept at 20°C.

Thermal Treatment

Nabertherm muffle furnace (for experiment up to 900°C) and tubular furnace from Carbolite (for experiment above 900 C), under nitrogen flow

Electrochemistry tests

Electrodes were prepared by fixing a sample section to copper wire with electrical solder. For electrolysis of water using the cyber leaf, a solution of Na_2SO_4 (0.5% by weight) was prepared containing a few drops of phenolphthalein pH indicator solution. The leaf electrode was connected to a circuit as the anode with a platinum cathode. Both electrodes were dipped into the Na_2SO_4 solution, and a potential of 5 V was applied across the cell. For platinum deposition, the electrode was connected as the cathode to a cell with a platinum counter-electrode and Ag|AgCl|KCl reference electrode. The cell was filled with $K_2[PtCl_4]$ solution (1 mm or 5 mm) so that the lower half of the ceramic leaf was in contact with the solution. A voltage of 200 mV was applied for 600 s before the leaf was removed, washed three times with deionized water, and dried at 408C.

For the electro-deposition on the Minerva head experiments were conducted at 0.4 (and 1.5 V using a battery) in 1 M copper sulphate solution. Deposition takes 5-20 minutes, depending on the applied voltage (the higher the voltage, the faster the process).

11. Acknowledgments

I was born with a passion for learning. Everything. Constantly. Endless.

At the MPI-KG I found a perfect environment: I learnt a lot, and I grow up and developed in a more aware person and scientist.

Therefore, I will always be grateful to Prof. Markus Antonietti for this great chance that he was offering me to pursue science at MPI-KG. Setting up a new group in the Colloid Department of the MPI-KG was a beautiful challenge, a pleasure, an amazing experience. *Viis gratias Mentor meus.* For everything I learnt from you, for all the wide-ranging discussions and contests.

In the last years I had the fortune to have in my group and work with many young, motivated and clever people. Without them, this *habilitation* work would not have been possible: Alex (Dr. Kraupner), Betty (Dr. Milke), Stefan *MacGyver* (Dr. Glatzel), Sarah (Ms. Metzke), Fonzi (Dr. Garcia-Marquez), Constanze (Dr. Schliehe), Guylhaine (Dr. Clavel), Valerio (Mr. Molinari), Vince (Dr. Maurice), Maria (Dr. Efremova), Weitang (Dr. Yao), Wei Wei (Dr. Lei), Xiaofeng (Dr. Liu), Qingsheng (Dr. Gao), Tristan (Dr. Corbiere), Zoe (Dr. Schnepp), Claudia (Ms. Kästner), Sabine (Ms. Eisold), David (Dr. Portehault), Regina (Ms. Hafner), Wen (Dr. Yang). Thanks a lot! It was a pleasure to work with all of you. I learnt something from each of you.

I'm especially indebted with Alex, Alfonso, Constanze, Guylhaine, Irina, Katharina, Sarah, Stefan and Valerio for the precious help in the last few weeks. It was a tough time, but you all make it easier!

A thank from the heart goes to Katharina (Ms. Otte) and Irina (Ms. Shekova). Thanks for the great job girls and all the lab work done!

I am largely grateful to Prof. Robert Schlögl (FHI Berlin) for precious advice and discussion, and for giving me the possibility to use the HR-TEM instruments by myself. I learnt a lot about my systems watching them through the microscope lenses. Thank you very much for this opportunity and thanks to all the friends at the AC department for their valuable help: Manfred, Marc, Nobbi, Rosita, Wiebke, Gisela and all of you.

Part of this thesis was conceived and written in a *"mignon lieu de travail"* at the TU-Berlin/Stranski Lab, in the group of Prof. Michael Gradzielski. To all of them I want to express my sincere gratitude for the warm hospitality during all my stays! I feel home there.

I am also grateful that I had/have the chance to collaborate with many scientists from the national/international research scene: Prof. John Texter (Michigan University, PILs project), Prof. Maximilian Fichtner and Dr. Clemens Wall (Ulm University/KIT, battery tests), Prof.

12. References

[1] D. E. Newton, *Chemistry of new materials*. New York: Facts on File, 2007.

[2] Deville Saint-Claire H. and Wöhler F., "Über das Stickstoffsilicium," *Ann. Chem. Pharm.*, vol. 104, no. 2, pp. 256–256, 1857.

[3] "Friedrich Wöhler," *Wikipedia*.

[4] F. Wöhler, "Über künstliche Bildung des Harnstoffs," *Ann. Phys. Chem.*, vol. 88, no. 2, pp. 253–256, 1828.

[5] Cheng, AM., "The Real Death of Vitalism: Implications of the Wöhler Myth," *Penn Bioeth. J.*, vol. 1, no. 1, pp. 1–3.

[6] Wolfgang Ostwald, *Die Welt der Vernachlässigten Dimensionen*. Theodor Steinkopff, Dresden und Leipzig, 1915.

[7] R. Zsigmondy, "Ueber wässrige Lösungen metallischen Goldes," *Justus Liebigs Ann. Chem.*, vol. 301, no. 1, pp. 29–54, 1898.

[8] R. P. Feynman, "There's plenty of room at the bottom," *J. Microelectromechanical Syst.*, vol. 1, no. 1, pp. 60–66, 1992.

[9] P. Colomban, "Gel technology in ceramics, glass-ceramics and ceramic-ceramic composites," *Ceram. Int.*, vol. 15, no. 1, pp. 23–50, 1989.

[10] P. Colomban, "The Use of Metal Nanoparticles to Produce Yellow, Red and Iridescent Colour, from Bronze Age to Present Times in Lustre Pottery and Glass: Solid State Chemistry, Spectroscopy and Nanostructure," *J. Nano Res.*, vol. 8, pp. 109–132, 2009.

[11] C. J. Murphy, A. M. Gole, S. E. Hunyadi, and C. J. Orendorff, "One-Dimensional Colloidal Gold and Silver Nanostructures," *Inorg. Chem.*, vol. 45, no. 19, pp. 7544–7554, 2006.

[12] A. A. Levin, D. C. Meyer, M. Reibold, W. Kochmann, N. Pätzke, and P. Paufler, "Microstructure of a genuine Damascus sabre," *Cryst. Res. Technol.*, vol. 40, no. 9, pp. 905–916, 2005.

[13] V.A. Bogatyrev and L.A. Dykman, "Gold nanoparticles: preparation, functionalisation and applications in biochemistry and immunochemistry.," *Russ Chem Rev*, vol. 76, pp. 181–194, 2007.

[14] L. E. Toth, *Transition metal carbides and nitrides*. New York: Academic Press, 1971.

[15] A. I. Gusev, A.A. Rempel, A. J. Magerl, *Disorder and order in strongly nonstoichiometric compounds: transition metal carbides, nitrides, and oxides*. Berlin; New York: Springer, 2001.

[16] A. L. Ivanovskii, "Platinum group metal nitrides and carbides: synthesis, properties and simulation," *Russ. Chem. Rev.*, vol. 78, no. 4, pp. 303–318, 2009.

[17] E. Gregoryanz, C. Sanloup, M. Somayazulu, J. Badro, G. Fiquet, H. Mao, and R. J. Hemley, "Synthesis and characterization of a binary noble metal nitride," *Nat. Mater.*, vol. 3, no. 5, pp. 294–297, 2004.

[18] J. C. Crowhurst, "Synthesis and Characterization of the Nitrides of Platinum and Iridium," *Science*, vol. 311, no. 5765, pp. 1275–1278, 2006.

[19] V. Mankad, N. Rathod, S. D. Gupta, S. K. Gupta, and P. K. Jha, "Stable structure of platinum carbides: A first principles investigation on the structure, elastic, electronic and phonon properties," *Mater. Chem. Phys.*, vol. 129, no. 3, pp. 816–822, 2011.

[20] D. Åberg, P. Erhart, J. Crowhurst, J. M. Zaug, A. F. Goncharov, and B. Sadigh, "Pressure-induced phase transition in the electronic structure of palladium nitride," *Phys. Rev. B*, vol. 82, no. 10, 2010.

[21] X. Li, X. P. Du, and Y. X. Wang, "Structural, Mechanical Stability, and Physical Properties of Iridium Carbides with Various Stoichiometries: First-Principles Investigations," *J. Phys. Chem. C*, vol. 115, no. 14, pp. 6948–6953, 2011.

[22] X.-Y. Yi, H.-Y. Ng, I. D. Williams, and W.-H. Leung, "Formation of a Dinuclear Imido Complex from the Reaction of a Ruthenium(VI) Nitride with a Ruthenium(II) Hydride," *Inorg. Chem.*, vol. 50, no. 4, pp. 1161–1163, 2011.

[23] E. Kwan Huang, W.-M. Cheung, H. H. Y. Sung, I. D. Williams, and W.-H. Leung, "Reactions of a Ruthenium(VI) Nitride with Rhodium(III) and Iridium(III) Aryl Complexes. Insertion of the Ru≡N Group into the Rh–C Bonds of Trimesitylrhodium(III)," *Organometallics*, vol. 32, no. 3, pp. 733–736, 2013.

[24] K. Niwa, D. Dzivenko, K. Suzuki, R. Riedel, I. Troyan, M. Eremets, and M. Hasegawa, "High Pressure Synthesis of Marcasite-Type Rhodium Pernitride," *Inorg. Chem.*, vol. 53, no. 2, pp. 697–699, 2014.

[25] L. Šiller, N. Peltekis, S. Krishnamurthy, Y. Chao, S. J. Bull, and M. R. C. Hunt, "Gold film with gold nitride—A conductor but harder than gold," *Appl. Phys. Lett.*, vol. 86, no. 22, p. 221912, 2005.

[26] J. A. Mathews and L. L. Watters, "The Carbide of Gold.," *J. Am. Chem. Soc.*, vol. 22, no. 2, pp. 108–111, 1900.

[27] Y. Cohen, V. Bernshtein, E. Armon, A. Bekkerman, and E. Kolodney, "Formation and emission of gold and silver carbide cluster ions in a single C_{60}^- surface impact at keV energies: Experiment and calculations," *J. Chem. Phys.*, vol. 134, no. 12, p. 124701, 2011.

[28] E. S. Shanley and J. L. Ennis, "The chemistry and free energy of formation of silver nitride," *Ind. Eng. Chem. Res.*, vol. 30, no. 11, pp. 2503–2506, 1991.

[29] "Copper acetylide," *Wikipedia*.

[30] J. A. Montoya, A. D. Hernandez, C. Sanloup, E. Gregoryanz, and S. Scandolo, "OsN_2: Crystal structure and electronic properties," *Appl. Phys. Lett.*, vol. 90, no. 1, p. 011909, 2007.

[31] "Plutonium compounds: plutonium nitride," *WebElements*.

[32] "Uranium compounds: uranium nitride," *WebElements*.

[33] K. Maeda and K. Domen, "New Non-Oxide Photocatalysts Designed for Overall Water Splitting under Visible Light," *J. Phys. Chem. C*, vol. 111, no. 22, pp. 7851–7861, 2007.

[34] G. Hitoki, T. Takata, J. N. Kondo, M. Hara, H. Kobayashi, and K. Domen, "An oxynitride, TaON, as an efficient water oxidation photocatalyst under visible light irradiation (< 500 nm)," Chem. Commun., no. 16, pp. 1698–1699, 2002.

[35] S. S. K. Ma, K. Maeda, T. Hisatomi, M. Tabata, A. Kudo, and K. Domen, "A Redox-Mediator-Free Solar-Driven Z-Scheme Water-Splitting System Consisting of Modified Ta_3N_5 as an Oxygen-Evolution Photocatalyst," *Chem. - Eur. J.*, vol. 19, no. 23, pp. 7480–7486, 2013.

[36] Q. Gao, C. Giordano, and M. Antonietti, "Controlled Synthesis of Tantalum Oxynitride and Nitride Nanoparticles," *Small*, vol. 7, no. 23, pp. 3334–3340, 2011.

[37] S. T. Oyama, *The chemistry of transition metal carbides and nitrides*. London: Blackie Academic & Professional, 1996.

[38] G. Hägg, *Zeitschrift fuer physikalische Chemie. Eigenschaften der Phasen von Übergangselementen in binären Systeme mit Bor, Kohlenstoff und Stickstoff*, vol. 6. 1929.

[39] L. Brewer, "A most striking confirmation of the Engel metallic correlation," *Acta Metall.*, vol. 15, no. 3, pp. 553–556, 1967.

[40] International Conference on the Science of Hard Materials, *Science of hard materials: proceedings of the International Conference on the Science of Hard Materials held in Rhodes, 23-28 September, 1984*. Bristol, England ; Boston: Published on behalf of the Institute of Physics by A. Hilger, 1986.

[41] R. B. Levy and M. Boudart, "Platinum-Like Behavior of Tungsten Carbide in Surface Catalysis," *Science*, vol. 181, no. 4099, pp. 547–549, 1973.

[42] V. A. Gubanov, *Electronic structure of refractory carbides and nitrides*. Cambridge [England] ; New York: Cambridge University Press, 1994.

[43] L. Johansson, "Electronic and structural properties of transition-metal carbide and nitride surfaces," *Surf. Sci. Rep.*, vol. 21, no. 5–6, pp. 177–250, 1995.

[44] H. Chhina, S. Campbell, and O. Kesler, "Thermal and electrochemical stability of tungsten carbide catalyst supports," *J. Power Sources*, vol. 164, no. 2, pp. 431–440, Feb. 2007.

[45] K. Machida, A. Nakamoto, and G. Adachi, "Low-Temperature Synthesis of $NdFe_{11}TiC_xN_y$ via Plasma Carbonitriding.," *Chem. Lett.*, no. 8, pp. 1381–1384, 1993.

[46] Z. Gu, W. Lai, X.-F. Zhong, and W. Ching, "Electronic and magnetic structure of the ternary compound $Nd_2Fe_{17}N$," *Phys. Rev. B*, vol. 46, no. 21, pp. 13874–13880, 1992.

[47] Z. Gu and W. Lai, "Calculated electronic and magnetic structures of the new ternary rare-earth–iron nitride $Nd_2Fe_{17}N_3$," *J. Appl. Phys.*, vol. 71, no. 8, p. 3911, 1992.

[48] R. Kojima and K. Aika, "Molybdenum nitride and carbide catalysts for ammonia synthesis," *Appl. Catal. Gen.*, vol. 219, no. 1–2, pp. 141–147, 2001.

[49] B. Vidick, "Control of the catalytic activity of tungsten carbides III. Activity for ethylene hydrogenation and cyclohexane dehydrogenation," *J. Catal.*, vol. 99, no. 2, pp. 439–448, 1986.

[50] S. T. Oyama, "Preparation and catalytic properties of transition metal carbides and nitrides," *Catal. Today*, vol. 15, no. 2, pp. 179–200, 1992.

[51] G. Ranhotra, "Catalysis over molybdenum carbides and nitrides II. Studies of CO hydrogenation and C2H6 hydrogenolysis," *J. Catal.*, vol. 108, no. 1, pp. 40–49, 1987.

[52] F. Ribeiro, "Catalytic reactions of n-Alkanes on beta;-W2C and WC: The effect of surface oxygen on reaction pathways," *J. Catal.*, vol. 130, no. 2, pp. 498–513, 1991.

[53] M. J. Ledoux, C. P. Huu, J. Guille, and H. Dunlop, "Compared activities of platinum and high specific surface area Mo_2C and WC catalysts for reforming reactions I. Catalyst activation and stabilization: Reaction of n-hexane," *J. Catal.*, vol. 134, no. 2, pp. 383–398, 1992.

[54] A. M. Alexander and J. S. J. Hargreaves, "Alternative catalytic materials: carbides, nitrides, phosphides and amorphous boron alloys," *Chem. Soc. Rev.*, vol. 39, no. 11, p. 4388, 2010.

[55] H. Böhm, "New Non-noble Metal Anode Catalysts for Acid Fuel Cells," *Nature*, vol. 227, no. 5257, pp. 483–484, 1970.

[56] J. Choi, "Influence of the Degree of Carburization on the Density of Sites and Hydrogenating Activity of Molybdenum Carbides," *J. Catal.*, vol. 193, no. 2, pp. 238–247, 2000.

[57] S. T. Oyama and G. L. Haller, "Catalysis by carbides, nitrides, and Group VIII intermetallic compounds," in *Catalysis*, vol. 5, G. C. Bond and G. Webb, Eds. Cambridge: Royal Society of Chemistry, pp. 333–365, 1982.

[58] T. Xiao, A. Hanif, A. P. E. York, Y. Nishizaka, and M. L. H. Green, "Study on the mechanism of partial oxidation of methane to synthesis gas over molybdenum carbide catalyst," *Phys. Chem. Chem. Phys.*, vol. 4, no. 18, pp. 4549–4554, 2002.

[59] J. S. Lee and M. Boudart, "Hydrodesulfurization of thiophene over unsupported molybdenum carbide," *Appl. Catal.*, vol. 19, no. 1, pp. 207–210, 1985.

[60] E. Markel, "Catalytic hydrodesulfurization by molybdenum nitride," *J. Catal.*, vol. 126, no. 2, pp. 643–657, 1990.

[61] K. S. Lee, H. Abe, J. A. Reimer, and A. T. Bell, "Hydrodenitrogenation of Quinoline over High-Surface-Area Mo$_2$N," *J. Catal.*, vol. 139, no. 1, pp. 34–40, 1993.

[62] E. de Smit and B. M. Weckhuysen, "The renaissance of iron-based Fischer–Tropsch synthesis: on the multifaceted catalyst deactivation behaviour," *Chem. Soc. Rev.*, vol. 37, no. 12, p. 2758, 2008.

[63] R. Kojima and K. Aika, "Cobalt molybdenum bimetallic nitride catalysts for ammonia synthesis," *Appl. Catal. Gen.*, vol. 219, no. 1–2, pp. 157–170, 2001.

[64] R. Schlögl, "Catalytic Synthesis of Ammonia -A 'Never-Ending Story'?," *Angew. Chem. Int. Ed.*, vol. 42, no. 18, pp. 2004–2008, 2003.

[65] B. Dhandapani, T. St. Clair, and S. T. Oyama, "Simultaneous hydrodesulfurization, hydrodeoxygenation, and hydrogenation with molybdenum carbide," *Appl. Catal. Gen.*, vol. 168, no. 2, pp. 219–228, 1998.

[66] E. Furimsky, "Metal carbides and nitrides as potential catalysts for hydroprocessing," *Appl. Catal. Gen.*, vol. 240, no. 1–2, pp. 1–28, 2003.

[67] M. K. Neylon, S. Choi, H. Kwon, K. E. Curry, and L. T. Thompson, "Catalytic properties of early transition metal nitrides and carbides: n-butane hydrogenolysis, dehydrogenation and isomerization," *Appl. Catal. Gen.*, vol. 183, no. 2, pp. 253–263, 1999.

[68] P. Krawiec, P. L. De Cola, R. Gläser, J. Weitkamp, C. Weidenthaler, and S. Kaskel, "Oxide Foams for the Synthesis of High-Surface-Area Vanadium Nitride Catalysts," *Adv. Mater.*, vol. 18, no. 4, pp. 505–508, 2006.

[69] A. P. E. York, C. Pham-Huu, P. Del Gallo, and M. J. Ledoux, "Molybdenum oxycarbide hydrocarbon isomerization catalysts: cleaner fuels for the future," *Catal. Today*, vol. 35, no. 1–2, pp. 51–57, 1997.

[70] F. Solymosi, "Aromatization of Methane over Supported and Unsupported Mo-Based Catalysts," *J. Catal.*, vol. 165, no. 2, pp. 150–161, 1997.

[71] R. Ganesan and J. S. Lee, "Tungsten Carbide Microspheres as a Noble-Metal-Economic Electrocatalyst for Methanol Oxidation," *Angew. Chem. Int. Ed.*, vol. 44, no. 40, pp. 6557–6560, 2005.

[72] S. Kaskel, K. Schlichte, and T. Kratzke, "Catalytic properties of high surface area titanium nitride materials," *J. Mol. Catal. Chem.*, vol. 208, no. 1–2, pp. 291–298, 2004.

[73] D. J. Sajkowski and S. T. Oyama, "Catalytic hydrotreating by molybdenum carbide and nitride: unsupported Mo_2N and $Mo_2CAl_2O_3$," *Appl. Catal. Gen.*, vol. 134, no. 2, pp. 339–349, 1996.

[74] A. Miura, M. E. Tague, J. M. Gregoire, X.-D. Wen, R. B. van Dover, H. D. Abruña, and F. J. DiSalvo, "Synthesis of Pt−Mo−N Thin Film and Catalytic Activity for Fuel Cells," *Chem. Mater.*, vol. 22, no. 11, pp. 3451–3456, 2010.

[75] H. H. Hwu, J. G. Chen, K. Kourtakis, and J. G. Lavin, "Potential Application of Tungsten Carbides as Electrocatalysts. 1. Decomposition of Methanol over Carbide-Modified W(111)," *J. Phys. Chem. B*, vol. 105, no. 41, pp. 10037–10044, 2001.

[76] M. Nie, P. K. Shen, M. Wu, Z. Wei, and H. Meng, "A study of oxygen reduction on improved Pt-WC/C electrocatalysts," *J. Power Sources*, vol. 162, no. 1, pp. 173–176, 2006.

[77] H. Meng and P. K. Shen, "Novel Pt-free catalyst for oxygen electroreduction," *Electrochem. Commun.*, vol. 8, no. 4, pp. 588–594, Apr. 2006.

[78] G. T. Burstein, D. R. McIntyre, and A. Vossen, "Relative Activity of a Base Catalyst toward Electro-oxidation of Hydrogen and Methanol," *Electrochem. Solid-State Lett.*, vol. 5, no. 4, p. A80, 2002.

[79] X. G. Yang and C. Y. Wang, "Nanostructured tungsten carbide catalysts for polymer electrolyte fuel cells," *Appl. Phys. Lett.*, vol. 86, no. 22, p. 224104, 2005.

[80] S. K. Bej, C. A. Bennett, and L. T. Thompson, "Acid and base characteristics of molybdenum carbide catalysts," *Appl. Catal. Gen.*, vol. 250, no. 2, pp. 197–208, 2003.

[81] G. V. Naik, J. Kim, and A. Boltasseva, "Oxides and nitrides as alternative plasmonic materials in the optical range ," *Opt. Mater. Express*, vol. 1, no. 6, p. 1090, 2011.

[82] J. Vetter, E. Lugscheider, and S. S. Guerreiro, "(Cr:Al)N coatings deposited by the cathodic vacuum are evaporation," *Surf. Coat. Technol.*, vol. 98, no. 1–3, pp. 1233–1239, 1998.

[83] Z. B. Zhao, Z. U. Rek, S. M. Yalisove, and J. C. Bilello, "Nanostructured chromium nitride films with a valley of residual stress," *Thin Solid Films*, vol. 472, no. 1–2, pp. 96–104, 2005.

[84] M. Brama, N. Rhodes, J. Hunt, A. Ricci, R. Teghil, S. Migliaccio, C. D. Rocca, S. Leccisotti, A. Lioi, M. Scandurra, G. De Maria, D. Ferro, F. Pu, G. Panzini, L. Politi, and R. Scandurra, "Effect of titanium carbide coating on the osseointegration response in vitro and in vivo," *Biomaterials*, vol. 28, no. 4, pp. 595–608, 2007.

[85] Sudipta Seal, "Transition metal nitride functional coatings," *JOM-J. Miner. Met. Mater. Soc.*, vol. 53, Issue 9, pp. 51–54, 2001.

[86] Jericho McCune, "Titanium Carbon Nitride Uses." http://www.ehow.com/list_6618018_titanium-carbon-nitride-uses.html#ixzz2XygbTZ6C

[87] M. Herrmann, C. Schuber, A. Rendtel, and H. Hübner, "Silicon Nitride/Silicon Carbide Nanocomposite Materials: I, Fabrication and Mechanical Properties at Room Temperature," *J. Am. Ceram. Soc.*, vol. 81, no. 5, pp. 1095–1108, 2005.

[88] R. A. Andrievski, "Nanomaterials based on high-melting carbides, nitrides and borides," *Russ. Chem. Rev.*, vol. 74, no. 12, pp. 1061–1072, 2005.

[89] N. B. Dahotre, P. Kadolkar, and S. Shah, "Refractory ceramic coatings: processes, systems and wettability/adhesion," *Surf. Interface Anal.*, vol. 31, no. 7, pp. 659–672, 2001.

[90] G. E. Hollox, "Microstructure and mechanical behavior of carbides," *Mater. Sci. Eng.*, vol. 3, no. 3, pp. 121–137, 1968.

[91] M. Erola, J. Keinonen, A. Anttila, and J. Koskinen, "TiN films prepared by nitrogen implantation on Ti-coated fused SiO_2," *Sol. Energy Mater.*, vol. 12, no. 5, pp. 353–359, 1985.

[92] C. Ernsberger, "Contact resistance behavior of titanium nitride," *J. Vac. Sci. Technol. Vac. Surf. Films*, vol. 3, no. 6, p. 2303, 1985.

[93] I. Suni, "Thermal Stability of Hafnium and Titanium Nitride Diffusion Barriers in Multilayer Contacts to Silicon," *J. Electrochem. Soc.*, vol. 130, no. 5, p. 1215, 1983.

[94] K. Luo, Y. Liu, F. Wang, M. Gao, and H. Pan, "Hydrogen storage in a Li–Al–N ternary system," *Int. J. Hydrog. Energy*, vol. 34, no. 19, pp. 8101–8107, 2009.

[95] G. C. Hadjipanayis, "Nanophase hard magnets," *J. Magn. Magn. Mater.*, vol. 200, no. 1–3, pp. 373–391, 1999.

[96] B. Claflin, "Interface studies of tungsten nitride and titanium nitride composite metal gate electrodes with thin dielectric layers," *J. Vac. Sci. Technol. Vac. Surf. Films*, vol. 16, no. 3, p. 1757, 1998.

[97] Q. Guo and A. Yoshida, "Temperature Dependence of Band Gap Change in InN and AlN," *Jpn. J. Appl. Phys.*, vol. 33, no. Part 1, No. 5A, pp. 2453–2456, 1994.

[98] J. Wu, W. Walukiewicz, K. M. Yu, J. W. Ager, E. E. Haller, H. Lu, and W. J. Schaff, "Small band gap bowing in $In_{1-x}Ga_xN$ alloys," *Appl. Phys. Lett.*, vol. 80, no. 25, p. 4741, 2002.

[99] I. Vurgaftman and J. R. Meyer, "Band parameters for nitrogen-containing semiconductors," *J. Appl. Phys.*, vol. 94, no. 6, p. 3675, 2003.

[100] S. Senda, H. Jiang, and T. Egawa, "AlInN-based ultraviolet photodiode grown by metal organic chemical vapor deposition," *Appl. Phys. Lett.*, vol. 92, no. 20, p. 203507, 2008.

[101] P. E. Malinowski, J.-Y. Duboz, P. De Moor, K. Minoglou, J. John, S. M. Horcajo, F. Semond, E. Frayssinet, P. Verhoeve, M. Esposito, B. Giordanengo, A. BenMoussa, R. Mertens, and C. Van Hoof, "Extreme ultraviolet detection using AlGaN-on-Si inverted Schottky photodiodes," *Appl. Phys. Lett.*, vol. 98, no. 14, p. 141104, 2011.

[102] M. Razeghi, "III-Nitride Optoelectronic Devices: From Ultraviolet Toward Terahertz," *IEEE Photonics J.*, vol. 3, no. 2, pp. 263–267, 2011.

[103] X. Wang and T.-T. Lim, "Solvothermal synthesis of C–N codoped TiO_2 and photocatalytic evaluation for bisphenol A degradation using a visible-light irradiated LED photoreactor," *Appl. Catal. B Environ.*, vol. 100, no. 1–2, pp. 355–364, 2010.

[104] S. K. Rawal, A. K. Chawla, R. Jayaganthan, and R. Chandra, "The influence of various sputtering parameters on structural, wettability and optical properties of Zr_2ON_2 thin films," *Mater. Sci. Eng. B*, vol. 181, pp. 16–23, 2014.

[105] P. Carvalho, F. Vaz, L. Rebouta, L. Cunha, C. J. Tavares, C. Moura, E. Alves, A. Cavaleiro, P. Goudeau, E. Le Bourhis, J. P. Rivière, J. F. Pierson, and O. Banakh, "Structural, electrical, optical, and mechanical characterizations of decorative ZrO_xN_y thin films," *J. Appl. Phys.*, vol. 98, no. 2, p. 023715, 2005.

[106]   S. C. Tsang, V. Caps, I. Paraskevas, D. Chadwick, and D. Thompsett, "Magnetically Separable, Carbon-Supported Nanocatalysts for the Manufacture of Fine Chemicals," *Angew. Chem. Int. Ed.*, vol. 43, no. 42, pp. 5645–5649, 2004.

[107]   A.-H. Lu, W. Schmidt, N. Matoussevitch, H. Bönnemann, B. Spliethoff, B. Tesche, E. Bill, W. Kiefer, and F. Schüth, "Nanoengineering of a Magnetically Separable Hydrogenation Catalyst," *Angew. Chem. Int. Ed.*, vol. 43, no. 33, pp. 4303–4306, 2004.

[108]   A. A. Voevodin, J. P. O'Neill, and J. S. Zabinski, "Nanocomposite tribological coatings for aerospace applications," *Surf. Coat. Technol.*, vol. 116–119, pp. 36–45, 1999.

[109]   V. D. Krstic, M. D. Vlajic, and R. A. Verrall, *Advanced Ceramic Materials*, vol. 122–1. Switzerland: Trans Tech Publications Ltd, 1996.

[110]   R. A. Andrievski, "Films of interstitial phases: synthesis and properties," *J. Mater. Sci.*, vol. 32, no. issue 17, pp. 4463–4484, 1997.

[111]   P. Schaaf, M. Kahle, and E. Carpene, "Reactive laser synthesis of carbides and nitrides," *Appl. Surf. Sci.*, vol. 247, no. 1–4, pp. 607–615, 2005.

[112]   A. Friedrich, B. Winkler, E. A. Juarez-Arellano, and L. Bayarjargal, "Synthesis of Binary Transition Metal Nitrides, Carbides and Borides from the Elements in the Laser-Heated Diamond Anvil Cell and Their Structure-Property Relations," *Materials*, vol. 4, no. 12, pp. 1648–1692, 2011.

[113]   J. A. Nelson and M. J. Wagner, "High Surface Area Nanoparticulate Transition Metal Carbides Prepared by Alkalide Reduction," *Chem. Mater.*, vol. 14, no. 10, pp. 4460–4463, 2002.

[114]   B. M. Eick and J. P. Youngblood, "Carbothermal reduction of metal-oxide powders by synthetic pitch to carbide and nitride ceramics," *J. Mater. Sci.*, vol. 44, no. 5, pp. 1159–1171, 2009.

[115]   B. Vaidhyanathan and K. J. Rao, "Synthesis of Ti, Ga, and V Nitrides: Microwave-Assisted Carbothermal Reduction and Nitridation," *Chem. Mater.*, vol. 9, no. 5, pp. 1196–1200, 1997.

[116]   J. F. LePage, R. Schlgl, M. S. Wainwright, F. Sch, K. Unger, E. I. Ko, H. Jacobsen, P. Kleinschmit, R. G. Menon, B. Delmon, K.-Y. Lee, M. Misino, and S. T. Oyama, "Preparation of Solid Catalysts: Sections 2.0 and 2.1," in *Handbook of Heterogeneous Catalysis*, G. Ertl, H. Knzinger, and J. Weitkamp, Eds. Weinheim, Germany: Wiley-VCH Verlag GmbH, pp. 49–138.

[117]   S. Kaskel, K. Schlichte, G. Chaplais, and M. Khanna, "Synthesis and characterisation of titanium nitride based nanoparticles," *J. Mater. Chem.*, vol. 13, no. 6, p. 1496, 2003.

[118]   O. I. Mićić, S. P. Ahrenkiel, D. Bertram, and A. J. Nozik, "Synthesis, structure, and optical properties of colloidal GaN quantum dots," *Appl. Phys. Lett.*, vol. 75, no. 4, p. 478, 1999.

[119]   F. C. Sauls and L. V. Interrante, "Coordination compounds of aluminum as precursors to aluminum nitride," *Coord. Chem. Rev.*, vol. 128, no. 1–2, pp. 193–207, 1993.

[120]   H. Y. Leng, T. Ichikawa, S. Hino, N. Hanada, S. Isobe, and H. Fujii, "Synthesis and decomposition reactions of metal amides in metal–N–H hydrogen storage system," *J. Power Sources*, vol. 156, no. 2, pp. 166–170, 2006.

[121]   A. Manz, A. Birkner, M. Kolbe, and R. A. Fischer, "Solution Synthesis of Colloidal Gallium Nitride at Unprecedented Low Temperatures," *Adv. Mater.*, vol. 12, no. 8, pp. 569–573, 2000.

[122] Z. A. Munir, "Synthesis of High-Temperature Materials by Self-Propagating Combustion Methods," *Am. Ceram. Soc. Bull.*, vol. Vol. 67 Issue 2, pp. 342–349, 1988.

[123]   A. Varma and J. P. Lebrat, "Combustion synthesis of advanced materials," *Chem. Eng. Sci.*, vol. 47, no. 9–11, pp. 2179–2194, 1992.

[124]   V. Schwartz and S. T. Oyama, "Study of Niobium Oxynitride: Synthesis, Characterization, and Reactivity," *Chem. Mater.*, vol. 9, no. 12, pp. 3052–3059, 1997.

[125]   J. Wang, L. Grocholl, and E. G. Gillan, "Facile Azidothermal Metathesis Route to Gallium Nitride Nanoparticles," *Nano Lett.*, vol. 2, no. 8, pp. 899–902, . 2002.

[126]   Y. Huang, Y. Gu, M. Zheng, Z. Xu, W. Zeng, and Y. Liu, "Synthesis of nanocrystalline titanium nitride by reacting titanium dioxide with sodium amide," *Mater. Lett.*, vol. 61, no. 4–5, pp. 1056–1059, 2007.

[127]   T. Wade, C. B. Ross, and R. M. Crooks, "Electrochemical Synthesis of Ceramic Materials. 5. An Electrochemical Method Suitable for the Preparation of Nine Metal Nitrides," *Chem. Mater.*, vol. 9, no. 1, pp. 248–254, 1997.

[128]   K. Sardar, F. L. Deepak, A. Govindaraj, M. M. Seikh, and C. N. R. Rao, "InN Nanocrystals, Nanowires, and Nanotubes," *Small*, vol. 1, no. 1, pp. 91–94, 2004.

[129]   S. Desmoulins-Krawiec, C. Aymonier, A. Loppinet-Serani, F. Weill, S. Gorsse, J. Etourneau, and F. Cansell, "Synthesis of nanostructured materials in supercritical ammonia: nitrides, metals and oxides," *J. Mater. Chem.*, vol. 14, no. 2, p. 228, 2004.

[130]   L. Grocholl, J. Wang, and E. G. Gillan, "Solvothermal Azide Decomposition Route to GaN Nanoparticles, Nanorods, and Faceted Crystallites," *Chem. Mater.*, vol. 13, no. 11, pp. 4290–4296, 2001.

[131]   I. Kim and P. N. Kumta, "Hydrazide sol-gel synthesis of nanostructured titanium nitride: precursor chemistry and phase evolution," *J. Mater. Chem.*, vol. 13, no. 8, p. 2028, 2003.

[132]   J. Buha, I. Djerdj, M. Antonietti, and M. Niederberger, "Thermal Transformation of Metal Oxide Nanoparticles into Nanocrystalline Metal Nitrides Using Cyanamide and Urea as Nitrogen Source," *Chem. Mater.*, vol. 19, no. 14, pp. 3499–3505, 2007.

[133]   K. J. Rao, B. Vaidhyanathan, M. Ganguli, and P. A. Ramakrishnan, "Synthesis of Inorganic Solids Using Microwaves," *Chem. Mater.*, vol. 11, no. 4, pp. 882–895, 1999.

[134]   A. Kafizas, C. J. Carmalt, and I. P. Parkin, "CVD and precursor chemistry of transition metal nitrides," *Coord. Chem. Rev.*, vol. 257, no. 13–14, pp. 2073–2119, 2013.

[135]   C. Giordano and M. Antonietti, "Synthesis of crystalline metal nitride and metal carbide nanostructures by sol–gel chemistry," *Nano Today*, vol. 6, no. 4, pp. 366–380, 2011.

[136]   C. Giordano, C. Erpen, W. Yao, B. Milke, and M. Antonietti, "Metal Nitride and Metal Carbide Nanoparticles by a Soft Urea Pathway," *Chem. Mater.*, vol. 21, no. 21, pp. 5136–5144, 2009.

[137]   P. D. Godfrey, R. D. Brown, and A. N. Hunter, "The shape of urea," *J. Mol. Struct.*, vol. 413–414, pp. 405–414, 1997.

[138]   F. Kurzer and P. M. Sanderson, "Urea in the history of organic chemistry: Isolation from natural sources," *J. Chem. Educ.*, vol. 33, no. 9, p. 452, 1956.

[139] J. A. Swift, A. M. Reynolds, and M. D. Ward, "Cooperative Host−Guest Recognition in Crystalline Clathrates: Steric Guest Ordering by Molecular Gears," *Chem. Mater.*, vol. 10, no. 12, pp. 4159–4168, 1998.

[140] K. A. Wood, R. G. Snyder, and H. L. Strauss, "Analysis of the vibrational bandwidths of alkane–urea clathrates," *J. Chem. Phys.*, vol. 91, no. 9, p. 5255, 1989.

[141] F.M. Lee and L. E. Lahti, "Solubility of urea in water-alcohol mixtures," *J. Chem. Eng. Data*, vol. 17, no. 3, pp. 304–306, 1972.

[142] B. M. Bhanage, S. Fujita, Y. Ikushima, and M. Arai, "Non-catalytic clean synthesis route using urea to cyclic urea and cyclic urethane compounds," *Green Chem.*, vol. 6, no. 2, p. 78, 2004.

[143] K. Nakamoto, *Infrared and Raman Spectra of Inorganic and Coordination Compounds*. Hoboken, NJ, USA: John Wiley & Sons, Inc., 2008.

[144] T. Theophanides and P. D. Harvey, "Structural and spectroscopic properties of metal-urea complexes," *Coord. Chem. Rev.*, vol. 76, pp. 237–264, 1987.

[145] R. Keuleers, H. O. Desseyn, B. Rousseau, and C. Van Alsenoy, "Vibrational Analysis of Urea," *J. Phys. Chem. A*, vol. 103, no. 24, pp. 4621–4630, 1999.

[146] S. Podsiadło, "Stages of the synthesis of gallium nitride with the use of urea," *Thermochim. Acta*, vol. 256, no. 2, pp. 367–373, 1995.

[147] S. Podsiadło, "Stages of the synthesis of indium nitride with the use of urea," *Thermochim. Acta*, vol. 256, no. 2, pp. 375–380, 1995.

[148] Y. Qiu and L. Gao, "Novel Synthesis of Nanocrystalline Gallium Nitride Powder from Gallium(III)-Urea Complex," *Chem. Lett.*, vol. 32, no. 8, pp. 774–775, 2003.

[149] Y. Qiu and L. Gao, "Metal-Urea Complex-A Precursor to Metal Nitrides," *J. Am. Ceram. Soc.*, vol. 87, no. 3, pp. 352–357, 2004.

[150] K. Sardar, M. Dan, B. Schwenzer, and C. N. R. Rao, "A simple single-source precursor route to the nanostructures of AlN, GaN and InN," *J. Mater. Chem.*, vol. 15, no. 22, p. 2175, 2005.

[151] A. Patterson, "The Scherrer Formula for X-Ray Particle Size Determination," *Phys. Rev.*, vol. 56, no. 10, pp. 978–982, 1939.

[152] P. Scherrer, "Estimation of the size and structure of colloidal particles by Rontgen rays," *Nachrichten Von Koniglicher Ges. Wiss. Zu Gottingen Math.-Phys. Kl.*, vol. 2, pp. 96–100, 1918.

[153] X. X. Bi, K. D. Chowdhury, R. Ochoa, W. T. Lee, S. Bandow, M. S. Dresselhaus, and P. C. Eklund, "Structural characterization of nanocrystalline Mo and W carbide and nitride catalysts produced by CO_2 laser pyrolysis," *Mater. Res. Soc. Symp. Proc.*, vol. 69, no. 368, pp. 69–74, 1995.

[154] G. M. Pound and V. K. L. Mer, "Kinetics of Crystalline Nucleus Formation in Supercooled Liquid Tin," *J. Am. Chem. Soc.*, vol. 74, no. 9, pp. 2323–2332, 1952.

[155] C. Giordano, C. Erpen, W. Yao, and M. Antonietti, "Synthesis of Mo and W Carbide and Nitride Nanoparticles via a Simple 'Urea Glass' Route," *Nano Lett.*, vol. 8, no. 12, pp. 4659–4663, 2008.

[156] Milke Bettina, "Synthese von Metallnitrid- und Metalloxinitridnanopartikeln für energierelevante Anwendungen Dissertation," University of Potsdam, Potsdam, 2012.

[157] D. H. Jack and K. H. Jack, "Invited review: Carbides and nitrides in steel," *Mater. Sci. Eng.*, vol. 11, no. 1, pp. 1–27, 1973.

[158]   Q. Gao, S. Wang, Y. Ma, Y. Tang, C. Giordano, and M. Antonietti, "SiO$_2$-Surface-Assisted Controllable Synthesis of TaON and Ta$_3$N$_5$ Nanoparticles for Alkene Epoxidation," *Angew. Chem. Int. Ed.*, vol. 51, no. 4, pp. 961–965, 2012.

[159]   H. Sigel, "Interactions of metal ions with nucleotides and nucleic acids and their constituents," *Chem. Soc. Rev.*, vol. 22, no. 4, p. 255, 1993.

[160]   I. Corral, O. Mó, M. Yáñez, J.-Y. Salpin, J. Tortajada, and L. Radom, "Gas-Phase Reactions between Urea and Ca^{2+}: The Importance of Coulomb Explosions," *J. Phys. Chem. A*, vol. 108, no. 46, pp. 10080–10088, 2004.

[161]   M. Noguera, J. Bertran, and M. Sodupe, "A Quantum Chemical Study of Cu^{2+} Interacting with Guanine−Cytosine Base Pair. Electrostatic and Oxidative Effects on Intermolecular Proton-Transfer Processes," *J. Phys. Chem. A*, vol. 108, no. 2, pp. 333–341, 2004.

[162]   C. Schliehe and C. Giordano, "Bottom-up synthesis of Zn$_{1.7}$GeN$_{1.8}$O nanoparticles for photocatalytic application," *Nanoscale*, vol. 5, no. 8, p. 3235, 2013.

[163]   M. Maunaye and J. Lang, "Preparation et proprietes de ZnGeN$_2$," *Mater. Res. Bull.*, vol. 5, no. 9, pp. 793–796, 1970.

[164]   F. G. McIntosh, K. S. Boutros, J. C. Roberts, S. M. Bedair, E. L. Piner, and N. A. El-Masry, "Growth and characterization of AlInGaN quaternary alloys," *Appl. Phys. Lett.*, vol. 68, no. 1, p. 40, 1996.

[165]   W. Lei, D. Liu, Y. Ma, X. Chen, F. Tian, P. Zhu, X. Chen, Q. Cui, and G. Zou, "Scandium-Doped AlN 1D Hexagonal Nanoprisms: A Class of Room-Temperature Ferromagnetic Materials," *Angew. Chem. Int. Ed.*, vol. 49, no. 1, pp. 173–176, 2010.

[166]   W. Lei, D. Liu, X. Chen, P. Zhu, Q. Cui, and G. Zou, "Ferromagnetic Properties of Y-Doped AlN Nanorods," *J. Phys. Chem. C*, vol. 114, no. 37, pp. 15574–15577, 2010.

[167]   F. S. Liu, Q. L. Liu, J. K. Liang, G. B. Song, L. T. Yang, J. Luo, Y. Q. Zhou, H. W. Dong, and G. H. Rao, "Low-temperature synthesis and characterization of GaN nanocrystals from gallium trichloride precursor," *J. Mater. Res.*, vol. 19, no. 12, pp. 3484–3489, 2011.

[168]   Y. Xiong, Y. Xie, Z. Li, X. Li, and R. Zhang, "Aqueous synthesis of group IIIA nitrides at low temperature," *New J. Chem.*, vol. 28, no. 2, p. 214, 2004.

[169]   M.P. Pileni, "Magnetic Fluids: Fabrication, Magnetic Properties, and Organization of Nanocrystals," *Adv. Funct. Mater.*, vol. 11, no. 5, pp. 323–336, 2001.

[170]   T. Hyeon, "Chemical synthesis of magnetic nanoparticles," *Chem. Commun.*, no. 8, pp. 927–934, 2003.

[171]   A. K. Gupta and M. Gupta, "Synthesis and surface engineering of iron oxide nanoparticles for biomedical applications," *Biomaterials*, vol. 26, no. 18, pp. 3995–4021, 2005.

[172]   S. Mornet, S. Vasseur, F. Grasset, and E. Duguet, "Magnetic nanoparticle design for medical diagnosis and therapy," *J. Mater. Chem.*, vol. 14, no. 14, p. 2161, 2004.

[173]   A. A. Kuznetsov, V. I. Filippov, O. A. Kuznetsov, V. G. Gerlivanov, E. K. Dobrinsky, and S. I. Malashin, "New ferro-carbon adsorbents for magnetically guided transport of anti-cancer drugs," *J. Magn. Magn. Mater.*, vol. 194, no. 1–3, pp. 22–30, 1999.

[174]   A. Jordan, P. Wust, H. Fählin, W. John, A. Hinz, and R. Felix, "Inductive heating of ferrimagnetic particles and magnetic fluids: Physical evaluation of their potential for hyperthermia," *Int. J. Hyperthermia*, vol. 9, no. 1, pp. 51–68, 1993.

[175]   D. W. Elliott and W. Zhang, "Field Assessment of Nanoscale Bimetallic Particles for Groundwater Treatment," *Environ. Sci. Technol.*, vol. 35, no. 24, pp. 4922–4926,2001.

[176]   M. Takafuji, S. Ide, H. Ihara, and Z. Xu, "Preparation of Poly(1-vinylimidazole)-Grafted Magnetic Nanoparticles and Their Application for Removal of Metal Ions," *Chem. Mater.*, vol. 16, no. 10, pp. 1977–1983, May 2004.

[177]   Y. Wang and B. H. Davis, "Fischer–Tropsch synthesis. Conversion of alcohols over iron oxide and iron carbide catalysts," *Appl. Catal. Gen.*, vol. 180, no. 1–2, pp. 277–285,1999.

[178]   J. Park, K. An, Y. Hwang, J.-G. Park, H.-J. Noh, J.-Y. Kim, J.-H. Park, N.-M. Hwang, and T. Hyeon, "Ultra-large-scale syntheses of monodisperse nanocrystals," *Nat. Mater.*, vol. 3, no. 12, pp. 891–895, 2004.

[179]   W. Yang, J. Lee, S. Hong, J. Lee, J. Lee, and D.-W. Han, "Difference between Toxicities of Iron Oxide Magnetic Nanoparticles with Various Surface-Functional Groups against Human Normal Fibroblasts and Fibrosarcoma Cells," *Materials*, vol. 6, no. 10, pp. 4689–4706, 2013.

[180]   G. Liu, J. Gao, H. Ai, and X. Chen, "Applications and Potential Toxicity of Magnetic Iron Oxide Nanoparticles," *Small*, vol. 9, no. 9–10, pp. 1533–1545, 2013.

[181]   Y. F. Li and C. Chen, "Fate and Toxicity of Metallic and Metal-Containing Nanoparticles for Biomedical Applications," *Small*, vol. 7, no. 21, pp. 2965–2980, 2011.

[182]   S.I. Hirano and S. Tajima, "Synthesis and magnetic properties of Fe_5C_2 by reaction of iron oxide and carbon monoxide," *J. Mater. Sci.*, vol. 25, no. 10, pp. 4457–4461, 1990.

[183]   S. Tajima and S. Hirano, "Synthesis and Magnetic Properties of Fe_7C_3 Particles with High Saturation Magnetization," *Jpn. J. Appl. Phys.*, vol. 29, no. Part 1, No. 4, pp. 662–668,1990.

[184]   F. Cheng, "Characterization of aqueous dispersions of Fe_3O_4 nanoparticles and their biomedical applications," *Biomaterials*, vol. 26, no. 7, pp. 729–738,2005.

[185] J. G. Kim, K. H. Han, C. K. Lee, J. Y. Jeong, and K. H. Shin, "Crystallographic and magnetic properties of nanostructured hematite synthesized by the sol-gel process," *J. KOREAN Phys. Soc.*, no. Vol.38 Issue 6, pp. 798–802, 2001.

[186]   H. Naganuma, Y. Endo, R. Nakatani, Y. Kawamura, and M. Yamamoto, "Magnetic properties of weak itinerant ferromagnetic ζ-Fe_2N film," *Sci. Technol. Adv. Mater.*, vol. 5, no. 1–2, pp. 83–87, 2004.

[187]   S. Kurian and N. S. Gajbhiye, "Magnetic and Mössbauer study of ε-Fe_yN ($2<y<3$) nanoparticles," *J. Nanoparticle Res.*, vol. 12, no. 4, pp. 1197–1209,2009.

[188]   K. Mitsuoka, H. Miyajima, H. Ino, and S. Chikazumi, "Induced Magnetic Moment in Ferromagnetic Fe Alloys by Tetragonally Elongated Lattice Expansion," *J. Phys. Soc. Jpn.*, vol. 53, no. 7, pp. 2381–2390, 1984.

[189]   N. Ji, L. F. Allard, E. Lara-Curzio, and J.-P. Wang, "N site ordering effect on partially ordered $Fe_{16}N_2$," *Appl. Phys. Lett.*, vol. 98, no. 9, p. 092506, 2011.

[190]   M. Takahashi and H. Shoji, "α″-$Fe_{16}N_2$ problem - giant magnetic moment or not," *J. Magn. Magn. Mater.*, vol. 208, no. 3, pp. 145–157,2000.

[191]   J. H. Kim, J. Kim, J. H. Park, C. K. Kim, C. S. Yoon, and Y. Shon, "Synthesis of carbon-encapsulated iron carbide nanoparticles on a polyimide thin film," *Nanotechnology*, vol. 18, no. 11, p. 115609, 2007.

[192] A. Tsuzuki, S. Sago, S.-I. Hirano, and S. Naka, "High temperature and pressure preparation and properties of iron carbides Fe_7C_3 and Fe_3C," *J. Mater. Sci.*, vol. 19, no. 8, pp. 2513–2518, 1984.

[193] G. Huang, J. Hu, H. Zhang, Z. Zhou, X. Chi, and J. Gao, "Highly magnetic iron carbide nanoparticles as effective T2 contrast agents," *Nanoscale*, vol. 6, no. 2, p. 726, 2014.

[194] W. Tang, Z. Zhen, C. Yang, L. Wang, T. Cowger, H. Chen, T. Todd, K. Hekmatyar, Q. Zhao, Y. Hou, and J. Xie, "Fe_5C_2 Nanoparticles with High MRI Contrast Enhancement for Tumor Imaging," *Small*, p. n/a–n/a, 2013.

[195] C. Yang, H. Zhao, Y. Hou, and D. Ma, "Fe_5C_2 Nanoparticles: A Facile Bromide-Induced Synthesis and as an Active Phase for Fischer–Tropsch Synthesis," *J. Am. Chem. Soc.*, vol. 134, no. 38, pp. 15814–15821, 2012.

[196] *The archaeometallurgy of the Asian old world*. Philadelphia: Museum University of Pennsylvania, 1999.

[197] D. Johnson, J. Tyldesley, T. Lowe, P. J. Withers, and M. M. Grady, "Analysis of a prehistoric Egyptian iron bead with implications for the use and perception of meteorite iron in ancient Egypt," *Meteorit. Planet. Sci.*, vol. 48, no. 6, pp. 997–1006, 2013.

[198] V. Manfredi, *The Last Legion: a novel*, 1st Washington Square Press trade pbk. ed. New York: Washington Square Press, 2005.

[199] D. Hughes, *The British chronicles*. Westminster, Md.: Heritage Books, 2007.

[200] C. M. Fang, M. A. van Huis, and H. W. Zandbergen, "Structural, electronic, and magnetic properties of iron carbide Fe_7C_3 phases from first-principles theory," *Phys. Rev. B*, vol. 80, no. 22, 2009.

[201] V. A. Barinov, V. A. Tsurin, and V. T. Surikov, "Study of mechanically synthesized carbide Fe_7C_3," *Phys. Met. Metallogr.*, vol. 110, no. 5, pp. 474–484, 2010.

[202] X. X. Bi, B. Ganguly, G. P. Huffman, F. E. Huggins, M. Endo, and P. C. Eklund, "Nanocrystalline α–Fe, Fe_3C, and Fe_7C_3 produced by CO2 laser pyrolysis," *J. Mater. Res.*, vol. 8, no. 07, pp. 1666–1674, 2011.

[203] A. K. Schaper, H. Hou, A. Greiner, and F. Phillipp, "The role of iron carbide in multiwalled carbon nanotube growth," *J. Catal.*, vol. 222, no. 1, pp. 250–254, 2004.

[204] I. K. Herrmann, R. N. Grass, D. Mazunin, and W. J. Stark, "Synthesis and Covalent Surface Functionalization of Nonoxidic Iron Core−Shell Nanomagnets," *Chem. Mater.*, vol. 21, no. 14, pp. 3275–3281, 2009.

[205] Y. Koltypin, X. Cao, R. Prozorov, J. Balogh, D. Kaptas, and A. Gedanken, "Sonochemical synthesis of iron nitride nanoparticles," *J. Mater. Chem.*, vol. 7, no. 12, pp. 2453–2456, 1997.

[206] R. S. Ningthoujam and N. S. Gajbhiye, "Magnetic study of single domain ε-Fe3N nanoparticles synthesized by precursor technique," *Mater. Res. Bull.*, vol. 43, no. 5, pp. 1079–1085, 2008.

[207] C. Giordano, A. Kraupner, S. C. Wimbush, and M. Antonietti, "Iron Carbide: An Ancient Advanced Material," *Small*, vol. 6, no. 17, pp. 1859–1862, 2010.

[208] R. B. Penland, S. Mizushima, C. Curran, and J. V. Quagliano, "Infrared Absorption Spectra of Inorganic Coördination Complexes. X. Studies of Some Metal-Urea Complexes," *J. Am. Chem. Soc.*, vol. 79, no. 7, pp. 1575–1578, 1957.

[209]   A. Ahniyaz, G. A. Seisenbaeva, L. Häggström, S. Kamali, V. G. Kessler, P. Nordblad, C. Johansson, and L. Bergström, "Preparation of iron oxide nanocrystals by surfactant-free or oleic acid-assisted thermal decomposition of a Fe(III) alkoxide," *J. Magn. Magn. Mater.*, vol. 320, no. 6, pp. 781–787, 2008.

[210]   M. Antonietti, M. Niederberger, and B. Smarsly, "Self-assembly in inorganic and hybrid systems: beyond the molecular scale," *Dalton Trans.*, no. 1, p. 18, 2008.

[211]   L. J. E. Hofer and E. M. Cohn, "Saturation Magnetizations of Iron Carbides," *J. Am. Chem. Soc.*, vol. 81, no. 7, pp. 1576–1582, 1959.

[212]   Kraupner Alexander, "Neuartige Synthese magnetischer Nanostrukturen: Metallcarbide und Metallnitride der Übergangsmetalle Fe/Co/Ni," University of Potsdam, Potsdam, 2011.

[213]   Robert G. Charles, W. M. Hickam, and Joan von Hoene, "The Pyrolysis of Acetylacetone," *J. Phys. Chem.*, vol. 63, no. 12, pp. 2084–2085, 1959.

[214]   A. Kraupner, Markus Antonietti, R. Palkovits, K. Schlicht, and C. Giordano, "Mesoporous Fe_3C sponges as magnetic supports and as heterogeneous catalyst," *J. Mater. Chem.*, vol. 20, no. 29, p. 6019, 2010.

[215]   Z. Schnepp, M. Thomas, S. Glatzel, K. Schlichte, R. Palkovits, and C. Giordano, "One pot route to sponge-like Fe_3N nanostructures," *J. Mater. Chem.*, vol. 21, no. 44, p. 17760, 2011.

[216]   C. Giordano, A. Kraupner, I. Fleischer, C. Henrich, G. Klingelhöfer, and M. Antonietti, "Non-conventional Fe_3C-based nanostructures," *J. Mater. Chem.*, vol. 21, no. 42, p. 16963, 2011.

[217]   B. L. V. Prasad, H. Sato, T. Enoki, S. Cohen, and T. P. Radhakrishnan, "Copper(II) complexes of a novel ligand 4,5-dicyanoimidazole: structural and magnetic studies," *J. Chem. Soc. Dalton Trans.*, no. 1, pp. 25–30, 1999.

[218]   M. R. Wixom, "Chemical Preparation and Shock Wave Compression of Carbon Nitride Precursors," *J. Am. Ceram. Soc.*, vol. 73, no. 7, pp. 1973–1978, 1990.

[219]   C. Schliehe, J. Yuan, S. Glatzel, K. Siemensmeyer, K. Kiefer, and C. Giordano, "Iron Nitride and Carbide: from Crystalline Nanoparticles to Stable Aqueous Dispersions," *Chem. Mater.*, vol. 24, no. 14, pp. 2716–2721, 2012.

[220]   O. Ayyad, D. Muñoz-Rojas, J. Oró-Solé, and P. Gómez-Romero, "From silver nanoparticles to nanostructures through matrix chemistry," *J. Nanoparticle Res.*, vol. 12, no. 1, pp. 337–345, 2009.

[221]   A. G. Nasibulin, A. Moisala, H. Jiang, and E. I. Kauppinen, "Carbon nanotube synthesis from alcohols by a novel aerosol method," *J. Nanoparticle Res.*, vol. 8, no. 3–4, pp. 465–475, 2006.

[222]   Wang Y., Bai X. D., and Liang J., *New Carbon Mater.*, vol. 20, p. 103, 2005.

[223]   Z. Schnepp, S. C. Wimbush, M. Antonietti, and C. Giordano, "Synthesis of Highly Magnetic Iron Carbide Nanoparticles via a Biopolymer Route," *Chem. Mater.*, vol. 22, no. 18, pp. 5340–5344, 2010.

[224]   P. Z. Hong, S.-D. Li, C.-Y. Ou, C.-P. Li, L. Yang, and C. H. Zhang, "Thermogravimetric analysis of chitosan," *J. Appl. Polym. Sci.*, vol. 105, no. 2, pp. 547–551, 2007.

[225]   Z. A. C. Schnepp, S. C. Wimbush, S. Mann, and S. R. Hall, "Structural Evolution of Superconductor Nanowires in Biopolymer Gels," *Adv. Mater.*, vol. 20, no. 9, pp. 1782–1786, 2008.

[226] G. T. Grant, E. R. Morris, D. A. Rees, P. J. C. Smith, and D. Thom, "Biological interactions between polysaccharides and divalent cations: The egg-box model," *FEBS Lett.*, vol. 32, no. 1, pp. 195–198, 1973.

[227] S. Kurian and N. S. Gajbhiye, "Low temperature and in-field Mössbauer spectroscopic studies of ε-Fe$_3$N particles synthesized from iron–citrate complex," *Chem. Phys. Lett.*, vol. 493, no. 4–6, pp. 299–303, 2010.

[228] A. Ōya and S. Ōtani, "Catalytic graphitization of carbons by various metals," *Carbon*, vol. 17, no. 2, pp. 131–137, 1979.

[229] Metzke Sarah, "Synthesis and Characterization of Transition Metal Nitrides and Carbides for Catalysis and Electrochemistry Application," University of Potsdam, Potsdam, 2013.

[230] S. Glatzel, Z. Schnepp, and C. Giordano, "From Paper to Structured Carbon Electrodes by Inkjet Printing," *Angew. Chem. Int. Ed.*, vol. 52, no. 8, pp. 2355–2358, 2013.

[231] Glatzel Stefan, "Cellulose Based Transition Metal Nano-Composites Structuring and Development," University of Potsdam, Potsdam, 2012.

[232] A. V. Neimark, Y. Lin, P. I. Ravikovitch, and M. Thommes, "Quenched solid density functional theory and pore size analysis of micro-mesoporous carbons," *Carbon*, vol. 47, no. 7, pp. 1617–1628, 2009.

[233] P. Judeinstein and C. Sanchez, "Hybrid organic-inorganic materials: a land of multidisciplinarity," *J. Mater. Chem.*, vol. 6, no. 4, p. 511, 1996.

[234] *Hybrid materials: synthesis, characterization, and applications*. Weinheim: Wiley - VCH, 2007.

[235] V. Castelvetro and C. De Vita, "Nanostructured hybrid materials from aqueous polymer dispersions," *Adv. Colloid Interface Sci.*, vol. 108–109, pp. 167–185, 2004.

[236] P. Sonström, M. Adam, X. Wang, M. Wilhelm, G. Grathwohl, and M. Bäumer, "Colloidal Nanoparticles Embedded in Ceramers: Toward Structurally Designed Catalysts," *J. Phys. Chem. C*, vol. 114, no. 33, pp. 14224–14232, 2010.

[237] C. Giordano and T. Corbiere, "A step forward in metal nitride and carbide synthesis: from pure nanopowders to nanocomposites," *Colloid Polym. Sci.*, vol. 291, no. 6, pp. 1297–1311, 2012.

[238] B. Milke, C. Wall, S. Metzke, G. Clavel, M. Fichtner, and C. Giordano, "A simple synthesis of MnN$_{0.43}$@C core-shell nanoparticles for battery applications," *Submitted*.

[239] D. Mitoraj and H. Kisch, "Analysis of Electronic and Photocatalytic Properties of Semiconductor Powders through Wavelength-Dependent Quasi-Fermi Level and Reactivity Measurements," *J. Phys. Chem. C*, vol. 113, no. 49, pp. 20890–20895, 2009.

[240] G. Clavel, V. Molinari, A. Kraupner, and C. Giordano, "Easy access to Ni$_3$N- and Ni-carbon nanocomposite catalysts," *submitted*.

[241] Z. Smekal, F. Brezina, Z. Sindelar, R. Klicka, and M. Nadvornik, "Polynuclear complexes of chromium(III), copper(II) or nickel(II) with thiocyanate as a bridging ligand," *Transit. Met. Chem.*, vol. 22, no. 3, pp. 299–301, 1997.

[242] Z. Smekal, F. Brezina, Z. Sindelar, R. Klicka, and M. Nadvornik, "Polynuclear complexes of nickel(II) with cyanide as bridging ligand," *Chem. Pap.*, vol. 51, no. 2, pp. 95–98, 1997.

[243] S. Pagano, G. Montana, C. Wickleder, and W. Schnick, "Urea Route to Homoleptic Cyanates-Characterization and Luminescence Properties of [M(OCN)$_2$ (urea)] and M(OCN)$_2$ with M=Sr, Eu," *Chem. - Eur. J.*, vol. 15, no. 25, pp. 6186–6193, 2009.

[244] C. Giordano, W. Yang, A. Lindemann, R. Crombez, and J. Texter, "Waterborne WC nanodispersions," *Colloids Surf. Physicochem. Eng. Asp.*, vol. 374, no. 1–3, pp. 84–87, 2011.

[245] V. Khare, A. Kraupner, A. Mantion, A. Jeličić, A. F. Thünemann, C. Giordano, and A. Taubert, "Stable Iron Carbide Nanoparticle Dispersions in [Emim][SCN] and [Emim][N(CN)$_2$] Ionic Liquids," *Langmuir*, vol. 26, no. 13, pp. 10600–10605, 2010.

[246] T. Aida and T. Fukushima, "Soft materials with graphitic nanostructures," *Philos. Trans. R. Soc. Math. Phys. Eng. Sci.*, vol. 365, no. 1855, pp. 1539–1552, 2007.

[247] T. Fukushima, "Molecular Ordering of Organic Molten Salts Triggered by Single-Walled Carbon Nanotubes," *Science*, vol. 300, no. 5628, pp. 2072–2074, 2003.

[248] J. Sun, S. Zhou, P. Hou, Y. Yang, J. Weng, X. Li, and M. Li, "Synthesis and characterization of biocompatible Fe$_3$O$_4$ nanoparticles," *J. Biomed. Mater. Res. A*, vol. 80A, no. 2, pp. 333–341, 2007.

[249] M. Antonietti, Y. Shen, T. Nakanishi, M. Manuelian, R. Campbell, L. Gwee, Y. A. Elabd, N. Tambe, R. Crombez, and J. Texter, "Single-Wall Carbon Nanotube Latexes," *ACS Appl. Mater. Interfaces*, vol. 2, no. 3, pp. 649–653, 2010.

[250] F. Yan and J. Texter, "Surfactant ionic liquid-based microemulsions for polymerization," *Chem. Commun.*, no. 25, p. 2696, 2006.

[251] F. Yan and J. Texter, "Solvent-Reversible Poration in Ionic Liquid Copolymers," *Angew. Chem. Int. Ed.*, vol. 46, no. 14, pp. 2440–2443, 2007.

[252] K. Tauer, N. Weber, and J. Texter, "Core–shell particle interconversion with di-stimuli-responsive diblock copolymers," *Chem. Commun.*, no. 40, p. 6065, 2009.

[253] M. Zhao and R. M. Crooks, "Homogeneous Hydrogenation Catalysis with Monodisperse, Dendrimer-Encapsulated Pd and Pt Nanoparticles," *Angew. Chem. Int. Ed.*, vol. 38, no. 3, pp. 364–366, 1999.

[254] E. Amstad, T. Gillich, I. Bilecka, M. Textor, and E. Reimhult, "Ultrastable Iron Oxide Nanoparticle Colloidal Suspensions Using Dispersants with Catechol-Derived Anchor Groups," *Nano Lett.*, vol. 9, no. 12, pp. 4042–4048, 2009.

[255] E. van den Pol, A. V. Petukhov, D. M. E. Thies-Weesie, and G. J. Vroege, "Simple Rectangular Columnar Phase of Goethite Nanorods and Its Martensitic Transition to the Centered Rectangular Columnar Phase," *Langmuir*, vol. 26, no. 3, pp. 1579–1582, 2010.

[256] C. J. Murphy, T. K. Sau, A. M. Gole, C. J. Orendorff, J. Gao, L. Gou, S. E. Hunyadi, and T. Li, "Anisotropic Metal Nanoparticles: Synthesis, Assembly, and Optical Applications," *J. Phys. Chem. B*, vol. 109, no. 29, pp. 13857–13870, 2005.

[257] H. Hou, J. J. Ge, J. Zeng, Q. Li, D. H. Reneker, A. Greiner, and S. Z. D. Cheng, "Electrospun Polyacrylonitrile Nanofibers Containing a High Concentration of Well-Aligned Multiwall Carbon Nanotubes," *Chem. Mater.*, vol. 17, no. 5, pp. 967–973, 2005.

[258] A. García-Márquez, D. Portehault, and C. Giordano, "Chromium nitride and carbide nanofibers: from composites to mesostructures," *J. Mater. Chem.*, vol. 21, no. 7, p. 2136, 2011.

[259]   J. Zha and H. Roggendorf, "Sol-gel science, the physics and chemistry of sol-gel processing, Ed. by C. J. Brinker and G. W. Scherer, Academic Press, Boston 1990, xiv, 908 pp., 0-12-134970-5," *Adv. Mater.*, vol. 3, no. 10, pp. 522–522, 1991.

[260]   U. Schubert, "Cluster-based inorganic–organic hybrid materials," *Chem. Soc. Rev.*, vol. 40, no. 2, p. 575, 2011.

[261]   D. Chaira, B. K. Mishra, and S. Sangal, "Efficient synthesis and characterization of iron carbide powder by reaction milling," *Powder Technol.*, vol. 191, no. 1–2, pp. 149–154, 2009.

[262]   Z. Schnepp, W. Yang, M. Antonietti, and C. Giordano, "Biotemplating of Metal Carbide Microstructures: The Magnetic Leaf," *Angew. Chem. Int. Ed.*, vol. 49, no. 37, pp. 6564–6566, 2010.

[263] V. Maurice, G. Clavel, M. Antonietti, and C. Giordano, "Aerosol assisted synthesis of porous TiNxOy@C nanocomposites," *Submitted*

[264]   C. Boissiere, D. Grosso, A. Chaumonnot, L. Nicole, and C. Sanchez, "Aerosol Route to Functional Nanostructured Inorganic and Hybrid Porous Materials," *Adv. Mater.*, vol. 23, no. 5, pp. 599–623, 2011.

[265]   G. L. Messing, S.-C. Zhang, and G. V. Jayanthi, "Ceramic Powder Synthesis by Spray Pyrolysis," *J. Am. Ceram. Soc.*, vol. 76, no. 11, pp. 2707–2726,1993.

[266]   J. D. Orbell, E. K. Tan, M. Coutts, S. W. Bigger, and L. N. Ngeh, "Cleansing Oiled Feathers – Magnetically," *Mar. Pollut. Bull.*, vol. 38, no. 3, pp. 219–221, 1999.

[267]   A. Pavía-Sanders, S. Zhang, J. A. Flores, J. E. Sanders, J. E. Raymond, and K. L. Wooley, "Robust Magnetic/Polymer Hybrid Nanoparticles Designed for Crude Oil Entrapment and Recovery in Aqueous Environments," *ACS Nano*, vol. 7, no. 9, pp. 7552–7561, 2013.

[268]   J. Huang, Y. Cui, and X. Wang, "Visible Light-Sensitive ZnGe Oxynitride Catalysts for the Decomposition of Organic Pollutants in Water," *Environ. Sci. Technol.*, vol. 44, no. 9, pp. 3500–3504, 2010.

[269]   B. Dou, M. Zhang, J. Gao, W. Shen, and X. Sha, "High-Temperature Removal of NH_3, Organic Sulfur, HCl, and Tar Component from Coal-Derived Gas," *Ind. Eng. Chem. Res.*, vol. 41, no. 17, pp. 4195–4200, 2002.

[270]   W. Mojtahedi and J. Abbasian, "Catalytic decomposition of ammonia in a fuel gas at high temperature and pressure," *Fuel*, vol. 74, no. 11, pp. 1698–1703, 1995.

[271]   A. Boisen, S. Dahl, J. Norskov, and C. Christensen, "Why the optimal ammonia synthesis catalyst is not the optimal ammonia decomposition catalyst," *J. Catal.*, vol. 230, no. 2, pp. 309–312, 2005.

[272]   W. Yao, P. Makowski, C. Giordano, and F. Goettmann, "Synthesis of Early-Transition-Metal Carbide and Nitride Nanoparticles through the Urea Route and Their Use as Alkylation Catalysts," *Chem. - Eur. J.*, vol. 15, no. 44, pp. 11999–12004, 2009.

[273]   A. Villa, S. Campisi, C. Giordano, K. Otte, and L. Prati, "Mo and W Carbide: Tunable Catalysts for Liquid Phase Conversion of Alcohols," *ACS Catal.*, vol. 2, no. 7, pp. 1377–1380, 2012.

[274]   P. J. Cordeiro and T. D. Tilley, "Enhancement of Epoxidation Efficiencies for Ta-SBA15 Catalysts. The Influence of Modification with –EMe₃ (E = Si, Ge, Sn) Groups," *Langmuir*, vol. 27, no. 10, pp. 6295–6304, 2011.

[275] D. A. Ruddy and T. D. Tilley, "Highly selective olefin epoxidation with aqueous H$_2$O$_2$ over surface-modified TaSBA15 prepared via the TMP method," *Chem. Commun.*, no. 32, p. 3350, 2007.

[276] D. A. Ruddy and T. D. Tilley, "Kinetics and Mechanism of Olefin Epoxidation with Aqueous H$_2$O$_2$ and a Highly Selective Surface-Modified TaSBA15 Heterogeneous Catalyst," *J. Am. Chem. Soc.*, vol. 130, no. 33, pp. 11088–11096, 2008.

[277] M. Guidotti, C. Pirovano, N. Ravasio, B. Lázaro, J. M. Fraile, J. A. Mayoral, B. Coq, and A. Galarneau, "The use of H$_2$O$_2$ over titanium-grafted mesoporous silica catalysts: a step further towards sustainable epoxidation," *Green Chem.*, vol. 11, no. 9, p. 1421, 2009.

[278] H. Li, Q. Lei, X. Zhang, and J. Suo, "Nitrogen-Incorporated TS-1 Zeolite Obtained by Post-Synthetic Nitridation," *ChemCatChem*, vol. 3, no. 1, pp. 143–145, 2011.

[279] V. Molinari, C. Giordano, M. Antonietti, and D. Esposito, "Titanium Nitride-Nickel Nanocomposite as Heterogeneous Catalyst for the Hydrogenolysis of Aryl Ethers," *J. Am. Chem. Soc.*, vol. 136, no. 5, pp. 1758–1761, 2014.

[280] A. Fernández Guillermet and K. Frisk, "Thermodynamic properties of ni nitrides and phase stability in the Ni-N system," *Int. J. Thermophys.*, vol. 12, no. 2, pp. 417–431, 1991.

[281] F. Badway, N. Pereira, F. Cosandey, and G. G. Amatucci, "Carbon-Metal Fluoride Nanocomposites," *J. Electrochem. Soc.*, vol. 150, no. 9, p. A1209, 2003.

[282] Y. Ma and S. H. Garofalini, "Atomistic Insights into the Conversion Reaction in Iron Fluoride: A Dynamically Adaptive Force Field Approach," *J. Am. Chem. Soc.*, vol. 134, no. 19, pp. 8205–8211, 2012.

[283] R. Prakash, C. Wall, A. K. Mishra, C. Kübel, M. Ghafari, H. Hahn, and M. Fichtner, "Modified synthesis of [Fe/LiF/C] nanocomposite, and its application as conversion cathode material in lithium batteries," *J. Power Sources*, vol. 196, no. 14, pp. 5936–5944, 2011.

[284] C. Wall, R. Prakash, C. Kübel, H. Hahn, and M. Fichtner, "Synthesis of [Co/LiF/C] nanocomposite and its application as cathode in lithium-ion batteries," *J. Alloys Compd.*, vol. 530, pp. 121–126, 2012.

[285] M. A. Reddy, B. Breitung, V. S. K. Chakravadhanula, C. Wall, M. Engel, C. Kübel, A. K. Powell, H. Hahn, and M. Fichtner, "CF$_x$ Derived Carbon-FeF$_2$ Nanocomposites for Reversible Lithium Storage," *Adv. Energy Mater.*, vol. 3, no. 3, pp. 308–313, 2013.

[286] Q. Sun and Z.-W. Fu, "Mn$_3$N$_2$ as a novel negative electrode material for rechargeable lithium batteries," *Appl. Surf. Sci.*, vol. 258, no. 7, pp. 3197–3201, 2012.

[287] Y. Sharma, N. Sharma, G. V. S. Rao, and B. V. R. Chowdari, "Nano-(Cd$_{1/3}$Co$_{1/3}$Zn$_{1/3}$)CO$_3$: a new and high capacity anode material for Li-ion batteries," *J. Mater. Chem.*, vol. 19, no. 28, p. 5047, 2009.

13. Publications List (anti chronological order)

Manuscripts Submitted

IV Milke B., Wall C., Metzke S., Clavel G., Fichtner M., Giordano C., "A simple synthesis of $MnN_{0.43}$@C core-shell nanoparticles for battery applications", *submitted*

III Glatzel S., Schnepp Z., Giordano C., "Magnetic Fe_3C/C Nano-Composites through Biomorphology Replication as Novel Absorber and Filtration Agents", *submitted*

II Maurice V., Antonietti M., Giordano C., "Aerosol assisted synthesis of porous titanium nitride nanoparticles", *submitted to J. Mater. Chem. (under revision)*

I Clavel G., Molinari V., Kraupner A., Giordano C., "Easy access to Ni_3N- and Ni-carbon nanocomposite catalysts", *submitted*

Reviews

46 **2013** Giordano C., Corbiere T., "A step forward in metal nitride and carbide synthesis: from pure nanopowders to nanocomposites", *Colloids and Polymer Science,* 291, 6, 1297-1311*,* <u>Invited paper</u>

45 **2011** Giordano C., Antonietti M., "Synthesis of Crystalline Metal nitride and Metal carbide Nanostructures by Sol-Gel Chemistry", *Nano Today*, *6*, 366

Publications from the habilitation work

2014

44 Skorupska K., Giordano C., Zoladek S., Zurowki A., Milke B., Gao Q.S., Ramirez A., Fiechter S., Lewerenz H.J., Kulesza P.J., Semiconducting Ta_3N_5-polymer Nanohybrid that Photoelectrolyze Water, *ECS Transactions*, *(accepted)*

43 Molinari V., Esposito D., Giordano C., Antonietti M., "Titanium Nitride-Nickel Nanocomposites as Heterogeneous Catalysts for the Hydrogenolysis of Aryl Ethers: toward depolymerization of Lignin", *JACS (accepted)*

2013

42 Shalom M., Molinari V., Esposito D., Clavel G., Ressnig D., Giordano C., Antonietti M., "Sponge like Nickel and Nickel Nitride Structures for Catalytic Applications", *Advanced Materials*, adma.201304288R1 *accepted*

41 Gupta S., Giordano C., Gradzielski M., Mehta K, "Microwave-Assisted Synthesis of Small Ru Nanoparticles and Their role in Degradation of Congo Red", *accepted*

40 Kaur R., Giordano C., Gradzielski M., Mehta S., "Synthesis of Long-Time Stable, Water Dispersible Copper Nanoparticles as Catalysts for Nitrobenzene Reduction" *Chemistry: An Asian Journal, accepted*

39 Liu X., Giordano C., Antonietti M., "A Facile Molten-Salt Route to Graphene Synthesis", *Small*, **2013**, DOI: 10.1002/smll.201300812

38 Glatzel S., Schnepp Z., Giordano C., "From paper to structured carbon electrodes by inkjet printing, *Angew. Chem. Int. Ed.*, 52, 2355-2358, **2013**

37 Schliehe C., Giordano C., "Bottom-up Synthesis of $Zn_{1.7}GeN_{1.8}O$ Nanoparticles for Photocatalytic applications", *Nanoscale,* 5, 3235-3239, **2013**, <u>Advance Article</u>

36 Liu X., Giordano C., Antonietti M., Manipulation of phase and microstructure at nanoscale for SiC with molten salt synthesis: an unconventional ionothermal route", *Chem. Mat,* 25, 2021-2027, **2013**

35 Corbiere T., Ressnig D., Giordano C., Antonietti M., "Focused Radiation Heating for Controlled High temperature Chemistry, exemplified with the Preparation of Vanadium Nitride Nanoparticles", *RCS Advances, accepted*

34 Petkov V., Hessel C. M., Ovtchinnikoff J., Guillaussier A., Korgel B.A., Liu X, Giordano C., "Structure-Properties Correlation in Si Nanoparticles by Total Scattering and Computer Simulations", *Chem. Mat., DOI: 10.1021/cm401099q*

2012

33 Gao Q., Wang S., Ma Y., Tang Y., Giordano C., Antonietti M, "SiO_2-Surface-Assisted Controllable Synthesis of TaON and Ta_3N_5 Nanoparticles for Alkene Epoxidation", *Angew. Chem. Int. Ed.*, 51, 961–965, **2012**

32 Gao Q. S., Wang S. N., Tang Y., Giordano C., "Preparation of organic-inorganic hybrid Fe-MoOx/polyaniline nanorods as efficient catalysts for alkene epoxidation. *Chemical Communications* 48, 2, 260-262, **2012**

31 Liu X., Giordano C., Antonietti M, "A molten-salt route for synthesis of Si and Ge nanoparticles: chemical reduction of oxides by electrons solvated in salt melt", *Journal of Materials Chemistry, 22*, 12, 5454-5459, **2012**

30 Schliehe C., Yuan J., Glatzel S., Siemensmeyer K., Kiefer K., Giordano C., "Iron nitride and carbide: from crystalline nanoparticles to stable aqueous dispersions", *Chemistry of Materials*, *24, 2716−2721,* **2012**

29 Göbel R., Xie Z.L., Neumann M., Günter C., Löbbicke R., Kubo S., Titirici M.M., Giordano C., Taubert A., Synthesis of mesoporous carbon/iron carbide hybrids with unusually high surface areas from the ionic liquid precursor [Bmim][FeCl₄]", *CrystEngComm, 14, 4946–4951,* **2012**

28 Villa A., Campisi S., Giordano C., Otte K., Prati L., "Mo and W carbide: tunable catalysts for liquid phase oxidation of alcohols", *ACS Catal. 2, 1377−1380,* **2012**

2011

27 Garcia-Marquez A., Portehault D., Giordano C., "Chromium Nitride and Carbide

Nanofibers: from Composites to Mesostructures", *Journal of Materials Chemistry*, 21, 2136, **2011**

26 Portehault D., Devi S., Beaunier P., Gervais, C., Giordano C., Sanchez S., Antonietti M., *"A General Solution Route toward Metal Boride Nanocrystals." Angewandte Chemie Int. Ed., 50*, 3262, **2011**, <u>VIP paper</u>

25 Yuan J., García Márquez A., Reinacher J., Giordano C., Janek J., Antonietti M., "Nitrogen-doped carbon fibers and membranes by carbonization of electrospun poly(ionic liquid)s", *Polymer Chemistry*, *2*, 1654, **2011**

24 Giordano C., Yang W., Lindemann A., Crombez R., Texter J., "Waterbone WC Nanodispersions", *Colloids and Surfaces A: Physicochem. Eng. Aspects*, 374, 84, **2011**

23 Yuan J., Schlaad H., Giordano C., Antonietti M., *Europ. Polym. Journal*, Special Issue, *47*, 775, **2011**

22 Giordano C., Kraupner A., Fleischer I., Henrich C., Klingelhöfer G., Antonietti M., "Non-Conventional Fe$_3$C-based nanostructures", *Journal of Materials Chemistry*, *21*, 42, 16963-16967, **2011**

21 Gao Q., Giordano C. , Antonietti M., "Controlled Synthesis of Tantalum Oxynitride and Nitride Nanoparticles", *Small*, 7, 23, 3334-3340, **2011**

20 Schnepp Z., Thomas M., Glatzel S., Schlicht K., Palkovits R., Giordano C., "One-pot route to sponge-like Fe$_3$N nanostructure", *Journal of Materials Chemistry*, *21*, 44, 17760-17764, **2011**

2010

19 Kraupner A., Antonietti M., Palkovits R., Schlicht K., Giordano C., "Mesoporous Fe$_3$C sponges as magnetic supports and as heterogeneous Catalyst", *Journal of Materials Chemistry*, 20, 6019, **2010**, <u>highlighted paper</u>

18 Texter J., Tambe N., Crombez R., Antonietti M., Giordano C., "Stimuli responsive coatings of carbon nanotubes and nanoparticles using ionic liquid-based nanolatexes", *Polymeric Materials: Science & Engineering, 102,* 401, **2010**

17 Schnepp Z., Yang W., Antonietti M., Giordano C., "Biotemplating of Metal and Metal Carbide Microstructures: The Magnetic Leaf", *Angewandte Chemie Int. Ed., 49*, 6564, **2010**

16 Portehault D., Giordano C., Sanchez C., Antonietti M., "Non Aqueous Route toward a Nanostructured Hybrid Titanate" *Chemistry of Materials*, *22*, 2125, **2010**

15 Portehault D., Giordano C., Gervais C., Senkovska I., Sanchez C., Antonietti M. "High-Surface-Area Nanoporous Boron Carbon Nitrides for Hydrogen Storage", *Advanced Functional Materials, 20*, 1827, **2010**

14 Khare V., Kraupner A., Mantion A., Jelicic A., Thunemann A., Giordano C. and

Taubert A., "Stable iron carbide nanoparticle dispersions in [Emim][SCN] and [Emim][N(CN)$_2$] ionic liquids", *Langmuir, 26,* 10600, **2010**

13 Giordano C. , Kraupner A., Wimbush C.S., Antonietti M., "Iron Carbide: An Ancient Advanced Material", *Small*, *6*, 1859, **2010**

12 Yuan J., Giordano C., Antonietti M., "Ionic Liquids Monomers and Polymers as Precursors of highly Conductive, Mesoporous, Graphitic Carbon Nanostructures", *Chemistry of Materials*, *22*, 5003, **2010**

11 Schnepp Z., Wimbush S., Antonietti M., Giordano C. , "Synthesis of Highly Magnetic Iron Carbide Nanoparticles via a Biopolymer Route", *Chemistry of Materials*, *22*, 5340, **2010**

Publications from the Post-Doc work

10 Giordano C., Erpen C., Yao W.T, Milke B., Antonietti M., "Metal Nitride and Metal Carbide Nanoparticles by a Soft Urea Pathway", *Chemistry of Materials*, 21, (21), 5136, **2009**

9 Yao W. T., Makowski P., Giordano C., Goettmann F., "Synthesis of Early Transition Metal Carbides and Nitrides Nanoparticles via the Urea Route and their Use as Alkylation Catalysts", *Chemistry - A European Journal*, 15, (44), 11999, **2009**

8 Milke B., Antonietti M., Giordano C., *Nanoscale*, 1, (1), 110, **2009**

7 Giordano C. , Erpen C., Yao W. T., Antonietti M., "Synthesis of Mo and W Carbide and Nitride Nanoparticles via a Simple "Urea Glass″ Route" *Nano Letters*, 8, (12), 4659, **2008**

Publications from the PhD work

6 Calandra P., Giordano C., Longo A., Turco Liveri V., "Physicochemical investigation of surfactant-coated gold nanoparticles synthesized in the confined space of dry reversed micelles" *Materials Chemistry and Physics* 98, 494-499, **2006**

5 Longo A., Calandra P., Casaletto M.P, Giordano C., Venezia A.M., Turco Liveri V., "Synthesis and physico-chemical characterization of gold nanoparticles softly coated by AOT" *Materials Chemistry and Physics* 96, 66-72, 2006, **2006**

4 Giordano C., Longo A., Ruggirello A., Turco Liveri V., Venezia, A.M., "Physicochemical Investigation of Cobalt-Iron Cyanide Nanoparticles Synthesized by a Novel Solid-Solid Reaction in Confined Space", *Coll. Polym. Sci*, 283, 265-276, **2004**

3 Calandra P., Giordano C., Ruggirello A., Turco Liveri V., "Physico-chemical investigation of acrylamide solubilisation in sodium bis(2-ethylhexyl) sulfosuccinate and lecithin reversed micelles", *J. Coll. Interf. Sci.,* 277, 206-214, **2004**

2 Buongiorno D., Ceraulo L., Ferrugia M., Filizzola F., Giordano C., Ruggirello A.,

Turco Liveri V., "1H-NMR and FT-IR study of the state of melatonin confined in membrane models: location and interactions of melatonin in water free lecithin and AOT reversed micelles", ARKIVOC 251, **2004**

Publication from the Diploma work

1   Giordano C., Longo A., Turco Liveri V., Venezia A.M., "Physico-Chemical Investigation of the Solubilization of Cobalt Nitrate in AOT Reverse Micelles", *Coll. Polym. Sci*, 281, 229-238, **2003**

Others

Press release

From the Paper "Gratzel S., Schnepp Z., Giordano C., "From paper to structured carbon electrodes by inkjet printing, *Angew. Chem. Int. Ed.*, 52, 2355-2358, **2013**

- http://www.mpg.de/6963505/Papier_Elektronik
- Several requested interviews (Bayrischer Rundfunk, B5 Aktuell, *Berliner Curier*, VDI (Association of German Engineers)
- Press article on Chemistry World "Origami Carbon Electrode" (p.5) March 2013
- Press article on Swiss journal CHEMIEXTRA (www.chemiextra.com), (p.36-37) April 2013

From the Paper "Biotemplating of Metal and Metal Carbide Microstructures: The Magnetic Leaf", Angewandte Chemie Int. Ed., 2010, 49, 6564, **2010**

- http://www.mpg.de/603519/pressemitteilung20100913

Giordano, C., Ruggirello, A. and Turco Liveri, V.: "Sistemi Microeterogenei per la Sintesi di Nanoparticelle" (Microheterogeneus systems in Nanoparticle Synthesis)

- Nanotec IT Newsletter, 1, 15-16, **2004**

Blogs

- Paper "Biotemplating of Metal and Metal Carbide Microstructures: The Magnetic Leaf", Angewandte Chemie Int. Ed., 2010, 49, 6564, **2010**

  http://www.scienceinseconds.com/blog/The-Wolverine-Leaf